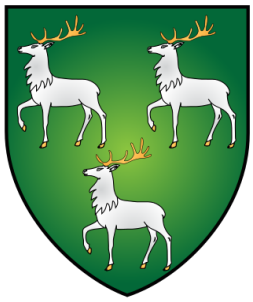
Phenomenological studies of top quark production in the forward region of phase space at the LHC

Rhorry Gauld
Jesus College, Oxford





CERN-THESIS-2014-266
21/08/2014



Thesis submitted in fulfilment of the requirements for the degree of Doctor of Philosophy at the University of Oxford

Trinity Term, 2014

Abstract

This thesis contains phenomenological studies of top quark production in the forward region of phase space at the Large Hadron Collider (LHC). The production of highly forward top quarks has so far not been observed in nature. As the LHCb detector at the LHC is instrumented in the forward region, this opens the possibility of studying top quark properties in this yet unexplored region of phase space. This feasibility of performing cross section and charge asymmetry measurements of top quark pairs with available and future LHCb data is studied in detail. In both cases, potential analysis strategies are proposed, and sophisticated theoretical predictions are provided for both signal and background. By studying the expected experimental sensitivity of cross section measurements, the potential constraints on parton distribution functions is quantified. The sensitivity of the proposed charge asymmetry measurements with the full Run II LHCb data is also considered.

To Isabel, for your continued love and support.

Thank you for always being there for me, and for making me happy.

Acknowledgements

I would firstly like to thank Ulrich Haisch for his advice, support and friendship over the last few years. I feel fortunate to have had such a thoughtful, friendly and intelligent supervisor. I have also learnt a great deal of physics which has substantially improved the quality of my work and the way I think about physics problems. Thank you for also trying to (unsuccessfully) teach me the rules of Doppelkopf. I would also like to thank Malcolm John and Andrei Nomerotski for their advice at different times throughout my time here in Oxford.

Thanks to my colleagues at Oxford. In particular, I would like to thank Emanuele Re, Juan Rojo, and Amanda Cooper-Sarkar who have all offered me help and advice in my research. I would also like to thank my colleagues on LHCb whom I have received many useful suggestions from — Henry Brown, Victor Coco, Stephen Farry, and Cedric Potterat. Also, to my LHCb colleagues based in Oxford — Denis Derkach, Andrew Powell, and Christopher Thomas. I would also like to thank my collaborator Florian Goertz who has also taught me many things. I am also grateful for the college supervision I received from Phil Burrows - I could not have asked for a more friendly or wise mentor.

In addition I would like to thank the support of the Unix team in Oxford. Especially Sean Brisbane, who has always been quick to offer useful advice and help. My research has been funded by a Science and Technology Facilities Council studentship, and I am grateful for this opportunity. I have also received financial support from Jesus College, which has allowed me to attend a workshop at CERN as well as a summer school in Trieste.

On a more personal note, I would like to thank all of my friends in Oxford who have made my time here more fun, especially — Edmundo, Ed, Richard, Felix, Llorenz, Liam, Mike. Also, to my undergraduate friends — Kenny, Robin, Nick, Jeff, Geoff, Niall 'd', Huw, Mike, Mehmet, Julez, Scott, Stu, Raami, and many more. Thank you to all my friends based at CERN, who made me feel welcome every time I visited. Finally, to all the friends I have made during my time at conferences, schools and workshops — Juri, Michael, Tomas, Daniele, and the Kings College crew. You made them much more enjoyable. I feel very fortunate to have so many interesting and caring friends.

Of course, I would never be here if it weren't for the loving support of my family. Thank you for believing in me and for providing me with support my entire life. Thanks to my big brother Dylan, who beats me at Monopoly to show me who the boss is. A special thank you to my mother Lesley, for everything you have done. I am also thankful to Ann, Greg, Jemma and Pat who have made me feel welcome into their family. Finally, to Isabel, for caring for me, keeping me sane, introducing me to new types of food, but most importantly for making me happy.

Contents

Preface **1**

1 The Standard Model **3**
1.1 Introduction . . . 3
1.2 Electroweak Theory . . . 4
1.2.1 Gauge sector . . . 5
1.2.2 Higgs sector . . . 6
1.2.3 Matter content . . . 10
1.3 QCD . . . 14
1.3.1 QCD Lagrangian and colour algebra . . . 14
1.3.2 Gauge fixing and ghosts . . . 16
1.3.3 Feynman rules . . . 16
1.3.4 Renormalisation . . . 18
1.4 Summary . . . 22

2 Predicting LHC observables **24**
2.1 Introduction . . . 24
2.2 Fixed-order calculations and factorisation . . . 27
2.2.1 Fixed-order calculations . . . 27
2.2.2 Factorisation: the soft limit . . . 29
2.2.3 Factorisation: the collinear limit . . . 32
2.3 All-orders approach . . . 37
2.3.1 DGLAP Evolution . . . 38
2.3.2 Sudakov Form Factor . . . 43
2.4 NLO+PS . . . 44
2.4.1 POWHEG Method . . . 45
2.5 LPHD . . . 48
2.5.1 Hadronisation . . . 48
2.5.2 Jets . . . 49
2.6 PDFs . . . 52
2.6.1 Approaches to global fits . . . 53
2.6.2 Bayesian reweighting . . . 57
2.7 Summary . . . 59

3 Top quark production and decay **61**
3.1 Introduction . . . 61
3.2 Top quark properties . . . 63
3.2.1 Mass . . . 63
3.2.2 Couplings . . . 66
3.2.3 Decay . . . 67
3.3 Top quark production . . . 71
3.3.1 LO cross section . . . 72
3.3.2 NLO cross section . . . 77
3.3.3 Charge production asymmetry . . . 79
3.4 Motivations for high pseudorapidity measurements . . . 89
3.5 Summary . . . 92

4 Cross section measurements at LHCb **94**
4.1 Introduction . . . 94
4.2 Feasibility . . . 95
4.2.1 Final state selection . . . 96
4.3 Signal and background . . . 100
4.3.1 lepton+jets . . . 100
4.3.2 dilepton+jets . . . 104
4.4 Constraining the gluon PDF . . . 108
4.4.1 Theoretical systematics . . . 108
4.4.2 Reweighting analysis . . . 114
4.4.3 Potential sensitivity . . . 118
4.5 Summary . . . 121

5 Charge asymmetry measurements at LHCb **123**
5.1 Introduction . . . 123
5.2 Fixed-order asymmetries . . . 125
5.2.1 Top quark rate asymmetry . . . 127
5.2.2 Leptonic rate asymmetry . . . 131
5.2.3 Top quark forward-backward asymmetry . . . 134
5.2.4 Leptonic forward-backward asymmetry . . . 136
5.3 Experimental sensitivity . . . 138
5.3.1 Leptonic rate asymmetry . . . 138
5.3.2 Leptonic forward-backward asymmetry . . . 141
5.4 (N)LO+PS asymmetries . . . 142
5.5 Summary . . . 147

Conclusions **149**

A CKM Matrix **152**

B Quark self-energy **154**

Bibliography **158**

Preface

The Large Hadron Collider (LHC), at the European Organisation for Nuclear Research (CERN) is the world's largest and most powerful particle accelerator. The LHC accelerates two beams of oppositely travelling particles to extremely high energies. In a highly controlled environment, these two beams are independently guided around the LHC ring to specific crossing points where the beams are brought into contact. These interaction points correspond to the position of four particle detectors - ATLAS, ALICE, CMS, and LHCb.

By measuring the properties of these collisions, it is possible to test the theoretical framework which is used to describe physical interactions at the energy scales probed by the colliding beams. This framework is called the 'Standard Model' of particle physics, and will be discussed in detail in Chapter 1. This theory, which describes the electromagnetic, weak, and strong interactions of particles is extremely successful in providing explanations for experimentally observed phenomena. One of the most recent successes of the theory was the discovery of a Higgs boson like particle by the ATLAS and CMS experiments [1, 2] at 125 GeV. The Standard Model necessarily predicts the existence of the Higgs boson, and so the observation of this particle therefore adds to its success in providing an accurate description of nature.

There are however several other experimental observations which indicate the presence of physics beyond the scope of the Standard Model. It is therefore important to look for this new physics, by testing the Standard Model in as many ways as possible. At the LHC, one of the ways this can be achieved is to measure the properties of known particles. By precisely measuring the production rates, or distributions of known particles it is possible to test this framework by comparing these observations with the corresponding theoretical prediction.

One particle which is particularly interesting to study is the top quark. As the most massive elementary particle to have been observed in nature thus far, it has unique production and decay mechanisms. In this thesis, the prospects of measuring top quark pair production will be studied. In particular, top quarks which are produced at very small scattering angles with respect to the colliding beams. The LHCb detector is instrumented in such a region, and therefore opens the possibility of measuring top quark production in this region. The main goal of this these will be to demonstrate the feasibility of such measurements with the available and future LHCb data.

To do this, it will first be necessary to review how Standard Model predictions for LHC observables can be made. This will be the topic of Chapter 2. In Chapter 3, the properties of the top quark will be reviewed in detail, eventually leading to a discussion of the motivations for studying top quark pair production at LHCb. In Chapter 4, the prospects of top quark pair cross section measurements will be discussed. This will include the proposal of several potential analysis strategies, as well as a study of the potential sensitivity to particular theoretical uncertainties. In Chapter 5, predictions will be provided for the presence of top quark pair production asymmetries. The potential sensitivity of performing measurements of these asymmetries will also be quantified.

This thesis is based on original research which has been presented in [3–5] and contains no material that has already been accepted, or is currently being submitted, for any degree or diploma or certificate or qualification at the University of Oxford or elsewhere.

To the best of my knowledge and belief this thesis contains no material previously published or written by another person, except where due reference is made in the text.

Chapter 1

The Standard Model

This Section will be dedicated to reviewing the details of the Standard Model (SM) of electroweak (EW) and strong interactions, a necessary step before calculating meaningful physical quantities in later Chapters. The theory of strong interactions, Quantum Chromodynamics (QCD), is a non-abelian gauge theory of the gauge group $SU(3)_c$ coupled to fermions in the fundamental representation. The theory of weak and electromagnetic interactions of fermions is described by the gauge symmetry $SU(2)_L \times U(1)_Y$. In the case of QCD, the gauge bosons are massless while for EW interactions the gauge bosons are massive. The origin of massive gauge bosons, and fermion masses, can be understood as a result of the Higgs mechanism, in which the original EW symmetry is spontaneously broken to $U(1)_Q$. A general overview of the particle content, symmetries, and origin of fermion and boson masses will be provided in Section 1.2. The strong interactions will be discussed in more detail in Section 1.3.

1.1 Introduction

Quantum field theories constructed to obey the conservation of local symmetries provide robust predictions for the interactions of fundamental particles. For certain theories, the success of these predictions in describing physical processes suggests that symmetries are, to good approximation, an accurate description of nature. The local symmetry is generally a unitary transformation of a set of fields of the theory. Therefore, specifying the field content and symmetries of the theory fixes the form of the interactions and leaves just the

experimental determination of certain parameters. The physical quantities which are predicted, and compared to experimental observation, are scattering amplitudes of interacting particles. To ease the calculation of these amplitudes, a set of Feynman rules will be derived which allows a diagrammatic approach. One way of introducing this approach is through the method of functional integration. This amounts to integrating over all physically distinct quantum paths, where interactions are introduced by performing perturbation theory on the interaction Lagrangian density (Lagrangian). In this approach, the expectation values of spatially separated field operators (or Green's functions) have the form

$$G^{(N)}(y_1, ..., y_N) = \frac{\int [d\phi]\phi(y_1)...\phi(y_N)e^{iS_0+i\int \mathcal{L}_I(x)d^dx}}{\int [d\phi]e^{iS_0+i\int \mathcal{L}_I(x)d^dx}}\,, \tag{1.1}$$

corresponding to the expectation value of N fields. The connection between these Green's functions and scattering amplitudes is then provided by the LSZ formula [6]. Performing perturbation theory with the interaction Lagrangian $\mathcal{L}_\mathcal{I}$ leads to a series of higher order corrections to lowest order scattering processes. In order to derive the Feynman rules necessary for computing relevant amplitudes, a review of EW and QCD is provided. In the case of QCD, it will also be necessary to identify the energy scale at which the perturbative expansion remains reliable. More detail on these topics can be found in [7–11] which provide a thorough analysis of the SM, QCD and other quantum field theories.

1.2 Electroweak Theory

The EW sector is composed of two gauge couplings, g' corresponding to weak-hypercharge $U(1)_Y$, and g to weak isospin $SU(2)_L$ where the subscript L (left-handed) indicates the chiral nature of the interactions. Decomposing the Lagrangian $\mathcal{L}_{EW}$ into a gauge, Higgs, and fermion sector will allow each sector of the theory to be treated sequentially. It should be noted that this decomposition is rather arbitrary, as each of these sectors interacts with one another. With this particular decomposition in mind, the Lagrangian has the following

form

$$\mathcal{L}_{EW} = \mathcal{L}_{\text{gauge}} + \mathcal{L}_{\text{Higgs}} + \mathcal{L}_{\text{fermion}} \,. \tag{1.2}$$

1.2.1 Gauge sector

The EW gauge sector $SU(2)_L \times U(1)_Y$ is non-abelian with an abelian hypercharge subgroup. The gauge fields, which transform in the adjoint representation, corresponding to $SU(2)_L$ are labelled as W^i_μ, where $i = 1, .., 3$, and the gauge field associated to $U(1)_Y$ by B_μ. The field strength tensors in this sector are

$$\begin{aligned} B_{\mu\nu} &= \partial_\mu B_\nu - \partial_\nu B_\mu \,, \\ W^i_{\mu\nu} &= \partial_\mu W^i_\nu - \partial_\nu W^i_\mu - g\epsilon^{ijk} W^j_\mu W^k_\nu \,, \end{aligned} \tag{1.3}$$

where ϵ^{ijk} represents the $SU(2)$ structure constant (the fully antisymmetric Levi-Civita tensor). The Lagrangian, to mass dimension four, within the gauge sector is therefore

$$\mathcal{L}_{\text{gauge}} = -\frac{1}{4} B_{\mu\nu} B^{\mu\nu} - \frac{1}{4} W^i_{\mu\nu} W^{i,\mu\nu} \,. \tag{1.4}$$

The infinitesimal transformations of the gauge fields leaving this Lagrangian invariant are

$$\begin{aligned} \delta B_\mu &= -\frac{1}{g'} \partial_\mu \xi^Y \,, \\ \delta W^i_\mu &= -\frac{1}{g} \partial_\mu \xi^i + \epsilon^{ijk} W^j_\mu \xi^k \,. \end{aligned} \tag{1.5}$$

where ξ^Y and ξ^i are the infinitesimal parameters of $U(1)_Y$ and $SU(2)_L$ respectively. The field strength tensor for the non-abelian gauge fields is no longer gauge invariant, a consequence of its non-trivial transformation. However, gauge invariant quantities can be constructed by combining the three field strength tensors, such as the kinetic term for the W gauge fields present in (1.5). Note that the non-abelian term in the Lagrangian leads to self-couplings of the fields — this results in significant differences in the behaviour of the interactions with respect to an abelian theory, particularly after quantisation.

As the gauge transformations of the field must leave the Lagrangian invariant, it is not possible to write a term quadratic in the field which is gauge invariant. Therefore, it is not possible to include gauge invariant mass terms for gauge bosons without introducing a new mechanism for generating mass.

1.2.2 Higgs sector

The mechanism required to account for massive gauge bosons in a gauge invariant way, originating from the spontaneous symmetry breaking (SSB) of local symmetries, was proposed independently by Higgs, Brout and Englert, and Guralnik, Hagen and Kibble [12–14]. The Higgs mechanism, within the context of the EW sector, is also motivated by the requirement of constructing gauge invariant mass terms for fermions, this will be discussed in the following subsections.

In the SM, the most simple way to spontaneously break the EW gauge symmetry $SU(2)_L \times U(1)_Y$ is to couple the gauge fields to a complex scalar field which transforms as a doublet of $SU(2)_L$. This scalar field (ϕ) is

$$\phi = \begin{pmatrix} \phi^{\dagger} \\ \\ \phi^{0} \end{pmatrix} , \tag{1.6}$$

which is chosen to transform with hypercharge $Y = +1/2$. The corresponding Lagrangian is

$$\mathcal{L}_{\text{Higgs}} = (D_{\mu}\phi)^{\dagger}(D^{\mu}\phi) - V(\phi^{\dagger}\phi) \, , \tag{1.7}$$

where the covariant derivative coupling the scalar field to the gauge fields is

$$D_{\mu} = \partial_{\mu} + ig\tau^{i}W_{\mu}^{i} + ig'YB_{\mu} \, . \tag{1.8}$$

The generators Y and τ^{i} correspond to the gauge groups $U(1)_Y$ and $SU(2)_L$ respectively

(evaluated in the representation of the field). The potential for the scalar field is defined as

$$V(\phi^\dagger\phi) = -\mu^2\phi^\dagger\phi + \lambda(\phi^\dagger\phi)^2\,, \tag{1.9}$$

where λ must be positive so that the potential is bounded from below for large field values — a necessary requirement for the stability of the Universe. The infinitesimal field transformations leaving this Lagrangian invariant are

$$\delta\phi = i(\xi^Y Y + \xi^i\tau^i)\phi\,. \tag{1.10}$$

If the value of μ^2 in (1.9) is negative, the minimum of the potential — corresponding to a vacuum expectation value (VEV) — is at zero, and the vacuum state preserves the gauge symmetries. If, however, the value of μ^2 is positive, the minimum of the potential can be found at

$$\langle\phi^\dagger\phi\rangle = \frac{\mu^2}{2\lambda}\,. \tag{1.11}$$

There are an infinite number of equivalent possible solutions mapping out the surface of a sphere in $SU(2)$ space. The selection of a specific ground state is the process responsible for breaking the symmetry. Making the choice

$$\langle\phi\rangle = \frac{1}{\sqrt{2}}\begin{pmatrix}0\\ \\ v\end{pmatrix}\,, \tag{1.12}$$

demonstrates that the vacuum state is not left invariant under the previous field transformations. This vacuum state is however left invariant under the following transformation

$$\delta\phi' = i(\xi^Y Y + \xi^3\tau^3)\phi\,, \tag{1.13}$$

corresponding to a residual non-trivial $U(1)_Q$ subgroup of $SU(2)_L \times U(1)_Y$, with the generator $Q = Y + \tau^3$. Having selected a particular direction for the VEV, the properties of the theory can then be obtained by expanding around the classical ground state. This is

done by reparameterising the scalar field (1.6) in terms of the ground state. One possible reparameterisation is

$$\phi = \exp\left(i\tau^i \frac{\chi_i}{v}\right) \frac{1}{\sqrt{2}} \begin{pmatrix} 0 \\ v+h \end{pmatrix} \approx \frac{1}{\sqrt{2}} \begin{pmatrix} i\sqrt{2}\omega^+ \\ v+h-i\omega^0 \end{pmatrix}, \tag{1.14}$$

where $\omega^\pm$ ($\sqrt{2}(\chi_1 \mp i\chi_2)$) and ω^0 ($2\chi_3$) are Goldstone bosons and h is a scalar degree of freedom which, in total, correspond to the four original degrees of freedom of the scalar field. Noting that this reparameterisation is simply a gauge transformation under $SU(2)_L$, it is possible to perform a gauge transformation to align the field in the direction of the VEV as

$$\phi' = \frac{1}{\sqrt{2}} \begin{pmatrix} 0 \\ v+h \end{pmatrix}. \tag{1.15}$$

Alternatively, ϕ can be inserted in its current form while simultaneously performing the gauge transformation on the covariant derivative — this explicitly demonstrates how the gauge bosons absorb the degrees of freedom of the scalar field. Substituting in the parameterisation, after aligning the field with the VEV, the Higgs Lagrangian becomes

$$\mathcal{L}_{\text{Higgs}} = \left| \frac{1}{\sqrt{2}} \begin{pmatrix} 0 \\ \partial_\mu h \end{pmatrix} + \frac{ig}{2\sqrt{2}}(v+h) \begin{pmatrix} W^1_\mu - iW^2_\mu \\ -W^3_\mu + \frac{g'}{g}B_\mu \end{pmatrix} \right|^2 + \frac{\mu^2}{2}(v+h)^2 - \frac{\lambda}{4}(v+h)^4 . \tag{1.16}$$

At this stage, it becomes clear that the mass matrix for the neutral gauge bosons will not be diagonal due to the mixing of the W^3_μ and B_μ fields. This can be remedied by performing an orthogonal rotation of the gauge fields. The form of the physical charged gauge bosons (a mixture of W^1_μ and W^2_μ) is also apparent from inspection of the first row of the scalar-gauge coupling in (1.16). Together, these observations suggest the definitions

$$\begin{pmatrix} A_\mu \\ Z_\mu \end{pmatrix} = \begin{pmatrix} c_w & s_w \\ -s_w & c_w \end{pmatrix} \begin{pmatrix} B_\mu \\ W^3_\mu \end{pmatrix}, \qquad W^\pm_\mu = \frac{1}{\sqrt{2}}(W^1_\mu \mp iW^2_\mu), \tag{1.17}$$

where $s_w = \sin\theta_w$, $c_w = \cos\theta_w$, and θ_w is the weak mixing angle. The mixing angle θ_w is related to the couplings of the gauge groups through the relations

$$s_w^2 = \frac{g'^2}{g^2 + g'^2}\,, \qquad c_w^2 = \frac{g^2}{g^2 + g'^2}\,. \tag{1.18}$$

The origin of this rotation angle is easily understood. Calculating the mass matrix for the gauge bosons W_μ^3 and B_μ in the original basis results in an off-diagonal matrix. The two eigenvalues of this matrix are M_Z and 0, and the rotation necessary to diagonalise the mass matrix is exactly this orthogonal transformation with the angle θ_w.

As the mass eigenstates are the physical eigenstates of the propagating Hamiltonian, it is logical to present the interactions in terms of the physical fields. The covariant derivative in the physical basis is

$$D_\mu = \partial_\mu + \frac{ig}{\sqrt{2}} W^\pm \tau^\pm + \frac{ig}{c_w}(\tau^3 - s_w^2 Q) Z_\mu + ieQA_\mu\,. \tag{1.19}$$

The broken generators and the coupling strength e associated to the generator of the subgroup $U(1)_Q$ are defined as

$$e = \frac{gg'}{\sqrt{g^2 + g'^2}}\,, \qquad \tau^\pm = \tau^1 \mp i\tau^2\,. \tag{1.20}$$

The Higgs Lagrangian finally may be written

$$\mathcal{L}_{\text{Higgs}} = \frac{1}{2}(\partial_\mu h)^2 + \frac{g^2}{4}(v+h)^2 \left(W_\mu^+ W^{-\mu} + \frac{1}{2c_w^2} Z_\mu Z^\mu \right) - \mu^2 h^2 - \frac{\mu^2 v^2}{4}\left(\frac{h^4}{v^4} - \frac{4h^3}{v^3} - 1 \right), \tag{1.21}$$

where the relation involving the Higgs self-coupling, $\mu^2 = \lambda v^2$, has been used. The mass terms for charged and neutral bosons of the EW sector are therefore

$$m_W = \frac{gv}{2}, \qquad m_Z = \frac{gv}{2c_w}, \qquad m_A = 0, \qquad m_h = \sqrt{2}\mu\,. \tag{1.22}$$

The photon can be associated with the gauge field A_μ which remains massless after symmetry

breaking. The photon must remain massless, as the generator Q corresponding to the non-trivial subgroup $U(1)_Q$ is unbroken. The electric charge quantum number Q, is therefore with associated coupling strength e. The absorption of the Goldstone bosons as the helicity zero modes of the $W^{\pm}$ and Z bosons, which occurs as the $SU(2)$ transformation aligns the scalar field with the VEV, results in gauge invariant mass terms. The form of the couplings and masses appearing in the Higgs Lagrangian is a consequence of the symmetry breaking pattern which is invoked by a scalar $SU(2)$ doublet. High precision tests of these couplings and their internal consistency is now one of the main goals of the LHC, as well as proposed future e^+e^- linear colliders.

1.2.3 Matter content

To accommodate the $V-A$ structure of the weak interactions, the representation for fermions is chosen by placing the left-handed fermions in a doublet, transforming under $SU(2)_L \times U(1)_Y$, while the right handed fermions are represented by a singlet, transforming under $U(1)_Y$. A summary of these representations for the first generation of fermions which includes their charges under the third component of weak isospin, hypercharge, and electric charge is provided in Table 1.1.

Representation	τ^3	Y	Q
u_R	0	$+2/3$	$+2/3$
$\begin{pmatrix} u \\ d \end{pmatrix}_L$	$+1/2$	$+1/6$	$+2/3$
	$-1/2$		$-1/3$
d_R	0	$-1/3$	$-1/3$
ν_{eR}			
$\begin{pmatrix} \nu_e \\ e \end{pmatrix}_L$	$+1/2$	$-1/2$	0
	$-1/2$		-1
e_R	0	-1	-1

Table 1.1: Matter content of the SM. The charges of the multiplets under the third component of weak isospin, τ^3, hypercharge, Y, and electromagnetic charge, Q, is provided.

The matter content of the SM is organised into three generations, with each of these gen-

erations having the same structure and charges as those presented in Table 1.1. The corresponding fermion fields for quarks and leptons are

$$\begin{aligned} L^I_{i,L} &= \begin{pmatrix} \nu^I_e \\ e^I \end{pmatrix}_L , \begin{pmatrix} \nu^I_\mu \\ \mu^I \end{pmatrix}_L , \begin{pmatrix} \nu^I_\tau \\ \tau^I \end{pmatrix}_L , \\ Q^I_{i,L} &= \begin{pmatrix} u^I \\ d^I \end{pmatrix}_L , \begin{pmatrix} c^I \\ s^I \end{pmatrix}_L , \begin{pmatrix} t^I \\ b^I \end{pmatrix}_L , \\ l^I_{i,R} &= e^I_R, \mu^I_R, \tau^I_R \,, \\ u^I_{i,R} &= u^I_R, c^I_R, t^I_R \,, \\ d^I_{i,R} &= d^I_R, s^I_R, b^I_R \,. \end{aligned} \tag{1.23}$$

In a similar fashion to the Higgs Lagrangian, the interactions of fermions to the gauge fields are introduced through the covariant derivative as

$$\mathcal{L}_{\mathrm{g-f}} = \sum_i^3 \left(\bar{L}^I_{i,L} i \not{D} L^I_{i,L} + \bar{Q}^I_{i,L} i \not{D} Q^I_{i,L} + \bar{l}^I_{i,R} i \not{D} l^I_{i,R} + \bar{u}^I_{i,R} i \not{D} u^I_{i,R} + \bar{d}^I_{i,R} i \not{D} d^I_{i,R} \right) , \tag{1.24}$$

and the covariant derivative, in the slashed notation $\not{D} \equiv D_\mu \gamma^\mu$, has previously been defined in (1.8). The covariant derivative is evaluated in the representation of the fields upon which it acts, noting that the right-handed fields are singlets under weak isospin. The index 'I' ('Interaction') denotes that the chosen basis for fermion fields ensures that the gauge-fermion interactions are diagonal, and the summation over the three fermion generations of each field is included explicitly. This Lagrangian possesses a global flavour symmetry $U(3)^5$, corresponding to rotations in flavour space for each of the matter fields. The infinitesimal

field transformations leaving this Lagrangian invariant are

$$\begin{aligned}
\delta L^I_{i,L} &= i(\xi^Y Y + \xi^i \tau^i) L^I_{i,L}\,, \\
\delta Q^I_{i,L} &= i(\xi^Y Y + \xi^i \tau^i) Q^I_{i,L}\,, \\
\delta l^I_{i,R} &= i(\xi^Y Y) l^I_{i,R}\,, \\
\delta u^I_{i,R} &= i(\xi^Y Y) u^I_{i,R}\,, \\
\delta d^I_{i,R} &= i(\xi^Y Y) d^I_{i,R}\,.
\end{aligned} \tag{1.25}$$

Having introduced a scalar field ϕ (1.6) in the Higgs sector, with hypercharge $Y = +1/2$, it is possible to write gauge invariant Yukawa interaction terms between the fermions and the scalar field of the form

$$\mathcal{L}_{\text{Yukawa}} = \sum_{i,j}^{3} \left(Y^l_{ij} \bar{L}^I_{i,L} \phi l^I_{j,R} + Y^D_{ij} \bar{Q}^I_{i,L} \phi d^I_{j,R} + Y^U_{ij} \bar{Q}^I_{i,L} \tilde{\phi} u^I_{j,R} \right)\,, \tag{1.26}$$

where Y^F_{ij} are complex 3×3 matrices. After the scalar field acquires a non-zero VEV, these fermions become massive. If these matrices are off-diagonal or complex, then this leads to flavour or charge-parity (CP) violation respectively. Note also the use of $\tilde{\phi} \equiv 2i\tau^2\phi^*$, which is a doublet with hypercharge $Y = -1/2$, ensuring gauge invariance under $U(1)_Y$ for the third Yukawa term. Importantly, the lack of a right-handed neutrino singlet within the SM forbids a mass term for neutrinos — the corresponding Yukawa interaction does not exist. Given the freedom to redefine the fermion fields, the matrices Y^F_{ij} can be diagonalised by suitable unitary transformations. However, after the scalar field has acquired a non-zero VEV, the left handed components of the quark field become distinguishable, leading to the following redefinition of the fields

$$\begin{aligned}
l_{i,L} &= \sum_j^3 U^{l,L}_{ij} l^I_{j,L}\,, \quad u_{i,L} \;= \sum_j^3 U^{u,L}_{ij} u^I_{j,L}\,, \quad d_{i,L} = \sum_j^3 U^{d,L}_{ij} d^I_{j,L}\,, \quad \nu_{i,L} \;= \sum_j^3 U^{l,L}_{ij} \nu^I_{j,L}\,, \\
l_{i,R} &= \sum_j^3 U^{l,R}_{ij} l^I_{j,R}\,, \quad u_{i,R} \;= \sum_j^3 U^{u,R}_{ij} u^I_{j,R}\,, \quad d_{i,R} = \sum_j^3 U^{d,R}_{ij} d^I_{j,R}\,.
\end{aligned} \tag{1.27}$$

A consequence of this field redefinition is the appearance of a set of diagonal mass matrices

transforming as

$$y^l = U^{l,L} Y^l (U^{l,R})^\dagger \,, \qquad y^d = U^{d,L} Y^D (U^{d,R})^\dagger \,, \qquad y^u = U^{u,L} Y^U (U^{u,R})^\dagger \,. \tag{1.28}$$

This results in the following fermion mass terms for charged leptons, and up- and down-type quarks

$$m_i^l = \frac{v}{\sqrt{2}} y_{ii}^l \,, \qquad m_i^u = \frac{v}{\sqrt{2}} y_{ii}^u \,, \qquad m_i^d = \frac{v}{\sqrt{2}} y_{ii}^d \,. \tag{1.29}$$

In principle, the Yukawa couplings for the fermions can be extracted by comparing the experimentally observed masses to independent measurements of EW observables (which allow for an independent extraction of the VEV ($v \approx 246$ GeV [15]). In practice, this is not straight forward in the quark sector as free quarks are not observed in nature.

With the expressions for the fermion fields in the mass basis, the gauge-fermion interactions appearing in $\mathcal{L}_{\mathrm{g-f}}$ can also be transformed into this basis. This allows the Feynman rules, which are necessary to calculate relevant cross sections and decay rates, to be easily obtained for future reference. Distinguishing between fermion types f, the Lagrangian becomes

$$\begin{aligned} \mathcal{L}_{\mathrm{g-f}} = & \sum_{i}^{3} \sum_{f=\nu,l,u,d} \left(\bar{f}_i i \not{\partial} f_i - \frac{g}{c_w} (\tau^3 \bar{f}_{i,L} \not{Z} f_{i,L} - s_w^2 Q \bar{f}_i \not{Z} f_i) - eQ \bar{f}_i \not{A} f_i \right) \\ & \sum_{i,j}^{3} -\frac{g}{\sqrt{2}} \left(\bar{u}_{i,L} \not{W}^+ [(U^{u,L})^\dagger U^{d,L}]_{ij} d_{j,L} + \bar{d}_{i,L} \not{W}^- [(U^{d,L})^\dagger U^{u,L}]_{ij} u_{j,L} \right) \\ & \sum_{i}^{3} -\frac{g}{\sqrt{2}} \left(\bar{\nu}_{i,L} \not{W}^+ l_{i,L} + \bar{l}_{i,L} \not{W}^- \nu_{i,L} \right) . \end{aligned} \tag{1.30}$$

If the unitary transformations of left-handed quark fields $U^{u,L}$ and $U^{d,L}$ are not equivalent, then the combination $(U^{u,L})^\dagger U^{d,L}$ is not a flavour symmetry transformation of the original global symmetries. This combination $(U^{u,L})^\dagger U^{d,L} = V_{CKM}$ is known as the Cabibo-Kobayashi-Maskawa (CKM) matrix and is parameterised by three mixing angles and a single complex phase. This complex phase leads CP violation in the quark sector — see Appendix A for the experimentally observed values of its elements and its parameterisation.

The Lagrangian (1.30) also ensures that charged current interactions involving leptons couple with universal strength, as there is no equivalent CKM matrix in the leptonic sector of the SM. This also means that lepton flavour is conserved for each fermion generation, as the components of the left-handed lepton doublet are indistinguishable. And finally, there are no flavour-changing neutral currents (FCNC) at tree level as the generators of the neutral gauge bosons are diagonal in matrix representation, and therefore do not mix fermion flavours.

1.3 QCD

The theory of strong interactions of quarks and gluons, with coupling g_3, is a non-abelian gauge theory of $SU(3)_c$ coupled to quarks in the fundamental representation. In contrast to EW theory, the gauge symmetry $SU(3)_c$ is unbroken and therefore the gauge bosons of the theory remain massless, resulting in extremely different phenomenology. It is also necessary to discuss the quantum nature of QCD, which demands the use of several theoretical techniques to accurately describe the behaviour of interactions across a range of different energy scales.

1.3.1 QCD Lagrangian and colour algebra

The classical Lagrangian can be constructed following the same procedure as adopted in the previous Section. The gauge fields of $SU(3)_c$, transforming in the adjoint representation, are labelled as G^A where $A = 1, .., 8$, while the quark fields, transforming in the fundamental representation, are labelled as q^a where $a = 1, .., 3$. The field strength tensor is

$$G^A_{\mu\nu} = \partial_\nu G^A_\mu - \partial_\mu G^A_\nu - g_3 f^{ABC} G^B_\mu G^C_\nu \,, \tag{1.31}$$

where f^{ABC} are the structure constants of $SU(3)_c$. The classical Lagranigan is

$$\mathcal{L}_{\text{classical}} = -\frac{1}{4} G^A_{\mu\nu} G^{A,\mu\nu} + \sum_{\text{flavours}} \bar{q}_a (i \not{D} - m)_{ab} q_b \,, \tag{1.32}$$

where each flavour of quark is represented by a triplet in colour space, and the covariant derivative takes the form

$$(D_\mu)_{ab} = \partial_\mu \delta_{ab} + i g_3 (t^C G^C_\mu)_{ab} \,, \qquad (D_\mu)_{AB} = \partial_\mu \delta_{AB} + i g_3 (T^C G^C_\mu)_{AB} \,, \tag{1.33}$$

when acting upon fields in either the fundamental or adjoint representations respectively. The corresponding generators for these representations are t^A and T^A, and these generators satisfy the relations

$$[t^A, t^B] = i f^{ABC} t^C, \qquad [T^A, T^B] = i f^{ABC} T^C, \qquad (T^A)_{BC} = -i f^{ABC} \,. \tag{1.34}$$

The infinitesimal transformations under $SU(3)_c$ leaving the classical Lagrangian invariant are

$$\begin{aligned} \delta q_a &= i(\xi^A t^A)_{ab} q_b \,, \\ \delta G^A_\mu &= -\frac{1}{g_s} \partial \xi^A + f^{ABC} G^B_\mu \xi^C \,, \end{aligned} \tag{1.35}$$

where ξ^A is the infinitesimal parameter of $SU(3)_c$, corresponding to the representation of generators t^A. The following identities will also prove useful for the calculation of colour factors in later chapters:

$$\begin{aligned} Tr(t^A t^B) &= \frac{\delta^{AB}}{2} \,, & \sum_A t^A_{ab} t^A_{bc} &= \frac{N^2-1}{2N} \delta_{ac} = C_F \delta_{ac} \,, \\ Tr(T^A T^B) &= \sum_{C,D} f^{CDA} f^{CDB} = C_A \delta^{AB} \,, & \{t^A, t^B\} &= \frac{\delta^{AB}}{N} + d^{ABC} t^C \,, \\ \sum_{A,B} d^{ABC} d^{ABD} &= \frac{N^2-4}{N} \delta^{CD}, d^{AAC} = 0 \,. \end{aligned} \tag{1.36}$$

The term d^{ABC} is the symmetric structure constant. These relations hold for general $SU(N)$ gauge theories, however in the case of strong sector, $N = 3$. Before deriving the Feynman rules, it is necessary to discuss two important technical aspects related to gauge theories.

1.3.2 Gauge fixing and ghosts

To define a non-singular gauge boson propagator, it is necessary to add a gauge-fixing term. The requirement of this extra term can be understood when performing quantisation in the functional integration approach [16]. The gauge-fixing term ensures that physical field configurations are counted only once. This can be done explicitly for covariant gauges by including the term

$$\mathcal{L}_{\text{gauge-fixing}} = -\frac{1}{2\lambda}(\partial^\mu G^A_\mu)^2\,, \tag{1.37}$$

with the free gauge parameter λ. This additional term breaks gauge invariance, however the physical quantities calculated from the derived Feynman rules of the Lagrangian are λ-independent. One further complication arises in the case of non-abelian theories, in which the infinitesimal gauge transformation of the field depends upon the field itself (see (1.35)). It then becomes necessary to add a ghost term, representing unphysical degrees of freedom, to the Lagrangian with the form

$$\mathcal{L}_{\text{ghost}} = \partial_\mu \eta^{A,\dagger}(D^\mu_{AB}\eta^B)\,, \tag{1.38}$$

where η is a scalar complex field which obeys Fermi statistics. The extra term is required to cancel unphysical degrees of freedom, introduced for example by the triple gluon vertex in the process $gg \to q\bar{q}$. Practically, this removes the contribution from longitudinally polarised gluons states which are not physically present. The QCD Lagrangian is finally given by

$$\mathcal{L}_{\text{QCD}} = -\frac{1}{4}G^A_{\mu\nu}G^{A,\mu\nu} + \sum_{\text{flavours}} \bar{q}_a(i\not{D} - m)_{ab}q_b - \frac{1}{2\lambda}(\partial^\mu G^A_\mu)^2 + \partial_\mu \eta^{A,\dagger}(D^\mu_{AB}\eta^B)\,. \tag{1.39}$$

1.3.3 Feynman rules

The QCD and relevant EW Feynman rules for external legs, propagators and vertices are listed in Figure 1.1.

The rules for diagrams including loops are also provided:

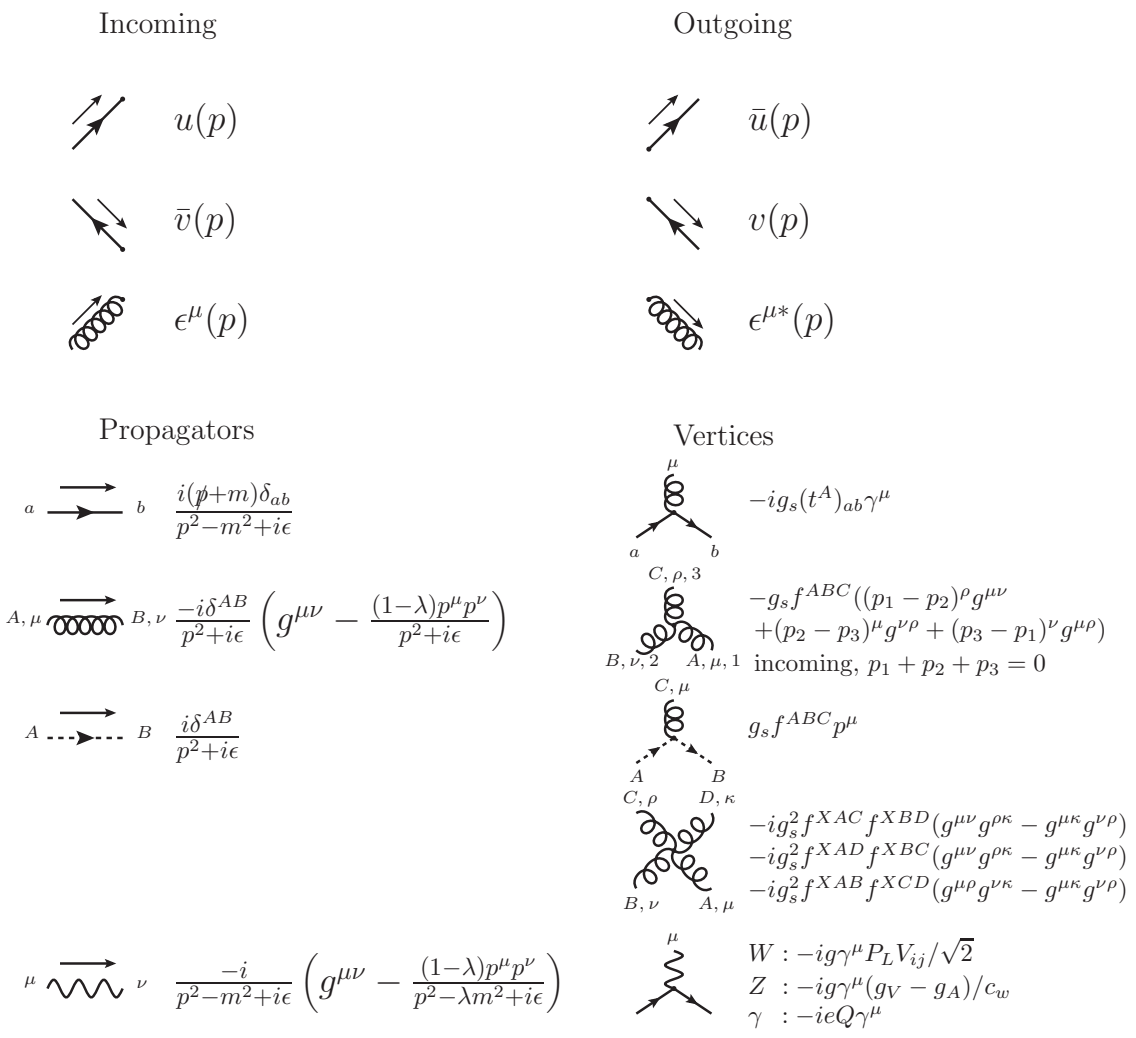


Figure 1.1: Feynman rules for QCD and relevant EW interactions. Fermions, gluons, EW bosons and ghosts are represented by solid, springy, wavy and dashed lines respectively. Where appropriate, the flow of momentum has been included.

- integrate over loop momentum, l, with the measure $\dfrac{d^4l}{(2\pi)^4}$,
- include a factor of -1 for fermion and ghost loops,
- include a symmetry factor of $\dfrac{1}{n!}$ for n identical gluons.

These rules allow the extraction of the amplitude for a given process to any order in perturbation theory. The prediction representing the physical quantity is then obtained from averaging and summing over initial and final state spins/polarisations. Therefore, the following completeness relations for spin and polarisation states of external quarks and gluons

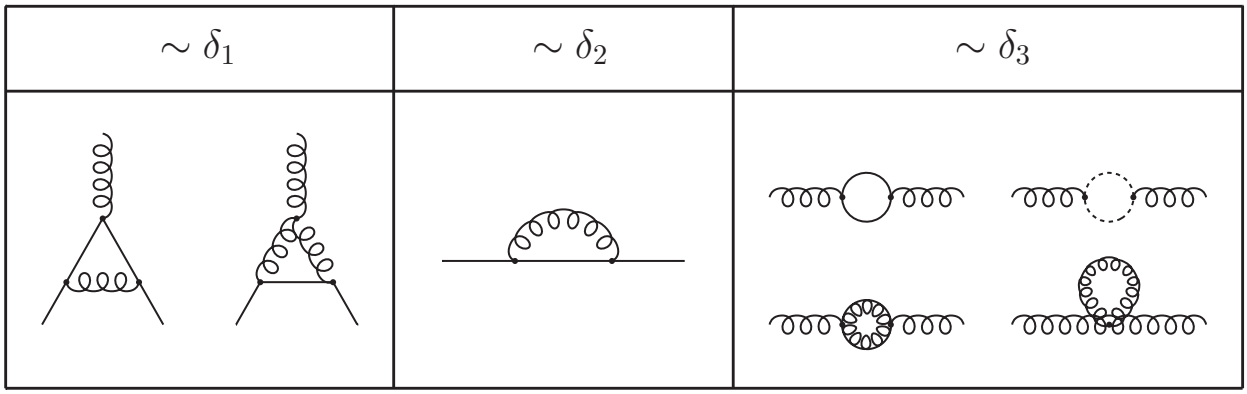


Figure 1.2: Divergent one-loop corrections to the $q\bar{q}g$ vertex, quark self-energy and gluon self-energy whose counterterms are necessary to calculate the β-function to first order.

are also provided

$$\sum_{\text{spins}} u(p)\bar{u}(p) = \not{p} + m\,, \qquad \sum_{\text{spins}} v(p)\bar{v}(p) = \not{p} - m\,, \qquad \sum_{\text{pol.}} \epsilon_\mu(p)\epsilon^*_\nu(p) = -g_{\mu\nu}\,. \tag{1.40}$$

The sum over polarisations states has assumed the choice of gauge parameter $\lambda = 1$. This choice requires the additional calculation of processes involving the ghost fields.

1.3.4 Renormalisation

Comparing the theoretical consistency of QCD with observed phenomena clearly relies on the predictive power of the theory. Including higher-order corrections to the prediction of physical observables, and understanding when this perturbative expansion is reliable, is crucial for a meaningful comparison. In quantum field theories such as QCD, it is necessary to perform *renormalisation* for the theory to be predictive. For example, consider the calculation of the quark self-energy as depicted in the centre of Figure 1.2, and calculated in Appendix B. In this case the integration over the loop momentum has the form

$$\mathcal{I} = \int \frac{d^4l}{(2\pi)^4} \frac{1}{l^2(l-k)^2}\,, \tag{1.41}$$

which contains an ultraviolet (UV) divergence as $l \to \infty$. There are several consistent mathematical techniques which can be used to circumvent these divergences and provide

finite predictions of physical observables which include higher-order corrections. To do so, the infinite integral must first be regularised. This can be done by including a momentum cut-off scale μ or by continuing the number of dimensions such that $d < 4$. Having performed this *regularisation*, the divergent terms can then be absorbed into a redefinition of fields or parameters, this is the procedure known as renormalisation. Both of these regulation techniques introduce an arbitrary unphysical scale μ into the prediction of physical observables, however this unphysical scale must have no impact on the final result in the full theory. As the prediction relies on full knowledge of the perturbative expansion, which is truncated at some fixed order, there is always some residual uncertainty due to the unknown dependence of higher order terms on this choice of μ. One of the consequences of the renormalisation scale independence of renormalisation is the running of the QCD coupling.

It is easy to see why this running arises by examining the form of the renormalised QCD Lagrangian at one-loop level. Writing the Lagrangian in terms of the renormalised fields and couplings, ignoring quark masses, gives

$$\mathcal{L}_{\text{one-loop}} = -\frac{1}{4} Z_3 G^A_{\mu\nu} G^{A,\mu\nu} + \sum_{\text{flavours}} (Z_2 \bar{q}_a i \partial\!\!\!/_{ab} q_b - \mu^\epsilon Z_\alpha g_s \bar{q}_a G\!\!\!/_{ab} q_b) + \cdots \tag{1.42}$$

where the term μ^ϵ is introduced to ensure the coupling remains dimensionless after dimensional regularisation. The following notation has been used

$$Z_\alpha = Z_1 Z_2^{-1} Z_3^{-1/2}\,, \qquad Z_i = (1 + \delta_i)\,, \tag{1.43}$$

where $\delta_i = 1, 2, 3$, correspond to the counterterms required to ensure the one-loop Green's functions are finite for the $q\bar{q}g$ vertex, quark self-energy, and gluon self-energy corrections respectively. The Feynman diagrams corresponding to each of these one-loop counterterms are shown in Figure 1.2. Defining the coupling, α_s, in the usual way

$$\alpha_3 = \frac{g_3^2}{4\pi}\,, \qquad \alpha_s(\mu^2) = \frac{g_s^2}{4\pi}\,, \tag{1.44}$$

noting in particular the scale independence of the bare coupling α_3. This scale independence

leads to the following relation

$$\mu^2 \frac{d\alpha_3}{d\mu^2} = \mu^2 \frac{d}{d\mu^2} \left(\mu^{2\epsilon} Z_\alpha^2(\alpha_s(\mu^2)) \alpha_s(\mu^2) \right) = 0 \,, \tag{1.45}$$

which evaluates to

$$\epsilon \alpha_s + \frac{2\alpha_s}{Z_\alpha} \frac{dZ_\alpha}{d\alpha_s} \mu^2 \frac{d\alpha_s}{d\mu^2} + \mu^2 \frac{d\alpha_s}{d\mu^2} = 0 \,. \tag{1.46}$$

Omitting the explicit μ dependence of α_s ($\alpha_s(\mu^2) = \alpha_s$) and defining the QCD β-function as

$$\beta(\alpha_s) = \mu^2 \frac{d\alpha_s}{d\mu^2} = \frac{d\alpha_s}{dt} \,, \qquad t = ln(\mu^2) \,, \tag{1.47}$$

leads to the relation

$$\beta(\alpha_s) = \frac{-\epsilon \alpha_s}{1 + 2 \frac{\alpha_s}{Z_\alpha} \frac{dZ_\alpha}{d\alpha_s}} \,. \tag{1.48}$$

Therefore, by calculating each of the counterterms δ_i provided in Appendix A and expanding in α_s, the β-function is

$$\beta(\alpha_s) = -b_0 \alpha_s^2 + \mathcal{O}(\alpha_s^2, \epsilon) \,, \qquad b_0 = \frac{1}{12\pi}(33 - 2n_f) \,. \tag{1.49}$$

The variable n_f corresponds to the number of active quark flavours running in the fermion loop. For a constraint on the number of flavours, $n_f < 17$, the β-function is negative and results in the coupling strength decreasing with increasing energy — it is said to be *asymptotically free* [17]. Solving the β-function, truncated at one-loop, leads to the relation

$$\alpha_s(Q^2) = \frac{\alpha_s}{1 + \alpha_s b_0 \log(\frac{Q^2}{\mu^2})} \,, \tag{1.50}$$

which explicitly expresses α_s at the scale Q^2 as a function of α_s evaluated at some other scale μ. Although the definition of α_s clearly depends on μ, physical observables such as cross sections are calculated from a combination of the coupling and the matrix element for a given process. Performing renormalisation introduces an unphysical scale dependence in both the coupling and the matrix element in such a way that, in the full theory. It is this cancellation

which justifies the extraction of α_s evaluated at a scale Q, corresponding to the physical scale of the process being measured. The full cancellation relies on knowledge of all terms in the expansion for each order in α_s. Unknown terms in the series introduce an associated scale uncertainty as previously mentioned. If this uncertainty is taken into account when extracting values of α_s from measurements at different energy scales, it allows the prediction of the running to be tested to high precision. Generally, extractions of α_s from measurement are subsequently run to the common scale of m_Z^2. This allows a straightforward comparison, as well as combination, of the observed value of α_s for many different experiments.

The commonly used world average is $\alpha_s(m_Z^2) = 0.1184 \pm 0.0007$ [18], which is dominated by lattice QCD results, at $Q = 7.5$ GeV, which have an extremely small uncertainty [19]. As QCD phenomenology is extremely sensitive to the value of α_s, including new precision measurements of this coupling is important as an input for an updated average, as well as a cross check of the consistency of results from lattice.

Historically, the coupling was also expressed with respect to the fundamental scale Λ at which the coupling tends to infinity, leading to the expression

$$\alpha_s(Q^2) = \frac{1}{b_0 \log(\frac{Q^2}{\Lambda^2})} \,. \tag{1.51}$$

The running of $\alpha_s(Q^2)$ is plotted with respect to energy scale in Figure 1.3 at both one and two-loop level for the following choices of Λ: $\Lambda_{\mathrm{one-loop}} = 0.255$ GeV; $\Lambda_{\mathrm{two-loop}} = 0.206$ GeV. The number of active flavours has been fixed to $n_f = 5$ for simplicity. This particular choice of $\Lambda_{\mathrm{two-loop}}$ corresponds to $\alpha_s(m_Z^2) = 0.116$. Importantly, at a scale of $\mathcal{O}(1$ GeV$)$ the coupling exceeds unity and perturbation theory is no longer reliable.

Although the QCD Lagrangian is known, and there are many tests confirming the reliability of its perturbative expansion for $Q \gg \Lambda$, less is known about its behaviour in the strong coupling regime $\mathcal{O}(1$ GeV$)$. In particular, coloured objects such as quarks and gluons have not been experimentally observed in isolation — the phenomenon is known as *confinement*. A fundamental description of the transition from coloured objects to colour singlet

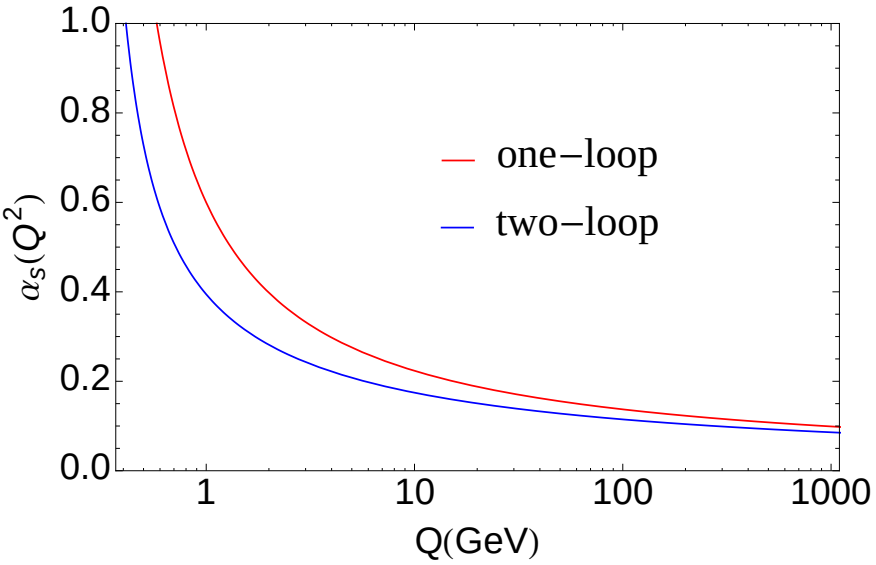


Figure 1.3: Running of the strong coupling evaluated at one and two-loop level. The reference scales for infinite coupling are chosen to be $\Lambda_{\text{one-loop}} = 0.255$ GeV, $\Lambda_{\text{two-loop}} = 0.206$ GeV. The number of active flavours is held fixed at $n_f = 5$.

hadrons is still lacking. The following Chapter will be dedicated to discussing some of these issues and how QCD can be used to make predictions for colour singlet observables produced from the collisions of strongly-bound hadrons.

1.4 Summary

The basic features of the SM, which are necessary for the upcoming discussion of LHC observables, have been introduced. This includes the content, masses, and interactions of the fundamental particles. It has been stressed that the inclusion of higher-order corrections is necessary to provide a meaningful comparison between theoretical predictions and observable phenomena. This prompted the discussion of renormalisation, a necessary step to provide finite higher-order predictions. One of the consequences of this renormalisation procedure is the running of the coupling α_s, which leads to the behaviour of asymptotic freedom. As the predictions for observables predominantly rely on performing perturbation theory in the coupling, a regime of validity for the prediction of interactions can be obtained. The corresponding energy scale, at which the coupling exceeds unity, is $\mathcal{O}(1$ GeV). The

electromagnetic and weak couplings α_e and α_w remain in the perturbative regime for all energy scales considered when performing LHC phenomenology.

Chapter 2

Predicting LHC observables

The goal of this thesis is to provide realistic predictions for the production of high pseudorapidity top quarks at the LHC. In the previous Chapter, a set of Feynman rules was derived to allow the calculation of quantum amplitudes which represent physical processes. At hadron colliders such as the LHC, providing predictions for observables is substantially more complicated than computing a single amplitude for the following reasons: the incoming partons appearing in the amplitude for a hard subprocess are constituent particles of the colliding hadrons; fixed-order calculations must be extended to all-orders to correctly describe exclusive observables, particularly those sensitive to neglected multiple emissions; the transition from coloured off-shell partons into colour singlet objects must be modelled to satisfy the criterion of confinement. Each of these topics and their overall compatibility will be considered, leading finally to a recipe for the prediction of experimental signals.

2.1 Introduction

Hadron-hadron collisions at the LHC provide an interesting laboratory to study many aspects of fundamental interactions which occurr across a large range of energy scales. Providing realistic predictions for these collisions is necessary if comparisons to experimental data are to be used to improve the current understanding of the fundamental interactions of nature. These predictions are generally provided by Monte Carlo (MC) event generators which rely on repeated random sampling to obtain numerical results. The MC method is well suited to simulating LHC collisions for many reasons, a few of the main motivations are outlined below.

- Quantum mechanics is probabilistic. It is impossible to know the outcome of the

collisions on an event-by-event basis. The random sampling in these event generators mimics this effect allowing the construction of a probability distribution for observables.

- The LHC collisions are complicated to predict. As will be discussed, an LHC collision can be structured into several different subprocesses. The MC method allows each of these different subprocesses to be considered sequentially which simplifies the prediction of the full process.

- LHC events have a large number of final state particles. The associated number of degrees of freedom is therefore very large. Numerical integration over many dimensions is feasible with the MC method in which the convergence is stochastic.

In order to implement these methods, it is first necessary to discuss the structure of an LHC collision in detail. This will be limited to the discussion of hard scattering processes, referring to processes in which the interaction occurs with large momentum exchange — top quark production falls into this category. As the colliding hadrons are strongly-bound composite objects of interacting quarks and gluons, the details of their underlying structure must be included when making predictions. Fortunately, this complication can be simplified by factoring the full scattering process into a combination of both long- and short-distance effects [20]. This factorisation procedure introduces an arbitrary unphysical energy scale μ_F which separates the full scattering process into effects occurring at scales below (long-distance) and above μ_F (short-distance).

The long-distance effects are factored into parton distribution functions (PDFs) which represent a probability density in the space of parton distributions ($a = u, \bar{u}, ..., g$). The PDFs, which model the density of partons inside the hadron, are perturbatively evolved to to a virtuality μ_F^2 which accounts for multiple parton splittings occurring below this scale. It is therefore necessary to present the PDF for each parton flavour a as a function of its momentum fraction (x_a) and the factorisation scale (μ_F^2) as $f_{a/A}(x_a, \mu_F^2)$. The choice of the arbitrary scale μ_F^2 should be such that it corresponds to the expected physical momentum exchange Q^2 of the process being studied. Note that, although the unphysical scale dependence enters at $\mathcal{O}(\mu_F^2)$, it will often be convenient to refer to this dependence simply as

μ_F.

Above the scale μ_F, the interaction is described by the short-distance subprocess $\hat{\sigma}_{ab\to X}$ which describes the interaction of the constituent partons a and b which scatter to produce final state X. This subprocess can be calculated perturbatively using Feynman diagrams. As higher-order corrections are included in both the parton evolution and subprocess, the dependence on μ_F decreases as the cancellation between μ_F-dependent terms improves. In the full theory, there would be no need to introduce this factorisation whatsoever. Schematically, this factorisation procedure is

$$\sigma_{AB\to X} = \sum_{a,b} \int dx_a dx_b f_{a/A}(x_a, \mu_F^2) f_{b/B}(x_b, \mu_F^2) d\hat{\sigma}_{ab\to X}(\hat{s}, \mu_F^2, \mu_R^2, \alpha_s) \,, \tag{2.1}$$

where the μ_R dependence of α_s ensures the short-distance cross section is μ_R-independent. It is also important to note that this formulation is only valid for interactions with momentum scale exchange $Q^2 \gg \Lambda_{QCD}$ — otherwise, the contribution from non-factorisable corrections can typically be large $\mathcal{O}(\Lambda_{QCD}^2/Q^2)$.

The short-distance cross section is obtained from the invariant matrix element as

$$d\hat{\sigma}_{ab\to X} = \frac{1}{2s_{ab}} \overline{\sum} |\mathcal{M}_{ab\to X}|^2 d\phi_n \,, \qquad d\phi_n = \prod_i^n \frac{d^3 p_i}{(2\pi)^3 2E_i} (2\pi)^4 \delta^{(4)} \left(p_a + p_b - \sum_i^n p_i \right) . \tag{2.2}$$

The following notation has been introduced, $s_{ab} = p_{ab}^2 = (p_a + p_b)^2 \underset{m_{a,b}\to 0}{=} 2p_a \cdot p_b$. The first term in the first equation is a flux factor ($\mathcal{F} = 2s_{ab}$) for the incoming partons, the second term is the squared matrix element which has been averaged (summed) over initial (final) state colour and spin, and the final term $d\phi_n$ is the phase space for the n-body final state X. The matrix element, which represents a quantum amplitude, is given by the sum over all contributing Feynman diagrams $\mathcal{M}_{ab\to X} = \sum_i \mathcal{D}^i_{ab\to X}$ which, when squared, is generally truncated at some fixed-order in the coupling.

Finally, to make predictions for observables at the level of hadrons (colour singlet objects), it is also necessary to include long-distance effects in the final state. This is required

to evolve the off-shell final state from the factorisation scale down to the hadronisation scale. Performing this evolution is beneficial as theoretical predictions can then be compared directly to experiment at the level of hadrons. Each of the components contributing to the full scattering cross section will now be considered in turn.

2.2 Fixed-order calculations and factorisation

2.2.1 Fixed-order calculations

Consider first the evaluation of the partonic (short-distance) cross section for the production of the final state X. The differential cross section for an observable $\mathcal{O}$ may be written as

$$\frac{d\hat{\sigma}_X}{d\mathcal{O}} = \frac{1}{\mathcal{F}} \sum_{k=0}^{\infty} \int d\phi_{X+k} \left| \sum_{l=0}^{\infty} \mathcal{M}^l_{X+k} \right|^2 \delta(\mathcal{O} - \mathcal{O}(\phi_{X+k})) \,. \tag{2.3}$$

The following notation has been introduced: the sum over k corresponds to production of X (for example Z production) in association with k final state partons (real corrections); the sum over l accounts for the inclusion of loop processes (virtual corrections). The phase space integral is altered to account for the correct number of final state partons accordingly, and the delta function projects out the contribution from different momentum configurations in phase space for a fixed value of $\mathcal{O}$. This notation encapsulates the general aspects of fixed-order calculations.

There are several benefits of including higher-order corrections: the cancellation of theoretical uncertainty, introduced through the unphysical scales required to perform renormalisation and factorisation, increases order-by-order; new production channels and final states are introduced by real corrections; processes may contain large logarithms introduced after divergent contributions are regulated.

As the reliability of a prediction generally depends on whether the higher-order corrections are relatively small, obtaining these corrections is therefore an important test of the

convergence of the perturbative series. One example of a process with poor convergence is the inclusive cross section for Higgs production. The next-to-LO (NLO) corrections are substantial, and require the next-to-NLO (NNLO) correction for a reliable prediction [21]. In fact, the evaluation of these corrections at next-to-NNLO [22] is also underway. As the number of diagrams grows approximately factorially per order, calculating higher-order corrections beyond $k + l = n > 2$ is computationally challenging, and currently only available for a small number of specific processes.

It is also necessary for higher-order corrections to be computed to fixed n — meaning that real and virtual corrections of the same order must be computed simultaneously to obtain finite predictions, a consequence of the Kinoshita-Lee-Nauenberg (KLN) theorem [23, 24]. This theorem states that the infrared (IR) divergences, introduced independently by both real and virtual corrections, cancel exactly with one another order-by-order for fixed n. The real divergences arise from momentum configurations in which the emission of an additional parton in the final state is either collinear or soft, resulting in a singular contribution to the matrix element for the $X + k$ process. The virtual corrections contain IR divergences for all momentum configurations — however, unlike the real correction they inhabit the ϕ_X phase space. Performing and implementing a higher-order correction essentially becomes the task of finding a suitable way to cancel these divergences, which occupy different phase spaces, and yield numerically finite results for both X and $X + k$ processes independently. Schematically, an NLO cross section is structured as

$$\sigma\mathcal{F} = \int d\phi_X |\mathcal{M}_X^0|^2 + \int d\phi_X 2\mathrm{Re}|\mathcal{M}_X^1|^2 + \int d\phi_{X+1} |\mathcal{M}_{X+1}^0|^2 \,, \tag{2.4}$$

where the second and third terms are individually IR divergent. It is also assumed that the second term has been renormalised to remove UV ($l \to \infty$) divergences — this may be done through the procedure of field renormalisation after dimensional regularisation (see Appendix B). One approach to calculating NLO cross sections is to perform numerical integration independently over the relevant X and $X + n$ phase space. As the virtual and real corrections are independently divergent, it is then necessary to adapt the form of (2.4) to

predict finite results. One approach, the method of subtraction, is to introduce a generic function C with the following properties: the function must have the same singular behaviour as the real contribution, therefore acting as a local counterterm to the real contribution when subtracted; it must also be exactly integrable analytically in d dimensions over the single parton subspace, and integrate to give the IR divergences which exactly cancel those from the virtual contribution. The result of this implementation is to generate finite partonic events for both X and $X+1$ final states separately. Schematically, it has the following form

$$\sigma\mathcal{F} = \int d\phi_X |\mathcal{M}_X^0|^2 + \int d\phi_X \left(2\mathrm{Re}|\mathcal{M}_X^1|^2 + \int d\phi_1 C \right) + \int d\phi_{X+1} \left(|\mathcal{M}_{X+1}^0|^2 - C \right) . \quad (2.5)$$

The presence of IR singularities in fixed-order calculations is an indication of long-distance effects which are not described by truncated perturbation theory. It is therefore important to understand how these long-distance effects can otherwise be accounted for. Before doing so, it is necessary to discuss the universal behaviour of IR singularities which appear in gauge theory amplitudes.

2.2.2 Factorisation: the soft limit

As demonstrated in the previous Section, the predictive power of fixed-order calculations relies on the convergence of the perturbative series. However, there are particular regions of phase space in which the higher-order corrections are enhanced, and the description of exclusive observables in this region may be poorly modelled by the fixed-order calculation. The treatment of these regions of phase space relies on the universal factorisation of IR divergences, and it is therefore instructive to demonstrate this factorisation in both soft and collinear configurations.

Consider first the limit in which a soft gluon is radiated in the final state of a process such as $\gamma \to q\bar{q}(g)$. The leading process (Born level) and the real correction diagrams are

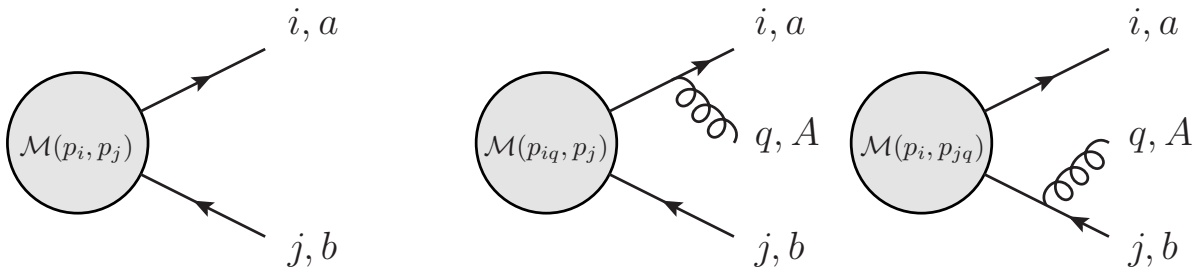


Figure 2.1: Amplitude for the production of final state X and $X + g$. The external legs are labelled by their momentum i, j, q and colour space labels a, b, A.

depicted in Figure 2.1. The Born level amplitude is

$$\mathcal{M}_X^0 = \bar{u}_a(p_i)\mathcal{M}^{ab}(p_i, p_j)v_b(p_j)\delta_{ab}\,. \tag{2.6}$$

The real correction term, including the amplitudes in which a gluon with momentum q is radiated off each external leg, is given by

$$\begin{aligned}\mathcal{M}_{X+g}^0 = \bar{u}_a(p_i)\Big((-ig_s t^A_{ab})\not{\epsilon}^{*A}\frac{i(\not{p}_i + \not{q} + m)}{(p_i+q)^2 - m^2}\mathcal{M}^{ab}(p_i+q, p_j) \\ + \mathcal{M}^{ab}(p_i, p_j+q)\frac{-i(\not{p}_j + \not{q} - m)}{(p_j+q)^2 - m^2}(-ig_s t^A_{ab})\not{\epsilon}^{*A}\Big)v_b(p_j)\,.\end{aligned} \tag{2.7}$$

In the approximation of soft radiation ($q \ll p_i, p_j$), this simplifies to

$$\mathcal{M}_{X+g}^0 \simeq \bar{u}_a(p_i)(-ig_s t^A_{ab})\mathcal{M}^{ab}(p_i, p_j)v_b(p_j)\left(\frac{p_i\cdot\epsilon^*}{p_i\cdot q} - \frac{p_j\cdot\epsilon^*}{p_j\cdot q}\right)\,. \tag{2.8}$$

In this limit, the colour-correlated Born amplitude factorises at the amplitude level. Squaring this amplitude and summing over final state colour, polarisation, and spin leads to the result

$$|\mathcal{M}_{X+g}^0|^2 = |\mathcal{M}_X^0|^2 C_F g_s^2\left(\frac{2p_i\cdot p_j}{(p_i\cdot q)(p_j\cdot q)} - \frac{m_i^2}{(p_i\cdot q)} - \frac{m_j^2}{(p_j\cdot q)}\right)\,. \tag{2.9}$$

In this form, it is clear that the soft divergence occurs as $|q| \to 0$. Considering the case of massless partons, this divergence becomes maximal when the intermediate propagators for each process simultaneously go on-shell. As the origin of the soft divergence is simply due to intermediate propagators going on-shell, this explains why the factorisation of these

divergences is a universal property of gauge theory amplitudes. An interesting consequence of the soft divergence becomes apparent when the phase space is included

$$\begin{aligned} d\sigma_{X+g} &= d\phi_X |\mathcal{M}_X^0|^2 \frac{d^3q}{(2\pi)^3 2E_q} C_F 4\pi\alpha_s \frac{2p_i \cdot p_j}{(p_i \cdot q)(p_j \cdot q)} \,, \\ &= d\sigma_X \frac{dq_0}{E_q} \frac{d\phi}{2\pi} \frac{C_F \alpha_s}{\pi} dcos\,\theta \frac{1 - cos\,\theta_{ij}}{(1 - cos\,\theta_{iq})(1 - cos\,\theta_{jq})} \,. \end{aligned} \tag{2.10}$$

This formulation demonstrates the presence of both soft and collinear singularities, which occur when the soft gluon is emitted in the direction parallel to either parton i or j. In fact, further insight can be gained by defining the set of radiation functions

$$\begin{aligned} W_{ij}^i &= \frac{1}{2(1 - cos\,\theta_{iq})} \left(1 + \frac{cos\,\theta_{iq} - cos\,\theta_{ij}}{1 - cos\,\theta_{jq}} \right) \,, \\ W_{ij}^j &= W_{ij}^i [j \leftrightarrow i] \,. \end{aligned} \tag{2.11}$$

These functions have the property of angular ordering which ensures subsequent emissions must occur within a progressively decreasing angular cone. This constraint is provided when performing the angular integration

$$\int \frac{d\phi_{iq}}{2\pi} W_{ij}^i = \begin{cases} \frac{1}{1 - cos\theta_{iq}} & \theta_{iq} < \theta_{ij} \,, \\ 0 & \text{otherwise} \,. \end{cases} \tag{2.12}$$

This coherence effect is a general property of soft emissions in gauge theories. Coherence can therefore be taken into account by limiting final state emissions to be ordered by an energy-weighted emission angle. To understand this, consider a process in which a gluon splits into a collinear $q\bar{q}$ pair followed by a soft- and wide-angled gluon emission. If the collinear splitting is unresolvable, then the $q\bar{q}$ pair appears as a single colour octet source. The soft contribution is then equivalent to a wide-angle $g \to gg$ splitting occurring prior to the collinear $g \to q\bar{q}$ splitting. In this way, the coherence effect can be accounted for correctly by collinear evolution, when a suitable ordering parameter for parton emissions is included.

Alternative approaches to angular ordering, such as that present in dipole showering, take some $k_\perp$ (transverse momentum) variable as the ordering parameter [25, 26]. When applied to multiple emissions, these types of ordering also ensure that sequential branchings of particles result in a collimated 'jet' of particles which are localised in phase space. This is particularly important for colour-connected particles which should eventually form colour singlet objects — this will be discussed in more detail towards the end of the Chapter.

2.2.3 Factorisation: the collinear limit

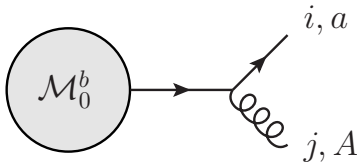
The discussion of factorisation can also be extended to collinear singularities which are not necessarily soft. This factorisation procedure provides the basis for the description of long-distance effects which are not accounted for by fixed-order calculations. When this factorisation is applied sequentially to multiple splittings, it acts to resum splittings occurring below the scale μ_F^2 to all-orders. To understand the validity of this statement, the leading contribution to the spin-averaged parton splitting $q \to qg$ will be calculated, demonstrating the origin of universal splittings kernels. Following the notation of [27], the collinear limit in which two massless partons p_i and p_j become parallel is defined as follows

$$\begin{aligned} p_i^\mu &= zp^\mu + k_\perp^\mu - \frac{k_\perp^2}{z}\frac{n^\mu}{2p\cdot n}\,, & p_j^\mu &= (1-z)p^\mu - k_\perp^\mu - \frac{k_\perp^2}{1-z}\frac{n^\mu}{2p\cdot n}\,, \\ s_{ij} &= -\frac{k_\perp^2}{z(1-z)}\,, & k_\perp &\to 0\,. \end{aligned} \tag{2.13}$$

The vector $k_\perp$ denotes the momentum transverse to the the collinear direction, defined by the light-like vector p^μ. The auxiliary light-like vector n^μ is required to ensure the correct scaling of the space-like vector $k_\perp^\mu$ such that $k_\perp \cdot p = k_\perp \cdot n = 0$. The prefactor for the auxiliary vector can easily be evaluated by requiring both p_i and p_j to be light-like. The leading contribution to the collinear singularity arises from the self-interference of the singular term.

The amplitude for the singular term is

$$\mathcal{M}_{q+g} = \quad , \tag{2.14}$$



$$= \bar{u}_a^s(p_i)[-ig_s t_{ab}^A \gamma^\mu] \frac{i\not{p}_{ij}}{p_{ij}^2} \epsilon_\mu^{A*} \mathcal{M}_0^b \,.$$

In this notation, a spinor has been extracted from a generic Born level amplitude ($\mathcal{M}_q$), and $\mathcal{M}_0^b$ represents the reduced amplitude with this leg removed. The contribution from a collinear splitting interfering with itself is then easily calculated by including the emission of a gluon with finite momentum from the external leg. The labels a and A are the quark and gluon colour space indices while the labels i and j correspond to the momentum carried by the external partons after the splitting. The squared amplitude is then

$$|\mathcal{M}_{q+g}|^2 = \frac{g_s^2 t_{ab}^A t_{cd}^B}{s_{ij}^2} Tr\{\mathcal{M}_0^{c*} \not{p}_{ij} \gamma^\nu u_d^s(p_i) \bar{u}_a^s(p_i) \gamma^\mu \not{p}_{ij} \mathcal{M}_0^b\} \epsilon_\mu^{A*} \epsilon_\nu^B \,, \tag{2.15}$$

which can be solved using the following completeness relations

$$\sum_{\text{pol.}} \epsilon_\mu^{A*}(q) \epsilon_\nu^B(q) \to \left(-g_{\mu\nu} + \frac{q_\mu n_\nu + n_\mu q_\nu}{n \cdot q} \right) \delta^{AB} \,, \qquad \sum_s u_a^s(p) \bar{u}_b^s(p) = \not{p} \delta_{ab} \,. \tag{2.16}$$

For the process considered, this completeness relation ensures that only physical polarisations contribute. Summing over final state polarisation and spin gives

$$|\mathcal{M}_{q+g}|^2 = \frac{g_s^2 C_F}{s_{ij}^2} Tr\{\mathcal{M}_0^{c*} \not{p}_{ij} \gamma^\nu \not{p}_i \gamma^\mu \not{p}_{ij} \mathcal{M}_0^c\} \cdot \left(-g_{\mu\nu} + \frac{(p_j)_\mu n_\nu + n_\mu (p_j)_\nu}{n \cdot p_j} \right) . \tag{2.17}$$

Calculating the first term leads to

$$\begin{aligned} |\mathcal{M}_\alpha|^2 &= -\frac{g_s^2 C_F}{s_{ij}^2} Tr\{\mathcal{M}_0^{c*} \not{p}_{ij} \gamma^\nu \not{p}_i \gamma_\nu \not{p}_{ij} \mathcal{M}_0^c\} \,, \\ &= \frac{2 g_s^2 C_F}{s_{ij}^2} Tr\{\mathcal{M}_0^{c*} \not{p}_j \not{p}_i \not{p}_j \mathcal{M}_0^c\} \,. \end{aligned} \tag{2.18}$$

Using the spinor completeness relation this becomes

$$\begin{aligned}
|\mathcal{M}_\alpha|^2 &= \frac{2g_s^2 C_F}{s_{ij}^2} \sum_{s_1,s_2} Tr\{\mathcal{M}_0^{c*} u^{s_1}(p_j)\bar{u}^{s_1}(p_j) \not{p}_i u^{s_2}(p_j)\bar{u}^{s_2}(p_j)\mathcal{M}_0^c\}\,, \\
&= \frac{2g_s^2 C_F}{s_{ij}^2} \sum_{s_1,s_2} (\mathcal{M}_0^{c*})_i [u^{s_1}(p_j)]_i [\bar{u}^{s_1}(p_j)]_j [\not{p}_i]_{jk} [u^{s_2}(p_j)]_k [\bar{u}^{s_2}(p_j)]_l (\mathcal{M}_0^c)_l\,, \\
&= \frac{2g_s^2 C_F}{s_{ij}^2} \sum_{s_1,s_2} Tr\{\mathcal{M}_0^{c*} u^{s_1}(p_j)\bar{u}^{s_2}(p_j)\mathcal{M}_0^c\} Tr\{\bar{u}^{s_1}(p_j)\not{p}_i u^{s_2}(p_j)\}\,.
\end{aligned} \tag{2.19}$$

Making use of the following spinor identity, $\bar{u}^{s_1}\not{p}u^{s_2} = \delta_{s_1,s_2}\bar{u}^{s_1}\not{p}u^{s_1}$, this evaluates to

$$|\mathcal{M}_\alpha|^2 = \frac{2g_s^2 C_F}{s_{ij}^2} \sum_{s_1} Tr\{\mathcal{M}_0^{c*} u^{s_1}(p_j)\bar{u}^{s_1}(p_j)\mathcal{M}_0^c\} Tr\{\bar{u}^{s_1}(p_j)\not{p}_i u^{s_1}(p_j)\}\,. \tag{2.20}$$

The second trace is spin independent, and may be written

$$|\mathcal{M}_\alpha|^2 = \frac{g_s^2 C_F}{s_{ij}^2} Tr\{\mathcal{M}_0^{c*}\not{p}_j\mathcal{M}_0^c\} Tr\{\not{p}_j\not{p}_i\}\,. \tag{2.21}$$

Using the substitution $\not{p}_j = (1-z)\not{p}_{ij} + \mathcal{O}(k_\perp)$ from the definitions in (2.13) and taking the limit $k_\perp \to 0$ this becomes

$$|\mathcal{M}_\alpha|^2 = \frac{g_s^2 C_F}{p_i \cdot p_j}(1-z) Tr\{\mathcal{M}_0^{c*}\not{p}_{ij}\mathcal{M}_0^c\}\,. \tag{2.22}$$

The second term can be calculated in a similar way

$$|\mathcal{M}_\beta|^2 = \frac{g_s^2 C_F}{s_{ij}^2}\frac{1}{n\cdot p_j}\left((p_j)_\mu n_\nu + n_\mu (p_j)_\nu\right) Tr\{\mathcal{M}_0^{c*}\not{p}_{ij}\gamma^\nu\not{p}_i\gamma^\mu\not{p}_{ij}\mathcal{M}_0^c\}\,. \tag{2.23}$$

Performing the substitution $\not{p}_i = z\not{p}_{ij} + \mathcal{O}(k_\perp)$, inserting completeness relations, and again taking the limit $k_\perp \to 0$ this becomes

$$|\mathcal{M}_\beta|^2 = \frac{g_s^2 C_F}{s_{ij}^2}\frac{1}{zn\cdot p_j}\sum_{s_1} Tr\{\mathcal{M}_0^{c*} u^{s_1}(p_j)\bar{u}^{s_1}(p_j)\mathcal{M}_0^c\} Tr\{\bar{u}^{s_1}(p_i)[\not{p}_j\not{p}_i\not{n} + \not{n}\not{p}_i\not{p}_j]u^{s_1}(p_i)\}\,. \tag{2.24}$$

Note the use of the spin relation $\bar{u}^{s_1}\not{a}\not{b}\not{c}u^{s_2} = \delta_{s_1,s_2}\bar{u}^{s_1}\not{a}\not{b}\not{c}u^{s_1}$. Using the cylicity of the trace, the spin independence of the second trace, and the quartic gamma matrix relation gives

$$\begin{aligned} |\mathcal{M}_\beta|^2 &= \frac{g_s^2 C_F}{s_{ij}^2}\frac{1}{zn\cdot p_j} Tr\{\mathcal{M}_0^{c*}\not{p}_i\mathcal{M}_0^c\}8(p_i\cdot p_j)(p_i\cdot n)\,, \\ &= \frac{2g_s^2 C_F}{p_i\cdot p_j}\frac{p_i\cdot n}{n\cdot p_j} Tr\{\mathcal{M}_0^{c*}\not{p}_{ij}\mathcal{M}_0^c\}\,. \end{aligned} \tag{2.25}$$

Finally, the ratio of the product of momentum with the auxiliary vector n^μ can be found by contracting the vectors using the definitions provided in (2.13), leading to

$$|\mathcal{M}_\beta|^2 = \frac{g_s^2 C_F}{p_i\cdot p_j}\frac{2z}{1-z} Tr\{\mathcal{M}_0^{c*}\not{p}_{ij}\mathcal{M}_0^c\}\,. \tag{2.26}$$

Combining this with the result for the first term gives

$$|\mathcal{M}_{q+g}|^2 = \frac{g_s^2}{p_i\cdot p_j}C_F\left(1-z+\frac{2z}{1-z}\right) Tr\{\mathcal{M}_0^{c*}\not{p}_{ij}\mathcal{M}_0^c\}\,. \tag{2.27}$$

Noting that the remaining trace is simply the contribution from the Born amplitude. The final result is therefore

$$|\mathcal{M}_{q+g}|^2 = \frac{g_s^2}{p_i\cdot p_j}C_F\left(\frac{1+z^2}{1-z}\right)|\mathcal{M}_q|^2\,. \tag{2.28}$$

In the collinear limit this contribution behaves like $\mathcal{O}(1/k_\perp^2)$ as $p_i\cdot p_j \to \mathcal{O}(k_\perp^2)$. The cross-terms can be shown to behave as $\mathcal{O}(1/k_\perp)$, and are therefore sub-leading. The term which has been factored is universal and contains the so-called spin averaged Altarelli-Parisi [28] splitting function for the process $q \to qg$

$$\langle\hat{P}_{qq}(z)\rangle = C_F\left(\frac{1+z^2}{1-z}\right)\,. \tag{2.29}$$

The subscript labels qq correspond to the outgoing parton with momentum i and parent parton which undergoes splitting with momentum ij respectively — this is sufficient to label

all possible splittings in a unique way. Therefore, the splitting $q(p_{ij}) \to g(p_i)q(p_j)$ is

$$\langle \hat{P}_{gq}(z) \rangle = \langle \hat{P}_{qq}(1-z) \rangle = C_F \left(\frac{1+(1-z)^2}{z} \right) . \tag{2.30}$$

Similar calculations for the spin-averaged $g \to q\bar{q}, g \to gg$ splittings lead to the following kernels [28]

$$\begin{aligned} \langle \hat{P}_{gg}(z) \rangle &= C_A \left(\frac{1-z}{z} + \frac{z}{1-z} + z(1-z) \right) , \\ \langle \hat{P}_{qg}(z) \rangle &= \frac{1}{2} \left(z^2 + (1-z)^2 \right) . \end{aligned} \tag{2.31}$$

This set of splitting kernels forms the basis for parton evolution. Consider now inclusion of the phase space factor required to compute the cross section for the full process including the $q \to qg$ splitting — this has the form

$$d\phi_{q+g} = ... \frac{d^3p_i}{(2\pi)^3 2E_i} \frac{d^3p_j}{(2\pi)^3 2E_j} . \tag{2.32}$$

The correction arising from the splitting becomes

$$|\mathcal{M}_{q+g}|^2 d\phi_{q+g} = ... \frac{d^3p_i}{(2\pi)^3 2E_i} \frac{d^3p_j}{(2\pi)^3 2E_j} \frac{g_s^2}{p_i \cdot p_j} C_F \left(\frac{1+z^2}{1-z} \right) |\mathcal{M}_q|^2 . \tag{2.33}$$

Making the replacements, $E_i = zE_{ij}$ and $d^3p_i = d^3p_{ij}$ for fixed p_j leads to

$$d\sigma_{q+g} = \frac{|\mathcal{M}_q|^2}{\mathcal{F}} ... \frac{d^3p_{ij}}{(2\pi)^3 2E_{ij}} \frac{d^3p_j}{(2\pi)^3 2E_j} \frac{1}{z} \frac{g_s^2}{p_i \cdot p_j} C_F \left(\frac{1+z^2}{1-z} \right) . \tag{2.34}$$

It is useful to rewrite this correction by making a change of variables for the gluon phase space

$$\frac{d^3p_j}{(2\pi)^3 2E_j} = \frac{d(p_j)_\parallel}{E_j} \frac{d\phi}{2\pi} \frac{1}{8\pi^2} \frac{d(p_j)_\perp^2}{2} = \frac{pdz}{p(1-z)} \frac{d\phi}{2\pi} \frac{1}{8\pi^2} \frac{dk_\perp^2}{2} , \tag{2.35}$$

which follows from the definitions in (2.13) and requires the corresponding Jacobian to be calculated. The differential cross section correction then becomes

$$d\sigma_{q+g} = d\sigma_q \frac{dk_\perp^2}{k_\perp^2} \frac{\alpha_s}{2\pi} dz \frac{d\phi}{2\pi} C_F \left(\frac{1+z^2}{1-z} \right) . \tag{2.36}$$

This result highlights several important points. First of all, the splitting kernels $\langle \hat{P}_{ba}(z) \rangle$ are derived by summing over final state spins/polarisations and therefore exhibit no azimuthal dependence. However, extending this derivation to include spin correlations between the parent parton and its decay products provides information about the preferred plane of branching of the decay products — see for example Chapter 5 of [8]. To this extent, the factorisation of the collinear divergences is only approximate, as the splitting kernel is an operator in the helicity space of the parent parton — the factorisation is only true after summing over spin/polarisation states. Secondly, the splitting functions are also unregulated, containing soft divergences at $z = 0, 1$. These divergences can be accounted for by including the relevant contribution from virtual corrections, which cancel order-by-order by the KLN theorem. Finally, the choice of variable $k_\perp$ is arbitrary as there are other equivalent choices. However, this choice is well motivated as a lower cut-off (regularisation) for $k_\perp$ can be chosen to correspond to the physical scale below which emissions are experimentally unresolvable. It is therefore a physically motivated cut-off scale for the evolution of partons appearing in the final state.

As this factorisation procedure can be recursively applied to splittings an arbitrary number of times, it can be used to describe the effects of multiple splittings. To examine how this is done, multiple splittings in the initial state will be considered before generalising the technique to multiple splittings in both initial and final states. This will lead to a discussion of extending fixed-order calculations to include all-orders effects, and how PDFs are extracted from experimental measurements.

2.3 All-orders approach

Before considering the treatment of parton evolution in PDFs, it is first necessary to generalise the previous result to the case of initial state splittings. To do this, consider the two scenarios depicted in Figure 2.2. The left amplitude depicts a final state (time-like) branching, and the right amplitude depicts a series of initial state (space-like) branchings.

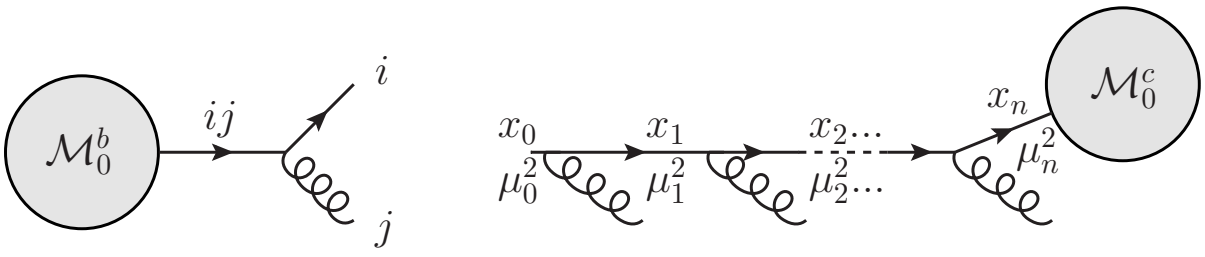


Figure 2.2: Amplitudes depicting parton branchings in both the final (time-like) and initial (space-like) states.

For a single splitting, the propagators have the form

$$\begin{aligned} \text{time-like} &= \frac{i(\not{p}_{ij} + m)}{2p_i \cdot p_j}\,, \\ \text{space-like} &= \frac{i(\not{p}_i + m)}{-2p_{ij} \cdot p_j}\,, \end{aligned} \tag{2.37}$$

where the incoming quark propagator and radiated gluon for the space-like branching have momentum labels i and j. As the external massless partons are assumed to be on-shell, the time-like and space-like branchings must have positive and negative virtuality respectively — hence the name. The result for the enhancement to the cross section arising from a space-like branching is then easily obtained by including the relevant phase space

$$d\phi_{n+g} = d\phi_n \frac{d^3 p_j}{(2\pi)^3 2E_j}\,. \tag{2.38}$$

This result is therefore identical to the case of a time-like branching as the flux-factor for the incoming quark propagator receives the following alteration during the splitting: $\mathcal{F}' = z\mathcal{F}$.

2.3.1 DGLAP Evolution

The factorisation theorem which was introduced at the start of this Chapter, which must be applied when performing truncated perturbation theory, separates the full scattering process into both short- and long-distance effects. The short-distance effects are computed using fixed-order perturbation theory, while the long-distance approximate all-orders effects are absorbed into a probability density function which describes the distribution of partons

within the hadron.

To justify this, consider the scenario in which a quark inside a hadron evolves from very low virtuality μ_0^2 (with large x_0) to large virtuality μ_n^2 (with small x_n) before finally participating in a hard subprocess at the scale Q^2. This is depicted in Figure 2.2, in which a chain of space-like branchings lead up to a hard interaction denoted by the amplitude $\mathcal{M}_0^c$. In the approximation of strongly-ordered transverse momenta — and introducing the notation $\mu_i^2 \equiv k_{\perp,i}^2$ — the following kinematic ordering is ensured

$$\begin{aligned} x_0 > x_1 > x_2 > ... > x_n \,, \\ \mu_0^2 \ll \mu_1^2 \ll \mu_2^2 \ll ... \ll \mu_n^2 \ll Q^2 \,. \end{aligned} \tag{2.39}$$

Using the previous result for the correction from a single splitting, this evolution can be written as

$$\begin{aligned} &\int_{\mu_0^2}^{Q^2} \frac{\alpha_s(\mu_n^2)}{2\pi}\frac{d\mu_n^2}{\mu_n^2} ... \int_{\mu_0^2}^{\mu_3^2} \frac{\alpha_s(\mu_2^2)}{2\pi}\frac{d\mu_2^2}{\mu_2^2} \int_{\mu_0^2}^{\mu_2^2} \frac{\alpha_s(\mu_1^2)}{2\pi}\frac{d\mu_1^2}{\mu_1^2} \,, \\ &= \prod_{i=1}^{n} \frac{\alpha_s(Q^2)}{2\pi} \int_{\mu_0^2}^{\mu_{i+1}^2} \frac{d\mu_i^2}{\mu_i^2} \left(1 + \alpha_s(Q^2) b_0 ln\frac{Q^2}{\mu_i^2} + \mathcal{O}(\alpha_s^2)\right) . \end{aligned} \tag{2.40}$$

Keeping only the leading terms in powers of $\alpha_s(Q^2)$, the above result can be approximated by

$$\frac{1}{n!}\left(\frac{\alpha_s(Q^2)}{2\pi} ln\frac{Q^2}{\mu_0^2}\right)^n . \tag{2.41}$$

The resummation of these logarithms to all-orders is known as the leading logarithmic approximation (LLA) and is a necessary feature of realistic predictions of observables. For example, to calculate the cross section for the hard subprocess $\mathcal{M}_0^c$, it is necessary to know the probability density describing the quark distribution as a function of the quarks momentum fraction x_n at a given scale μ_n^2. This must account for all the possible paths which contribute to the density at these values. To see this, consider the change of a generic PDF $f(x, \mu^2)$ when the virtuality is increased by an infinitesimal step $\mu^2 \to \mu^2 + \delta\mu^2$. The PDF will change if a parton undergoes a splitting or if a parton at higher x' splits and produces it (see Figure 2.3). Using the result from (2.36), this is summarised as

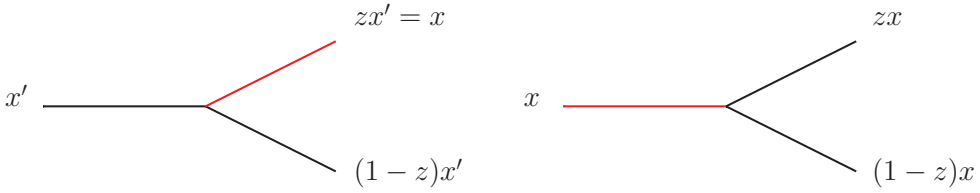


Figure 2.3: Kinematic configurations for PDF evolution.

$$\delta f(x,\mu^2) = \frac{\delta\mu^2}{\mu^2}\left(\int_x^1 dx'dz\frac{\alpha_s}{2\pi}\langle\hat{P}(z)\rangle f(x',\mu^2)\delta(zx'-x) - \int_0^1 dz\frac{\alpha_s}{2\pi}\langle\hat{P}(z)\rangle f(x,\mu^2)\right). \tag{2.42}$$

Rearranging and integrating over x' gives

$$\begin{aligned}\mu^2\frac{\partial f(x,\mu^2)}{\partial\mu^2} &= \frac{\alpha_s}{2\pi}\left(\int_0^1\frac{dz}{z}\langle\hat{P}(z)\rangle f(\frac{x}{z},\mu^2) - \int_0^1 dz\langle\hat{P}(z)\rangle f(x,\mu^2)\right), \\ &= \frac{\alpha_s}{2\pi}\int_0^1 dz\langle\hat{P}(z)\rangle\left(\frac{1}{z}f(\frac{x}{z},\mu^2) - f(x,\mu^2)\right).\end{aligned} \tag{2.43}$$

This can be rewritten by introducing the plus prescription

$$\int_0^1 dx h_+(x)g(x) = \int_0^1 h(x)\left(g(x)-g(1)\right), \tag{2.44}$$

where $g(x)$ is a regular function. After defining the regularised splitting function as $\langle\hat{P}(z)\rangle_+ = P(z)$, the evolution can be written

$$\mu^2\frac{\partial f(x,\mu^2)}{\partial\mu^2} = \frac{\alpha_s}{2\pi}\int_x^1\frac{dz}{z}P(z)f(\frac{x}{z},\mu^2). \tag{2.45}$$

This evolution equation can be generalised to include all splittings which may contribute to a specific flavour or type of parton distribution $\delta f_a(x,\mu^2)$. This leads to a set of coupled differential equations — the Dokshitzer-Gribov-Lipatov-Altarelli-Parisi (DGLAP) evolution equations [28–30]

$$\begin{aligned}\mu^2\frac{\partial f_a(x,\mu^2)}{\partial\mu^2} &= \sum_b\frac{\alpha_s}{2\pi}\int_x^1\frac{dz}{z}P_{ab}(z)f_b(\frac{x}{z},\mu^2), \\ &= \sum_b P_{ab}\otimes f_b(\mu^2).\end{aligned} \tag{2.46}$$

The labels a and b correspond to the parton type (quark or gluon). Since the original work of

DGLAP, the splitting functions are now known at NNLO [31–34]. The splitting functions P_{ab} are therefore formally an expansion in α_s, and these corrections are necessary to consistently factor the calculation of a hard subprocess, at a given fixed-order, into the PDF at the same order in α_s. For simplicity, only the LO splitting functions will be considered in the following qualitative discussion — at LO they have a clear probabilistic meaning. In this notation, the evolution of the flavour i quark and gluon PDFs are given by

$$\begin{aligned} \mu^2 \frac{\partial q_i(x,\mu^2)}{\partial \mu^2} &= P_{qq} \otimes q_i(\mu^2) + P_{qg} \otimes g(\mu^2)\,, \\ \mu^2 \frac{\partial g(x,\mu^2)}{\partial \mu^2} &= P_{gq} \otimes \sum_i^{\mathrm{n_f}} \left(q_i(\mu^2) + \bar{q}_i(\mu^2)\right) + P_{gg} \otimes g(\mu^2)\,. \end{aligned} \tag{2.47}$$

These equations allow for PDFs to be evolved to arbitrary scales. Therefore, measurements constraining the PDFs at a given scale can be used to make predictions for processes at any other scale. As the PDFs are evolved to different scales, the tower of logarithms appearing in (2.41), which arise from multiple splittings, are automatically resummed. The parton evolution in PDFs is to this extent an all-orders effect.

In the derivation of the evolution equations, the regularised splittings functions $\langle \hat{P}(z) \rangle_+ = P(z)$ were introduced. These functions contain a virtual correction term $c_{ab}\delta(1-z)$ which universally cancels soft divergences, occurring for gluon emission in the limit $z \to 1$. The coefficient of the virtual correction c_{ab} can be calculated by imposing charge and momentum sum rules. For example, the coefficient in the function $P_{qq}(z)$ is be obtained by requiring that charge sum rules are scale independent

$$\int_0^1 dz P_{qq}(z) = 0\,. \tag{2.48}$$

This leads to

$$\int_0^1 dz \left(\frac{1+z^2}{1-z}\right)_+ = -\int_0^1 dz \delta(1-z) c_{qq}\,. \tag{2.49}$$

Using the definition of the plus prescription, the coefficient c_{qq} may be evaluated as

$$c_{qq} = -\int_0^1 \frac{dz}{1-z}\left((1+z^2) - (1+z^2)|_{z=1}\right) = \frac{3}{2}\,. \tag{2.50}$$

A similar calculation, using the momentum sum rule, provides the correction to the process of gluon splitting. The full set of regularised splitting functions are

$$\begin{aligned}
P_{qq}(z) &= C_F\left(\frac{1+z^2}{(1-z)_+} + \frac{3}{2}\delta(1-z)\right)\,,\\
P_{gq}(z) &= C_A\left(\frac{1+(1-z)^2}{z}\right)\,,\\
P_{gg}(z) &= C_A\left(\frac{1-z}{z} + \frac{z}{(1-z)_+} + z(1-z)\right) + \frac{1}{6}(11C_A - 2n_f)\delta(1-z)\,,\\
P_{qg}(z) &= \frac{1}{2}\left(z^2 + (1-z)^2\right)\,.
\end{aligned} \tag{2.51}$$

Before discussing the practical implementation of the evolution equations, it is important to consider the validity of both the lower and upper choices for the scale cut-off in the PDF evolution (μ_0^2, μ_F^2). The lower cut-off μ_0^2 is required to factor out the non-perturbative nature of the hadron dynamics appearing at scales $\mathcal{O}(\Lambda_{\rm QCD})$. The counterpart of this cut-off in QED is the electron mass, which regulates collinear singularities. However, as the quark is strongly bound within the hadron, it is hard to say exactly what quark mass should actually appear in the propagator. As PDFs can be constrained with measurements of processes occurring with $Q^2 \gg \mu_0^2$, it is not actually necessary to provide a description of dynamics occurring below μ_0^2 (typically a few GeV), avoiding potential ambiguities. The upper cut-off μ_F^2 introduces an unphysical logarithmic dependence $\sim ln(Q^2/\mu_F^2)$ into the evaluation of the hard subprocess. As previously discussed, the choice of μ_F^2 should therefore be process dependent, and chosen to match the physical scale Q^2. This avoids large logarithms that may introduce artificially large theoretical uncertainty.

2.3.2 Sudakov Form Factor

To practically implement parton evolution using a MC method, it will prove useful to first derive a no-emission form factor. To begin, a separate notation for time-like evolution ($q_i^2 \equiv k_{\perp,i}^2$) is introduced to distinguish it from the space-like evolution in the PDF. The probability for an emission of a resolvable parton to occur within the virtuality interval $q^2 \to q^2 + \delta q^2$ is

$$\delta\mathcal{P}(z, q^2) = \frac{\alpha_s(q^2)}{2\pi}\frac{\delta q^2}{q^2}\int_{z_0}^{1} dz\langle\hat{P}(z)\rangle\,, \tag{2.52}$$

where the unregulated splitting function is regulated by the cut-off $z_0(q_0^2, q^2)$. Note that emissions below the cut-off scale q_0^2 are physically unresolvable. It follows from this definition that the probability for no emissions to occur within the interval $[Q^2, q^2]$ can be found by considering a chain of infinitesimal subintervals ($q_i^2 = (Q^2 - q^2)/n$) as

$$\begin{aligned}
\Delta_s(Q^2, q^2) &= \lim_{n\to\infty}\prod_{i=1}^{n}\left(1 - \mathcal{P}(q_i^2, q_{i-1}^2)\right)\,, \\
&= \exp\left[-\lim_{n\to\infty}\sum_{i=1}^{n}\mathcal{P}(q_i^2, q_{i-1}^2)\right]\,, \\
&= \exp\left[-\int_{q^2}^{Q^2}\frac{\alpha_s(k_\perp^2)}{2\pi}\frac{dk_\perp^2}{k_\perp^2}\int_{z_0}^{1} dz\langle\hat{P}(z)\rangle\right]\,.
\end{aligned} \tag{2.53}$$

This function is known as the Sudakov form factor, and has the benefit of being easily implemented via MC methods. For example, given an initial condition Q^2 for the virtuality of a subprocess, the scale of a subsequent emission can be found by solving the equation

$$\Delta_s(Q^2, q_1^2) = r_1\,, \tag{2.54}$$

where r_1 is a pseudorandom number uniform on the interval $[0, 1]$. The scale of the next emission is then found by solving

$$\Delta_s(q_1^2, q_2^2) = r_2\,, \tag{2.55}$$

which is iteratively performed until the virtuality of a subsequent emission falls below the lower cut-off $q_0^2 \sim \mathcal{O}(1\text{ GeV})$. This procedure, which produces a shower of partons, is known as the *parton shower* (PS). The lower cut-off q_0^2, the counterpart of μ_0^2 in the PDF, indicates the transition from the perturbative regime into the region of strong dynamics. At this stage, the PS is truncated and the transition from coloured partons with virtuality $\mathcal{O}(q_0^2)$ to on-shell colour singlets occurs. The PS approach allows the accurate modelling of exclusive observables in the region in which low energy and transverse momentum radiation is important. As the PS evolves off-shell partons to the hadronisation scale (where hadronisation is subsequently performed), the comparison between theory and experiment becomes more direct. The PS is also an extremely useful tool for simulating the effect of detector response, as it can be used to predict the multiplicity and momentum distribution of the decay products resulting from an inelastic pp collision.

2.4 NLO+PS

There are clear benefits to both fixed-order calculations and the all-orders PS approach. For example, an NLO QCD calculation of the differential Z boson cross section will provide a more accurate estimation of the inclusive cross section, and reliably describe the Z boson transverse momentum (p_T) shape and normalisation in the high-p_T range. However, at low-p_T, the differential cross section receives a large positive contribution resulting from the singular structure of the real emission as $p_T \to 0$. Although the inclusive cross section remains finite, as it must by the KLN theorem, the low-p_T region is poorly modelled as resummation of soft and collinear enhancements from further higher-order corrections have been neglected. The PS on the other hand accurately describes the low-p_T region, as it approximately accounts for all-order effects in the soft/collinear region. However, it poorly models the high-p_T range, as emissions in this region do not factorise.

At the LHC, it is becoming increasingly important to include accurate predictions for SM processes. Such improvements increase the reach of new physics searches and the sen-

sitivity to physical parameters. As many searches at the LHC now adopt techniques based on boosted decision trees, multi-variate analysis, and neural networks, which rely on the MC modelling of signal and background processes, there is a clear need for high precision predictions of exclusive observables. This has prompted a large theoretical effort in which two new developments have arisen, the first development was to match matrix elements with the PS (ME+PS) [35], and the second was to interface NLO calculations with the PS (NLO+PS) [36, 37]. There has also been recent progress to obtaining NNLO accuracy matched to a PS [38, 39]. These methods are reviewed in [40]. In later Chapters, the POWHEG method of interfacing NLO calculations [37, 41, 42] will be used to estimate both signal and background processes. The basics of this method will therefore be discussed for completeness.

2.4.1 POWHEG Method

The POsitive Weight Hardest Emission Generator (POWHEG) method is an adaptation of the standard MC PS procedure which generates a single NLO accurate parton emission, and is NLO accurate for inclusive observables. One of the main benefits of this method is that the generated output, a sample of parton level events, is independent of the PS program it is interfaced with. Also, for $k_\perp$ ordered PS programs such as `Pythia8` [43], the evolution scale for subsequent emissions is automatically fixed by the scale of the POWHEG generated emission.

To understand the implementation of this method, consider the production of a Z boson by a standard LO+PS program. The differential cross section including the hardest emission generated by the PS is given by

$$d\sigma_{PS} = d\phi_X \frac{|\mathcal{M}_X|^2}{\mathcal{F}} \left[\Delta(Q^2, Q_0^2) + \int \frac{\alpha_s}{2\pi} \frac{dq^2}{q^2} \int_{z_0}^{1} dz \langle \hat{P}(z) \rangle \Delta(Q^2, q^2) \right], \tag{2.56}$$

where $\Delta(Q^2, Q_0^2)$ is the Sudakov form-factor defined in (2.53). The first term corresponds to the production of a Z boson with Born phase space and kinematics — i.e. zero p_T. The

second term corresponds to the production of Z boson and a single parton, balanced in p_T, and is accurately modelled in the singular region where factorisation is applicable. The integral of this formula yields a total cross section equivalent to the Born cross section, as required by unitarity.

Before examining how the POWHEG method adapts this formula, the following notation will prove useful

$$\frac{|\mathcal{M}_X|^2}{\mathcal{F}} \to B\,, \qquad \frac{|\mathcal{M}_{X+1}|^2}{\mathcal{F}} \to R\,, \qquad \frac{2\mathrm{Re}|\mathcal{M}_X^1|^2}{\mathcal{F}} \to V\,. \tag{2.57}$$

The POWHEG method adapts the standard MC PS formula by making several replacements. To begin, the prefactor is altered according to

$$d\phi_X B \to d\phi_{\bar{B}} \bar{B}\,, \qquad \bar{B} = B + V + \int R d\phi_1\,. \tag{2.58}$$

This is equivalent to the NLO cross section (2.5), and can be calculated numerically by including a counterterm. The second adjustment is the replacement of the splitting kernel, which is only accurate in the singular region, with the NLO accurate real emission R as follows

$$\frac{dq^2}{q^2} dz \frac{\alpha_s}{2\pi} P(z) \to d\phi_1 \frac{R}{B}\,. \tag{2.59}$$

Finally, the modified Sudakov form factor with this replacement becomes

$$\Delta_{\texttt{POWHEG}}(Q^2, k_T^2) = \exp\left[- \int d\phi_1 \frac{R}{B} \Theta\left(k_T^2(\phi_1) - k_T^2\right) \right]\,. \tag{2.60}$$

The POWHEG differential cross section with these replacements is then

$$d\sigma_{\texttt{POWHEG}} = d\phi_{\bar{B}} \bar{B} \left[\Delta_{\texttt{POWHEG}}(Q^2, k_T^{min,2}) + \Delta_{\texttt{POWHEG}}(Q^2, k_T^2) \frac{R}{B} d\phi_1 \right]\,. \tag{2.61}$$

In analogy with the standard MC PS program, the first term is the no emission contribution, while the second term describes the production of a Z boson in association with an NLO accurate parton emission. The total cross section corresponds to the NLO cross section for Z

boson production. Full details of the POWHEG method and a recipe for implementing NLO calculations in the POWHEG-BOX is provided in [41]. From this point, the term `POWHEG` will refer to the implementation of the POWHEG method in the POWHEG-BOX computer framework.

To compare the various methods which have been discussed so far, the Z boson differential cross section with respect to transverse momentum is shown in Figure 2.4 at NLO (`MCFM` [44]), NLO+PS (`POWHEG` [45] matched to `Pythia8`), and LO+PS (`Pythia8`). The normalisation of the NLO and NLO+PS is equivalent. Notice in the case of the NLO distribution, the first bin is not visible in the plot as it is negative — arising from the virtual corrections. The distribution obtained with NLO+PS is harder in the moderate p_T range due to the presence of multiple splittings, which migrates the Z boson p_T to larger values. The prediction obtained with LO+PS falls off dramatically beyond the Z boson mass as the Sudakov upper limit is m_Z^2, the small fraction of events beyond this scale contain multiple emissions.

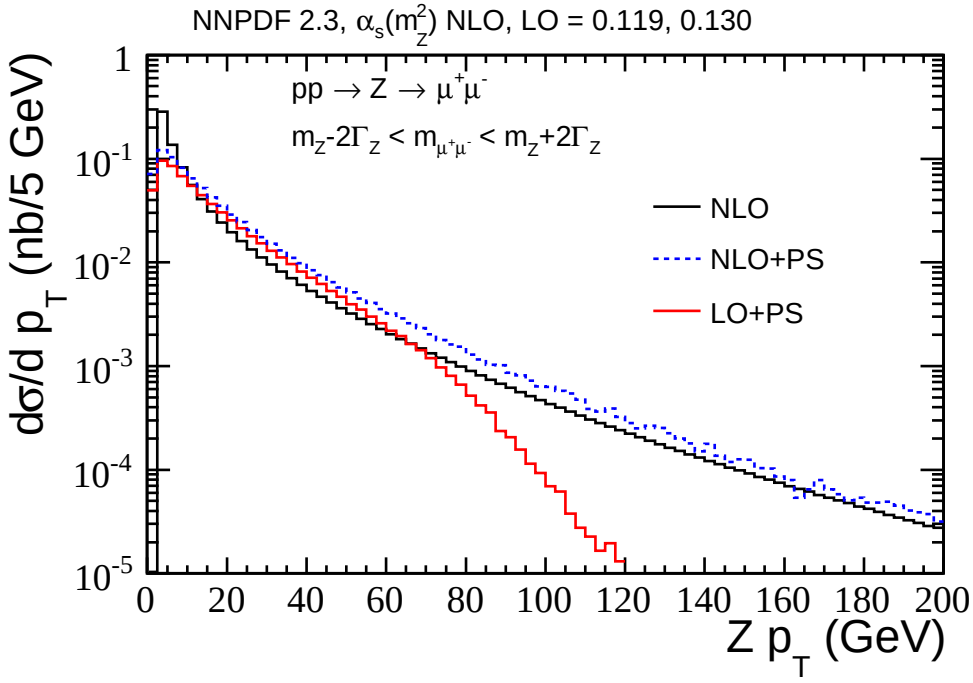


Figure 2.4: Comparison of NLO, NLO+PS, and LO+PS predictions for Z boson p_T spectrum for the process $pp \to Z$.

2.5 LPHD

Another important topic for the discussion LHC observables is the postulation of *local parton hadron duality* (LPHD) [46] — the flow of momentum and quantum numbers at the hadron level follows those established at the parton level. Due to the enhancement of processes with collinear and soft radiation, energetically produced coloured partons are experimentally observed as a cluster of hadronic activity localised in phase space (jets). In agreement with experimental observations, LPHD postulates that the majority of the energy of the cluster is carried by one hadron. For example, in the case of back-to-back $b\bar{b}$ production it would be expected that two corresponding back-to-back clusters would be experimentally observed, and that the majority of the energy of each cluster would be carried by the B-hadron decay products. It is this duality that allows fixed-order calculations with parton level final states to be compared with experimentally observed hadronic final states.

2.5.1 Hadronisation

Modelling of the transition from coloured off-shell partons into a colour singlet representation of a hadronic final state is necessary to directly compare theoretical models with experimental observations. The phenomenological modelling of this transition is referred to as *hadronisation*. As has been briefly alluded to in previous sections, the reason this modelling is phenomenological is because the transition occurs in the regime of strong coupling in which perturbation theory does not provide a reliable description. The two commonly adopted models are the *string* [47] and *cluster* [48,49] models based on the original proposals of [50–52]. These two models differ in that the transition into hadrons in the cluster model proceeds through an intermediatory clustering stage. The following discussion will be limited to the string model.

The basic motivation of the string model is linear confinement at large distances. Consider now the low energy back-to-back production of a colour singlet $q\bar{q}$ pair. As the partons move apart, they can be interpreted as colour flux tube being stretched as the spatial separation

between the quarks increases. If the string has uniform energy per unit length, then this leads to a natural picture of confinement in which the string potential is $V(r) = \kappa r$, where κ is associated with a string tension. If the string exceeds a certain length, then enough energy is available to spontaneously produce another light singlet $q'\bar{q}'$ pair in the colour field created by the separating partons. This procedure can be performed iteratively until localised colour singlets can form hadrons. The requirement that string ends do not change flavour also adheres to LPHD. This model is theoretically supported by quenched lattice QCD calculations [53] of the static $q\bar{q}$ potential which, for fixed κ, is observed to have the behaviour of a linear potential for large separations. The physical interpretation of this model is depicted in Figure 2.5. The version of the string model implemented in modern MC event generators like `Pythia8`, which has been tuned to experimental data, is substantially more complicated than the basic picture presented here.

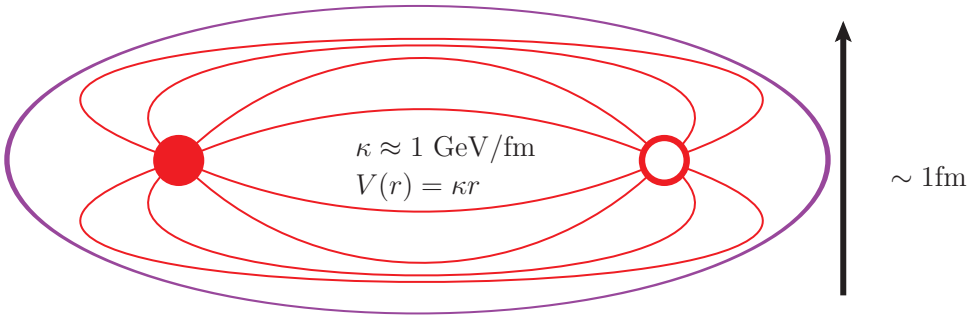


Figure 2.5: Pictorial representation of flux tube between quark and anti-quark.

2.5.2 Jets

Given that the experimentally observed clusters of particles are not fundamental, and have a topological and energetic structure which differs on an event-by-event basis, it is necessary to define how the cluster of particles (jet) is reconstructed. In particular, the algorithm for jet reconstruction should be both soft and collinear safe. Theoretically, this is necessary to produce finite results which can be compared to perturbative QCD predictions. Experimentally, a detector cannot resolve the effects of soft or collinear splittings.

To perform clustering, it is first necessary to define a 'measure' between all particles

in the event which the algorithm will attempt to reconstruct. A general measure in the rapidity-phi plane is

$$d_{ij} = \min[k_{t,i}^{2p}, k_{t,j}^{2p}]\frac{\Delta R_{ij}^2}{R^2}\,, \qquad \Delta R_{ij}^2 = (y_i - y_j)^2 + (\phi_i - \phi_j)^2\,. \tag{2.62}$$

The variable R is a global distance in rapidity-phi space which is generally fixed to some constant value. In the following Chapters, the choice $R = 0.5$ will made for all potential measurements considered at LHCb. The choice of the definition of the measure d_{ij}, and the corresponding global distance R should made to suit the process being studied. Take for example the choice $p = -1$ which corresponds to the anti-k_t algorithm [54]. The reconstruction algorithm then proceeds in the following way:

1. Calculate and minimise d_{ij} for all particles in the event.

2. If $\Delta R_{ij} < R$, then these two particles are clustered into a jet. Step 1 should be carried out again with particle i and j replaced with the new cluster ij.

3. If $R < \Delta R_{ij} < 2R$, then there will be two separated jets. However, neither jet will be perfectly conical as the two jets share a boundary, denoted by b, determined by the equality $\Delta R_{ib}/k_{t,i} = \Delta R_{jb}/k_{t,j}$.

4. If $\Delta R_{ij} > 2R$, then these two jets will be separated and conical (depending on the presence of other nearby softer jets).

Note that in the case of the anti-k_t algorithm, as the measure is minimised for $\min[k_{t,i}^{-2}, k_{t,j}^{-2}]$, soft particles tend to cluster with hard ones before themselves. This is why repeating Step 2 results in a circular jet centred around the hardest particle, which is often useful for experimental jet calibration. The jets are also required to have a minimum p_T, which separates the jet from the low-p_T radiation associated to the beam remnants. A comparison of different jet reconstruction algorithms can be found in [54]. An example of a reconstructed anti-k_t jet with $R = 0.5$ in data is shown in Figure 2.6. This is a $Z(\to \mu^+\mu^-)$+jet candidate event from 7 TeV collisions at the LHC, which has been reconstructed with the LHCb detector [55].

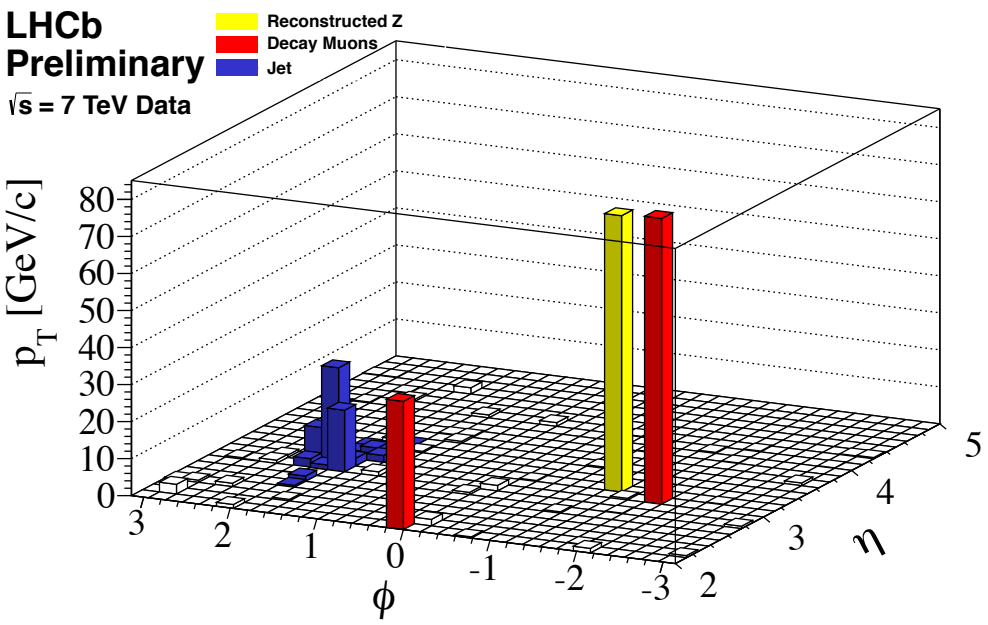


Figure 2.6: $Z(\rightarrow \mu^+\mu^-)$+jet event within LHCb.

The spread of momentum in the jet is clearly visible.

Another important property of jet reconstruction is the flavour tagging of jets, in particular those initiated by bottom quarks (b-jets). There are many physics processes, such as the decay of top quarks, the Higgs boson, as well as new-physics scenarios, which have b-jets in the final state. Accurately identifying b-jets (b-tagging) is necessary to study many of these processes for which backgrounds from light-jets would otherwise be overwhelming. There are various ways to identify b-jets, all of which take advantage of the long lifetimes and large masses of B-hadrons that results in jets with displaced vertices and relatively hard decay products. It is also possible to tag the charge of b-jets by looking for jets in which the B-hadron has decayed semi-leptonically — this technique has recently been applied by the LHCb collaboration in [56] to measure the production asymmetry of $b\bar{b}$ pairs at high pseudorapidity and invariant mass. The b-tagging algorithms currently employed by LHC experiments [57] rely on sophisticated learning algorithms. However, the final result is a b-tagging efficiency and mis-tag rate which is generally dependent on the p_T and rapidity of the reconstructed jet.

2.6 PDFs

As discussed throughout this Chapter, providing realistic predictions for physical processes in hadron collisions with truncated perturbation theory requires knowledge of the parton distributions. This is provided by measurements of different processes across a large range of x and μ_F^2. The DGLAP evolution equations, which allow PDFs to be evolved to arbitrary scales, can then be used to constrain a set of PDFs provided at some lower cut-off scale μ_0^2. In this way, the constrained PDFs can then be used to make predictions of other processes at different scales.

The prediction of almost all observables at the LHC rely on prior knowledge of the PDFs. In some processes, the largest source of uncertainty arises from the PDFs which are poorly constrained in certain regions of the (x, μ_F^2)-plane. Measuring processes which are sensitive to different PDF flavours in these particular regions of x and μ_F^2 is clearly important. However, it is equally important to discuss how the PDFs should be extracted from these measurements, and how uncertainties in the data should be propagated into the extracted PDFs.

There are several groups which provide modern PDF sets obtained from global fits to a large sample of data sets: ABM [58], CTEQ [59], HERAPDF [60], MSTW [61] and NNPDF [62] — the modern PDF sets provided by these groups are generally adopted to perform phenomenology. The result of the global fit depends on the experimental data included in the fit, the choice of PDF input parameterisation, including or fixing $\alpha_s(m_Z^2)$ as a parameter in the fit, the treatment of heavy flavours, and how uncertainties in the global fit are extracted. Although the PDF fitting and uncertainty propagation is treated in different ways by these aforementioned groups, the predictions of observables and the associated PDF uncertainty are generally comparable — or the cause of any substantial difference is known. For example, the treatment of heavy flavour PDFs as discussed in [63] which can have a large impact on the gluon PDF.

An overview of different approaches to global fits will be provided. This includes a

discussion of the Hessian approach to uncertainty propagation as well as the MC sampling approach adopted by NNPDF. The technique of reweighting will also be discussed.

2.6.1 Approaches to global fits

When performing a global fit to a large sample of different data sets, propagating the experimental uncertainties for the fitted data points into statistically meaningful uncertainties on the PDFs is a non-trivial task. In particular, some data are not provided with uncertainty correlations, or data from different experiments may be inconsistent. The first step of the fit is to perform a minimisation of an effective global χ^2 function which measures the quality of the fit between theoretical prediction and experiment. This minimisation can be performed with tools such as MINUIT [64] and has the form

$$\chi^2(\{a_i\}) = \sum_{j,k}^{\mathrm{N_{data}}} \left(F_j^{\mathrm{exp}} - F_j^{\mathrm{theory}}(\{a_i\})\right) C_{jk}^{-1} \left(F_k^{\mathrm{exp}} - F_k^{\mathrm{theory}}(\{a_i\})\right) , \tag{2.63}$$

where C_{ij} denotes the covariance matrix which contains information about the correlations in the experimental uncertainties.

Hessian method: the traditional approach is to assume a parametric form for the different PDFs at the cut-off scale μ_0^2

$$xf(x,\mu_0^2) = Ax^{\eta_1}(1-x)^{\eta_2}(1+\epsilon\sqrt{x}+\gamma x)\,. \tag{2.64}$$

This parameterisation is then applied to combinations of PDFs, motivated by the structure functions probed in deep inelastic scattering (DIS) experiments, which provide a set of unknown parameters $\{a_i\}$ — see for example [61]. Some of these parameters can be fixed by the quantum numbers of the hadron. For the proton, the applicable rules are

$$\int_0^1 (u(x)-\bar{u}(x))\,dx = 2\,, \quad \int_0^1 \left(d(x)-\bar{d}(x)\right)dx = 1\,, \quad \int_0^1 (s(x)-\bar{s}(x))\,dx = 0\,, \tag{2.65}$$

and the momentum sum rule leads to the relation

$$\int_0^1 \left(\sum_i^{n_f} (q_i(x) + \bar{q}_i(x)) + g(x) \right) x dx = 1 \,. \tag{2.66}$$

It was scale independence of the charge sum rules which allowed the coefficient of the regularised Altarelli-Parisi splitting function to be derived in the previous Section. In the end, the number of free parameters which must be minimised is of the order 20, depending on the specific parameterisation adopted. The propagation of uncertainties in the global fit can then be extracted using the Hessian method [65, 66]. This method relies on the χ^2 being quadratic around the global minimum, meaning that if there are large correlations between the parameters in $\{a_i\}$ then the linear error propagation would not be justifiable. To propagate the uncertainties, a global goodness-of-fit quantity χ^2_{global} is introduced which examines the local curvature around the global minimum (with n best fit parameters $\{a_i^0\}$)

$$\Delta\chi^2_{\text{global}} = \chi^2_{\text{global}} - \chi^2_{\text{min}} = \sum_{i,j=1}^{n} H_{ij}(a_i - a_i^0)(a_j - a_j^0) \,, \tag{2.67}$$

where the Hessian matrix H has the entries

$$H_{ij} = \frac{1}{2} \left. \frac{\partial^2 \chi^2_{\text{global}}}{\partial a_i \partial a_j} \right|_{\text{min}} \,. \tag{2.68}$$

Clearly the definition of the goodness-of-fit plays a crucial role. Strictly speaking, the choice $\Delta\chi^2_{\text{global}} = 1$ should account for an uncertainty on the input parameters of one standard deviation. However, this leads to an underestimate of the uncertainty, a consequence of inconsistent data and perhaps a lack of understanding in the theoretical input required to perform the minimisation [67]. To account for this uncertainty underestimate, inconsistent data can be removed from the full fit, or a tolerance parameter T can be introduced to inflate the allowed uncertainty such that $\Delta\chi^2_{\text{global}} < T^2$. For the latter, this tolerance parameter has been introduced in both a dynamical [61] and a global [68] way. In either case, it is convenient to diagonalise the covariance matrix, $C = H^{-1}$, and work in terms of its eigenvectors and eigenvalues. As the covariance matrix is symmetric, partial derivatives commute, and it has

a set of orthonormal eigenvectors $\vec{v}_k$ defined by

$$\sum_{j=1}^{n} C_{ij} v_{jk} = \lambda_k v_{ik} \,, \tag{2.69}$$

in which λ_k is the eigenvalue of k^{th} orthonormal eigenvector. The benefit of this orthonormal basis is that the departure from the global minimum, $\Delta\chi^2_{\text{global}}$, is now mapped out in a sheproid in the basis of vectors $\{v_i\}$. The displacements from the global minimum in this basis can be defined

$$a_i - a_0 = \sum_{k=1}^{n} e_{ik} z_k \,, \tag{2.70}$$

in which the eigenvectors have been rescaled as $e_{ik} = \sqrt{\lambda_k} v_{ik}$. In this basis, the deviation from the global minimum becomes

$$\Delta\chi^2_{\text{global}} = \sum_{k=1}^{n} z_k^2 \,. \tag{2.71}$$

The eigenvector PDF sets $\mathcal{S}_k^{\pm}$ are then produced to span the hypersphere defined by $\sum_{k=1}^{n} z_k^2 \leq T^2$. The displacements of the PDF parameters in this basis are

$$a_i(\mathcal{S}_k^{\pm}) = a_i^0 \pm t e_{ik} \,. \tag{2.72}$$

In principle, the deterioration of the χ^2 along any direction should be symmetric in the quadratic approximation. However, as this approximation is not exact, asymmetric uncertainties are obtained. The CTEQ, HERAPDF and MSTW groups provide $2n+1$ PDF sets which include the central PDF member $\mathcal{S}_0$, as well as a pair of eigenvector members $\mathcal{S}_k^{\pm}$ which account for the asymmetric displacements from the minimum for each eigenvector direction. The asymmetric uncertainties on a quantity F, derived from the central PDF

member $F(\mathcal{S}_0)$, are then found by applying the following formulas

$$\begin{aligned}\Delta F^+ &= \sqrt{\sum_{k=1}^{n}\left(\max[F_k^+ - F_0, F_k^- - F_0, 0]\right)^2}, \\ \Delta F^- &= \sqrt{\sum_{k=1}^{n}\left(\max[F_0 - F_k^+, F_0 - F_k^-, 0]\right)^2},\end{aligned} \tag{2.73}$$

where the shorthand notation $F_k^{\pm} = F(\mathcal{S}_k^{\pm})$ has been introduced. Alternatively, symmetric uncertainties can also be approximated as

$$\Delta F = \frac{1}{2}\sqrt{\sum_{k=1}^{n}\left(F_k^+ - F_k^-\right)^2}. \tag{2.74}$$

NN method: an alternative approach to the propagation of experimental uncertainties and correlations, which does not rely on a tolerance parameter or exclusion of data in the global fit, is the method adopted by the NNPDF collaboration — originally proposed in [69]. The main features can be summarised as follows:

- Replica sets of data points are produced following a multi-gaussian distribution which is centred on each data point and has a corresponding variance given by the experimental uncertainty. This reproduces the statistical distribution of the experimental data.

- A minimisation procedure is then performed for generically parameterised PDFs for each replica set. This provides a projection into the space of PDFs.

This procedure allows any statistical property of the parton distributions or any PDF dependent function to be calculated using standard statistical methods. As the PDFs are parameterised through the use of multilayer neural networks, with a large number of parameters, there is almost no parameterisation bias [70, 71]. The average and standard deviation

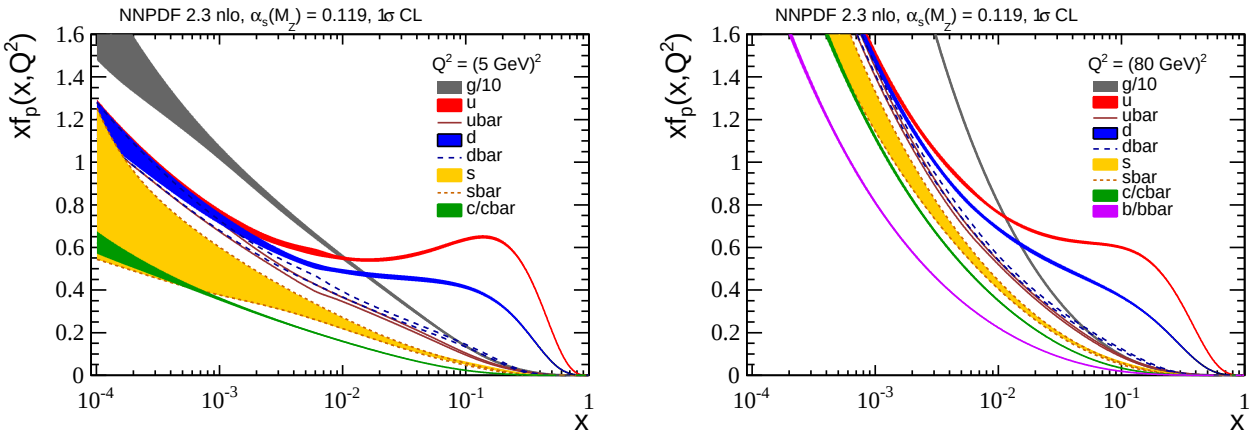


Figure 2.7: NNPDF 2.3 NLO parton distrubutions evolved to $Q^2 = (5\ \text{GeV})^2$ (left) and $Q^2 = (80\ \text{GeV})^2$ (right).

for an observable F calculated from the replica PDF set $\{\mathcal{R}_k\}$ with N_{rep} replicas is

$$\begin{aligned} \langle F \rangle &= \frac{1}{N_{\text{rep}}} \sum_{k=1}^{N_{\text{rep}}} F(\mathcal{R}_k)\,, \\ \Delta F &= \sqrt{\frac{N_{\text{rep}}}{N_{\text{rep}}-1}\left(\langle F^2 \rangle - \langle F \rangle^2\right)}\,. \end{aligned} \tag{2.75}$$

The NNPDF 2.3 PDFs with $\alpha_s(m_Z^2) = 0.119$ [72] provided at NLO are shown in Figure 2.7 with their associated 1σ confidence level (CL) uncertainty. In the left plot, the PDFs are evolved to $Q^2 = (5\ \text{GeV})^2$, while the PDFs in the right plot are evolved to $Q^2 = (80\ \text{GeV})^2$, in both cases the gluon PDF has been scaled down by a factor of 10. The evolution from the high-x valence content into the gluon and splittings into heavy $q\bar{q}$ pairs is clearly visible. The PDFs are accessed through the LHAPDF interface [73].

2.6.2 Bayesian reweighting

Another one of the benefits of the MC procedure adopted by the NNPDF collaboration, is that the effect of including new data within the fit can be easily evaluated. This is done through the procedure of reweighting, which applies a weight w_k to each PDF in the ensemble $\{\mathcal{R}_k\}$, through the rules of statistical inference, based on its compatibility with new input data. The appealing feature of this process is that it can be evaluated easily without having

to perform a global fit. This was originally applied by the NNPDF collaboration in [74, 75], and the technique was later adapted to reweight the Hessian PDF sets [76]. More recently there have been suggestions to extend the Hessian reweighting method to include the effects arising from the non-quadratic form of the χ^2 around the global minimum [77]. This may account for some incompatibilities found when comparing the result of a new global fit to a reweighted Hessian replica set [78].

The Hessian reweighting relies on first generating a replica ensemble. It was demonstrated in [76] that this generation can be consistently provided in both the basis of observables $\{F_i(\mathcal{S}_i)\}$ or at the level of the PDFs themselves $\{\mathcal{S}_i\}$. The benefit of working in the basis of observables is that calculating a replica set of observables can be done extremely quickly, while calculating observables from a large replica PDF ensemble can be computationally expensive. This technique applies random sampling at the level of the eigenvectors and observables in the following way, a set of replicas is first constructed as

$$F(\mathcal{R}_k) = F(\mathcal{S}_0) + \sum_{j=1}^{n} [F(\mathcal{S}_j^{\pm}) - F(\mathcal{S}_0)]|R_{kj}|\,, \tag{2.76}$$

where R_{kj} is a pseudorandom gaussian-distributed number with zero mean and variance of one. The choice of negative or positive displacements S_j^- or S_j^+ depends on the sign of R_{kj}. By storing the set of random numbers R_{kj} generated in producing the replica set, these numbers can then be used to generate an equivalent replica set for other observables. The reweighting procedure can then be performed by comparing the compatibility of the new data with the relevant replica set $\{F(\mathcal{R}_k)\}$ by calculating the χ_k^2 between the two. The relevant formulas are:

$$\langle F\rangle_{\text{old}} = \frac{1}{N_{\text{rep}}}\sum_{k=1}^{N_{\text{rep}}} F(\mathcal{R}_k)\,, \qquad \langle F\rangle_{\text{new}} = \frac{1}{N_{\text{rep}}}\sum_{k=1}^{N_{\text{rep}}} w_k(\chi_k^2)F(\mathcal{R}_k)\,, \tag{2.77}$$

where the weights are computed as

$$w_k(\chi_k^2) = \frac{W_k(\chi_k^2)}{\frac{1}{N_{\text{rep}}}\sum_{j=1}^{N_{\text{rep}}} W_j(\chi_k^2)}\,, \qquad W_k(\chi_k^2) = (\chi_k^2)^{\frac{1}{2}(N_{\text{pts.}}-1)}\exp\left(-\frac{1}{2}\chi_k^2\right)\,, \tag{2.78}$$

and the dominator fixing the normalisation is

$$\sum_{k=1}^{N_{\text{rep}}} w_k(\chi_k^2) = N_{\text{rep}}\,. \tag{2.79}$$

After applying this reweighting technique, the number of effective remaining replicas can be found after calculating the Shannon entropy as

$$N_{\text{eff}} = \exp\left(\frac{1}{N_{\text{rep}}}\sum_{k=1}^{N_{\text{rep}}} w_k \log(N_{\text{rep}}/w_k)\right)\,. \tag{2.80}$$

This procedure is relevant for quantifying how potential LHC measurements can improve the constraints on PDFs.

2.7 Summary

The main concept introduced in this Chapter is factorisation. This allows a full hadron-hadron scattering process to be considered as a chain of sequential subprocesses, each of which can be considered according the validity of theoretical techniques in the corresponding region of phase space.

At high Q^2, the subprocess is treated by fixed-order perturbation theory. This allows the contribution from the subprocess to be treated as a short-distance cross section for partonic events. These calculations must then be supplemented by long-distance effects, which approximately account for missing higher-order corrections.

Accounting for these long-distance effects relies on the universal factorisation of soft and collinear singularities in gauge theory amplitudes. Soft singularities factorise at the level of colour correlated amplitudes, while collinear singularities factorise at the level of the cross section. By recursively applying this factorisation in the soft/collinear region, approximate all-orders effects can be accounted for according to the DGLAP equations. These techniques are applied to multiple splittings in the initial state (PDFs), as well as the final state (PS), which evolves partons at high virtuality ($\approx Q^2$) down to a scale $\mathcal{O}(1\text{ GeV})$. The theoretical

development of interfacing NLO calculations with the PS were also discussed.

To make predictions for observable colour singlet objects in the final state, the PS must also be supplemented with a hadronisation model. These models perform the transition from off-shell coloured partons to on-shell colour singlet objects, allowing a direct comparison of these models to experimental observations. Experimentally, the production of hard coloured partons can be inferred by reconstructing clusters of particles localised in phase space. By defining theoretically and experimentally motivated pseudo objects (jets), it also becomes possible to compare fixed-order calculations to experiment.

Finally, as the prediction of LHC observables relies on knowledge of the PDFs, it is important to measure processes which will help improve the current constraints on the PDFs. To quantify how future measurements at LHCb may improve these constraints, a reweighting technique was introduced which allows the effect of including new data in a global fit to be estimated.

Chapter 3

Top quark production and decay

In this Chapter, the aspects of top quark production and decay necessary to perform detailed phenomenology at the LHC will be considered. As the heaviest elementary particle to date, the top quark holds a unique position in the SM in terms of its interesting production and decay mechanisms, but also contributes to many important processes through sizeable quantum corrections. The relevance of the large top quark mass for direct and indirect observables will be discussed. After considering how top quark decays may be experimentally identified, the symmetric and asymmetric structure of the pair production cross section will be discussed. Finally, the motivations for studying top quark pair production at high pseudorapidity will be highlighted.

3.1 Introduction

The top quark was discovered in $p\bar{p}$ collisions at the TeVatron in 1995 [79,80]. Understanding the properties of this particle is one of the main goals of the LHC physics program, adding to the extensive studies which have already been performed at the TeVatron.

The top quark is the most massive elementary particle that has been observed in nature thus far. As a consequence of its large mass, it decays weakly as a quasi-free particle before hadronisation can occur. Therefore, measurements of the branching fractions of top quark decays directly probe the CKM elements $|V_{tq}|$ which are otherwise observed only indirectly. Top quark production is also naturally sensitive to the high-x region of PDFs. In particular, at the hadronic centre of mass (CM) energies required to produce pairs of top quarks, there are sizeable contributions from several different production mechanisms. Also,

the production mechanisms which are normally relatively negligible for producing quark pairs introduce asymmetries in the quark angular distributions, arising from the structure of interfering amplitudes at NLO. Measurements of the asymmetric distributions of top quarks therefore provide a unique test of this perturbative expansion which is otherwise not accessible at hadron colliders.

In addition to direct observables, the top quark also plays an important role in several other processes. Many EW and flavour physics observables receive large corrections due to loop processes involving the top quark. For example, within the SM the W boson mass receives measurable corrections from both the top quark and the Higgs boson. The compatibility of these corrections is therefore an important test of the SM.

So far, measurements of top quark properties performed by D0 [81], CDF [82], ATLAS [83] and CMS [84] appear to be in full agreement with the SM expectations. The only exception being, the excess reported in several measurements of the $t\bar{t}$ forward-backward asymmetry by CDF [85, 86] and D0 [87–89].

Many top quark measurements performed by ATLAS and CMS in the central region with the 7 and 8 TeV data delivered in Run I are systematically limited. In Run II, the substantial increase in statistics will allow measurements of rare associated production processes such as $t(\bar{t})h$, $t(\bar{t})Z$, and $t\bar{t}Z(W)$ to become statistically feasible in the central region. These measurements are important as they allow precise determination of many top quark couplings directly. Besides associated production processes, it is also important to investigate the feasibility of top quark measurements in extreme kinematic regions of phase space, as these measurements may provide enhanced sensitivity to certain properties. As will be discussed in more detail, of particular interest is the high pseudorapidity LHCb acceptance

$$\eta = -ln\left(\tan\left(\frac{\theta}{2}\right)\right), \qquad \eta \in [2.0, 5.0]\,. \tag{3.1}$$

3.2 Top quark properties

The defining property of the top quark is its relatively large mass in comparison to other fermions. It is therefore important to discuss the relevance of this parameter within the SM. After highlighting the sensitivity of several important SM parameters to the top quark mass, the current experimental constraints from both direct and indirect measurements will be discussed.

As the top quark mass is so large, on-shell production and decay of the top quark has a rich phenomenology. To identify relevant aspects of this phenomenology, the strength of top quark couplings will be reviewed. In particular, the weak decay of the top quark will be derived, highlighting how top quarks may be experimentally identified.

3.2.1 Mass

As a fundamental parameter of the SM, a precise determination of the top quark mass is well motivated. To begin, it is necessary to define exactly what the top quark mass refers to. The two commonly adopted definitions of the top quark mass are the pole mass m_t^{pole} and the running mass $\overline{m}_t(\mu_R)$. The pole mass corresponds to the position of the pole appearing in the renormalised quark propagator at a given order in perturbation theory, while the running mass corresponds to a scheme and scale dependent renormalised mass (generally renormalised in the modified minimal subtraction $\overline{\text{MS}}$ scheme). The two masses are related through

$$\frac{m_t^{\text{pole}}}{\overline{m}_t} = \frac{Z_m^{\overline{\text{MS}}}}{Z_m^{\text{OS}}}\,, \tag{3.2}$$

where $Z_m^{\overline{\text{MS}}}$ and Z_m^{OS} are the $\overline{\text{MS}}$ and on-shell field renormalisation terms for quark masses, currently known at NNLO [90, 91].

Precision EW/flavour observables. Within the SM, the observed mass of the W boson receives quantum corrections which depend predominantly on the mass of the top quark and Higgs boson. Therefore, a highly constrained top quark mass is necessary to

precisely test the consistency of the recently discovered Higgs boson within the expectation of the SM framework. In fact, the uncertainty on the value of the top quark mass introduces an associated uncertainty in all loop processes involving top quarks. Important examples are: the Fermi constant G_F [92]; the determination of the $\Delta\rho$ parameter [93]; $\Delta F = 1, 2$ observables such as the decays $B \to sl^+l^-$ [94] and B_s mixing [95]; corrections to the Z boson branching fraction ratio, $\Gamma(Z \to b\bar{b})/\Gamma(Z \to q\bar{q})$, R_b [96].

Extrapolation of running couplings. The Higgs potential defined in (1.9) remains stable provided the Higgs self-coupling λ is positive. With the recent determination of the Higgs mass, $m_h \approx 126$ GeV, it is possible evaluate the running of λ as

$$\lambda(\mu) = \frac{G_F m_h^2}{\sqrt{2}} + \Delta\lambda(\mu)\,, \tag{3.3}$$

where $\Delta\lambda(\mu)$ represents relevant corrections which are present beyond tree level, and have recently been computed at NNLO accuracy [97]. The running of the gauge couplings e, g, g_s, the top and bottom Yukawa couplings (y_t,y_b), and the Higgs self-coupling λ are shown in Figure 3.1 (Obtained from Figure 1 of [97]). The effect of varying the top quark pole mass, $\alpha_s(m_Z^2)$, and m_h independently within the ranges $m_t \in [171.3, 174.9]$ GeV, $\alpha_s(m_Z^2) \in [0.1163, 0.1205]$ and $m_h \in [124.8, 126.6]$ GeV has been included. As the running of λ receives a large contribution from the top Yukawa, the precision of the top quark mass measurement at colliders is an important input in determining the stability of the SM Higgs potential. The prediction of an unstable vacuum would, thankfully, be evidence for new physics which would be required to alter the running of λ before the Planck scale.

World Average. A first combination of top quark mass measurements from both the ATLAS and CMS experiments at the LHC, and CDF and D0 experiments at the TeVatron has been presented in [98]. The combination reports the following result

$$m_t^{\mathrm{MC}} = 173.34 \pm 0.26\ (\mathrm{stat}) \pm 0.71\ (\mathrm{syst})\ \mathrm{GeV}\,, \tag{3.4}$$

from measurements based on the template [99] and matrix element [100] methods of mass

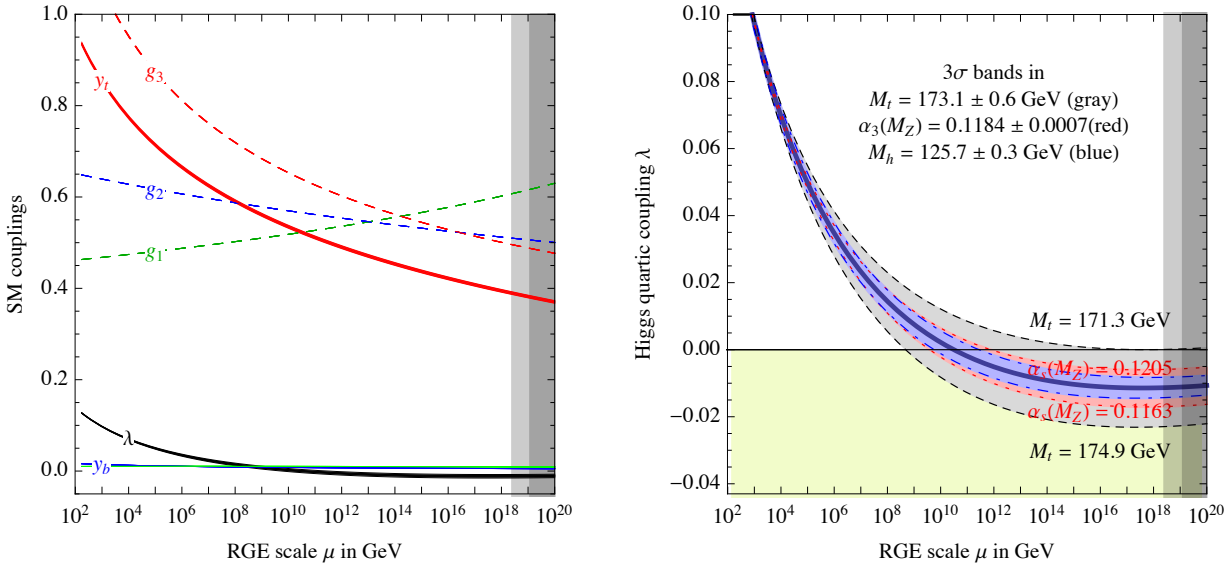


Figure 3.1: Left: RG evolution of the gauge couplings $g_1 = \sqrt{5/3}e$, $g_2 = g$, $g_3 = g_s$, of the top and bottom Yukawa couplings (y_t,y_b), and the Higgs self-coupling λ. All couplings are defined in the $\overline{\text{MS}}$ scheme. Right: RG evolution of λ while varying m_h, m_t and $\alpha_s(M_z)$ within three times the indicated uncertainty.

determination. In either determination, the experimentally extracted mass corresponds to the MC mass. This must be the case as a colour charged object is forbidden to go on-shell by confinement. In other words, as the top quark must be colour connected to other anticoloured particles in the event, it is always measured in association with effects arising at the hadronisation scale. As these effects are modelled phenomenologically, this introduces an ambiguity in the determination of the mass of $\mathcal{O}(\Lambda_{\text{QCD}})$, implying

$$m_t^{\text{pole}} = m_t^{\text{MC}} \pm \mathcal{O}(\Lambda_{\text{QCD}})\,. \tag{3.5}$$

These effects have been estimated to be $\delta m_t = \pm 0.5$ GeV [101] in the context of the string model. However, it is difficult to quantify how large the uncertainty is, as it depends on many parameters which have been tuned to data. Both the template and matrix element methods of mass determination are sensitive to these effects.

As it is not desirable to measure parameters which have uncertainties that ambiguously depend on long-distance effects, several other observables have been proposed to measure the top quark mass in a theoretically cleaner way. One such proposal is to use $t\bar{t}X$ cross

section measurements to determine $\overline{m}_t$ indirectly [102]. Although theoretically well-defined, the experimental uncertainties associated with this method due to the larger experimental uncertainties present in the available cross section measurements. Based on top quark pair cross section measurements at 7 and 8 TeV, ATLAS [103] has recently extracted a top quark pole mass of

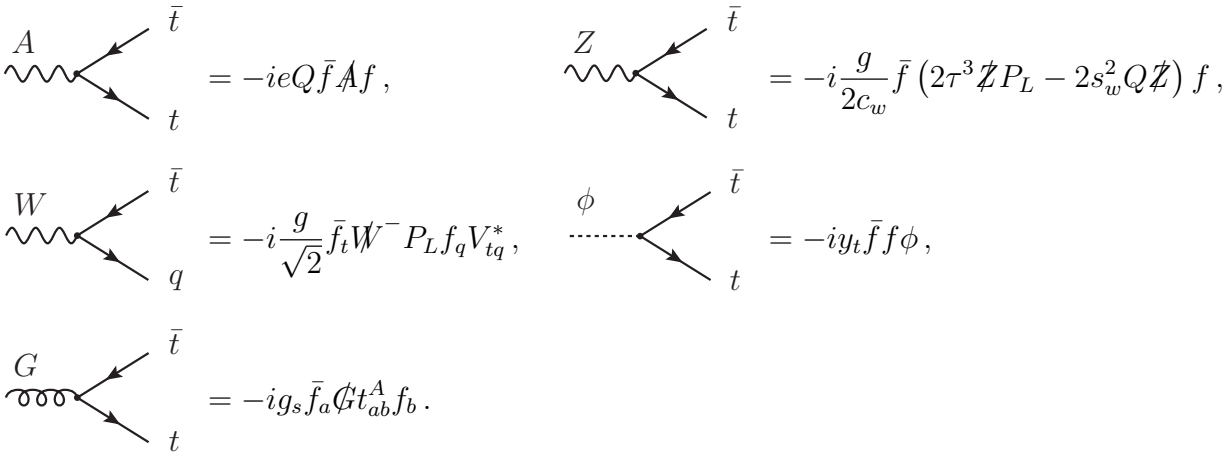
$$m_t^{\text{pole}} = \left(172.9^{+2.5}_{-2.6}\right)\ \text{GeV}\,. \tag{3.6}$$

Constraining the top mass using multiple measurement techniques will be necessary to reduce the dependence on long-distance effects, which are unavoidable at hadron colliders. With the aim of not being overly aggressive on assumed level of theoretical uncertainty in the determination of the MC mass, the following top pole mass (assumed to be the MC mass) and associated uncertainty will be used for the relevant studies:

$$m_t = (173.25 \pm 1.5)\ \text{GeV}\,. \tag{3.7}$$

3.2.2 Couplings

Measuring the couplings of the top quark to other SM particles is clearly an important test of the consistency of the SM. In particular, direct measurements of these couplings are highly desirable — this can be done by measuring the rate of associated production processes as suggested in [104, 105]. The relevant vertex factors are summarised below:



(3.8)

The strength of these couplings can also be used to quickly estimate the rates for different top quark production mechanisms. For reference, the relevant couplings, evaluated at the scale $m_t = 173.25$ GeV, are provided in Table 3.2.2.

g_e	g_Z	g_W	y_t	g_s
0.21	0.37	0.46	0.99	1.16

Table 3.1: Various top quark coupling strengths approximated at the scale $m_t = 173.25$ GeV.

The value for the strong coupling has been extracted using the definition for the two-loop running provided in Section 1.3.4. The other couplings appearing in the table are defined as $g_e = eQ$, $g_Z = g/2c_w$ and $g_W = g/\sqrt{2}$. Furthermore, for W boson interactions, the coupling to the down-type quarks must be supplemented with the relevant CKM element V_{tq}, which are provided in Appendix A.

3.2.3 Decay

Another important property of the top quark is the decay width. This can be easily evaluated by calculating the decay of a free top quark into an on-shell W boson and down-type quark. This calculation also highlights important features of the top quark decay, which can be experimentally tested. The amplitude for this process is

$$i\mathcal{M} = \frac{g}{\sqrt{2}}\bar{u}^{s_2}(p_2)V_{tq}^*\not{\epsilon}^*(p_3,\lambda)P_L u^{s_1}(p_1)\,. \tag{3.9}$$

The averaged and summed squared amplitude is evaluated as

$$\overline{\sum}|\mathcal{M}|^2 = \frac{g^2|V_{tq}|^2}{2}\frac{1}{2}\sum_{s_1,s_1,\lambda} Tr\left(\bar{u}^{s_2}(p_2)\not{\epsilon}^*(p_3,\lambda)P_L u^{s_1}(p_1)\bar{u}^{s_1}(p_1)\not{\epsilon}P_L u^{s_2}(p_2)\right)\,, \tag{3.10}$$

which, after computing the traces and summing over fermion spins, may be rewritten as

$$\overline{\sum}|\mathcal{M}|^2 = \frac{g^2|V_{tq}|^2}{4}\sum_{\lambda}\epsilon_\mu^*(p_3,\lambda)\epsilon_\nu(p_3,\lambda)Tr\left(\not{p}_2\gamma^\mu P_L\not{p}_1\gamma^\nu\right)\,. \tag{3.11}$$

Due to the chiral coupling of the W boson to fermions, the b quark is produced in a left-handed state. This necessarily means that the W boson can only be produced in either a left-handed (L) or longitudinal (0) polarisation state to conserve spin in the top quark decay. The left-handed polarisation receives the following contribution

$$\begin{aligned}\overline{\sum}|\mathcal{M}_L|^2 &= \frac{g^2|V_{tq}|^2}{4}(-g_{\mu\nu})Tr\left(\not{p}_2\gamma^\mu P_L\not{p}_1\gamma^\nu\right) , \\ &= g^2|V_{tq}|^2(p_2\cdot p_1) .\end{aligned} \tag{3.12}$$

Introducing the notation

$$x = \frac{m_W}{m_t} , \qquad y = \frac{m_b}{m_t} , \qquad G_F = \frac{\sqrt{2}}{8}\frac{g^2}{m_W^2} , \tag{3.13}$$

this contribution becomes

$$\overline{\sum}|\mathcal{M}_L|^2 = \frac{2G_F|V_{tq}|^2}{\sqrt{2}}m_t^4\left(2x^2(1+y^2-x^2)\right) . \tag{3.14}$$

The longitudinal contribution can be evaluated in the same way

$$\overline{\sum}|\mathcal{M}_0|^2 = \frac{g^2|V_{tq}|^2}{4}\left(\frac{(p_3)_\mu(p_3)_\nu}{m_W^2}\right)Tr\left(\not{p}_2\gamma^\mu P_L\not{p}_1\gamma^\nu\right) . \tag{3.15}$$

Performing the trace, and noting that the γ_5 contribution vanishes due to symmetry under $\mu \leftrightarrow \nu$ interchange, leads to the result

$$\begin{aligned}\overline{\sum}|\mathcal{M}_0|^2 &= \frac{4G_F|V_{tq}|^2}{\sqrt{2}}\left(2(p_3\cdot p_2)(p_3\cdot p_1) - m_W^2(p_2\cdot p_1)\right) , \\ &= \frac{2G_F|V_{tq}|^2}{\sqrt{2}}m_t^4\left(1-x^2-y^2(2+x^2-y^2)\right) .\end{aligned} \tag{3.16}$$

These results can now be used to calculate the rate of weak top quark decay. To do this, it is first necessary to include the two-body phase space

$$\Gamma_t = \frac{1}{2m_t}\int\frac{d^3p_2}{(2\pi)^3 2E_3}\frac{d^3p_3}{(2\pi)^3 2E_2}(2\pi)^4\delta^{(4)}(p_1-p_2-p_3)\overline{\sum}|\mathcal{M}|^2 . \tag{3.17}$$

As the power corrections from the b-quark mass are extremely small, they can be ignored. In the top quark rest frame this leads to the expression

$$\Gamma_t = \frac{1}{8\pi} \int \frac{p_2 dp_2}{m_t E_3} \delta^{(0)}(m_t - |\vec{p}_2| - E_3) \overline{\sum} |\mathcal{M}|^2 \,. \tag{3.18}$$

This can be solved by expanding in terms of the zeros of the delta function as

$$\int g(z)\delta\left(f(z)\right) dz = \frac{1}{|f'(z_i)|_{z_i=z^*}} g(z^*) \,. \tag{3.19}$$

After incorporating this expansion, the top quark decay width can be written

$$\Gamma_t = \frac{1}{16\pi m_t} (1 - x^2) \overline{\sum} |\mathcal{M}|^2 \,. \tag{3.20}$$

Numerically, the width and lifetime of the top quark ($m_t = 173.25$ GeV) are predicted to be

$$\Gamma_t \simeq 1.5 \text{ GeV} \,, \qquad \tau_t \simeq 4.4 \times 10^{-25} \text{ s} \,. \tag{3.21}$$

These values can be compared with experimental results from the D0 collaboration [106]

$$\Gamma_t(\text{exp.}) \simeq \left(2.00^{+0.47}_{-0.43}\right) \text{ GeV} \,, \qquad \tau_t(\text{exp.}) \simeq \left(3.29^{+0.90}_{-0.63}\right) \times 10^{-25} \text{ s} \,. \tag{3.22}$$

The extremely short lifetime of the top quark prevents the occurrence of hadronisation or spin decorrelation effects before the top quark undergoes weak decay. To this extent, the top quark decays as a quasi-free particle. An interesting consequence of the short lifetime of the top quark, with respect to its spin-flip time, is that measurements of the angular distributions of top quark decay products can be used to test the structure of the tWq coupling.

For example, as the polarisation state of the W boson in top quark decay controls the angular distribution of its decay products, measurements of the angular distribution of leptonic decays can be used to probe the tWq coupling. The expected fraction of left-handed

and longitudinal W polarisations in top quark decay is

$$f_L = \frac{\overline{\sum}|\mathcal{M}_L|^2}{\overline{\sum}|\mathcal{M}_L|^2 + \overline{\sum}|\mathcal{M}_0|^2} \approx 0.30\,, \qquad f_0 = \frac{\overline{\sum}|\mathcal{M}_0|^2}{\overline{\sum}|\mathcal{M}_L|^2 + \overline{\sum}|\mathcal{M}_0|^2} \approx 0.70\,. \tag{3.23}$$

Note that the longitudinal polarisation dominates for large values of x. These fractions have been recently measured by the ATLAS collaboration [107], by inferring the W boson polarisation through leptonic decays $t \to W(\to l\nu_l)b$, to be

$$f_L(\text{exp.}) = 0.32 \pm 0.04\,, \qquad f_0(\text{exp.}) = 0.67 \pm 0.07\,, \qquad f_R(\text{exp.}) = 0.01 \pm 0.05\,, \tag{3.24}$$

in full agreement with the SM prediction.

As top quarks decay weakly to a down-type quark and W boson, measurements of the branching fractions to different quark flavours provide constraints on the CKM elements $|V_{tq}|$. These constraints are complementary to tests of CKM unitarity provided by flavour observables, and also sensitive to various extensions of the SM [108,109]. Note also, the large CKM hierarchy

$$|V_{tb}|^2 \gg |V_{ts}|^2 \gg |V_{td}|^2\,, \tag{3.25}$$

ensures that top quarks decay almost entirely to b quarks ($t \to Wb$). As it is experimentally possible to discriminate against light jets, top quark events may be easily identified with the use of b-tagging. Background rates for top quark events involving light jets can then be highly suppressed, allowing precision measurements of top quark properties which would otherwise not be possible.

As top quarks decay predominantly through the process $t \to Wb$, top quark measurements may be categorised by the W boson decay channel. Each category therefore receives a factor corresponding to the relevant branching fraction:

$$\begin{aligned} &\text{(jets)} && t \to q\bar{q}'b && = 6/9\,, \\ &(l) && t \to l^+\nu_l b && = 2/9\,, \\ &(\tau) && t \to \tau^+\nu_\tau b && = 1/9\,, \end{aligned} \tag{3.26}$$

where l corresponds to either an electron e or muon μ. Different final states have different experimental efficiencies, backgrounds rates, and are generally sensitive to different observables. For example, the dilepton channel in pair production is sensitive to the spin production state of the $t\bar{t}$ system, through measurements of the spin correlations of the two final state leptons, and is also sensitive to the charge production asymmetry of top quark pairs. However, as there are two neutrinos in the event, direct top mass measurements are difficult to perform, and indirect measurements suffer from the low statistics (4/81) associated to this channel.

3.3 Top quark production

As a result of the large coupling of the top quark to the gluon, the dominant production mechanism for creating top quarks at hadron colliders is the production of top quark pairs proceeding via the strong interaction. This channel will be studied in great detail as it is statistically the most favourable. In the previous Chapter, it was demonstrated that the total cross section for a generic hard scattering process may be factorised in the following manner

$$\sigma_{AB\to X} = \sum_{a,b} \int dx_a dx_b f_{a/A}(x_a, \mu_F^2) f_{b/B}(x_b, \mu_F^2) d\hat{\sigma}_{ab\to X}(\hat{s}, \mu_F^2, \mu_R^2, \alpha_s)\,. \tag{3.27}$$

The full scattering process is calculated by convoluting the incoming parton luminosities with the short-distance subprocess $d\hat{\sigma}_{ab\to X}$. As the delivered parton luminosities are machine dependent, so too are the full scattering rates. The absolute $q\bar{q}$ and gg NNPDF2.3 NLO $\alpha_s(m_Z^2) = 0.119$ central parton luminosities delivered at $\sqrt{s} = 7$, 8, and 14 TeV in pp collisions at the LHC are plotted as a function of the partonic CM energy ($\sqrt{x_1 x_2 s}$) in Figure 3.2.

The phenomenology of $t\bar{t}$ production in a given region of phase space depends on the relative contribution of different production channels. To understand how different production mechanisms affect different observables, it is necessary to expand the short-distance

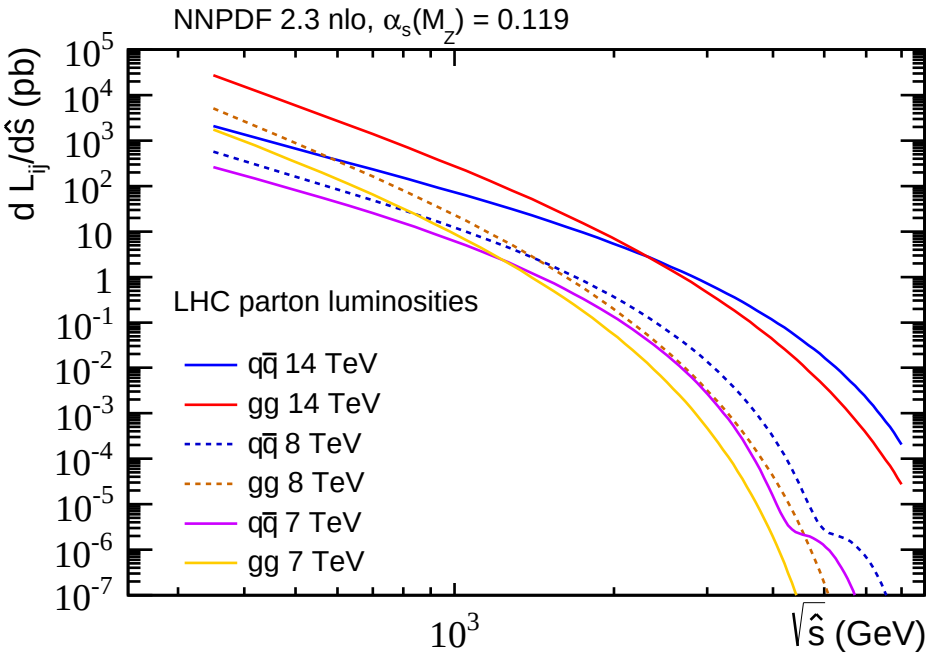


Figure 3.2: Parton luminosities delivered at $\sqrt{s} = 7$, 8, and 14 TeV at the LHC.

subprocess to at least NLO. This is not only required from the point of view of reducing scale uncertainties and improving the normalisation of distributions, but is also required to capture certain kinematical features which are not present at LO.

In this section, the general structure for the expansion of the short-distance subprocess will be described. The scaling functions are derived at LO, and the general features of higher-order corrections will be reviewed. Finally, the origin of the charge asymmetry will be discussed in detail, and the current status of experimental charge asymmetry measurements and their consistency with theoretical predictions will be discussed.

3.3.1 LO cross section

The cross section for the partonic $2 \to 2$ process is

$$d\hat{\sigma}_{ij\to t\bar{t}} = \frac{1}{2\hat{s}} \overline{\sum} |\mathcal{M}_{ij\to t\bar{t}}|^2 d\phi_2 \,. \tag{3.28}$$

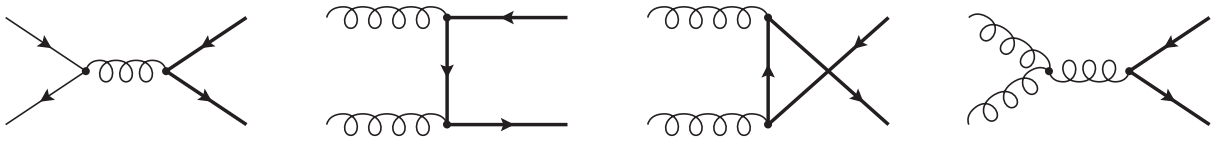


Figure 3.3: Feynman diagrams contributing to $t\bar{t}$ production at LO. Bold lines represent top quarks.

For $t\bar{t}$ production, the Born level amplitude receives contributions from the two following processes

$$\begin{aligned} q(p_1) + \bar{q}(p_2) &\to t(p_3) + \bar{t}(p_4)\,, \\ g(p_1) + g(p_2) &\to t(p_3) + \bar{t}(p_4)\,, \end{aligned} \tag{3.29}$$

where the four-momenta of the incoming partons are expressed as fractions of the colliding hadron momentum, $p_{1,2} = x_{1,2}P_{1,2}$. The contributing Feynman diagrams for both processes are depicted in Figure 3.3. The cross section can be evaluated as a function of the following kinematic invariants

$$\hat{s} = (p_1 + p_2)^2\,, \qquad t_H = (p_1 - p_3)^2 - m_t^2\,, \qquad u_H = (p_2 - p_3)^2 - m_t^2\,, \tag{3.30}$$

and noting that momentum conservation implies $\hat{s} + t_H + u_H = 0$.

It will prove useful to define these invariants in terms of the $t\bar{t}$ invariant mass $M_{t\bar{t}}^2 = (p_3 + p_4)^2$ and the scattering angle θ between the top quark and the incoming quark momentum. In the partonic CM frame this leads to the four-momentum configuration

$$p_1 = \frac{\sqrt{\hat{s}}}{2}(1, 1_z)\,, \qquad p_2 = \frac{\sqrt{\hat{s}}}{2}(1, -1_z)\,, \qquad p_3 = \frac{\sqrt{\hat{s}}}{2}(1, \vec{\beta})\,, \qquad p_4 = \frac{\sqrt{\hat{s}}}{2}(1, -\vec{\beta})\,, \tag{3.31}$$

where β is the top quark velocity. It follows that

$$t_H = -\frac{\hat{s}}{2}(1 - \beta\cos\theta)\,, \qquad u_H = -\frac{\hat{s}}{2}(1 + \beta\cos\theta)\,, \qquad \beta = \sqrt{1-\rho}\,, \qquad \rho = \frac{4m_t^2}{\hat{s}}\,. \tag{3.32}$$

The differential partonic cross section may be written

$$d\hat{\sigma}_{ij\to t\bar{t}} = \frac{1}{2\hat{s}}\overline{\sum}|\mathcal{M}_{ij\to t\bar{t}}|^2 \frac{d^3p_3}{(2\pi)^3 2p_3^0}\frac{d^3p_4}{(2\pi)^3 2p_4^0}(2\pi)^4\delta^{(4)}(p_1 + p_2 - p_3 - p_4)\,. \tag{3.33}$$

In the partonic CM frame this evaluates to

$$d\hat{\sigma}_{ij\to t\bar{t}} = \frac{1}{2\hat{s}}\overline{\sum}|\mathcal{M}_{ij\to t\bar{t}}|^2 \frac{d^3p_4}{(p_3^0)^2}\frac{1}{(4\pi)^2}\delta(\sqrt{\hat{s}} - 2p_4^0)\,. \tag{3.34}$$

Expanding in terms of the zeros of the delta function leads to

$$\begin{aligned} d\hat{\sigma}_{ij\to t\bar{t}} &= \frac{\pi}{2\hat{s}}\frac{1}{(4\pi)^2}\frac{|\vec{p}_4^{\,*}|}{p_3^0}\overline{\sum}|\mathcal{M}_{ij\to t\bar{t}}|^2 d\cos\theta\,, \\ &= \frac{\pi}{2\hat{s}}\frac{1}{(4\pi)^2}\beta\overline{\sum}|\mathcal{M}_{ij\to t\bar{t}}|^2 d\cos\theta\,. \end{aligned} \tag{3.35}$$

The contribution to the cross section from all subprocesses can then be evaluated after computing the relevant averaged and summed squared matrix elements.

Quark initiated process. The matrix element for the quark initiated process is

$$i\mathcal{M}_{q\bar{q}} = \frac{1}{\hat{s}}g_s^2\left(\bar{u}_a^{s_1}(p_3)t^A_{ab}\gamma^\mu v_b^{s_2}(p_4)\right)\left(\bar{v}_c^{s_3}(p_2)t^A_{cd}\gamma_\mu u_d^{s_4}(p_1)\right)\,. \tag{3.36}$$

Squaring this matrix element and averaging (summing) over initial (final) state colours and spins gives

$$\overline{\sum}|\mathcal{M}_{q\bar{q}}|^2 = \frac{1}{4}\frac{1}{9}Tr\left(t^At^B\right)Tr\left(t^At^B\right)\frac{g_s^4}{\hat{s}^2}Tr\left((\not{p}_3 + m_t)\gamma^\mu(\not{p}_4 - m_t)\gamma^\nu\right)Tr\left(\not{p}_2\gamma_\mu\not{p}_1\gamma_\nu\right)\,. \tag{3.37}$$

Evaluating the traces in the usual way leads to the result

$$\overline{\sum}|\mathcal{M}_{q\bar{q}}|^2 = \frac{g_s^4}{\hat{s}^2}\frac{16}{9}\left((p_2\cdot p_3)(p_1\cdot p_4) + (p_1\cdot p_3)(p_2\cdot p_4) + m_t^2(p_2\cdot p_1)\right)\,, \tag{3.38}$$

which can be conveniently written in terms of the previously defined invariants as

$$\overline{\sum}|\mathcal{M}_{q\bar{q}}|^2 = g_s^4\frac{4}{9}\left(\frac{t_H^2 + u_H^2}{\hat{s}^2} + \frac{\rho}{2}\right)\,. \tag{3.39}$$

Gluon initiated process. The calculation of the gluon-gluon fusion (gg) process is

more involved. The matrix element for the sum of the three contributing diagrams is

$$i\mathcal{M}_{gg} = i(\mathcal{M}_1 + \mathcal{M}_2 + \mathcal{M}_3)\,, \tag{3.40}$$

where the separate contributions from each diagram appearing in Figure 3.3 respectively are

$$\begin{aligned}
i\mathcal{M}_1 &= g_s^2 t^A_{ab} t^B_{bc} \bar{u}_a(p_3) \left(\frac{\gamma^\mu \not{p}_2 \gamma^\nu - 2p_3^\mu \gamma^\nu}{2p_2 \cdot p_3} \right) v_c(p_4) \epsilon_\mu(p_2) \epsilon_\nu(p_1)\,, \\
i\mathcal{M}_2 &= g_s^2 t^B_{ad} t^A_{dc} \bar{u}_a(p_3) \left(\frac{2\gamma^\nu p_4^\mu - \gamma^\nu \not{p}_2 \gamma^\mu}{2p_2 \cdot p_4} \right) v_c(p_4) \epsilon_\mu(p_2) \epsilon_\nu(p_1)\,, \\
i\mathcal{M}_3 &= \frac{g_s^2}{\hat{s}} [t^A, t^B]_{ac} \bar{u}_a(p_3) \left((\not{p}_2 - \not{p}_1) g^{\mu\nu} + \gamma^\nu 2p_1^\mu - \gamma^\mu 2p_2^\nu \right) v_c(p_4) \epsilon_\mu(p_2) \epsilon_\nu(p_1)\,.
\end{aligned} \tag{3.41}$$

To evaluate the third term the standard commutation relations for $SU(3)$ generators have been used, the choice of gauge $\lambda = 1$ has been adopted, and the relations for transverse polarisation vectors $p_2 \cdot \epsilon(p_2) = 0$ and $p_1 \cdot \epsilon(p_1) = 0$ have been used. Squaring the matrix element and averaging (summing) over initial (final) state colour and physical polarisations (spins) leads to the result

$$\overline{\sum} |\mathcal{M}_{gg}|^2 = g_s^4 \left(\frac{\hat{s}^2}{6 t_H u_H} - \frac{3}{8} \right) \left(\frac{t_H^2 + u_H^2}{\hat{s}^2} + \rho - \frac{\hat{s}^2 \rho^2}{4 t_H u_H} \right)\,. \tag{3.42}$$

The contribution from the short-distance subprocess $\hat{\sigma}$ can then be expressed in terms of a set of scaling functions $\mathcal{K}_{ij}$, α_s and m_t as

$$\hat{\sigma}_{ij}(s, m_t^2, \mu_F^2) = \frac{\alpha_s^2(\mu_R^2)}{m_t^2} \mathcal{K}_{ij}(\rho, m_t^2, \mu_F^2, \mu_R^2)\,. \tag{3.43}$$

The scaling functions $\mathcal{K}_{ij}$ can be evaluated by integrating over phase space as

$$\mathcal{K}_{ij} = \frac{m_t^2}{\alpha_s^2} \int_{-1}^{1} \frac{\pi}{2\hat{s}} \frac{1}{(4\pi)^2} \beta \overline{\sum} |\mathcal{M}_{ij \to t\bar{t}}|^2 d\cos\theta\,. \tag{3.44}$$

Performing this integration for the two LO processes leads to the functions

$$\begin{aligned} \mathcal{K}_{q\bar{q}}^{(0)} &= \frac{\pi\beta\rho(2+\rho)}{27}\,, \\ \mathcal{K}_{gg}^{(0)} &= \frac{\pi\beta\rho}{192}\left(\frac{2}{\beta}(16+16\rho+\rho^2)\mathrm{ArcTanh}(\beta)-28-31\rho\right)\,. \end{aligned} \tag{3.45}$$

The total cross section in this notation is therefore

$$\sigma_{\mathrm{tot}} = \frac{\alpha_s^2}{m_t^2}\sum_{i,j}\int dx_1 dx_2 f_i(x_1,\mu_F^2) f_j(x_2,\mu_F^2)\mathcal{K}_{ij}(\rho, m_t^2, \mu_F^2, \mu_R^2)\,. \tag{3.46}$$

Convoluting the results for the LO scaling functions with NNPDF2.3 LO PDFs with $\alpha_s(m_Z^2) = 0.130$ leads to the predictions provided in Table 3.2. These predictions, for pp collisions at $\sqrt{s} = 7, 8$ and 14 TeV, are compared to the available experimental results [110, 111], where the quoted experimental uncertainties have been added in quadrature.

The scale uncertainty δ_{scale} is found by varying both renormalisation and factorisation scales μ_R and μ_F independently within the range

$$\frac{1}{2} \leq \frac{\mu_R\mu_0}{\mu_F\mu_0} \leq 2\,. \tag{3.47}$$

The reference scale μ_0 is fixed to the chosen value of the top quark mass m_t. This procedure is used to evaluate the uncertainty due to unknown higher terms in the perturbative expansion.

$\sqrt{s}$ (TeV)	σ_{tot} (pb)	$\sigma_{q\bar{q}}/\sigma_{\mathrm{tot}}$	δ_{scale} (pb)	CMS (pb)
7	121.6	0.20	$^{+45.2}_{-30.2}$ $^{(+37.2\%)}_{(-24.8\%)}$	161.9 $^{+6.7}_{-6.6}$ $^{(+4.2\%)}_{(-4.1\%)}$
8	172.5	0.18	$^{+61.9}_{-41.8}$ $^{(+35.6\%)}_{(-24.3\%)}$	239 $^{+13}_{-13}$ $^{(+5.4\%)}_{(-5.4\%)}$
14	660.0	0.12	$^{+202.6}_{-143.6}$ $^{(+30.7\%)}_{(-21.7\%)}$	

Table 3.2: LO predictions for the inclusive $t\bar{t}$ production cross section performed at 7, 8 and 14 TeV collisions at the LHC. These predictions are compared to measurements by CMS where experimental uncertainties have been added in quadrature. See text for a discussion of the evaluation of scale uncertainties.

The scale variation results in an uncertainty $\approx (20-40)\%$ demonstrating the lack of precision achievable with a LO prediction. The main source of uncertainty arises from variation of $\alpha_s(\mu_R^2)$, where a decrease in the renormalisation scale μ_R causes an increase in the value of α_s, resulting in an upward shift of the cross section. Also, as the running of $\alpha_s(\mu_R^2)$ is asymptotic, this introduces scale uncertainties which are asymmetric. Besides the uncertainties from varying the renormalisation scale, there is also an effect of over-evolving the PDFs which occurs as μ_F is increased. This decreases the density of quark and gluon PDFs at high-x which is relevant for $t\bar{t}$ production. The ratio of quark initiated processes to the total cross section is also included, highlighting the dominance of the gg production mechanism.

With such large theoretical uncertainties, a comparison between experimental measurements and the predictions from QCD is not meaningful. For this reason, there have been large efforts in the QCD community to improve the precision of top quark pair production predictions. The NLO calculation of the differential and inclusive cross sections was performed over two decades ago [112–115] and the calculation for the inclusive cross section has recently been completed at NNLO [116–119]. There is also a long list of resummation calculations for both the inclusive and differential cross section at LL [120], NLL [121, 122] and NNLL [123–134]. As the aim of this work is to discuss the relevant aspects of high rapidity $t\bar{t}$ production, this requires the use of differential cross section calculations which are currently available at NLO in fixed order.

3.3.2 NLO cross section

At NLO, the expansion of the scaling functions $\mathcal{K}_{ij}(\rho, m_t^2, \mu^2)$ may be expressed as

$$\mathcal{K}_{ij}(\rho, m_t^2, \mu) = \mathcal{K}_{ij}^{(0)} + 4\pi\alpha_s(\mu^2)\left(\mathcal{K}_{ij}^{(1)} + \overline{\mathcal{K}}_{ij}^{(1)}\ln(\mu^2/m_t^2)\right), \tag{3.48}$$

where the scales μ_F and μ_R have been conveniently set equal to μ. The full μ_F and μ_R dependence can be restored by expressing $\alpha_s(\mu_F^2)$ in powers of $\alpha_s(\mu_R^2)$ as was demonstrated

in [124]. Presented in its current form, the coefficient of the term which controls the scale dependence may be obtained by renormalisation group arguments [112] as

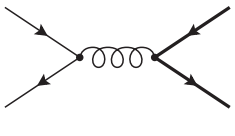
$$\overline{\mathcal{K}}_{ij}^{(1)}(\rho) = \frac{1}{8\pi^2}\left(4\pi b_0 \mathcal{K}_{ij}^{(0)}(\rho) - \int_\rho^1 dz_1 \sum_k \mathcal{K}_{kj}^{(0)}\left(\frac{\rho}{z_1}\right) P_{ki}(z_1) - \int_\rho^1 dz_2 \sum_k \mathcal{K}_{ik}^{(0)}\left(\frac{\rho}{z_2}\right) P_{kj}(z_2)\right). \tag{3.49}$$

This coefficient follows from the scale invariance of the total cross section to $\mathcal{O}(\alpha_s^3)$

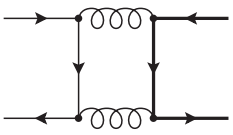
$$\mu^2 \frac{d\sigma_{\text{tot}}}{d\mu^2} = \mathcal{O}(\alpha_s^3)\,, \tag{3.50}$$

and can be evaluated using the one-loop β-function (1.49) and the DGLAP evolution equations (2.46). The functions $\mathcal{K}_{ij}^{(1)}$ were originally found using a numerically extracted fit [112] and then evaluated analytically in [135], a crucial step towards completing the full NNLO calculation. Examples of both virtual and real corrections to the $q\bar{q}$ initiated process are depicted below

$$|\mathcal{M}_{q\bar{q}\to t\bar{t}}|^2 = \Bigg|$$

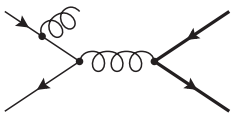


$$+$$

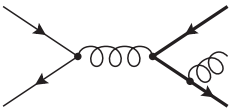


$$+\cdots\Bigg|^2\,, \tag{3.51}$$

$$|\mathcal{M}_{q\bar{q}\to t\bar{t}g}|^2 = \Bigg|$$



$$+$$



$$+\cdots\Bigg|^2\,.$$

In the full computation, both real and virtual corrections to the gg channel, as well as the leading contribution from the $q(\bar{q})g$ initiated process ($\mathcal{O}(\alpha_s^3)$), must also be included. The differential cross section calculation of $t\bar{t}$ production at NLO has been made available in several MC programs such as `MCFM` [44], `POWHEG` [136], `MC@NLO` [137] and its automated counterpart `aMC@NLO` [138].

The inclusive cross section predictions for the relevant LHC CM energies are provided in Table 3.3. These results are obtained with the program `MCFM` with NNPDF 2.3 NLO PDFs

with $\alpha_s(m_Z^2) = 0.119$. The ratio of contributions $\sigma_{q\bar{q}+|qg|}/\sigma_{\text{total}}$ is included to account for the scale dependence of the term $\overline{\mathcal{K}}_{qg}^{(1)}$. This term can be negative when μ_F is increased, as it compensates for an increase in the gg process. Although this ratio is unphysical, it will be relevant for the discussion of the charge asymmetry.

$\sqrt{s}$ (TeV)	σ_{tot} (pb)	$\sigma_{q\bar{q}+\|qg\|}/\sigma_{\text{tot}}$	δ_{scale} (pb)	CMS (pb)
7	158.7	0.18	$^{+19.6}_{-20.2}$ $^{(+12.4\%)}_{(-12.7\%)}$	161.9 $^{+6.7}_{-6.6}$ $^{(+4.2\%)}_{(-4.1\%)}$
8	227.8	0.16	$^{+27.9}_{-28.3}$ $^{(+12.3\%)}_{(-12.4\%)}$	239 $^{+13}_{-13}$ $^{(+5.4\%)}_{(-5.4\%)}$
14	894.5	0.10	$^{+107.6}_{-101.0}$ $^{(+12.0\%)}_{(-11.3\%)}$	

Table 3.3: NLO predictions for the inclusive $t\bar{t}$ production cross section performed at 7, 8 and 14 TeV collisions at the LHC. These predictions are compared to measurements by CMS where experimental uncertainties have been added in quadrature. See text for a discussion of the evaluation of scale uncertainties.

The scale uncertainty at NLO (of around 12%) is not competitive with the current experimental precision. Although the NNLO prediction (with a scale uncertainty of order 5%) for the inclusive cross section is now available, a direct comparison to experiment is not possible. The experimental measurements are of exclusive quantities which are extrapolated into inclusive quantities using the differential cross section prediction available at NLO. In general, it is expected that the differential NNLO calculation will improve the normalisation of distributions rather than their shapes [1], meaning that differential studies performed at NLO can be used to examine the potential sensitivity of exclusive observables to the various input parameters — such as m_t, α_s and the PDFs.

3.3.3 Charge production asymmetry

Within the SM, a charge asymmetry exists in the production of top quarks pairs as a function of the scattering angle between the incoming quark and outgoing top quark [114, 139–141]. This charge asymmetry arises at NLO due to the structure of interfering amplitudes in processes of the form $qX \to t\bar{t}Y$, which are asymmetric under exchange of top and antitop

[1] The exception being observables which are formally LO at $\mathcal{O}(\alpha_s^3)$, such as the transverse momentum distribution of the $t\bar{t}$-pair transverse momentum.

quarks in the final state. As the origin of the asymmetry is a result of the structure of amplitudes, the QCD asymmetry is equivalent to the asymmetry in the process $e^+e^- \to \mu^+\mu^-$ present in QED [142] — with an appropriate rescaling of couplings and colour factors. The differential (a)symmetric cross section may be written as

$$\frac{d\sigma_{s(a)}}{dO} = \frac{1}{2}\left(\frac{d\sigma^{pp\to t\bar{t}Y}}{dO} + (-)\frac{d\sigma^{pp\to \bar{t}tY}}{dO}\right), \tag{3.52}$$

where O is some suitably chosen variable which is sensitive to the asymmetric production. For example, the scattering angle θ between the incoming quark and outgoing top quark. It follows that the charge asymmetry may be defined as

$$A_c = \frac{\int dO \frac{d\sigma_a}{dO}}{\int dO \frac{d\sigma_s}{dO}}, \tag{3.53}$$

where appropriate integration variables must also be chosen. The prediction for the charge asymmetry can be expressed as an expansion in powers of the strong, electromagnetic and weak couplings in the following way

$$\begin{aligned} A_c &= \frac{\alpha_s^3\sigma_a^{s(1)} + \alpha_s^4\sigma_a^{s(2)} + \alpha_s^2\alpha_e\sigma_a^{e(1)} + \alpha_s^2\alpha_w\sigma_a^{w(1)} + \cdots}{\alpha_s^2\sigma_s^{s(0)} + \alpha_s^3\sigma_s^{s(1)} + \alpha_s^4\sigma_s^{s(2)} + \cdots}, \\ &= \alpha_s\frac{\sigma_a^{s(1)}}{\sigma_s^{s(0)}} + \alpha_e\frac{\sigma_a^{e(1)}}{\sigma_s^{s(0)}} + \alpha_w\frac{\sigma_a^{w(1)}}{\sigma_s^{s(0)}} + \cdots, \end{aligned} \tag{3.54}$$

where the superscript denotes the order and the relevant type of correction. Presented in this way, only the leading contributions to the asymmetry have been kept in the expansion.

There is no contribution from the Born QCD process to the asymmetry ($\sigma_a^{s(0)} = 0$), as the quark-gluon coupling is vector-like. Also, there is a neglected asymmetric contribution arising from the Born EW process, resulting from the axial component of the Z boson coupling to fermions. This contribution is negligible as the electroweak coupling enters at α^2, and the propagator must be off-shell for $t\bar{t}$ production. The relevant asymmetric contributions begin at NLO, and were originally computed for QCD in [140,141]. Note that, although the terms $\sigma^{s(1)}$ and $\sigma^{s(2)}$ are currently known [112,116], they do not formally appear in the prediction

for the asymmetry until $\mathcal{O}(\alpha_s^2)$. At this order, they are accompanied by other unknown terms (such as $\sigma_a^{s(2)}$), and the prediction must therefore be truncated to consistently neglect these terms.

Representative cut diagrams contributing to $\sigma_a^{s(1)}$ and $\sigma_a^{e/w(1)}$ are depicted in Figure 3.4. The upper diagrams, which correspond to both qg- and $q\bar{q}$ initiated states, both contribute to $\sigma_a^{s(1)}$. The lower diagrams contribute to either $\sigma_a^{e(1)}$ or $\sigma_a^{w(1)}$ depending on whether a photon or Z boson is exchanged.

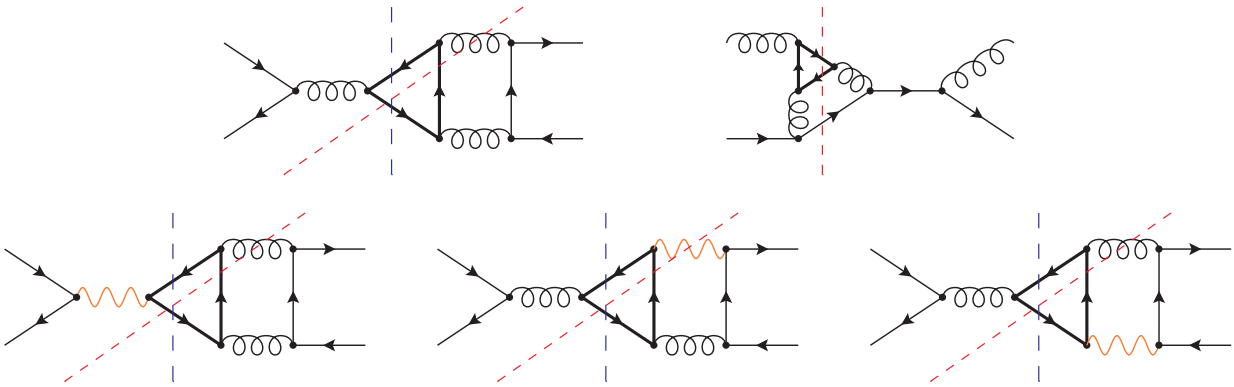


Figure 3.4: Representative cut diagrams contributing to A_c. The $\mathcal{O}(\alpha_s^3)$ contribution from $q\bar{q}$ and qg initiated states is depicted by the upper diagrams, while the $\mathcal{O}(\alpha_s^2\alpha_{e/w})$ contribution is depicted by the lower diagrams.

To calculate the contribution from the QCD process to the asymmetry, it is necessary to calculate the relevant colour factors for the asymmetric cross section. To see this, consider the corrections to the process $q_d(p_1)\bar{q}_c(p_2) \to t_a(p_3)\bar{t}_b(p_4)$, as depicted by the two configurations in Figure 3.5. The virtual (blue) cuts correspond to the interference of the Born amplitude with either the planar (left) or crossed (right) box diagrams. The colour factors at the amplitude level for the Born ($\mathcal{C}_B$), planar box ($\mathcal{C}_{\text{planar}}$) and crossed box ($\mathcal{C}_{\text{crossed}}$) diagrams are given by

$$\mathcal{C}_B = t^A_{ab}t^A_{cd}\,, \qquad \mathcal{C}_{\text{planar}} = t^B_{ae}t^C_{eb}t^B_{cf}t^C_{fd}\,, \qquad \mathcal{C}_{\text{crossed}} = t^B_{ae}t^C_{eb}t^C_{cf}t^B_{fd}\,. \tag{3.55}$$

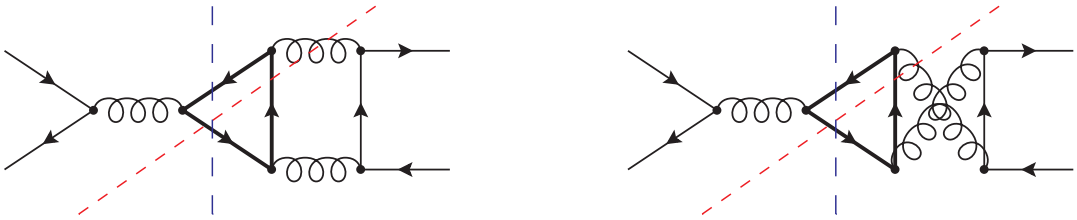


Figure 3.5: Representative cut diagrams to the squared amplitude for the process $q\bar{q} \to t\bar{t}X$. The symmetric colour factor between the diagrams provides the source of the charge asymmetry.

Therefore, the full colour factors for the squared amplitudes of these two configurations are

$$\begin{aligned} \mathcal{C}_{\text{left}} &= \overline{\sum} \mathcal{C}_B^* \mathcal{C}_{\text{planar}} \,, & \mathcal{C}_{\text{right}} &= \overline{\sum} \mathcal{C}_B^* \mathcal{C}_{\text{crossed}} \,, \\ \mathcal{C}_{\text{left}} &= \frac{1}{N^2} Tr\left(t^A t^B t^C\right) Tr\left(t^A t^B t^C\right) & \mathcal{C}_{\text{right}} &= \frac{1}{N^2} Tr\left(t^A t^B t^C\right) Tr\left(t^A t^C t^B\right) \,. \end{aligned} \tag{3.56}$$

The trace can be evaluated using the standard (anti-)commutation relations for $SU(3)$ generators. This follows as

$$\begin{aligned} Tr\left(t^A t^B t^C\right) &= Tr\left(\frac{1}{2}\left([t^A, t^B] + \{t^A, t^B\}\right) t^C\right) \,, \\ &= Tr\left(\frac{1}{2}\left(i f^{ABD} t^D + d^{ABD}\right) t^C\right) \,, \\ &= \frac{1}{2}(i f^{ABD} + d^{ABD}) Tr\left(t^D t^C\right) \,, \\ &= \frac{1}{4}(i f^{ABC} + d^{ABC}) \,. \end{aligned} \tag{3.57}$$

The full colour factors for the squared amplitudes simplify to

$$\mathcal{C}_{\text{left}} = \frac{1}{16N^2}(d_{ABC}^2 - f_{ABC}^2) \,, \qquad \mathcal{C}_{\text{right}} = \frac{1}{16N^2}(d_{ABC}^2 + f_{ABC}^2) \,, \tag{3.58}$$

noting that the cross terms proportional to $f^{ABC} d^{ABC}$ are zero. Excluding colour factors, the differential cross section obtained from the squared amplitudes are related by

$$d\sigma_{\text{left}}(p_3, p_4) = -d\sigma_{\text{right}}(p_4, p_3) \,, \tag{3.59}$$

which interchanges top quark momentum. It follows that the contribution to the charge

asymmetry, with respect to the scattering angle between incoming quark and outgoing top quark, is given by

$$\begin{aligned}\sigma_a^{s(1)} = \frac{1}{2}\int d\cos\theta \Bigg(&\left(\mathcal{C}_{\text{left}}\frac{d\sigma_{\text{left}}(p_3,p_4)}{d\cos\theta} + \mathcal{C}_{\text{right}}\frac{d\sigma_{\text{right}}(p_3,p_4)}{d\cos\theta}\right) \\ &- \left(\mathcal{C}_{\text{left}}\frac{d\sigma_{\text{left}}(p_4,p_3)}{d\cos\theta} + \mathcal{C}_{\text{right}}\frac{d\sigma_{\text{right}}(p_4,p_3)}{d\cos\theta}\right)\Bigg),\end{aligned} \tag{3.60}$$

which can be rearranged using (3.59) to give

$$\sigma_a^{s(1)} = \frac{d^2_{ABC}}{16N^2}\int d\cos\theta \left(\frac{d\sigma_{\text{right}}(p_3,p_4)}{d\cos\theta} - \frac{d\sigma_{\text{right}}(p_4,p_3)}{d\cos\theta}\right). \tag{3.61}$$

It follows that the contribution to A_c is

$$A_c^{\text{virt}} = \frac{\alpha_s}{\sigma_s^{s(0)}}\frac{d^2_{ABC}}{16N^2}\int d\cos\theta \left(\frac{d\sigma_{\text{left}}(p_3,p_4)}{d\cos\theta} + \frac{d\sigma_{\text{right}}(p_3,p_4)}{d\cos\theta}\right). \tag{3.62}$$

The differential cross section, stripped of colour factors and couplings, is equivalent to the original QED computation [142], which was later updated to include massive fermions in [143]. The QCD asymmetry can therefore be obtained from the QED result after making the following replacements for the asymmetric NLO and symmetric LO cross sections

$$\alpha_e^3 Q_q^3 Q_t^3 \to \alpha_s^3 \frac{d^2_{ABC}}{16N^2}, \qquad \alpha_e^2 Q_q^2 Q_t^2 \to \alpha_s^2 \frac{C_F}{2N}. \tag{3.63}$$

The final result for the QCD asymmetry is then found by making the following replacement to the QED asymmetry

$$\alpha_e Q_q Q_t \to \alpha_s \frac{5}{12}. \tag{3.64}$$

The contributions from mixed QED/weak corrections can be calculated in the same way. The mixed QED correction to the asymmetry can be found from the full QED result through the replacement

$$\alpha_e Q_q Q_t \to 3\alpha_e Q_q Q_t. \tag{3.65}$$

or by scaling the QCD asymmetry using the replacement

$$\alpha_s \to \frac{36}{5}\alpha_e Q_q Q_t \,. \tag{3.66}$$

Numerically, this contribution amounts to 23.5% relative to the QCD asymmetry for incoming up-type quarks, or −11.8% for down-type quarks. In the case of mixed weak corrections, there is no exact replacement due to the different propagator structure for Z boson exchange. An approximate replacement can be made under the assumption $\hat{s} \gg m_Z^2$. Under this assumption, the following replacement to the quark charges should be made

$$Q_q Q_t \to \frac{(2\tau_q^3 - 4s_w^2 Q_q)}{4s_w c_w}\frac{(2\tau_t^3 - 4s_w^2 Q_t)}{4s_w c_w} \,. \tag{3.67}$$

Therefore, the approximate mixed weak corrections to the asymmetry for up- and down-type quarks are obtained from the QCD asymmetry with the replacement

$$\alpha_s \to \frac{9}{20}\frac{\alpha_e}{s_w^2 c_w^2}\left(2\tau_q^3 - 4Q_q s_w^2\right)\left(1 - \frac{8}{3}s_w^2\right) \,. \tag{3.68}$$

Assuming a value of $s_w^2 = 0.231$, these replacements amount to a 2.7% and -4.9% relative shift with respect to the QCD asymmetry for up- and down-type quarks respectively. At the LHC, these contributions approximately cancel with one another as the ratio of contributions from $u\bar{u}$ and $d\bar{d}$ initial states is approximately two.

In principle, it is also possible to include mixed QED/weak corrections to the qg initiated states — as was done in [144]. These corrections are numerically small with respect to the corresponding corrections for the $q\bar{q}$ initiated process. As the QCD contribution to the asymmetry is not yet fully known at NLO, including such small effects is not meaningful until this correction is known. For this reason, all mixed corrections to the qg initiated process and mixed weak corrections to the $q\bar{q}$ initiated process are neglected.

The charge asymmetry implies that (anti)top quarks are produced preferentially in the direction of the incoming (anti)quark. At the TeVatron and the LHC, this asymmetry is

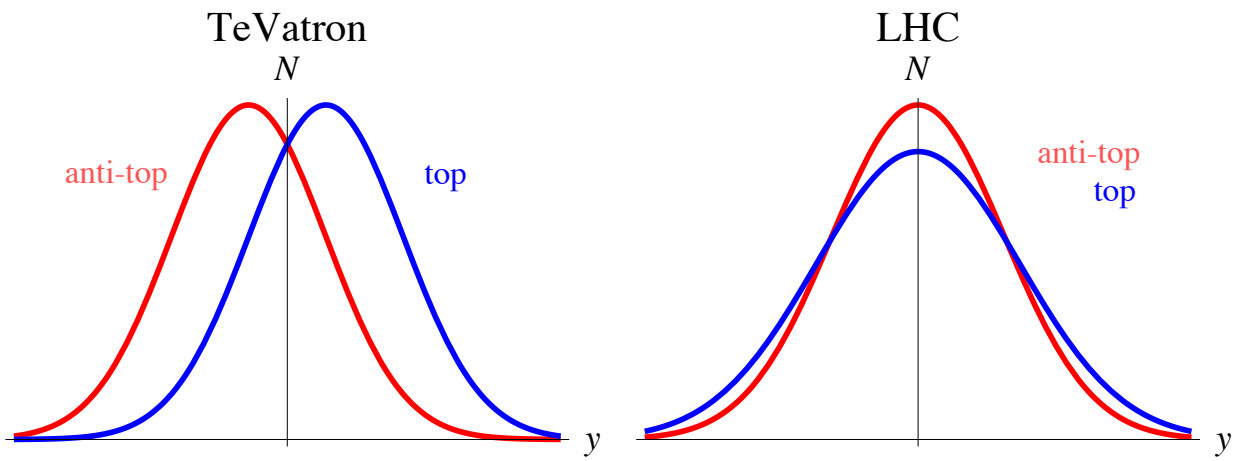


Figure 3.6: Illustrative effect of charge asymmetry on the top (blue) and antitop quark (red) rapidity distribution at the TeVatron (left) and LHC (right).

observable due to the presence of an asymmetry in the quark and antiquark PDFs of the colliding hadrons. At the TeVatron this is a consequence of the fixed direction of the proton and antiproton beams, and results in a forward-backward asymmetry. At the LHC, the asymmetry in the PDFs is present due to the valence content of the proton, and results in top quarks being preferentially produced at large positive and negative rapidities. It is important to notice that, at hadron colliders such as the TeVatron and LHC, there is no observable asymmetry from gg initiated processes to all orders in perturbation theory, as the gluon PDF is symmetric for both $p\bar{p}$ and pp initial states. The effects of the charge asymmetry on the top and antitop quark rapidity distributions within the lab frame are illustrated in Figure 3.6.

The forward-backward asymmetry at the TeVatron is related to charge asymmetry by the charge conjugation symmetry of QCD, and leads to the integrated asymmetry

$$A_{\text{fb}} = \frac{N(y_t > 0) - N(y_{\bar{t}} > 0)}{N(y_t > 0) + N(y_{\bar{t}} > 0)} = \frac{N(y_t > 0) - N(y_t < 0)}{N(y_t > 0) + N(y_t < 0)}, \tag{3.69}$$

where the top and antitop quark rapidities are simultaneously measured in the lab frame. As the top quark asymmetry also leads to a lepton asymmetry, a lepton forward-backward asymmetry (A^l_{fb}) can be defined by replacing the top quarks with their associated daughter leptons as $t \to l^+$ and $\bar{t} \to l^-$. This asymmetry can therefore be measured for both single

and dilepton final states. It is also possible to define a forward-backward asymmetry in the rest-frame of the $t\bar{t}$ system as

$$A_{\text{fb}}^{t\bar{t}} = \frac{N(\Delta_y > 0) - N(\Delta_y < 0)}{N(\Delta_y > 0) + N(\Delta_y < 0)}\,, \qquad \Delta_y = y_t - y_{\bar{t}}\,. \tag{3.70}$$

This asymmetry can be similarly adapted for dilepton final states (A_{fb}^{ll}).

At the LHC, the charge asymmetry emerges as a forward-central asymmetry, and may be measured with the variable

$$A_{\text{fc}} = \frac{N(\Delta_{|y|} > 0) - N(\Delta_{|y|} < 0)}{N(\Delta_{|y|} > 0) + N(\Delta_{|y|} < 0)}\,, \qquad \Delta_{|y|} = |y_t| - |y_{\bar{t}}|\,. \tag{3.71}$$

This asymmetry requires simultaneous measurement of top and antitop quark rapidities.

The charge asymmetry originates from production mechanisms which have phase space dependence. The behaviour of the asymmetry is therefore phase space dependent. For example, measuring the asymmetry as a function of the transverse momentum of the $t\bar{t}$ system ($p_T^{t\bar{t}}$) provides sensitivity to the contribution from real corrections. Typically, measurements of the asymmetry are performed as a function of $m_{t\bar{t}}$, $p_T^{t\bar{t}}$, and the (absolute) rapidity difference between top and antitop quarks. Recently, several new observables have also been proposed [145] which may be particularly sensitive to qg initiated processes at the LHC. It is also important to account for the phase space dependence of the symmetric gg channel. At the LHC, the dilution is substantial, and it is important to perform measurements of asymmetry in regions of phase space where this dilution is reduced.

Measurements of the charge asymmetry have now been performed by CDF [85, 86] and D0 [88, 89] with the full TeVatron data. The inclusive measurements, performed in different final states, are summarised in Table 3.4, and compared to corresponding theoretical predictions provided in [144]. These predictions include the leadings terms in (3.54), and have also included an uncertainty due to scale variance in the usual way. The quoted experimental uncertainties are statistical and systematic respectively. Interestingly, the central value for all of these measurements, including comparisons at the parton and lepton level, lie above

the respective theoretical prediction. Differentially, each of these measurements also suggest that the deviation is largest for very forwardly (backwardly) produced (anti)top quark. In the case of [85], the asymmetry is observed to increase for large top quark pair invariant mass and absolute rapidity difference as expected in SM. However, the expected rate at which the asymmetry increases, exceeds the SM prediction.

Asymmetry	$\sqrt{s}$ (TeV)	Data	$\int \mathcal{L}dt$ (fb^{-1})	Measured (%)	Theory (%)
$A_{\rm fb}^{t\bar{t}}(l\text{+jets})$	1.96	CDF [85]	9.4	16.4 $\pm$3.9 $\pm$2.6	8.8 $\pm$0.6 [144]
$A_{\rm fb}^{t\bar{t}}(l\text{+jets})$	1.96	D0 [87]	9.7	10.6 $\pm$2.7 $\pm$1.3	8.8 $\pm$0.6 [144]
$A_{\rm fb}^{l}$	1.96	CDF [86]	9.4	9.4 $\pm$2.4 $^{+2.2}_{-2.6}$	3.8 $\pm$0.3 [144]
$A_{\rm fb}^{l}$	1.96	D0 [88]	9.7	4.2 $\pm$2.0 $\pm$1.4	3.8 $\pm$0.3 [144]
$A_{\rm fb}^{ll}$	1.96	D0 [89]	9.7	12.3 $\pm$5.4 $\pm$1.5	4.8 $\pm$0.4 [144]

Table 3.4: Summary of measurements of forward-backward asymmetries at the TeVatron with the full data. Where appropriate, the measurement channel has also been highlighted. The uncertainties on the measured asymmetries are statistical and systematic respectively. The theoretical uncertainties arise from scale and PDF uncertainties — see references for details.

ATLAS and CMS have also performed measurements of the charge asymmetry. These measurements have been performed in the dilepton channel [146,147] by both collaborations with the 7 TeV data, and a combination of the results in the l+jets final state [148] with the 7 TeV data has also recently been presented. A preliminary measurement by CMS in the l+jets channel at 8 TeV [149] is also available. The results are summarised in Table 3.5, and compared to the predictions provided in [144]. Where relevant, the asymmetry variable, and final state is highlighted. Although the most precise results from the LHC disfavour the large asymmetry observed at the TeVatron, the results are still inconclusive.

The current status of the measurements performed at the TeVatron (left) and the LHC (right) are summarised in Figure 3.7. For the experimental uncertainties, the inner band corresponds to the statistical uncertainty, and the outer band corresponds to the total uncertainty found from adding statistical and systematic uncertainties in quadrature.

The measurements of the unexpectedly large asymmetry observed at the TeVatron has stimulated much work in the model building community. Although interesting, extending

Asymmetry	$\sqrt{s}$ (TeV)	Data	$\int \mathcal{L}dt$ (fb^{-1})	Measured (%)	Theory (%)
$A_{\mathrm{fc}}(ll)$	7	ATLAS [146]	4.7	5.7 $\pm$2.4 $\pm$1.5	1.23 $\pm$0.05 [144]
$A_{\mathrm{fc}}(ll)$	7	CMS [147]	5.0	-1.0 $\pm$1.7 $\pm$0.8	1.23 $\pm$0.05 [144]
$A_{\mathrm{fc}}(l$+jets)	7	comb. [148]	4.7 + 5.0	0.5 $\pm$0.7 $\pm$0.6	1.23 $\pm$0.05 [144]
$A_{\mathrm{fc}}(l$+jets)	8	CMS [149]	19.7	0.5 $\pm$0.7 $\pm$0.6	1.07 $\pm$0.04 [144]
A_{fc}^{ll}	7	ATLAS [146]	4.7	2.3 $\pm$1.2 $\pm$0.8	0.49 $\pm$0.01 [144]
A_{fc}^{ll}	7	CMS [147]	5.0	0.9 $\pm$1.0 $\pm$0.6	0.49 $\pm$0.01 [144]

Table 3.5: Summary of measurements of the forward-central asymmetries at the LHC. Where appropriate, the measurement channel has also been highlighted. The uncertainties on the measured asymmetries are statistical and systematic respectively. The theoretical uncertainties arise from scale and PDF uncertainties — see references for details.

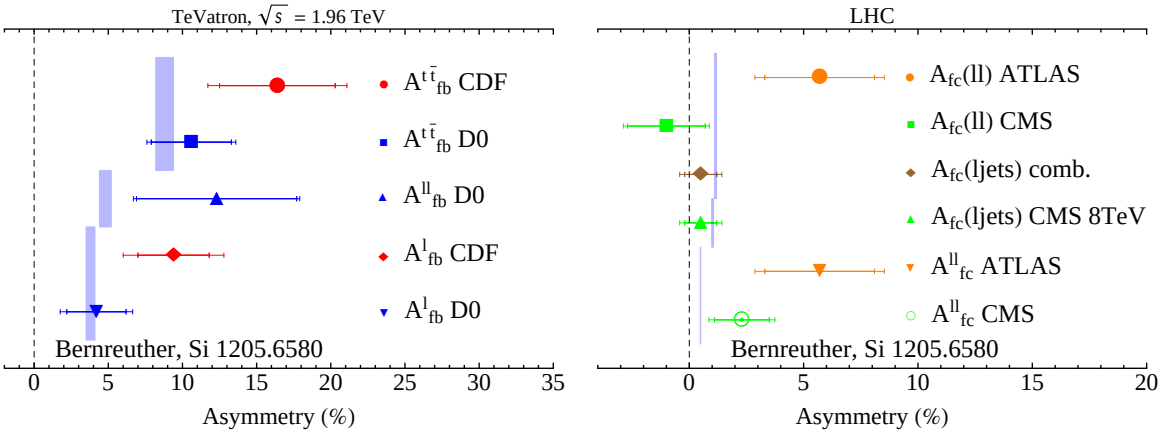


Figure 3.7: Charge asymmetry measurements performed at the TeVatron (left) and the LHC (right). Left: Forward-backward asymmetry results from the TeVatron. Right: Forward-central asymmetry results from the LHC performed at 7 TeV. A preliminary result from CMS at 8 TeV in the l+jets channel is also available. The blue band corresponds to LO theoretical predictions which include QCD and EW effects.

the SM to explain the observed excess in the asymmetry is difficult. These extensions are subject to constraints from all other $t\bar{t}$ observables which appear to be SM-like. A summary of these various extensions can be found in [150].

It is clear that the large data expected in Run II at the LHC will be required to confirm or refute the behaviour observed at the TeVatron. It is also important to note that the SM prediction for the inclusive forward-central asymmetry at 14 TeV is below the percent level [151], a result of the substantial gg dilution. As the systematic uncertainty for the corresponding measurements performed at 7 and 8 TeV amounts to $\approx 0.6\%$, future measure-

ments in this region will suffer from a total uncertainty of the order of the SM prediction. Although some improvement in the systematic uncertainties is expected, the dominant contribution to the uncertainty arises from generator and hadronisation modelling, which will not significantly improve. For this reason, it will be necessary to select regions of phase space where the asymmetry is enhanced to perform a significant measurement.

3.4 Motivations for high pseudorapidity measurements

The motivations for studying top quark production at high pseudorapidity can be summarised by studying the kinematics of the Born cross section for top quark pair production. For a general $2 \to 2$ partonic process, the following definitions can be made

$$x_{1,(2)} = \frac{m_T}{\sqrt{\hat{s}}}(e^{(-)y_3} + e^{(-)y_4}) \,, \qquad m_T = \sqrt{(m^2 + p_T^2)} \,, \qquad \hat{s} = 2m_T^2(1 + cosh\,\Delta y) \,. \quad (3.72)$$

Measurements of forwardly produced top quarks simultaneously probe high-x_1 and low-x_2 colliding partons. This is particularly interesting for top quark pair production for the following reasons:

- Production of top quark pairs proceeds predominantly through the gg process. Therefore, measurements of the $t\bar{t}$ cross section at high (pseudo)rapidity provides constraints on the gluon PDF at both high and low-x.
- The relative contribution from quark initiated processes to the differential top quark pair cross section increases at high (pseudo)rapidity. This is a consequence of the relative decline of the gluon PDF at large-x with respect to the quark valence content, and results in enhanced sensitivity to the charge asymmetry.

These points are summarised in Figure 3.8, where the high-x region of CT10wnlo $\alpha_s(m_Z^2) = 0.118$ PDFs (CT10w), evolved to $Q^2 = m_t^2$, are shown. In the left plot, relevant PDFs which contribute to the top quark pair cross section are shown, highlighting the dominance of the gluon PDF at moderate and low values of x. In the right plot, the relative uncertainty of

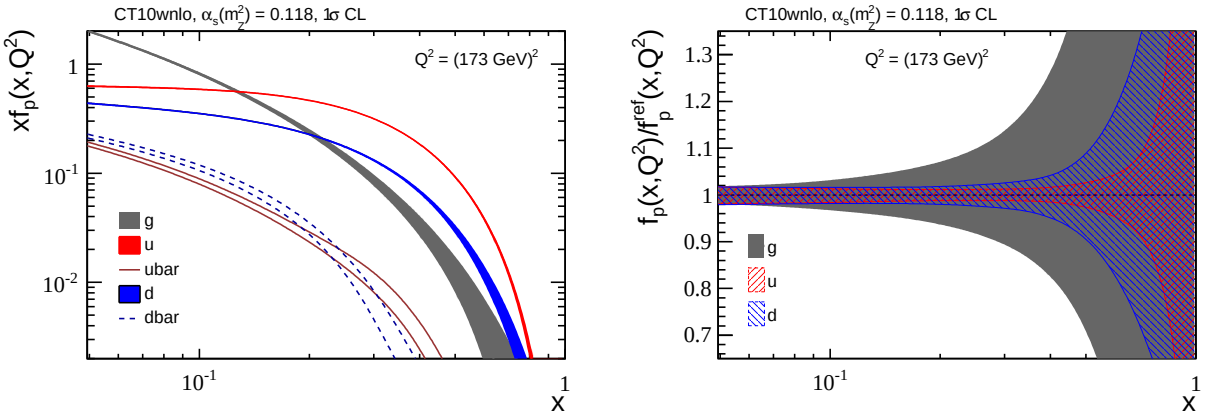


Figure 3.8: Relevant CT10wnlo $\alpha_s(m_Z) = 0.118$ PDFs contributing to top quark pair production at the LHC. The uncertainty corresponds to the 1σ CL. Right: PDFs have been plotted with respect to the central value member set.

the quark and gluon PDFs with respect to the central member is shown. In both cases, the PDF uncertainties are provided at 1σ. This is done by scaling the deviation from each eigenvector member from the central value by 1.645 (which scales the uncertainty from 90% to 68.3% CL). The quark PDFs are relatively well constrained by DIS measurements, while the gluon PDF is not.

Although high pseudorapidity measurements are sensitive to regions of the PDFs which are not well constrained, they also suffer from a lack of statistics due to the decline of PDFs at high-x. This can be seen explicitly by examining the pseudorapidity distributions of top quarks in pair production. It will be convenient to introduce a 'pseudotop' object as

$$\frac{d\sigma^{\tilde{t}}}{dX} = \frac{1}{2}\left(\frac{d\sigma^{t}}{dX} + \frac{d\sigma^{\bar{t}}}{dX}\right). \tag{3.73}$$

Although this variable is insensitive to the charge asymmetry, it is well suited to studying the differential cross section at high pseudorapidity. The corresponding differential cross section with respect to pseudorapidity is shown in Figure 3.9 at 7 (left) and 14 TeV (right). The blue uncertainty band is due to scale variation, and the red dashed line is the relative 1σ PDF uncertainty. The vertical error bars on the relative scale uncertainty demonstrate a the lack of sampling in certain regions of phase space. The prediction for the inclusive and LHCb cross sections is also provided. The LHCb cross section corresponds to the shaded region — the integral over the LHCb acceptance ($\eta \in [2.0, 5.0]$).

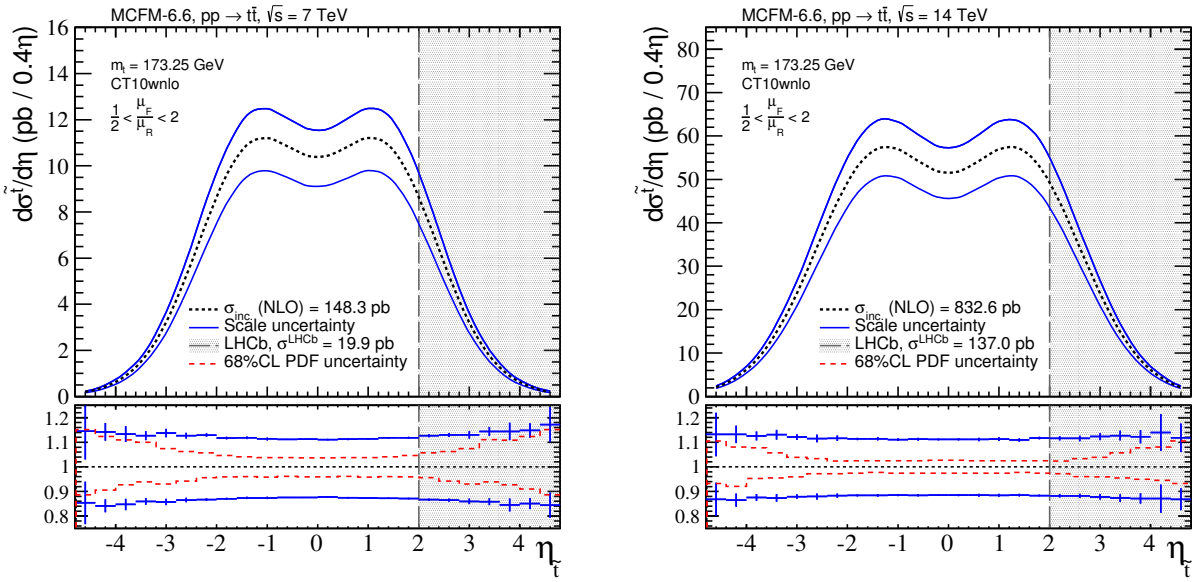


Figure 3.9: Differential pseudotop ($\tilde{t}$) cross section with respect to pseudorapidity at 7 (left) and 14 TeV (right). The CT10wnlo $\alpha_s(m_Z^2) = 0.118$ PDF set is used. The blue band corresponds to scale variance, and the red dashed band in the relative uncertainty corresponds to the PDF 1σ CL.

At both CM energies, the PDF uncertainties increase at high pseudorapidity as the PDFs are probed at large-x. The PDF uncertainties in a given pseudorapidity bin at 7 TeV are relatively larger than the corresponding prediction at 14 TeV, as this corresponds to a region of higher x. The dependence of both inclusive and LHCb cross sections on PDFs as well as other input parameters will be fully quantified in the following Chapter.

As previously mentioned, top quark measurements at high pseudorapidity may also be sensitive to the charge asymmetry. To see this, in Figure 3.10 the ratio of production mechanisms $(q\bar{q} + |qg|)$/total contributing to the total $t\bar{t}$ cross section is presented as a function of the pseudotop pseudorapidity at 7 (left) and 14 TeV (right). Although quark initiated processes are relatively enhanced at high pseudorapidity, the gg channel is still dominant across the entire range of phase space. The contribution from the qg initiated processes to the total cross section $\sigma^{s(1)}$ can be negative when μ_F is increased, however, its contribution to the asymmetric cross section $\sigma_a^{s(1)}$ remains positive. Therefore, to understand how the ratio of quark initiated production mechanisms enhances the charge asymmetry, it is necessary to include the modulus of the qg contribution.

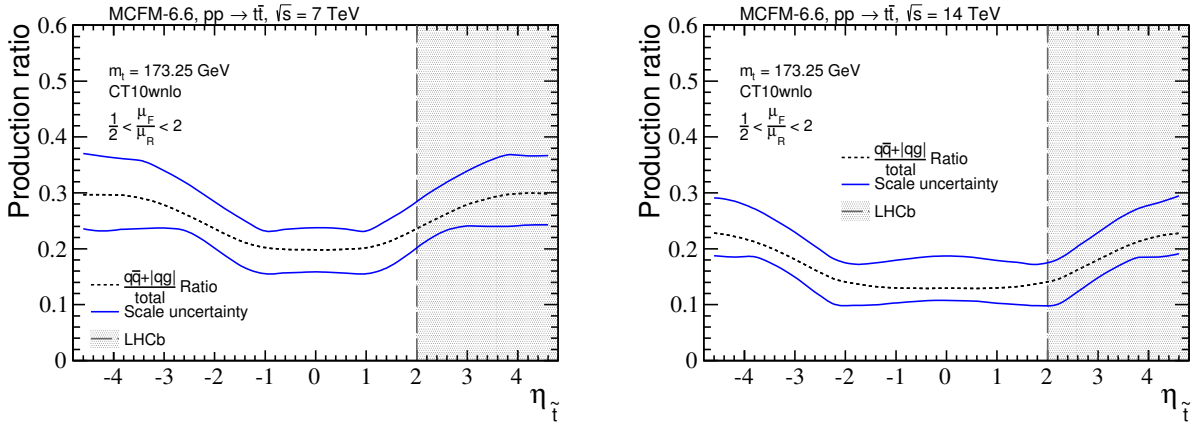


Figure 3.10: Ratio of production mechanisms of pseudotop as a function of pseudorapidity at 7 (left) and 14 TeV (right). The blue band corresponds to the uncertainty associated to scale variation.

As forwardly produced top quarks are sensitive to the high-x_1 region of PDFs, it is important to investigate the feasibility of top quark measurements within the LHCb acceptance. This is necessary to quantify how measurements in this region may improve the current constraints on PDFs. Also, to access the charge asymmetry it is necessary to define an experimentally accessible variable. To do this, a detailed analysis of expected signal and background rates for several different final states will be considered.

3.5 Summary

The relevant features of top quark production and decay, necessary to perform detailed phenomenology, have been introduced.

The importance of the top quark mass within the SM and the current experimental constraints have been discussed. The top quark was shown to decay weakly as a quasi-free particle. As a consequence of the CKM hierarchy $|V_{tb}|^2 \gg |V_{ts}|^2 \gg |V_{td}|^2$, this results in a very clear experimental signature — namely, $t \to Wb$. It then becomes possible to categorise top quark searches according to particular W boson decay channels. Also, as the polarisation of the W boson controls the angular distribution of its decay products, the distribution of leptons in $t \to (W \to l\nu_l)b$ decays are correlated with the top quark distribution.

The dominant production mechanism for top quarks at the LHC is the production of a pair of top quarks proceeding via the strong force. The general structure for the expansion of this short-distance subprocess was discussed, and predictions for the inclusive cross section at LO and NLO were provided. Although consistent with experimental measurements, these predictions have substantial scale uncertainties. To meaningfully compare theoretical predictions with experimental observations, it is necessary to improve the precision of top quark pair cross section predictions. Some of the theoretical developments were highlighted. In the meantime, performing feasibility studies with differential NLO distributions is sufficient to approximate event rates and highlight the potential sensitivity to particular variables and input parameters.

An interesting feature of top quark pair production is the presence of an asymmetry in the angular distribution of top and antitop quarks. This asymmetry is observable at TeVatron and LHC due to the presence of an asymmetry in the initial state PDFs. Measurements of this asymmetry at the TeVatron, which manifests as a forward-backward asymmetry, observe an unexpectedly large asymmetry with respect to the available SM prediction. On the other hand, measurements of the forward-central asymmetry at the LHC show no consistent pattern to support or refute this behaviour. With the large amount of data expected during Run II at the LHC, it will become important to select regions of phase space which are particularly sensitive to the charge asymmetry. This is mainly required to suppress the substantial dilution arising from the symmetric gg process.

The motivations for studying forwardly produced top quarks were also outlined. In terms of the kinematics, forwardly produced top quarks are sensitive to high-x_1 incoming partons. This suggests that cross section measurements within the LHCb acceptance may provide useful constraints on PDFs at high-x. As the dilution from gg initiated processes decreases for forwardly produced top quarks, it is also important to investigate the potential sensitivity of charge asymmetry measurements with the same data.

Chapter 4

Cross section measurements at LHCb

The feasibility of top quark pair cross section measurements with the LHCb detector will be studied in this Chapter. Using the tools which have been discussed in previous Chapters, predictions of signal and background will be provided for several potential measurement channels. After the statistical precision achievable with current and future data has been quantified, the theoretical systematics associated to pair production at high pseudorapidity is studied in detail. Upon comparing the sensitivity of inclusive and differential measurements to the various systematics, it will become clear that measurements at LHCb have an enhanced sensitivity to PDFs. To quantify this, a reweighting will be applied, based top quark pair cross section pseudodata, to both replica and Hessian PDFs.

4.1 Introduction

In the previous Chapter, the motivations for measuring the properties of top quark pair production at high pseudorapidity were outlined. In particular, it was shown that forwardly produced top quarks are particularly sensitive to the high-x region of PDFs. This provides an interesting test of perturbative QCD, due to the presence of asymmetric quark initiated production mechanisms which are relatively enhanced at high pseudorapidity — the prospects of charge asymmetry measurements at LHCb will be studied in Chapter 5. It was also noted that, as pair production is dominated by the gg process, measurements at high pseudorapidity may provide useful constraints on the gluon PDF. It should also be mentioned that top quarks produced at very high pseudorapidity have not yet been observed. As the LHCb experiment has recorded data within this region of phase space, it is important to develop a suitable analysis strategy to measure top quark properties with this data.

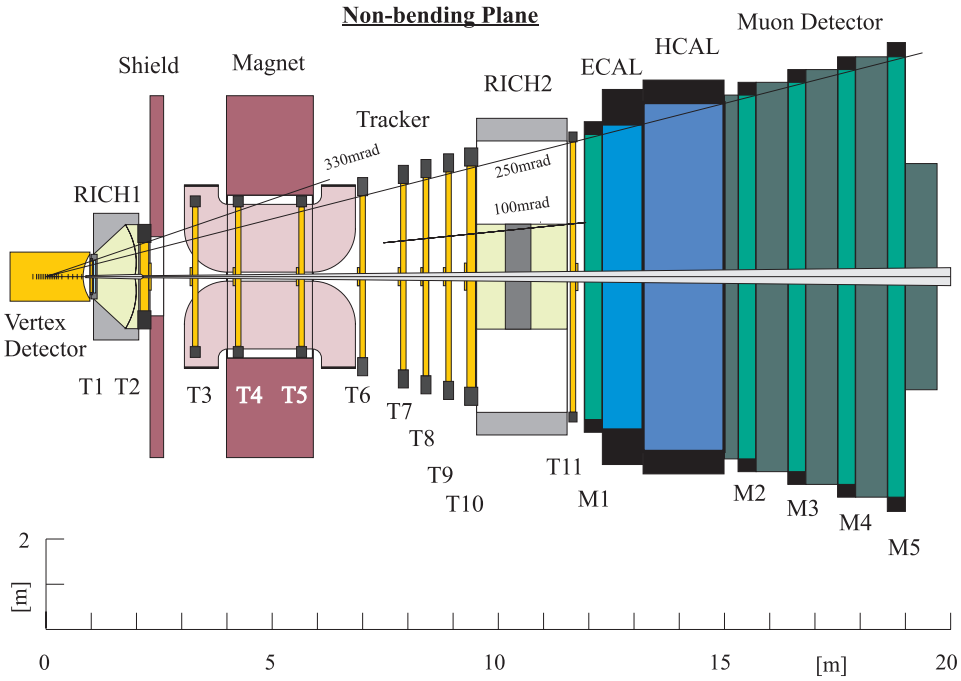


Figure 4.1: Schematic layout of the LHCb detector.

The statistical precision achievable for several final states will be considered at 7, 8, and 14 TeV. After discussing the feasibility of particular final states, including analysis of the relevant backgrounds, the potential constraints on the gluon PDF arising from future LHCb cross section measurements will be quantified.

4.2 Feasibility

The feasibility of measurements at LHCb depends on the recorded integrated lumonisities, as well as the detection efficiencies for different final state particles. It is therefore important to briefly review these features. The LHCb detector [152] is a single-arm forward spectrometer, covering the pseudorapidity range $2.0 < \eta < 5.0$, with the main physics goal of studying b and c hadron decays. A schematic layout of the LHCb detector, obtained from [153], is depicted in Figure 4.1. The important features of the detector and data relevant for this work are summarised below:

- The detector has excellent b hadron reconstruction efficiency, which is relevant for b-

tagging jets. Internal studies indicate that an efficiency to mis-tag rate of 70% to 1% is achievable for high-p_T (> 20GeV) jets.

- Muon reconstruction is possible within the pseudorapidity range $2.0 < \eta < 4.5$. A detection efficiency of 75% is achievable for high-p_T (> 20GeV) muons [154].

- The recorded integrated luminosities at 7 and 8 TeV are 1.1 and 2.1 fb^{-1} respectively.

- The expected integrated luminosity at 14 TeV is 5.0 fb^{-1} per year [155], amounting to ≈ 50 fb^{-1} by 2030.

- The reconstruction efficiencies evaluated with the 7 and 8 TeV data are expected to be good estimates of what can be achieved during 14 TeV running conditions. This is a consequence of the luminosity levelling at LHCb, which reduces the impact of pileup.

It was first proposed in [156] that top quark measurements at LHCb may be feasible by identifying top quarks through their decay $t \to (W \to \mu\nu_\mu)b$, where the muon and the b-jet are registered by the detector. It was noted that partial reconstruction of the full $t\bar{t}$ system is necessary to gain reasonable event rates. The analysis in [156] also demonstrated that this channel may also be used to measure the charge asymmetry. This is possible by measuring the rate of top and antitop quarks as a function of pseudorapidity, which can be inferred by the pseudorapidity and charge of the reconstructed muon. However, as the analysis was performed at LO, no prediction for the charge asymmetry was provided. Also, constant K-factors were used to scale the LO cross sections for signal and background rates. This scaling clearly does not take into account the phase space dependence of contributing subprocesses. In the analysis presented here, signal and background are generated at NLO+PS, and these samples are used to study the feasibility of several final states.

4.2.1 Final state selection

The limited acceptance of the LHCb detector makes full event reconstruction difficult as generally only part of the event is registered by the detector. It is therefore important to

understand the kinematic acceptance for the various decay channels of the top quarks. Due to the large QCD backgrounds present at the LHC, at least one isolated charged lepton should be required in the final state. Therefore, the two main categories considered are the lepton+X or dilepton+X channels. These channels can then be subcategorised by the number of jets within the acceptance and by how many of these jets are b-tagged. The single lepton channel with one associated b-jet (lb) has the largest acceptance, while high multiplicity final states such as $lbbjj$ have a relatively small acceptance. Note that b-jet(s) and jet(s) in the event are used to reduce background, while the sign of the charged lepton is used to identify the sign of the top quark charge. The minimum requirement of at least one b-tagged jet is necessary to reduce the otherwise overwhelming electroweak backgrounds.

Object definition

Jets are defined to have a global jet parameter distance $R = 0.5$ (2.62), a minimum p_T >15 GeV, and to be clustered with the anti-k_t algorithm using `FastJet3` [157] software. The charged leptons from W and Z boson decays, and all neutrinos, are excluded in the jet reconstruction. An isolation requirement is placed on the charged leptons to separate hadronic activity.

To identify b-jets, it is necessary to perform generator level b-tagging. This is done by matching either a parton or seed b quark (before hadronisation) from the hard process to a reconstructed jet in the rapidity-phi plane within R. A study of the matching of jets to b quarks from top decays in $t\bar{t}$ events at $\sqrt{s} = 7$ TeV found that over 90% of b quarks were successfully matched simultaneously to a b quark at both the parton and seed level. Of the remaining decays, 4% were matched at either the parton or seed level, and the remaining 6% were not uniquely matched. The majority of b quarks which are not b-tagged lie in the region of low-p_T — this is due to the minimum p_T requirement in the jet reconstruction algorithm. The fraction of events falling into the various b-tagging categories is presented as a function of the b parton p_T in Figure 4.2 (left). Studies on the impact of varying R in the jet reconstruction indicated that the generator level b-tagging efficiency improved for larger values of R, a result of the looser matching criterion. It was also found that the energy of the

b parton is better described by reconstructed jets with larger values of R — see Figure 4.2 (right). However, when lepton isolation is implemented, $\Delta R(l^{\pm}, \text{jet}) \geq R$, the choice of R = 0.5 was found to be optimal. The LHCb jet reconstruction algorithm is also calibrated to $\Delta R = 0.5$ anti-k_t jets [158]. Therefore, other choices of R would require a re-calibration of the LHCb jet reconstruction. Fully optimising the choice of R parameter for studies of top quark production at LHCb requires knowledge of the b-tagging performance and detector response — this should be studied in full detail for high statistics analyses performed at 14 TeV.

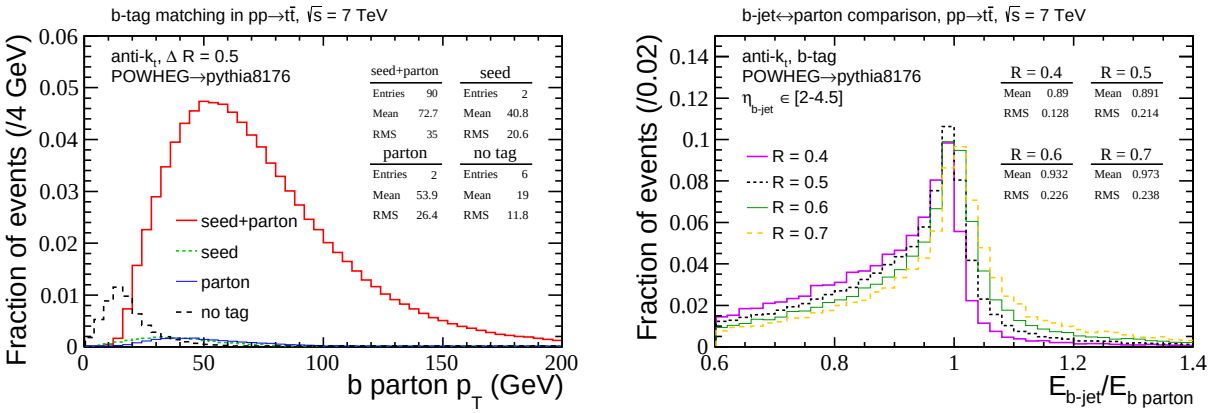


Figure 4.2: Left: fraction of events falling into various truth level b-tagging categories. The total sample is normalised to 100 events. Right: energy ratio of b-tagged jet (within the LHCb acceptance) to associated parton level b quark for various values of the jet parameter R. In both cases, the events ($t\bar{t}$) are generated with POWHEG at $\sqrt{s} = 7$ TeV and matched to Pythia8176.

Preliminary analysis

To estimate the feasibility of cross section measurements for different final states, a preliminary analysis of $t\bar{t}$ signal at $\sqrt{s} = 7$, 8 and 14 TeV is performed. This is simulated with `POWHEG` matched to `Pythia8176`. The central CT10wnlo PDF set is used, and an uncertainty due to scale variation is evaluated by generating samples with a 7-point scale variation according to (3.47). It is required that leptons and jets are within the LHCb acceptance — defined by the pseudorapidity range $2.0 < \eta < 4.5$. An isolation requirement on all leptons $\Delta R(l^{\pm}, \text{jet}) \geq R$ is applied which acts to reduce signal contamination from background QCD processes. Note that the distance parameter in the isolation requirement $R = 0.5$, is

the same value which is used in the jet reconstruction. For single lepton final states, the following kinematic cuts are applied:

- b-jet minimum $p_T > 60$ GeV,
- light jet, or secondary b-jet, minimum $p_T > 20$ GeV,
- $l^{\pm}$ minimum $p_T > 20$ GeV.

For dilepton final states, the following kinematic cuts are applied:

- b-jet minimum $p_T > 20$ GeV,
- $l^{\pm}$ minimum $p_T > 20$ GeV.

As previously mentioned, requiring the presence a of b-jet is necessary to reduce the background from EW processes. The differential cross section for different final states at 7, 8, and 14 TeV is provided in Table 4.1.

$d\sigma$(fb)	7 TeV	8 TeV	14 TeV
lb	291 ± 47	520 ± 72	4436 ± 615
lbj	100 ± 15	215 ± 27	2547 ± 323
lbb	34 ± 4	65 ± 8	870 ± 116
$lbbj$	11 ± 2	26 ± 4	487 ± 76
l^+l^-	33 ± 6	60 ± 11	444 ± 62
l^+l^-b	16 ± 4	32 ± 5	299 ± 35

Table 4.1: Summary of differential $t\bar{t}$ cross sections for various final states within the LHCb acceptance ($2.0 < \eta < 4.5$). The simulation is performed with `POWHEG` matched to `Pythia8176` at $\sqrt{s} = 7$, 8, 14 TeV LHC CM energies with the central CT10wnlo PDF. The uncertainty accounts for scale variation as described in the text.

The provided cross sections account for $W \to l\nu_l$ decays, where l corresponds to either a muon or an electron. The contribution from leptonic τ decays is not included. Another noteworthy effect in the single lepton channel is that the registered b-jet may not necessarily belong to the same decay chain as the lepton. Including these events is experimentally

necessary, as charge tagging of b-jets is extremely inefficient. At 7 and 8 TeV, the lb and lbj channels are statistically the most promising channels with the available data — corresponding to 1 and 2 fb^{-1} at $\sqrt{s} = 7$ and 8 TeV respectively. At 14 TeV, measurements in the dilepton channel with a single b-jet also become statistically feasible.

4.3 Signal and background

The feasibility of measurements in these channels also requires an estimation of the corresponding background rates. A realistic estimation of the statistical precision achievable in each channel can be made by applying the following reconstruction efficiencies: 75% efficiency for leptons [154]; 70% efficiency for b-jets; and 1% mis-tag rate for light jets [159].. In this study, the mis-tag rate for light jets is also applied to c-jets.

As the low multiplicity final states, lb and lbj, are statistically most promising at all CM energies, they will be studied in most detail. The dilepton channel will also be considered at 14 TeV. Although the other channels listed in Table 4.1 are not considered, experimentally studying these channels is important as they are each sensitive to different background processes.

4.3.1 lepton+jets

For the analysis of the lb and lbj channel, only muon final states are considered as the detection efficiency for muons is greater than for electrons — mainly a consequence of the triggering efficiency. Electron final states are also possible [160], but require a more careful consideration of background processes and have a poorer detection efficiency. The statistical precision presented in this analysis is therefore an underestimate of what should be achievable with current and future LHCb data when electrons are included.

As the cross section measurement does not differentiate between muon charge, the μb and μbj channels are labelled as $\tilde{t}_{\mu b}$ and $\tilde{t}_{\mu bj}$ respectively — corresponding to the sum μ^+

and μ^- events. The main backgrounds are identified as single top, W+(b)jets and Z+(b)jets. These backgrounds are simulated using `POWHEG` [161–164] with the central CT10w PDF set and then subsequently matched to `Pythia8176` — the only exception is $Z + b$jets where the matrix element is produced using `MadGraph5` [165] with cteq6ll.

Signal. The $t\bar{t}$ signal is found by fixing the factorisation and renormalisation scales equal to the top mass ($m_t = 173.25$ GeV). This corresponds to the central cross section evaluated in Table 4.1.

QCD. The QCD background originating from di-$b$jet production, where a secondary muon passes isolation and kinematic cuts, has previously been shown to be negligible [156]. Given a di-$b$jet background rejection of $\mathcal{O}(10^{-5})$, and that the relative increase in the ratio of $(pp \to t\bar{t})/(pp \to b\bar{b})$ from 7→14 TeV is ≈ 3, this background can also ignored for the 14 TeV analysis.

EW+jets. The W+(b)jets background can be separated into Wjets and Wbjets. In the first case, a light flavour jet is mis-tagged as a b-jet, and in the second case, a b-jet is correctly identified (where $g \to b\bar{b}$). In either case, the W boson decays to an isolated lepton. The Z+(b)jets background arises from leptonic decay of a Z boson where only one of the leptons is detected in association with either a correctly identified (in $Zb/Zg \to b\bar{b}$) or mis-tagged b-jet.

Single top. This process can be subcategorised into s-channel, t-channel, and tW. The s- and t-channel subprocesses correspond to Born contributions in which the virtual W is exchanged in either the s- or t-channel respectively. The tW subprocess is simply where the W boson is also produced in the final state. The t-channel single top process is modelled in both 4- and 5-flavour (ST, tch) schemes. The 4-flavour cross section is normalised to the prediction found in the 5-flavour scheme, and the average of these distributions is plotted with a systematic error associated to the envelope between the two descriptions[1]. In the 5-flavour scheme, the DGLAP evolution in the PDF automatically resums the contribution from $g \to b\bar{b}$ splittings, and therefore provides a more accurate prediction of the total cross

[1]The top decay is not included in the matrix element in the 4-flavour scheme.

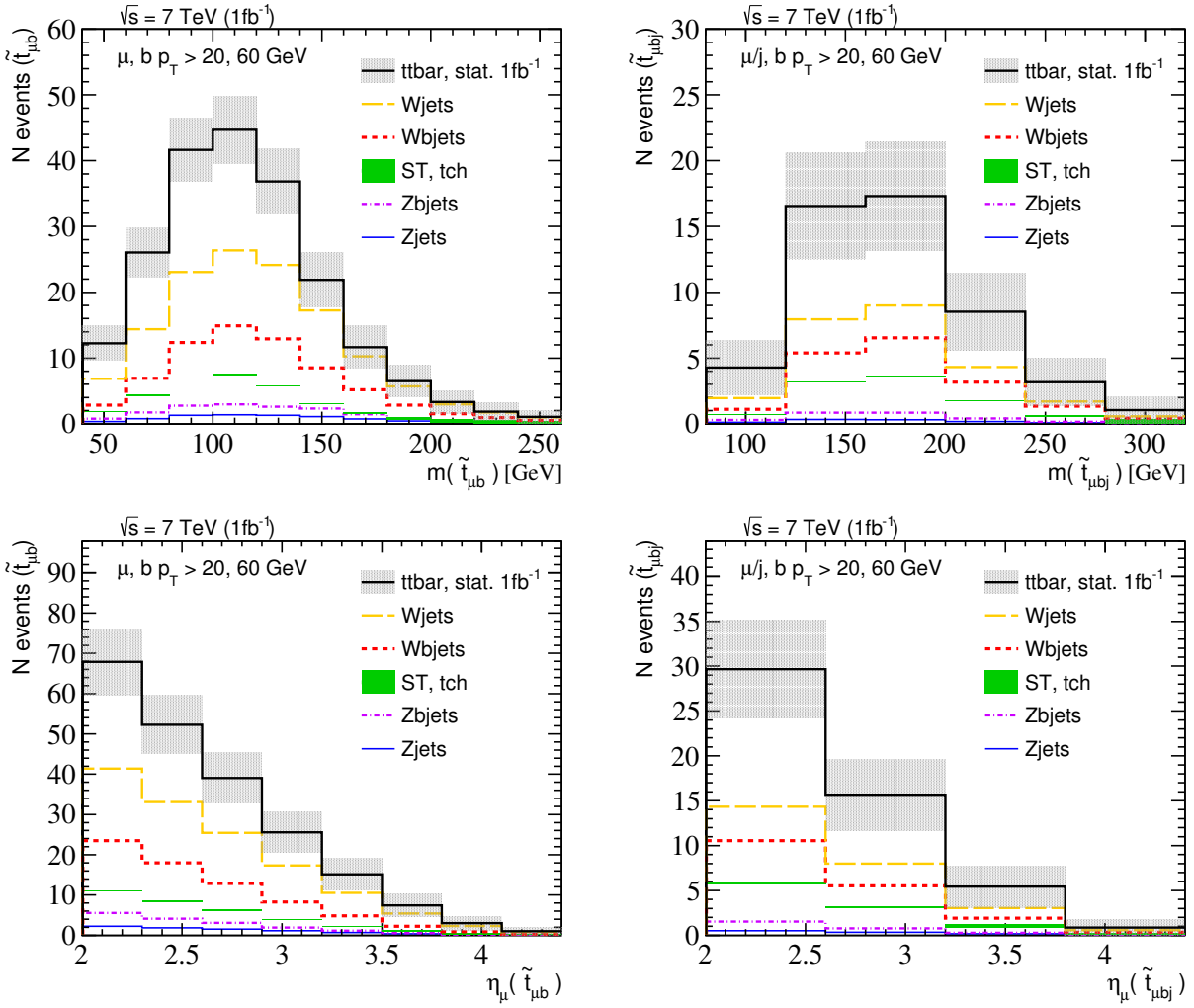


Figure 4.3: Expected signal and background as a function of reconstructed pseudotop ($\tilde{t}_{\mu b(j)}$) invariant mass (upper) and muon pseudorapidity (lower) at $\sqrt{s} = 7$ TeV with $\int \mathcal{L}dt = 1\text{fb}^{-1}$. Cuts on the b-jet and muon/light jet p_T of 60, 20 GeV are applied to the $\tilde{t}_{\mu b}$ (left) and $\tilde{t}_{\mu bj}$ (right) selections.

section. There is a small combined contribution (below 10% of $t\bar{t}$ signal) from tW and s-channel single top which is not included.

In the following analysis, the number of pseudotop events expected in 1, 2, and 5 fb^{-1} at 7, 8, and 14 TeV will be presented as a function of the final state invariant mass and muon pseudorapidity for both $\tilde{t}_{\mu b}$ and $\tilde{t}_{\mu bj}$ channels. In all plots, the signal and background are stacked, and the resultant uncertainty band corresponds to the statistical uncertainty found after applying all reconstruction efficiencies. At 14 TeV, an additional uncertainty band is also included which corresponds to the statistical uncertainty expected with 50 fb^{-1} — this amounts to the data expected after 10 years of running.

The 7 TeV results are presented in Figure 4.3. The dominant background is identified as Wjets, which has been scaled by a factor of 0.01 corresponding to the light jet mis-tag rate. This suggests that the experimental systematic uncertainty associated to the b-tagging mis-tag rate is likely to be important for normalisation of the background. A direct measurement of the Wjets process within the LHCb acceptance will be extremely important in determining the accuracy of the modelling of this process. It is also noticed that the single top prediction in the 4-flavour scheme tends to be larger for high invariant masses. This is due to the presence of events in which a collinear spectator b quark and lepton are reconstructed together within the acceptance, particularly beyond m_t. For the muon pseudorapidity distributions, although the statistical uncertainties are overwhelming at high pseudorapidity (beyond three), the signal is clearly separated from background events in the low pseudorapidity bins. This can be quantified by calculating the χ^2 between the total number of expected events (N) and background (B) as

$$\chi^2 = \sum_{i}^{\text{bins}} \frac{(N_i - B_i)^2}{(\Delta N_i)^2 + (\Delta B_i)^2} \,. \tag{4.1}$$

A background uncertainty (ΔB) of 5% is assumed. At 7 TeV, the χ^2/N_{dof} for the pseudorapidity distributions for $\tilde{t}_{\mu b}$ and $\tilde{t}_{\mu bj}$ final states are

$$\chi^2/N_{\text{dof}}(\mu b) = 25.7/8\,, \qquad \chi^2/N_{\text{dof}}(\mu bj) = 12.6/4\,. \tag{4.2}$$

The N_{dof} are 8 and 4 respectively, corresponding to the number of bins.

The same analysis is also performed at 8 TeV. The resulting muon pseudorapidity distributions are shown in Figure 4.4. Calculating the χ^2/N_{dof} in the same way gives

$$\chi^2/N_{\text{dof}}(\mu b) = 93.1/8\,, \qquad \chi^2/N_{\text{dof}}(\mu bj) = 52.0/4\,. \tag{4.3}$$

This study suggests that the $t\bar{t}$ process should be clearly visible with an analysis of the current data. Although rather naive in many of the assumptions made about detection

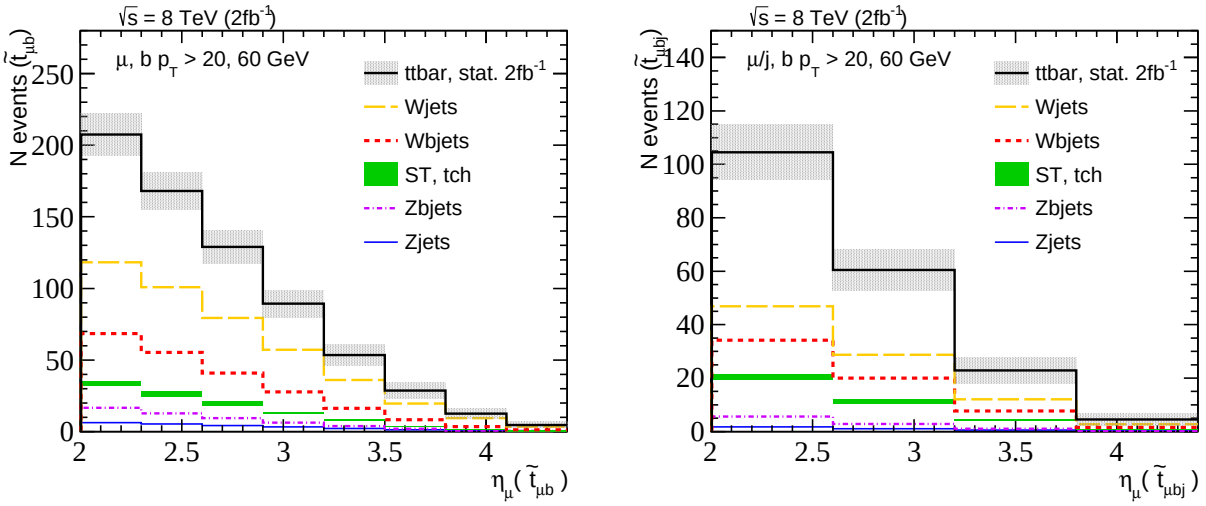


Figure 4.4: Expected signal and background as a function of muon pseudorapidity (lower) at $\sqrt{s} = 8$ TeV with $\int \mathcal{L}dt = 2\text{fb}^{-1}$. Cuts on the b-jet and muon/light jet p_T of 60, 20 GeV are applied to the $\tilde{t}_{\mu b}$ (left) and $\tilde{t}_{\mu bj}$ (right) selections.

efficiencies, this study suggests that performing an analysis in both $\tilde{t}_{\mu b}$ and $\tilde{t}_{\mu bj}$ channels with the 7 and 8 TeV data is worthwhile. Besides providing information about $t\bar{t}$ production at high pseudorapidity, it will be important preparation for high precision studies that will become possible with the expected integrated luminosities at 14 TeV.

The 14 TeV results are presented in Figure 4.5. The number of pseudotop events corresponds to 5 fb^{-1} — the data expected within the first year of running. In the same plot, the statistical precision expected with 50 fb^{-1} is represented by the black fill on the $t\bar{t}$ signal. In both cases, high statistical precision is clearly achievable. It is expected that experimental measurements will therefore be dominated by modelling systematics for both signal and background. Precisely understanding these types of systematics will be necessary to improve experimental accuracy, which ultimately determines how well measurements can be used to test perturbative QCD, and constrain theoretical inputs.

4.3.2 dilepton+jets

In the dilepton channel, selecting the subset of opposite flavour leptons (μe) significantly reduces the contribution from γ/Z background processes. Even with this selection in place, it is also necessary to require the presence of a b-jet which further suppresses the process

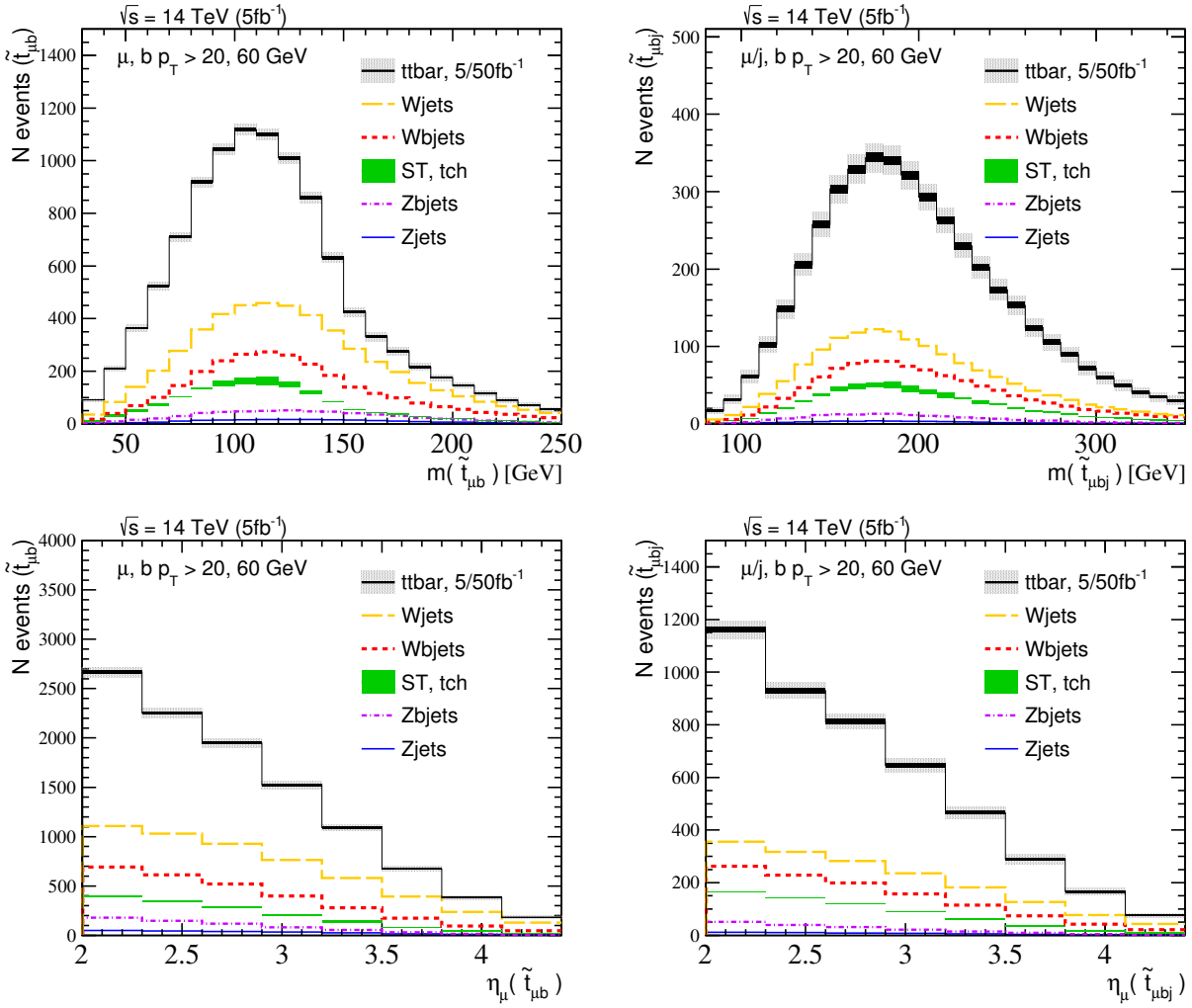


Figure 4.5: Expected signal and background as a function of reconstructed pseudotop ($\tilde{t}_{\mu b(j)}$) invariant mass (upper) and muon pseudorapidity (lower) at $\sqrt{s} = 14$ TeV with $\int \mathcal{L}dt = 5\text{fb}^{-1}$. Cuts on the b-jet and muon/light jet p_T of 60, 20 GeV are applied to the $\tilde{t}_{\mu b}$ (left) and $\tilde{t}_{\mu bj}$ (right) selections. The solid internal fill corresponds to the statistical uncertainty expected with $\int \mathcal{L}dt = 50\text{fb}^{-1}$.

$Z \to (\tau\tau \to \mu eX)$. The other backgrounds are identified as WW, WZ, tW, and QCD. Following the procedure taken for the μ+jets final states, these backgrounds are simulated using `POWHEG` [166, 167] with the central CT10w PDF set, and then subsequently matched to `Pythia8176`.

Signal. The $t\bar{t}$ signal is found by fixing the factorisation and renormalisation scales equal to the top mass ($m_t = 173.25$ GeV). This corresponds to the central cross section evaluated in Table 4.1.

QCD. The QCD background, which is expected to arise from multi jet production, is

not considered in this study. It is possible to account for this background experimentally by using data driven methods: an evaluation of the event rate and kinematic distributions of same sign charged μ and e leptons provides a reliable estimation of the QCD contribution. Internal studies with the 8 TeV data at LHCb indicate that, after isolation and impact parameter cuts, this QCD contribution is expected to be below 10% of the $t\bar{t}$ signal [168]. A careful consideration of control channels for the validation of this method will be necessary when applied at 14 TeV.

Diboson and tW. The ZW process can be accounted for by using the data driven method discussed above. An estimation of WW and tW processes will most likely rely on simulated MC samples which include detector response. These processes have been measured in the central region by both ATLAS and CMS [169–172] and appear to be mostly consistent with NLO predictions. The simulation of the tW process is performed with the Diagram Subtraction method [173]. This method is used to account for the potential interference of the Born level $t\bar{t}$ process with real corrections to tW. An investigation into the validity of this method, in particular when considering exclusive final states with a single b-jet, should be undertaken.

$\boldsymbol{Z \to \tau\tau}$. The fiducial cross section, before applying reconstruction efficiencies, for $\gamma/Z \to (\tau\tau \to \mu e X)$ is estimated to be:

$$\sigma^{\text{LHCb}}_{Z\to(\tau\tau\to\mu eX)} = 796 \text{ fb}\,. \tag{4.4}$$

This is approximately four times larger than the $e\mu$ signal provided in Table 4.1. Due to the long lifetime of τ leptons, this may be suppressed by studying the effect of an impact parameter cut. However, it is found that requiring an additional b-jet within the acceptance, with a p_T cut of 20 GeV, reduces the cross section by a factor of $\approx 10^3$. As this additional requirement reduces the signal expectation by only a factor of two, measurements in this channel should be pursued.

The expected number of pseudotop events expected in 5 fb^{-1} at 14 TeV is presented as a

function of the combined invariant mass of the muon, electron, and b-jet in Figure 4.6. This includes an efficiency for the b-tagging of 70% with a corresponding mis-tag rate of 1%. As this channel is extremely clean, relaxing the mis-tag rate in favour of b-tagging efficiency will improve the statistical precision. Also, it is sufficient to only apply the muon reconstruction efficiency to the μe pair, as this efficiency is mainly due to the trigger.

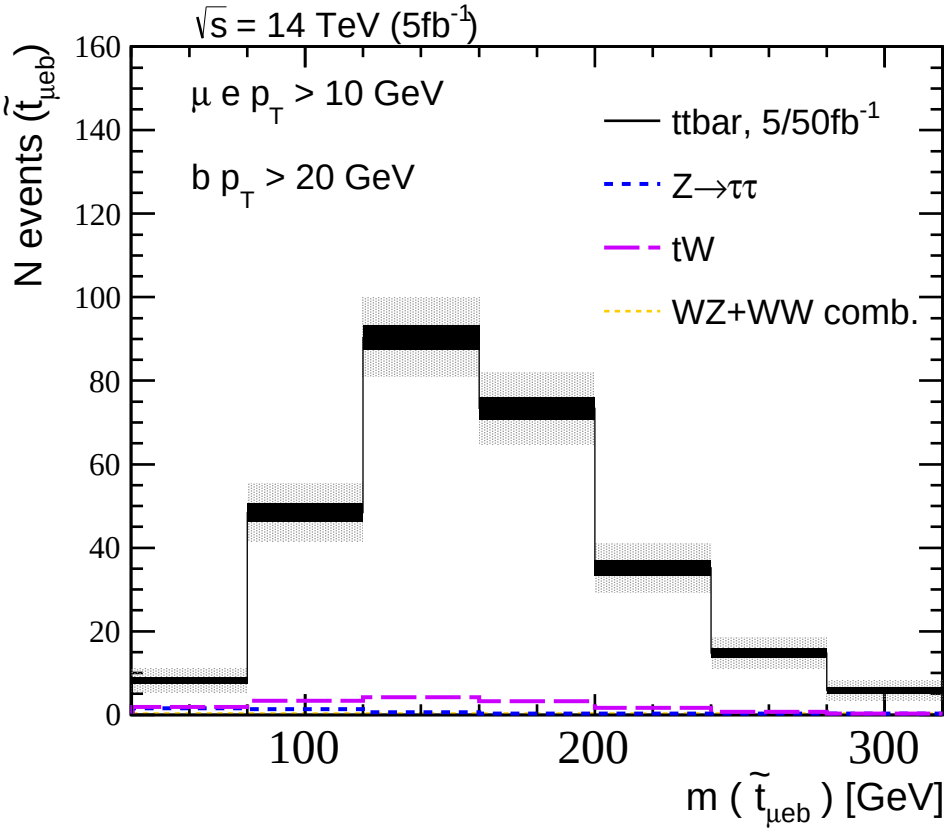


Figure 4.6: Expected signal and background as a function of reconstructed pseudotop ($\tilde{t}_{\mu eb}$) invariant mass at $\sqrt{s} = 14$ TeV with $\int \mathcal{L}dt = 5\text{fb}^{-1}$. Cuts on the b-jet, muon and electron of p_T of 20 GeV are applied in the selection. The solid internal fill corresponds to the statistical uncertainty expected with $\int \mathcal{L}dt = 50\text{fb}^{-1}$.

This channel is extremely clean. It is therefore expected that precision cross section measurements will be possible with 50 fb^{-1} at 14 TeV. This is also a promising channel for performing charge asymmetry measurements, as it is possible to measure the rapidity difference of the lepton pair.

4.4 Constraining the gluon PDF

Given that the $t\bar{t}$ process should be observable with the available 7 and 8 TeV data, and measurements at 14 TeV are expected to achieve high statistical precision, it is important to study the theoretical systematics associated to signal prediction within the LHCb acceptance. This is done by computing the differential cross section at NLO with `MCFM`, and studying how different input parameters impact the prediction within the LHCb acceptance. These results are then compared to a previous study of the inclusive cross section performed at NNLO+NNLL (NNLO*) [174].

Within the first few years of data collection at 14 TeV, measurements in the $\tilde{t}_{\mu b(j)}$ channel will be statistically most precise. Therefore, a corresponding variable is defined as

$$\sigma^{\text{LHCb}} = \int_{\eta=2.0} d\eta \frac{d\sigma^{\tilde{t}}}{d\eta} \,. \tag{4.5}$$

The introduction of this variable will allow a straightforward evaluation of theoretical systematics at fixed-order.

4.4.1 Theoretical systematics

The top quark pair cross section defined in section 3.3.1 depends on: the value of $\alpha_s(m_Z^2)$; PDFs; the top quark mass; and the scale uncertainties associated to unknown higher-order terms. The theoretical uncertainties associated to each of these input parameters are obtained in the following way.

Top quark mass. In accordance with the discussion in Section 3.2.1, the top quark pole mass is assumed to be 173.25 GeV. The dependence of the cross section on the top quark mass is then found by varying m_t in both directions by 1.5 GeV.

PDFs. The following NLO PDF sets are studied: ABM11 5flv (ABM); CT10wnlo (CT10w); HERAPDF1.5 (HERA); MSTW08nlo68cl (MSTW); and NNPDF2.3 (NNPDF), where the central value of $\alpha_s(m_z^2) = 0.118$; 0.118; 0.1176; 0.120; and 0.119 is chosen for each

set respectively. Asymmetric and symmetric uncertainties are found following the discussion in Chapter 2.6. The uncertainties obtained for each PDF collaboration are quoted at 1σ CL, where the CT10w uncertainties, which are provided at 90% CL, have been scaled down by a factor of 1.645. The NNLO* study presented in [174] include the corresponding NNLO PDFs at 1σ CL.

$\alpha_s(Q^2)$. The strong coupling uncertainty (δ_{α_s}) is evaluated by computing a linear fit for the cross section, which is found when varying $\alpha_s(m_Z^2)$ within the range $[0.116, 0.120]$. This range spans the preferred central value for all PDF sets. The uncertainty is then extracted by matching this fit to the current PDG average — as discussed in Section 1.3.4, this is $\alpha_s(m_Z^2) = 0.1184 \pm 0.0007$ [18, 175]. The fitting procedure is demonstrated in Figure 4.7.

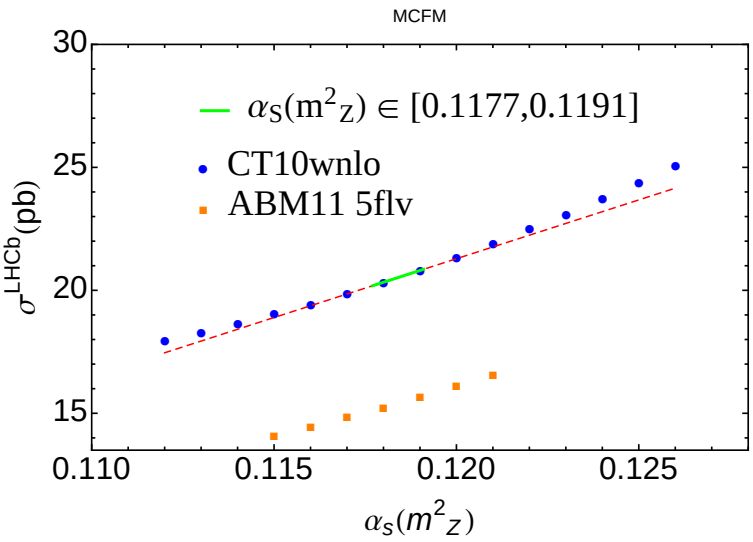


Figure 4.7: Linear fit of $\alpha_s(m_Z^2)$ within the range $\alpha_s(m_Z^2) \in [0.116, 0.120]$ at 7 TeV. The uncertainty is then calculated from this - see text for details.

A linear fit within this range is a good approximation of the expected leading quadratic behaviour. In the case of ABM PDFs, $\alpha_s(m_Z^2)$ is included as a parameter in the fit and an associated uncertainty is therefore already accounted for in the symmetric PDF uncertainty. ABM do however provide a range of PDFs for different values of $\alpha_s(m_Z^2)$; the results obtained from this variation are also included in Figure 4.7 for reference.

Scale. The scale uncertainty (δ_{scale}) is found by varying factorisation and renormalisation scales μ_F and μ_R independently by a factor of two in both directions of the top mass — see

(3.47). The central value is chosen as $\mu_0 = m_t$.

The contribution from each of these sources of systematic uncertainty to the LHCb cross section is evaluated and compared to the inclusive cross section evaluated at NLO and NNLO* [174]. The total uncertainty is found by combining the individual uncertainties following the recommendation of the Higgs Cross Section Working Group [176] as

$$\delta_{\text{total}} = \delta_{\text{scale}} + (\delta^2_{\text{PDF}} + \delta^2_{\alpha_s} + \delta^2_{m_t})^{\frac{1}{2}} . \tag{4.6}$$

The 7 and 14 TeV results are summarised in Tables 4.2 and 4.3 respectively. The NNLO* results are corrected to the chosen top mass range of $m_t \in [171.75, 174.75]$, where it is found that a 1 GeV uncertainty on m_t translates into a 3.0 and 2.7% uncertainty on the cross section at 7 and 14 TeV respectively. Secondly, the absolute shift of cross section (and relative shift) are provided.

Order	PDF	σ(pb)	δ_{scale} (pb)	δ_{PDF} (pb)	δ_{α_s} (pb)	δ_{m_t} (pb)	δ_{total} (pb)
NNLO*(inc.)	ABM	135.8	$^{+3.5}_{-4.2}$ ($^{+2.6\%}_{-3.1\%}$)	$^{+6.4}_{-6.4}$ ($^{+4.7\%}_{-4.7\%}$)	$^{+0.0}_{-0.0}$ ($^{+0.0\%}_{-0.0\%}$)	$^{+6.5}_{-6.3}$ ($^{+4.8\%}_{-4.7\%}$)	$^{+12.7}_{-13.2}$ ($^{+9.3\%}_{-9.7\%}$)
NLO(inc.)		123.5	$^{+14.6}_{-16.1}$ ($^{+11.8\%}_{-13.0\%}$)	$^{+2.3}_{-2.3}$ ($^{+1.9\%}_{-1.9\%}$)	$^{+0.0}_{-0.0}$ ($^{+0.0\%}_{-0.0\%}$)	$^{+5.8}_{-5.7}$ ($^{+4.7\%}_{-4.6\%}$)	$^{+20.8}_{-22.2}$ ($^{+16.9\%}_{-18.0\%}$)
NLO(LHCb)		15.2	$^{+1.9}_{-2.0}$ ($^{+12.4\%}_{-13.0\%}$)	$^{+0.3}_{-0.3}$ ($^{+2.1\%}_{-2.1\%}$)	$^{+0.0}_{-0.0}$ ($^{+0.0\%}_{-0.0\%}$)	$^{+0.8}_{-0.7}$ ($^{+5.0\%}_{-4.9\%}$)	$^{+2.7}_{-2.8}$ ($^{+17.8\%}_{-18.3\%}$)
NNLO*(inc.)	CT10(w)	172.5	$^{+4.6}_{-6.0}$ ($^{+2.7\%}_{-3.5\%}$)	$^{+8.0}_{-6.5}$ ($^{+4.6\%}_{-3.8\%}$)	$^{+3.7}_{-3.7}$ ($^{+2.2\%}_{-2.2\%}$)	$^{+8.0}_{-7.7}$ ($^{+4.6\%}_{-4.4\%}$)	$^{+16.5}_{-16.7}$ ($^{+9.5\%}_{-9.7\%}$)
NLO(inc.)		148.3	$^{+17.6}_{-19.2}$ ($^{+11.9\%}_{-13.0\%}$)	$^{+6.6}_{-6.3}$ ($^{+4.4\%}_{-4.2\%}$)	$^{+2.0}_{-2.0}$ ($^{+1.3\%}_{-1.3\%}$)	$^{+6.8}_{-6.6}$ ($^{+4.6\%}_{-4.4\%}$)	$^{+27.2}_{-28.5}$ ($^{+18.4\%}_{-19.2\%}$)
NLO(LHCb)		19.9	$^{+2.6}_{-2.7}$ ($^{+13.3\%}_{-13.7\%}$)	$^{+1.4}_{-1.1}$ ($^{+6.9\%}_{-5.5\%}$)	$^{+0.3}_{-0.3}$ ($^{+1.6\%}_{-1.6\%}$)	$^{+1.0}_{-0.9}$ ($^{+4.9\%}_{-4.8\%}$)	$^{+4.3}_{-4.2}$ ($^{+21.9\%}_{-21.1\%}$)
NNLO*(inc.)	HERA	177.2	$^{+4.8}_{-4.2}$ ($^{+2.7\%}_{-2.3\%}$)	$^{+4.0}_{-6.4}$ ($^{+2.3\%}_{-3.6\%}$)	$^{+3.0}_{-3.0}$ ($^{+1.7\%}_{-1.7\%}$)	$^{+8.1}_{-7.8}$ ($^{+4.6\%}_{-4.4\%}$)	$^{+14.3}_{-14.7}$ ($^{+8.1\%}_{-8.3\%}$)
NLO(inc.)		136.1	$^{+15.6}_{-16.3}$ ($^{+11.5\%}_{-12.0\%}$)	$^{+3.9}_{-3.4}$ ($^{+2.9\%}_{-2.5\%}$)	$^{+1.3}_{-1.3}$ ($^{+1.0\%}_{-1.0\%}$)	$^{+6.2}_{-6.1}$ ($^{+4.6\%}_{-4.5\%}$)	$^{+23.1}_{-23.3}$ ($^{+16.9\%}_{-17.1\%}$)
NLO(LHCb)		16.9	$^{+2.1}_{-2.0}$ ($^{+12.3\%}_{-12.0\%}$)	$^{+0.5}_{-0.3}$ ($^{+2.9\%}_{-1.6\%}$)	$^{+0.2}_{-0.2}$ ($^{+1.2\%}_{-1.2\%}$)	$^{+0.8}_{-0.8}$ ($^{+4.8\%}_{-4.7\%}$)	$^{+3.0}_{-2.9}$ ($^{+18.0\%}_{-17.1\%}$)
NNLO*(inc.)	MSTW	172.0	$^{+4.4}_{-5.8}$ ($^{+2.6\%}_{-3.4\%}$)	$^{+4.7}_{-4.7}$ ($^{+2.7\%}_{-2.7\%}$)	$^{+2.9}_{-2.9}$ ($^{+1.7\%}_{-1.7\%}$)	$^{+8.0}_{-7.7}$ ($^{+4.6\%}_{-4.4\%}$)	$^{+14.1}_{-15.2}$ ($^{+8.2\%}_{-8.9\%}$)
NLO(inc.)		158.4	$^{+19.6}_{-21.2}$ ($^{+12.4\%}_{-13.4\%}$)	$^{+4.0}_{-5.5}$ ($^{+2.6\%}_{-3.4\%}$)	$^{+2.1}_{-2.1}$ ($^{+1.3\%}_{-1.3\%}$)	$^{+7.2}_{-7.0}$ ($^{+4.6\%}_{-4.5\%}$)	$^{+28.1}_{-30.4}$ ($^{+17.7\%}_{-19.2\%}$)
NLO(LHCb)		20.8	$^{+2.9}_{-2.9}$ ($^{+13.9\%}_{-14.2\%}$)	$^{+0.7}_{-0.9}$ ($^{+3.2\%}_{-4.2\%}$)	$^{+0.3}_{-0.3}$ ($^{+1.5\%}_{-1.5\%}$)	$^{+1.0}_{-1.0}$ ($^{+4.8\%}_{-4.8\%}$)	$^{+4.1}_{-4.3}$ ($^{+19.9\%}_{-20.8\%}$)
NNLO*(inc.)	NNPDF	172.7	$^{+4.6}_{-6.0}$ ($^{+2.7\%}_{-3.5\%}$)	$^{+5.2}_{-5.2}$ ($^{+3.0\%}_{-3.0\%}$)	$^{+2.7}_{-2.7}$ ($^{+1.6\%}_{-1.6\%}$)	$^{+8.0}_{-7.8}$ ($^{+4.6\%}_{-4.5\%}$)	$^{+14.5}_{-15.8}$ ($^{+8.4\%}_{-9.1\%}$)
NLO(inc.)		158.7	$^{+19.6}_{-20.2}$ ($^{+12.4\%}_{-12.7\%}$)	$^{+4.0}_{-4.0}$ ($^{+2.5\%}_{-2.5\%}$)	$^{+2.3}_{-2.3}$ ($^{+1.5\%}_{-1.5\%}$)	$^{+7.3}_{-7.1}$ ($^{+4.6\%}_{-4.5\%}$)	$^{+27.2}_{-28.5}$ ($^{+17.8\%}_{-18.1\%}$)
NLO(LHCb)		20.2	$^{+2.8}_{-2.7}$ ($^{+14.0\%}_{-13.3\%}$)	$^{+0.7}_{-0.7}$ ($^{+3.4\%}_{-3.4\%}$)	$^{+0.4}_{-0.4}$ ($^{+1.8\%}_{-1.8\%}$)	$^{+1.0}_{-0.9}$ ($^{+4.9\%}_{-4.8\%}$)	$^{+4.1}_{-3.9}$ ($^{+20.2\%}_{-19.4\%}$)

Table 4.2: Summary of inclusive (inc.) and differential NLO(LHCb) cross sections, and associated uncertainty, at 7 TeV. The inclusive cross sections are provided at both NLO, and NNLO+NLLL (NNLO*).

The scale uncertainties exhibit a small dependence on pseudorapidity, due to differences in the physical scale Q^2 for forward events. This also applies to the top quark mass uncertainty. The PDF uncertainties increase with pseudorapidity, as events produced from both very high- and low-x partons probe PDFs which are not well constrained. There is also a pseudorapidity dependence of $\alpha_s(Q^2)$ which arises from uncertainty in the gluon PDF indirectly — an increase in $\alpha_s(Q^2)$ leads to a smaller gluon PDF at lower values of x while momentum sum rules compensate this by increasing the gluon PDF at large x, resulting in a pseudorapidity dependent uncertainty. The PDF and $\alpha_s(Q^2)$ uncertainties are relatively large in comparison to the corresponding uncertainties at 14 TeV. This is due to Bjorken scaling, which results in events at 14 TeV sampling the PDFs at more moderate-x values, where PDFs are more constrained.

Order	PDF	σ(pb)	δ_{scale} (pb)	δ_{PDF} (pb)	δ_{α_s} (pb)	δ_{m_t} (pb)	δ_{total} (pb)
NNLO*(inc.)	ABM	832.0	$^{+18.7}_{-27.4}$ $^{(+2.2\%)}_{(-3.3\%)}$	$^{+25.1}_{-25.1}$ $^{(+3.0\%)}_{(-3.0\%)}$	$^{+0.0}_{-0.0}$ $^{(+0.0\%)}_{(-0.0\%)}$	$^{+34.9}_{-33.7}$ $^{(+4.2\%)}_{(-4.1\%)}$	$^{+61.7}_{-69.7}$ $^{(+7.4\%)}_{(-8.4\%)}$
NLO(inc.)		771.9	$^{+91.0}_{-92.4}$ $^{(+11.8\%)}_{(-12.0\%)}$	$^{+9.4}_{-9.4}$ $^{(+1.2\%)}_{(-1.2\%)}$	$^{+0.0}_{-0.0}$ $^{(+0.0\%)}_{(-0.0\%)}$	$^{+32.3}_{-31.9}$ $^{(+4.2\%)}_{(-4.1\%)}$	$^{+124.7}_{-125.7}$ $^{(+16.1\%)}_{(-16.3\%)}$
NLO(LHCb)		117.2	$^{+14.5}_{-14.1}$ $^{(+12.3\%)}_{(-12.0\%)}$	$^{+2.0}_{-2.0}$ $^{(+1.7\%)}_{(-1.7\%)}$	$^{+0.0}_{-0.0}$ $^{(+0.0\%)}_{(-0.0\%)}$	$^{+5.2}_{-5.1}$ $^{(+4.4\%)}_{(-4.3\%)}$	$^{+20.0}_{-19.5}$ $^{(+17.1\%)}_{(-16.7\%)}$
NNLO*(inc.)	CT10(w)	952.8	$^{+23.3}_{-34.5}$ $^{(+2.4\%)}_{(-3.6\%)}$	$^{+22.4}_{-19.9}$ $^{(+2.3\%)}_{(-2.1\%)}$	$^{+14.0}_{-14.0}$ $^{(+1.5\%)}_{(-1.5\%)}$	$^{+39.2}_{-37.8}$ $^{(+4.1\%)}_{(-4.0\%)}$	$^{+70.6}_{-79.5}$ $^{(+7.4\%)}_{(-8.3\%)}$
NLO(inc.)		832.6	$^{+97.0}_{-96.7}$ $^{(+11.7\%)}_{(-11.6\%)}$	$^{+19.6}_{-20.2}$ $^{(+2.4\%)}_{(-2.4\%)}$	$^{+9.2}_{-9.2}$ $^{(+1.1\%)}_{(-1.1\%)}$	$^{+34.0}_{-33.3}$ $^{(+4.1\%)}_{(-4.0\%)}$	$^{+137.4}_{-136.6}$ $^{(+16.5\%)}_{(-16.4\%)}$
NLO(LHCb)		137.0	$^{+16.7}_{-16.4}$ $^{(+12.2\%)}_{(-12.0\%)}$	$^{+5.0}_{-4.6}$ $^{(+3.6\%)}_{(-3.4\%)}$	$^{+1.8}_{-1.8}$ $^{(+1.3\%)}_{(-1.3\%)}$	$^{+5.9}_{-5.8}$ $^{(+4.3\%)}_{(-4.2\%)}$	$^{+24.7}_{-24.0}$ $^{(+18.0\%)}_{(-17.5\%)}$
NNLO*(inc.)	HERA	970.5	$^{+22.1}_{-22.0}$ $^{(+2.3\%)}_{(-2.3\%)}$	$^{+15.7}_{-25.7}$ $^{(+1.6\%)}_{(-2.6\%)}$	$^{+12.8}_{-12.8}$ $^{(+1.3\%)}_{(-1.3\%)}$	$^{+39.6}_{-38.4}$ $^{(+4.1\%)}_{(-4.0\%)}$	$^{+66.6}_{-70.0}$ $^{(+6.9\%)}_{(-7.2\%)}$
NLO(inc.)		804.2	$^{+91.9}_{-87.6}$ $^{(+11.4\%)}_{(-10.9\%)}$	$^{+16.1}_{-21.9}$ $^{(+2.0\%)}_{(-2.7\%)}$	$^{+5.3}_{-5.3}$ $^{(+0.7\%)}_{(-0.7\%)}$	$^{+33.4}_{-32.4}$ $^{(+4.1\%)}_{(-4.0\%)}$	$^{+129.3}_{-127.1}$ $^{(+16.1\%)}_{(-15.8\%)}$
NLO(LHCb)		124.7	$^{+14.8}_{-13.7}$ $^{(+11.8\%)}_{(-11.0\%)}$	$^{+3.0}_{-3.0}$ $^{(+2.4\%)}_{(-2.4\%)}$	$^{+1.1}_{-1.1}$ $^{(+0.9\%)}_{(-0.9\%)}$	$^{+5.5}_{-5.3}$ $^{(+4.4\%)}_{(-4.3\%)}$	$^{+21.1}_{-19.9}$ $^{(+16.9\%)}_{(-15.9\%)}$
NNLO*(inc.)	MSTW	953.6	$^{+22.7}_{-33.9}$ $^{(+2.4\%)}_{(-3.6\%)}$	$^{+16.2}_{-17.8}$ $^{(+1.7\%)}_{(-1.9\%)}$	$^{+12.8}_{-12.8}$ $^{(+1.3\%)}_{(-1.3\%)}$	$^{+39.1}_{-37.9}$ $^{(+4.1\%)}_{(-4.0\%)}$	$^{+66.9}_{-77.7}$ $^{(+7.0\%)}_{(-8.1\%)}$
NLO(inc.)		885.6	$^{+107.2}_{-105.7}$ $^{(+12.1\%)}_{(-11.9\%)}$	$^{+16.0}_{-19.4}$ $^{(+1.8\%)}_{(-2.2\%)}$	$^{+10.1}_{-10.1}$ $^{(+1.1\%)}_{(-1.1\%)}$	$^{+36.2}_{-35.3}$ $^{(+4.1\%)}_{(-4.0\%)}$	$^{+148.1}_{-147.3}$ $^{(+16.7\%)}_{(-16.6\%)}$
NLO(LHCb)		144.4	$^{+18.6}_{-17.8}$ $^{(+12.8\%)}_{(-12.3\%)}$	$^{+3.5}_{-3.9}$ $^{(+2.4\%)}_{(-2.7\%)}$	$^{+1.9}_{-1.9}$ $^{(+1.3\%)}_{(-1.3\%)}$	$^{+6.2}_{-6.1}$ $^{(+4.3\%)}_{(-4.2\%)}$	$^{+25.9}_{-25.2}$ $^{(+18.0\%)}_{(-17.5\%)}$
NNLO*(inc.)	NNPDF	977.5	$^{+23.6}_{-35.4}$ $^{(+2.4\%)}_{(-3.6\%)}$	$^{+16.4}_{-16.4}$ $^{(+1.7\%)}_{(-1.7\%)}$	$^{+12.2}_{-12.2}$ $^{(+1.3\%)}_{(-1.3\%)}$	$^{+40.4}_{-39.1}$ $^{(+4.1\%)}_{(-4.0\%)}$	$^{+68.9}_{-80.0}$ $^{(+7.0\%)}_{(-8.1\%)}$
NLO(inc.)		894.5	$^{+107.6}_{-101.0}$ $^{(+12.0\%)}_{(-11.3\%)}$	$^{+12.8}_{-12.8}$ $^{(+1.4\%)}_{(-1.4\%)}$	$^{+9.9}_{-9.9}$ $^{(+1.1\%)}_{(-1.1\%)}$	$^{+36.6}_{-35.8}$ $^{(+4.1\%)}_{(-4.0\%)}$	$^{+147.6}_{-140.3}$ $^{(+16.5\%)}_{(-15.7\%)}$
NLO(LHCb)		142.5	$^{+18.1}_{-16.6}$ $^{(+12.7\%)}_{(-11.7\%)}$	$^{+3.0}_{-3.0}$ $^{(+2.1\%)}_{(-2.1\%)}$	$^{+2.0}_{-2.0}$ $^{(+1.4\%)}_{(-1.4\%)}$	$^{+6.2}_{-6.1}$ $^{(+4.4\%)}_{(-4.3\%)}$	$^{+25.2}_{-23.7}$ $^{(+17.7\%)}_{(-16.6\%)}$

Table 4.3: Summary of inclusive (inc.) and differential NLO(LHCb) cross sections, and associated uncertainty, at 14 TeV. The inclusive cross sections are provided at both NLO, and NNLO+NLLL (NNLO*).

The LHCb cross section and theoretical uncertainties are summarised in Figure 4.8. For both 7 (left) and 14 TeV (right) results, the inner and outer error bars correspond to the

scale and total uncertainties respectively.

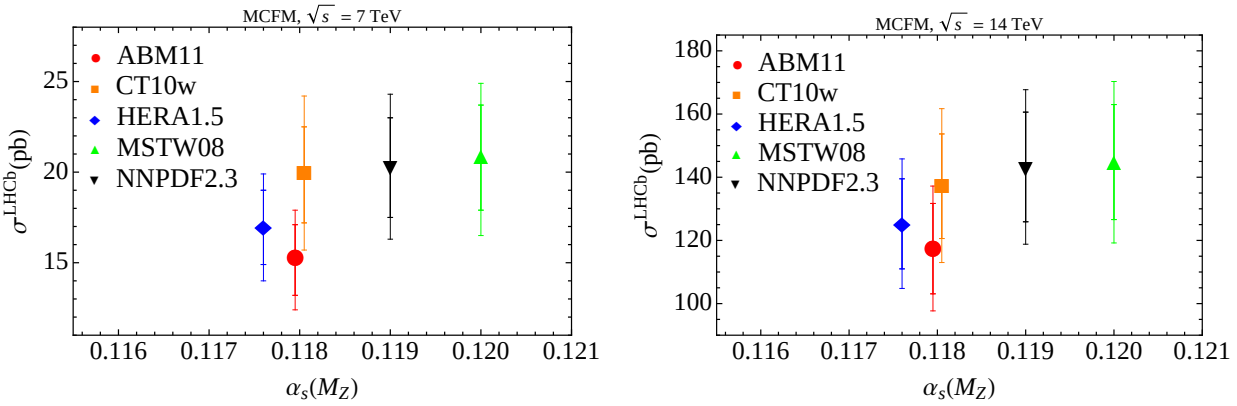


Figure 4.8: Summary of NLO cross section predictions within the LHCb fiducial region at $\sqrt{s} = 7$ (left) and 14 TeV (right). The inner and outer error bars correspond to the scale and total uncertainties respectively.

The enhanced sensitivity of measurements at high pseudorapidity can be evaluated by comparing the relative uncertainties of the NLO inclusive and differential LHCb cross section. This comparison is performed by taking the ratio of the relative uncertainties

$$\delta_X^{\mathrm{ratio}} = \frac{\delta_X^{\mathrm{LHCb}}}{\delta_X^{NLO}} \,. \tag{4.7}$$

These ratios at 7 (left) and 14 TeV (right) are summarised in Table 4.4. This ratio highlights the sensitivity of cross section measurements at LHCb to PDF uncertainties, in particular to the CT10w and NNPDF sets.

7 TeV	$\delta^{\mathrm{ratio}}_{\mathrm{scale}}$	$\delta^{\mathrm{ratio}}_{\mathrm{PDF}}$	$\delta^{\mathrm{ratio}}_{\alpha_s}$	$\delta^{\mathrm{ratio}}_{m_t}$	$\delta^{\mathrm{ratio}}_{\mathrm{total}}$
ABM	$^{+1.05}_{-1.00}$	$^{+1.11}_{-1.11}$	$^{+0.00}_{-0.00}$	$^{+1.06}_{-1.06}$	$^{+1.05}_{-1.02}$
CT10w	$^{+1.12}_{-1.06}$	$^{+1.56}_{-1.30}$	$^{+1.23}_{-1.23}$	$^{+1.07}_{-1.07}$	$^{+1.19}_{-1.10}$
HERA	$^{+1.07}_{-1.01}$	$^{+1.01}_{-0.65}$	$^{+1.25}_{-1.25}$	$^{+1.05}_{-1.06}$	$^{+1.06}_{-1.00}$
MSTW	$^{+1.12}_{-1.06}$	$^{+1.27}_{-1.23}$	$^{+1.13}_{-1.13}$	$^{+1.06}_{-1.08}$	$^{+1.12}_{-1.08}$
NNPDF	$^{+1.13}_{-1.05}$	$^{+1.34}_{-1.34}$	$^{+1.21}_{-1.21}$	$^{+1.07}_{-1.07}$	$^{+1.13}_{-1.08}$

14 TeV	$\delta^{\mathrm{ratio}}_{\mathrm{scale}}$	$\delta^{\mathrm{ratio}}_{\mathrm{PDF}}$	$\delta^{\mathrm{ratio}}_{\alpha_s}$	$\delta^{\mathrm{ratio}}_{m_t}$	$\delta^{\mathrm{ratio}}_{\mathrm{total}}$
ABM	$^{+1.05}_{-1.00}$	$^{+1.40}_{-1.40}$	$^{+0.00}_{-0.00}$	$^{+1.05}_{-1.05}$	$^{+1.06}_{-1.02}$
CT10w	$^{+1.05}_{-1.03}$	$^{+1.55}_{-1.40}$	$^{+1.20}_{-1.20}$	$^{+1.06}_{-1.05}$	$^{+1.09}_{-1.07}$
HERA	$^{+1.04}_{-1.01}$	$^{+1.19}_{-0.90}$	$^{+1.33}_{-1.33}$	$^{+1.07}_{-1.06}$	$^{+1.05}_{-1.01}$
MSTW	$^{+1.06}_{-1.03}$	$^{+1.35}_{-1.23}$	$^{+1.13}_{-1.13}$	$^{+1.05}_{-1.06}$	$^{+1.07}_{-1.05}$
NNPDF	$^{+1.05}_{-1.03}$	$^{+1.45}_{-1.45}$	$^{+1.27}_{-1.27}$	$^{+1.07}_{-1.07}$	$^{+1.07}_{-1.06}$

Table 4.4: Ratio of LHCb and inclusive NLO cross section uncertainties at 7 (left) and 14 TeV (right).

It is noted that the prediction obtained with ABM PDFs is substantially lower for both inclusive and differential predictions. At NNLO this can be understood from both a lower value for $\alpha_s(m_Z^2)$ and a softer gluon PDF at large-x [174,177]. At NLO, even for an identical

best fit value $\alpha_s(m_Z^2)$, the prediction from ABM is substantially lower than CT10w, as shown in Figure 4.7. In fact, the discrepancy between the central value of ABM and the other PDF groups is enhanced at high pseudorapidity.

The scale uncertainty provides the dominant contribution to the total uncertainty at NLO. However, given the recent theoretical advances in top quark pair production predictions, it is clear that a cross section measurement in the forward region can be used to constrain PDFs when a differential NNLO calculation is available. It is expected that the large ratio of the relative PDF uncertainties between inclusive and LHCb measurements will still be present at NNLO. This is supported by the comparison of the relative PDF and α_s uncertainties of the evolved gluon distribution between NLO and NNLO shown in Figure 4.9. This is also supported by approximate differential NNLO studies performed in [178].

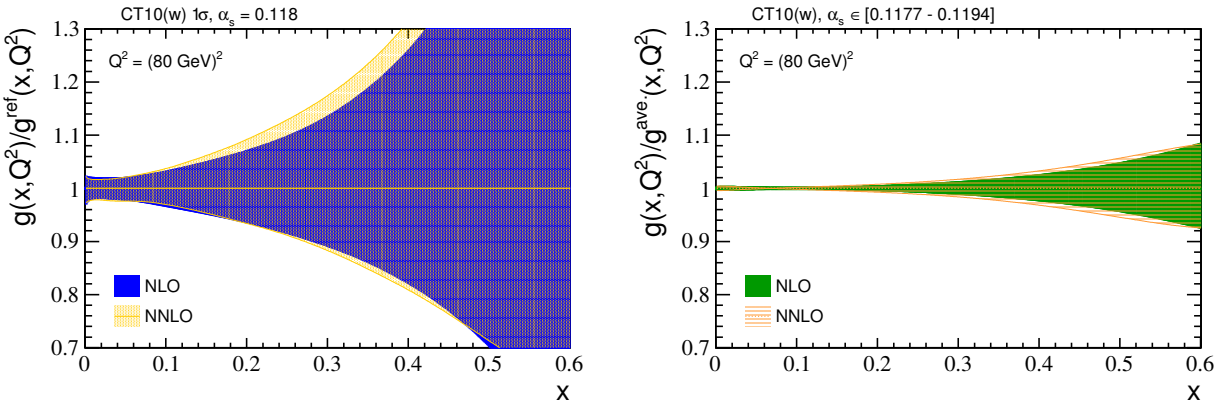


Figure 4.9: Relative uncertainty on the gluon PDF for CT10(w) NLO and NNLO sets for PDF and α_s variations.

Computing the theoretical uncertainties at 8 TeV will also be necessary when performing the experimental measurement. However, as the process of computing these uncertainties is computationally expensive, it is not worth performing this study until the experimental analysis is finalised. At this stage it will become more clear how a comparison to the experimental measurement should be performed.

4.4.2 Reweighting analysis

Due to the high statistical precision expected within one year of running (5 fb^{-1}) at 14 TeV, a differential measurement in bins of pseudorapidity across the entire LHCb acceptance is viable. To demonstrate the potential power of such a measurement on constraining PDFs, the reweighting technique discussed in Section 2.6.2 is applied to both the Hessian CT10w and replica NNPDF PDFs. The reweighting is performed in the cross section basis under the assumption of a hypothetical measurement of σ^{LHCb} (pseudodata) provided at the top quark level.

To apply the reweighting procedure to the Hessian set, it is first necessary to generate a set of random replicas. This is done simultaneously in the basis of σ^{LHCb} as well as the evolved gluon PDF. The weights of these replica members, calculated as a result of including the pseudodata, can then be applied to the evolved gluon PDF to quantify the improved constraints. For both NNPDF and CT10w reweighting, the value of the hypothetical measurement is generated from the prediction evaluated using the central PDF member as

$$\bar{\sigma}_0^{\text{LHCb}} = \frac{1}{N_{\text{rep}}} \sum_{k=1}^{N_{\text{rep}}} \sigma^{\text{LHCb}}(\mathcal{S}_0)[1 + R_{k0}], \tag{4.8}$$

where R_{k0} is a pseudorandom gaussian-distributed number with zero mean and variance of one. The effect of reweighting both NNPDF and CT10w PDF replica sets when pseudodata is generated from a different central PDF member will also be discussed. For the CT10w and NNPDF replica sets studied, the number of replicas are 1000 and 100 respectively.

In Figure 4.10, the generated CT10w replica set is compared to the original Hessian result at the level of the evolved gluon PDF $g(x, Q^2)$. The two parameterisations provide a similar description of the PDF central value and associated uncertainty, the only exception being at large-x where the PDF uncertainties are most asymmetric. Therefore, applying the reweighting technique to Hessian sets provides an estimate of how including new data into a global fit should improve constraints.

To apply the reweighting to the replica sets at the level of σ^{LHCb}, it is necessary to

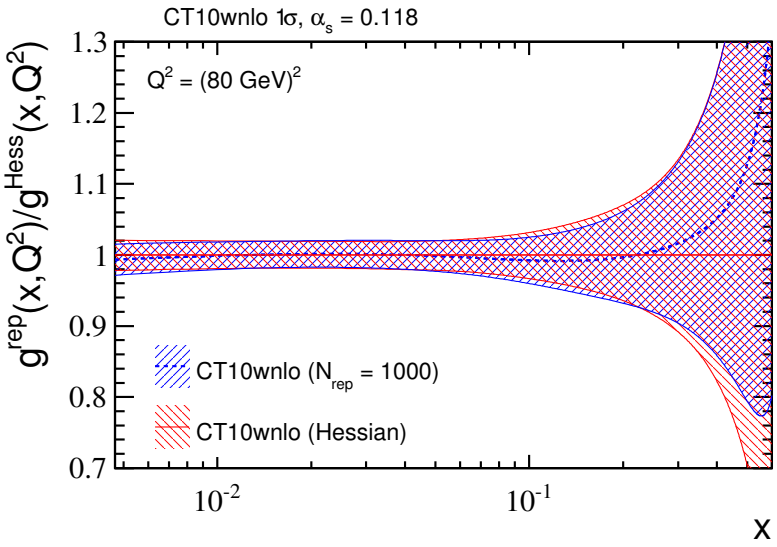


Figure 4.10: Relative uncertainty on CT10w NLO gluon PDF $g(x, Q^2)$ for both replica and Hessian sets shown with respect to the central Hessian member.

assume an experimental uncertainty on the pseudodata. Given that current cross section measurements by ATLAS [179] have already achieved a total relative uncertainty below 5%, it is not unreasonable to expect similar precision from measurements with the upgraded LHCb detector. Therefore, the reweighting is performed with an assumed experimental uncertainty within the range of 4-8%.

Performing the reweighting procedure for both replica sets results in a reduced number of effective replicas provided in Table 4.5. As the pseudodata is close to the central member prediction by construction, the effective number of replicas is not dramatically altered.

PDF	$\bar{\sigma}_0^{\text{LHCb}}$(pb)	Exp. uncertainty	N_{rep}	N_{eff}
CT10	137.3	4%	1000	942
		6%	1000	983
		8%	1000	994
NNPDF	145.1	4%	100	97
		6%	100	99
		8%	100	100

Table 4.5: Effective replicas after reweighting with the inclusion of an LHCb cross section measurement at 14 TeV. An experimental uncertainty within the range 4-8% is assumed.

The effect of this reweighting on the evolved gluon PDF is presented in Figure 4.11

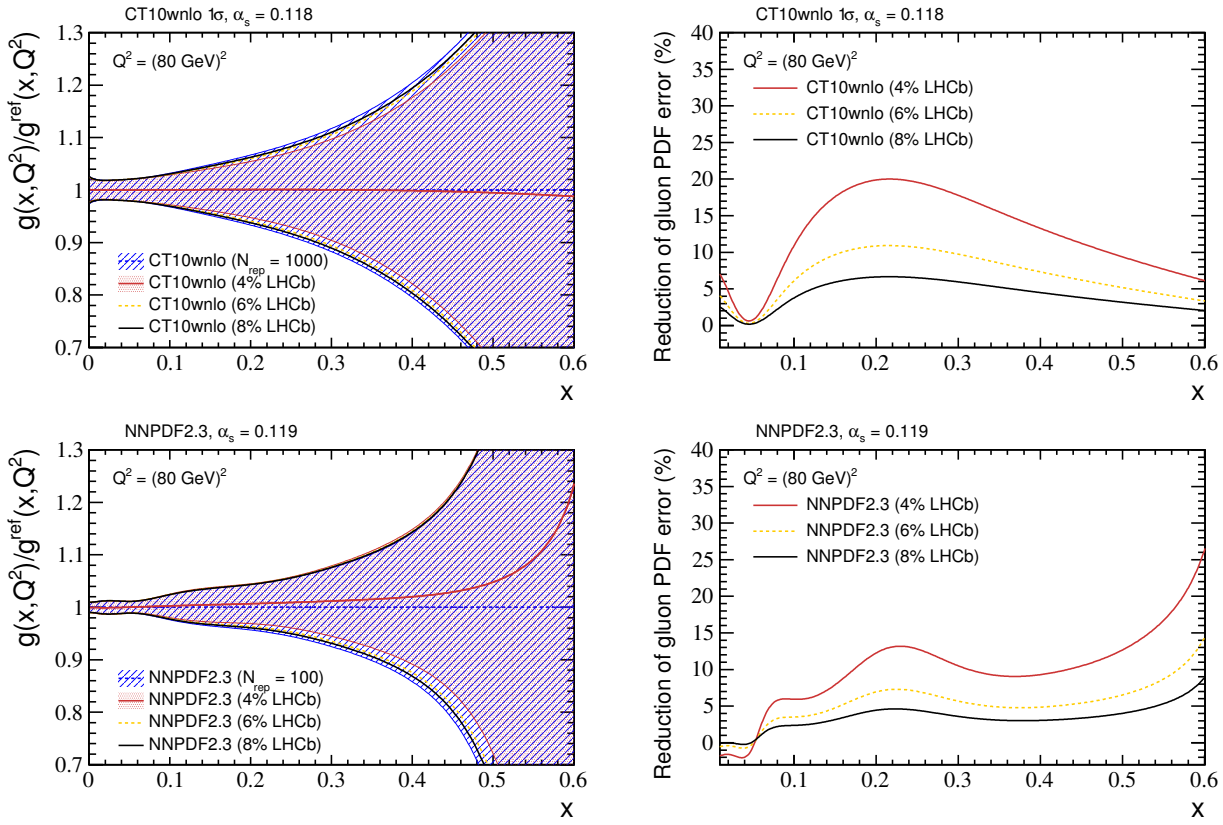


Figure 4.11: Potential constraint (left) on the gluon PDF for CT10wnlo (upper) and NNPDF2.3 (lower) replica sets with the inclusion of an LHCb cross section measurement at 14 TeV. An experimental uncertainty within the range 4-8% is assumed. The corresponding reduction of the PDF uncertainty is also shown (right).

for CT10w (upper) and NNPDF (lower) replica sets. On the left, the relative uncertainty of the gluon PDF with respect to the unweighted PDF ($g^{\text{ref}}(x, Q^2)$) is shown for assumed experimental uncertainties of 4, 6, and 8%. On the right, the relative reduction of the gluon PDF uncertainty for the same range of experimental uncertainties is shown.

The largest sensitivity is observed to be within the range of $0.1 < x < 0.3$. The experimental precision achievable with cross section measurements at LHCb will therefore have a large impact on future PDF fits within this range. To demonstrate how a cross section measurement may impact the PDF central value, it is necessary to generate pseudodata which is slightly displaced from the central value. This is done by generating the pseudodata with the HERA central value member. In this case, the effective number of replicas after reweighting does change significantly. The corresponding results are presented in Table 4.6.

The effect of the reweighting on the evolved gluon PDF with the HERA generated pseu-

PDF	$\bar{\sigma}_0^{\text{LHCb}}$(pb)	Exp. uncertainty	N_{rep}	N_{eff}
CT10	129.5	4%	1000	720
		6%	1000	895
		8%	1000	956
NNPDF	129.5	4%	100	53
		6%	100	85
		8%	100	95

Table 4.6: Effective replicas after reweighting with the inclusion of an LHCb cross section measurement generated from the HERA1.5 central value, the associated experimental uncertainty is within the range 4-8%.

dodata is shown in Figure 4.12. The results with an assumed experimental uncertainty of 6% have been omitted to improve visibility. The shift in the PDF with respect to the central value is clearly visible even with the conservative estimate of 8% uncertainty.

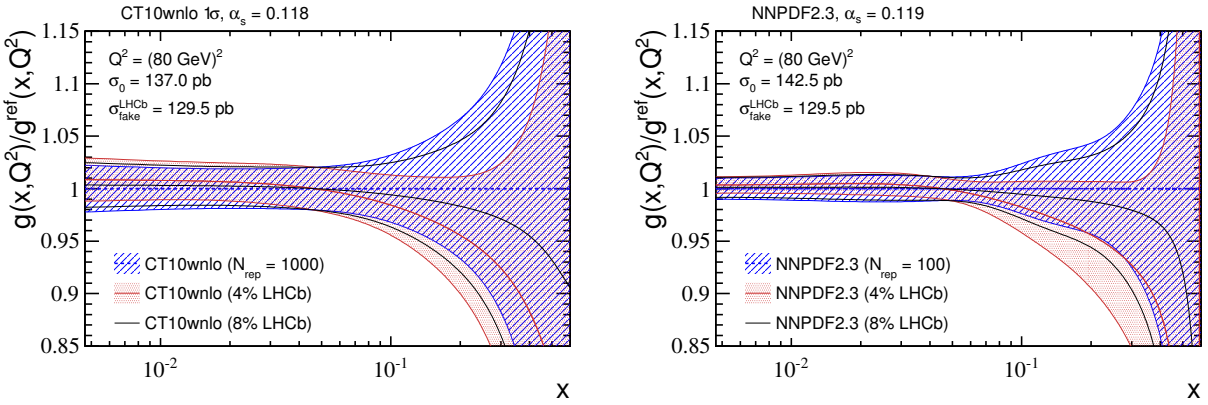


Figure 4.12: Potential shift in central value of the evolved gluon PDF for CT10wnlo (left) and NNPDF2.3 (right) after reweighting with respect to pseudodata generated from HERA1.5. The 1σ CL uncertainties are also included.

The sensitivity of top quark measurements at LHCb to particular eigenvectors can also be quantified. This is done by comparing the relative departure of each PDF member (corresponding to a particular eigenvector n and its direction) with respect to the central member as

$$\Delta\sigma_j^{\text{LHCb}} = \frac{\sigma^{\text{LHCb}}(\mathcal{S}_j) - \sigma^{\text{LHCb}}(\mathcal{S}_0)}{\sigma^{\text{LHCb}}(\mathcal{S}_0)}\,, \tag{4.9}$$

where the index j runs over the $2n$ eigenvector members. The relative deviations for the four studied Hessian PDF sets are shown in Figure 4.13.

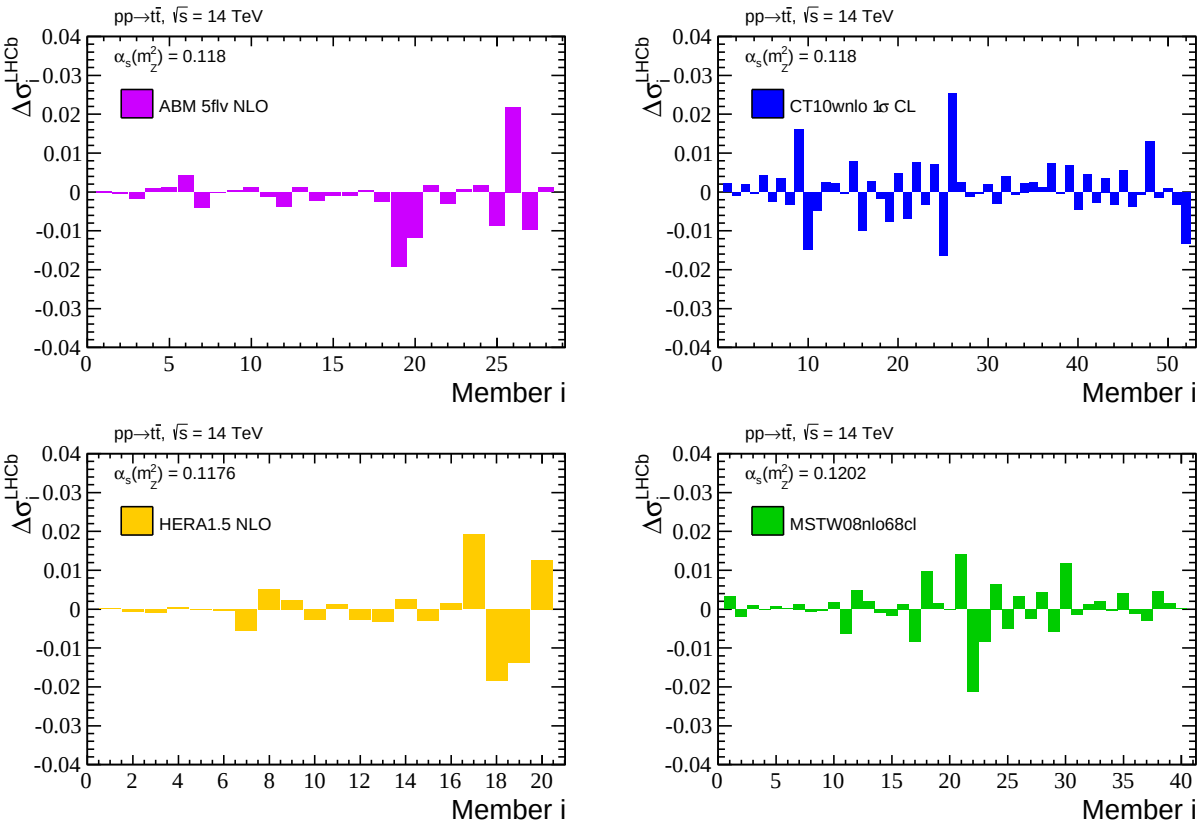


Figure 4.13: Relative departure of each PDF member from the central value for the prediction of σ^{LHCb} at 14 TeV.

The large displacements observed for particular PDF members can generally be traced to large displacements in the gluon PDF. However, some of these PDF members also have moderate displacements in the u and d PDF content at large x. As an example, eigenvector 13 (members 25 and 26) of CT10w exhibits a particularly large deviation. For reference, the evolved gluon, u, and d PDF content is plotted with respect to the central member in Figure 4.14 (left). The same PDFs are also plotted for HERA eigenvector 10 in Figure 4.14 (right). In the case of the HERA eigenvector, this demonstrates that the deviation is not necessarily due to the gluon PDF alone, but may also provide constraints on the valence content.

4.4.3 Potential sensitivity

It should be noted, that the displacements presented for each Hessian PDF set in Figure 4.13 are unique to exclusive high pseudorapidity measurements. Although an analysis of the

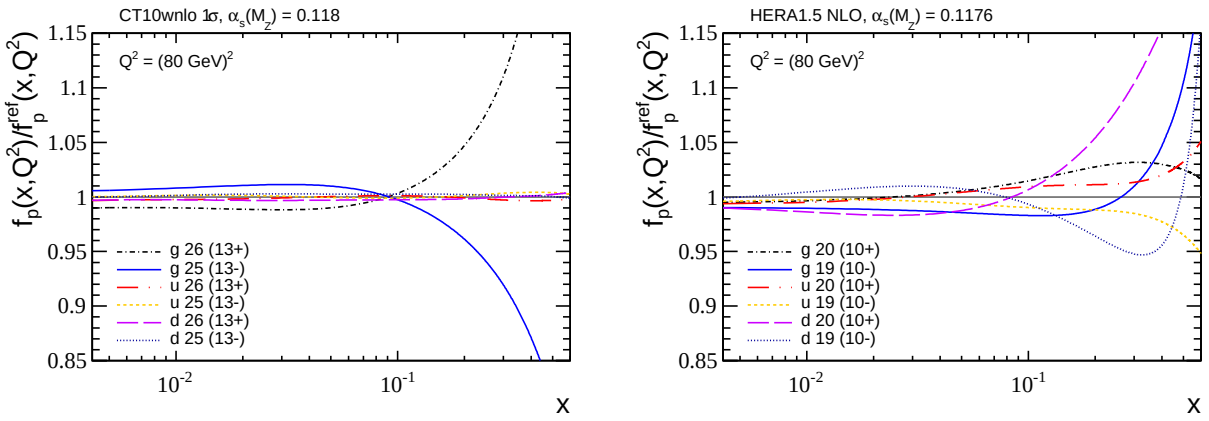


Figure 4.14: Ratio of evolved quark and gluon PDFs ($f_p(x, Q^2)$) with respect to their corresponding central value for selected members, as described in the text.

inclusive cross section is also sensitive to the gluon PDF [174], a lot of information is lost in such a study. As an example, the relative pseudorapidity cross section simulated with POWHEG with the CT10w eigenvector 13 is shown in Figure 4.15 (left).

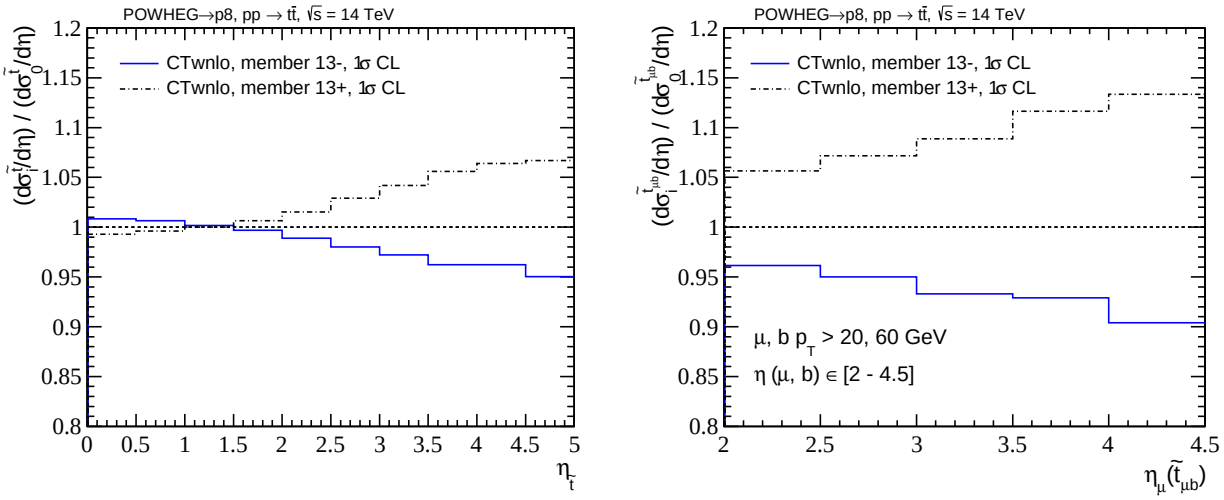


Figure 4.15: Ratio of pseudotop (left) and $\tilde{t}_{\mu b}$ (right) differential cross-sections for CT10wnlo eigenvector 13 with respect to the central value.

For the negative eigenvector direction, the cross section deviation is positive at low pseudorapidity, and negative at high pseudorapidity. The opposite behaviour is observed for the positive eigenvector direction. Therefore, there is partial cancellation across the entire phase space, reducing the sensitivity of comparisons to inclusive cross section measurements. As measurements of forwardly produced top quarks at 14 TeV are sensitive to the gluon PDF much beyond $x = 0.1$, they will provide useful constraints for several eigenvectors in this region.

Although it is clear that top quark measurements at LHCb will provide useful constraints on the PDFs, performing an analysis at the top quark level is naive, as this does not correspond to what can be experimentally measured at LHCb. Fully quantifying the sensitivity of measurements at LHCb requires knowledge of the eventual analysis cuts, and a corresponding study of all PDF members at NLO+PS with these cuts applied.

To estimate the effect of analysis cuts, the ratio of differential cross section for the $\tilde{t}_{\mu b}$ with analysis cuts applied is presented in Figure 4.15 (right). Only CT10w eigenvector 13 is studied, and the analysis cuts were defined in Section 4.3.1. When the analysis cuts are applied, the sensitivity to the high-x region of the PDFs increases as events are more likely to have been produced from partons at higher x_1. This is also demonstrated in Figure 4.16, where the incoming parton momentum fraction is plotted against the POWHEG event momentum scale squared (Q^2). The left plot corresponds to events in which a parton level top quark is within the LHCb acceptance, and the right plot corresponds to events passing the analysis cuts. Clearly, a larger fraction of events remain at high x_1 ($\langle x_1 \rangle = 0.28$) after the analysis cuts have been applied.

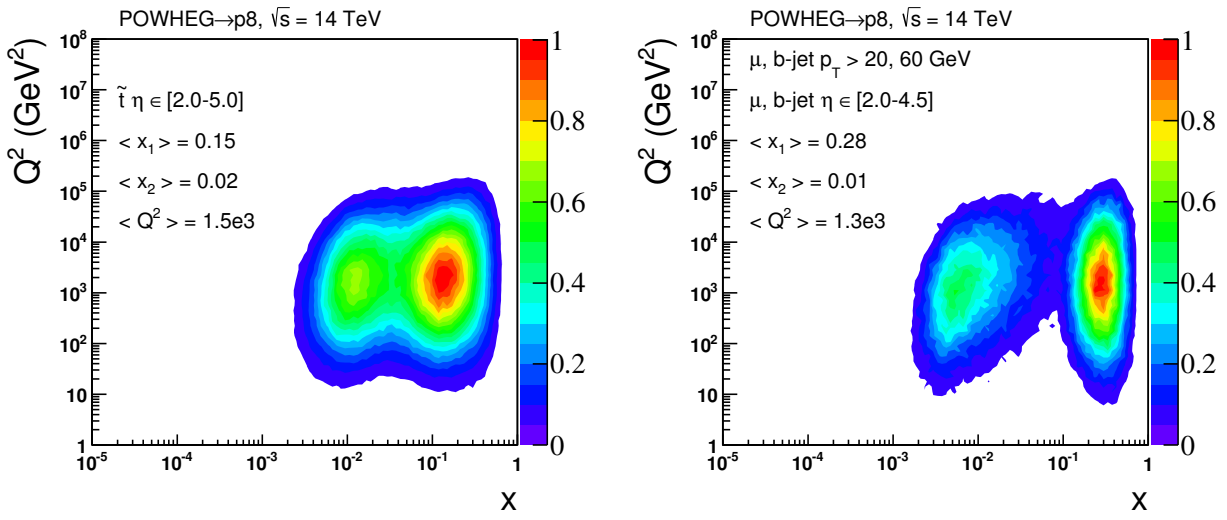


Figure 4.16: POWHEG event momentum scale Q^2 with respect to incoming parton momentum fraction x for a pseudotop within the LHCb acceptance (left) and pseudotop final state $\tilde{t}_{\mu b}$ passing analysis cuts (right).

4.5 Summary

An analysis strategy to perform top quark pair cross section measurements within the LHCb acceptance has been proposed.

A preliminary analysis of differential cross sections for various lepton+X and dilepton+X final states at 7, 8, and 14 TeV suggests that top quark pair measurements may be statistically feasible in several different final states. Notably, hundreds of events are expected in the $\tilde{t}_{\mu b}$ and $\tilde{t}_{\mu bj}$ channels in the available 7 and 8 TeV data. For these channels, the main backgrounds are identified as Wjets and Wbjets. The contribution from the Wjets process, where a light flavour jet is mis-tagged as a b-jet, is substantial. One way of managing this background is to require a low mis-tag rate for light jets $\approx$1%. Precisely knowing the mis-tag rate for light jets is therefore extremely important for improving the achievable experimental precision. As the background rates are correlated between different lepton+X channels, it may be possible to take advantage of this to reduce background uncertainties. Statistically precise measurements in the $\tilde{t}_{\mu b}$ and $\tilde{t}_{\mu bj}$ channels will not be possible until the 14 TeV data is available. With the data available at 14 TeV, measurements also become possible in the $\tilde{t}_{\mu eb}$ channel. Although this channel has a small event rate (400 events in the first year), there is essentially no background whatsoever.

The theoretical systematics for forwardly produced top quarks in pair production have not been studied in detail. The sensitivity of a suitably defined high pseudorapidity exclusive cross section was studied by varying the following theoretical inputs: $\alpha_s(m_Z^2)$; PDFs; top quark mass; and scale uncertainties. It was found that such measurements have enhanced sensitivity to PDF uncertainties. The sensitivity of top quark measurements at LHCb to particular eigenvector members was also demonstrated.

To quantify the potential sensitivity of a cross section measurement at 14 TeV, a reweighting procedure was performed, assuming a cross section measurement with an associated experimental uncertainty in the range of 4-8%. This demonstrated that the uncertainty on the gluon PDF may be improved by 5-25% within the range of $x \in [0.1, 0.3]$. It was also

discussed that a differential measurement within the LHCb acceptance, including analysis cuts, will most likely provide more stringent constraints on PDFs than a simple parton level analysis.

Chapter 5

Charge asymmetry measurements at LHCb

Having demonstrated the feasibility of top quark pair cross section measurements within the LHCb acceptance, it is important to investigate the potential sensitivity to charge asymmetry measurements for feasible final states. The $\tilde{t}_{\mu b}$ and $\tilde{t}_{\mu e b}$ channels appear to be most promising due to the high statistics and purity expected in each channel respectively. Fixed-order predictions for leptonic and top quark asymmetries will be provided in both of these channels. The top quark asymmetry results will then be compared to predictions computed at (N)LO+PS. Finally, the statistical precision achievable for measurements of both leptonic asymmetries with the full data at 14 TeV will be discussed.

5.1 Introduction

In Chapter 3, the origin of a charge asymmetry in the production of top quark pairs was discussed. Experimental measurements of this asymmetry provide a test of perturbative QCD at scales $Q^2 \simeq m_t^2$ at which the expansion is expected to be especially reliable. Measurements of the charge asymmetry are therefore well motivated. It is also interesting that measurements of the forward-backward asymmetry performed at the TeVatron [85–89] observe an enhanced asymmetry with respect to the SM prediction — see Table 3.4. This enhancement is particularly noticeable for large absolute rapidity differences, corresponding to forwardly (backwardly) produced (anti)top quarks. Although the TeVatron measurements are statistically limited, this observation suggests that similar measurements should be performed at the LHC.

Measurements performed by ATLAS and CMS in the central region [146–149] have so far been inconclusive in confirming or refuting the behaviour observed at the TeVatron. While the leptonic forward-central asymmetry A_{fc}^{ll} is observed to be slightly large in the 7 TeV data, measurements of the top quark forward central asymmetry A_{fc} in the l+jets channel at 7 and 8 TeV are consistent with both zero and the SM. Although the LHC analyses are performed with higher statistics than the TeVatron measurements, they are generally less sensitive to the charge asymmetry — predominantly due to the dominance of the symmetric gg channel present in pp collisions. At 14 TeV, the SM prediction for $A_{fc} \approx 0.7\%$ [144] is comparable in size to the total systematic uncertainty quoted for the 7 and 8 TeV measurements. Although some improvement in the understanding of the systematic uncertainties is expected, it is still important to select regions of phase space which are particularly sensitive to the charge asymmetry.

As demonstrated in Figure 3.10, forwardly produced top quarks at the LHC suffer from less dilution from the symmetric gg channel than centrally produced top quarks. This suggests that charge asymmetry measurements within the LHCb acceptance may be more sensitive than those performed centrally. In Chapter 4, the feasibility of performing top quark pair cross section measurements for a range different final states was discussed. In particular, this study suggests that the measurements in the $\tilde{t}_{\mu b}$ channel, corresponding to the partial reconstruction of the full $t\bar{t}$ system with a muon and b-jet, should reach high statistical precision within the first year of data taking at 14 TeV. Measurements in the extremely clean $\tilde{t}_{\mu eb}$ channel, corresponding to the reconstruction of an opposite flavour dilepton pair in association with b-jet, also become statistically possible at 14 TeV. It follows that the sensitivity and complementarity of charge asymmetry measurements in these two channels should be investigated.

In this Chapter, fixed-order predictions will be provided for leptonic and top quark rate and forward-backward asymmetries. An estimate of the experimental sensitivity for each of the leptonic asymmetries will be provided. Finally, the fixed-order top quark asymmetries will be compared to those obtained at (N)LO+PS.

5.2 Fixed-order asymmetries

Providing predictions of the charge asymmetry at both the top quark and lepton level is useful both theoretically and experimentally. Previous measurements performed at the TeVatron [85,87] and the LHC [146–149] have been unfolded from reconstruction to parton level. This unfolding procedure allows measurements to be compared at the level of on-shell $t\bar{t}$ intermediate states. As approximate differential top quark pair calculations at NNLO [133,178] are available at the top quark level, these unfolded measurements can then be compared to more precise theoretical predictions. Alternatively, as the top quark asymmetry also leads to a leptonic asymmetry, it is also possible to measure the asymmetry directly at the lepton level. As there is no uncertainty due to the unfolding procedure, these measurements can be performed more precisely.

The proposed measurements at LHCb never involve fully reconstructing a top quark, meaning that leptonic asymmetries are clearly most relevant. The top quark asymmetries will also be provided — this will allow the size of higher-order corrections to evaluated for the relevant region of phase space when they become available. The prediction of each asymmetry is computed at fixed-order by performing an expansion in the usual manner, see (3.54). In accordance with the discussion in Section 3.3.3, only the contributions to the numerator of $\mathcal{O}(\alpha_s^3)$ and $\mathcal{O}(\alpha_s^2\alpha_e)$ are evaluated. Including further QED/weak corrections is not particularly meaningful until the $\mathcal{O}(\alpha_s^4)$ contribution to the numerator is known. The $\mathcal{O}(\alpha_s^3)$ contribution to the asymmetry is computed with an adapted version of `MCFM` which separates the individual contributions from the $u\bar{u}$, $d\bar{d}$, and qg subprocesses. The mixed QED corrections $\mathcal{O}(\alpha_s^2\alpha_e)$ are then obtained by a rescaling of couplings and colour factors according to (3.66). For example, the scaling factors obtained for CT10w PDFs with $\alpha_s(m_Z^2) = 0.118$ are

$$R_{u\bar{u}}^{QED}(\mu = m_t/2) = 0.21\,, \qquad R_{u\bar{u}}^{QED}(\mu = m_t) = 0.23\,, \qquad R_{u\bar{u}}^{QED}(\mu = 2m_t) = 0.25\,. \quad (5.1)$$

It should be noted that NLO accuracy is also retained in top quark decay for the leptonic

asymmetries [180].

To estimate the potential source of theoretical uncertainty, the dependence on the choice of PDFs and scales is evaluated in the following way:

PDFs. The numerators of the various asymmetries are evaluated with the CT10w and NNPDF2.3 NLO PDFs with $\alpha_s(m_Z^2) = 0.118$ and 0.119 respectively. Potential uncertainty on the NNPDF asymmetry is then considered by calculating the corresponding denominator with the LO 0.119, LO 0.130, and NLO 0.119 NNPDF2.3 PDFs. For clarity, each of NNPDF sets will be referred to by the order and value of $\alpha_s(m_Z^2)$ within the text. For the CT10w asymmetry, the denominator is computed with the NLO CT10w PDFs. The denominators computed with the slightly outdated LO cteq6l, and cteq6ll PDFs are also included for reference. All the considered PDFs are summarised in Table 5.1. For each PDF set, the specific treatment of α_s is highlighted, and only the central PDF set is considered.

PDF	$\alpha_s(m_Z^2)$	α_s	DGLAP
CT10wnlo	0.118	NLO	NLO
cteq6l	0.118	NLO	LO
cteq6ll	0.130	LO	LO
NNPDF2.3 NLO 0.119	0.119	NLO	NLO
NNPDF2.3 LO 0.119	0.119	LO	LO
NNPDF2.3 LO 0.130	0.130	LO	LO

Table 5.1: PDF sets considered in the evaluation of the denominator of each asymmetry variable.

Scale. A scale uncertainty is evaluated by simultaneously computing the numerator and denominator of each asymmetry for a specific scale choice $\mu_F = \mu_R = \mu = \{m_t/2, m_t, 2m_t\}$. The central value is then found by averaging these three predictions, and a symmetric uncertainty is associated to the total envelope. Although this is a commonly adopted procedure [144, 151, 181], it is not a robust evaluation of higher-order corrections, as there is cancellation between the numerator and denominator for each scale choice.

5.2.1 Top quark rate asymmetry

A top quark asymmetry can be inferred in the high statistics $\tilde{t}_{\mu b}$ channel by comparing the rate of μ^- to μ^+ tagged events, as originally proposed in [156]. In this case, the relevant charge asymmetry variable is a rate asymmetry, which measures the asymmetry between the single particle pseudorapidity distribution of the top and antitop quark. The inclusive LHCb rate asymmetry is defined as

$$A^t = \int_{2.0} d\eta \left(\frac{d\sigma^t/d\eta - d\sigma^{\bar{t}}/d\eta}{d\sigma^t/d\eta + d\sigma^{\bar{t}}/d\eta} \right) . \tag{5.2}$$

In what follows, the contribution to the numerator of the asymmetry computed with both CT10w and NNPDF NLO 0.119 PDFs will be provided. The corresponding denominator points will then also be computed, which allows the asymmetry and associated uncertainty to be evaluated. This approach will be taken for all the considered asymmetries.

The contributions to the numerator computed with both CT10w and NNPDF NLO 0.119 PDFs are provided in Table 5.2. The separate contributions from each subprocess are included, highlighting the relevance of each particular correction. The effect of scale variation is also included.

CT10wnlo, $\alpha_s(m_Z^2) = 0.118$, 14 TeV

N^t (fb)		$\mu = m_t/2$	$\mu = m_t$	$\mu = 2m_t$
$\mathcal{O}(\alpha_s^3)$	$u\bar{u}$	671.1	500.2	381.1
	$d\bar{d}$	304.9	227.9	172.5
	qg	382.8	271.8	197.3
$\mathcal{O}(\alpha_s^2\alpha_e)$	$u\bar{u}$	141.0	116.1	96.9
	$d\bar{d}$	-32.0	-26.5	-21.9
Total		1467.7	1089.6	825.9

NNPDF2.3 NLO, $\alpha_s(m_Z^2) = 0.119$, 14 TeV

N^t (fb)		$\mu = m_t/2$	$\mu = m_t$	$\mu = 2m_t$
$\mathcal{O}(\alpha_s^3)$	$u\bar{u}$	699.9	521.0	407.1
	$d\bar{d}$	319.2	236.6	184.2
	qg	401.0	289.8	216.8
$\mathcal{O}(\alpha_s^2\alpha_e)$	$u\bar{u}$	145.8	120.0	101.9
	$d\bar{d}$	-33.2	-27.3	-23.1
Total		1532.6	1140.2	886.9

Table 5.2: The contributions to the numerator (in units of fb) of the rate asymmetry A^t within the LHCb acceptance at $\sqrt{s} = 14$ TeV. The results for the different scale choices $\mu_F = \mu_R = \mu$ are included. The choice of central PDFs is also highlighted.

It is found that the $\mathcal{O}(\alpha_s^3)$ qg contribution to the rate asymmetry is sizeable, exceeding the corresponding contribution arising from $d\bar{d}$ initial states. It is also observed that the

prediction obtained with NNPDF NLO 0.119 is several percent larger than the corresponding CT10w prediction — a consequence of the smaller value of $\alpha_s(m_Z^2)$ preferred by CT10w. Although the smaller value of $\alpha_s(m_Z^2)$ in the CT10w fit results in a slightly larger valence PDF at $x \simeq 0.1$, this compensation does not fully account for the larger value of $\alpha_s(m_Z^2)$ which contributes to the numerator at $\mathcal{O}(\alpha_s^3)$. The ratio of the CT10w and NNPDF NLO 0.119 valence PDF, $q_{val} \equiv (u - \bar{u}) + (d - \bar{d})$, is shown for reference in Figure 5.1. This is relevant as the valence PDF is ultimately responsible for the contribution to the numerator of each asymmetry.

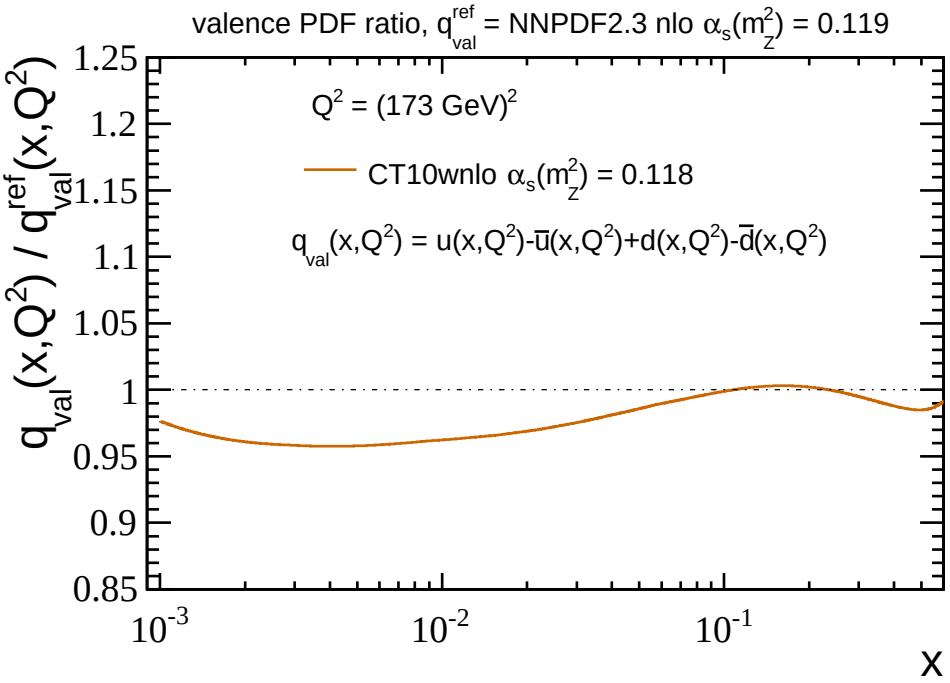


Figure 5.1: Ratio of CT10wnlo $\alpha_s(m_Z^2) = 0.118$ valence PDF content with respect to NNPDF2.3 NLO $\alpha_s(m_Z^2) = 0.119$.

The denominators computed with the various PDFs are provided in Table 5.3. Note that the denominators are consistent, within scale uncertainty, and accounting for a factor of two in the definitions, with the NLO pseudotop cross section analysis presented in Table 4.3. In the final column of this table, the resultant asymmetry for each particular denominator has been evaluated. For example, the value of $A^{t\bar{t}} = 0.67$ (3)% for cteq6l is obtained by dividing the CT10wnlo numerator in Table 5.2 by the denominator computed with cteq6l in Table 5.3 for each scale choice. The average of these asymmetries corresponds to $A^{t\bar{t}} = 0.67$, and the related uncertainty of 0.03% is simply the envelope of these three points.

		D^t (pb), 14 TeV			
PDF	$\alpha_s(m_Z^2)$	$\mu = m_t/2$	$\mu = m_t$	$\mu = 2m_t$	$A^{t\bar{t}}$ (%)
CT10wnlo	0.118	229.86	178.76	141.49	0.61 (3)
cteq6l	0.118	208.95	161.36	127.24	0.67 (3)
cteq6ll	0.130	251.01	190.69	148.09	0.57 (1)
NNPDF2.3 NLO	0.119	239.05	184.86	146.33	0.62 (2)
NNPDF2.3 LO	0.119	268.63	208.04	164.47	0.55 (2)
NNPDF2.3 LO	0.130	296.99	225.30	175.14	0.51 (1)

Table 5.3: The contribution to the denominator (in units of pb) of the top quark rate asymmetry A^t within the LHCb acceptance at $\sqrt{s} = 14$ TeV. The results for different (N)LO PDFs with differing values of $\alpha_s(m_Z^2)$ are indicated. The resultant asymmetry for each PDF set, with scale uncertainty, is also included.

The scale uncertainty on the final asymmetry for each PDF set is small, in the range (2-5)%. As previously mentioned, this is a consequence of simultaneously evaluating the numerator and denominator at the same scale. If the asymmetry is calculated with the denominator evaluated at $\mathcal{O}(\alpha_s^3)$, the scale uncertainty of the asymmetry is significantly larger — this is the method which is sometimes adopted by the experimental collaborations, and introduces incomplete terms of $\mathcal{O}(\alpha_s^2)$ in the expansion of the asymmetry (3.54). As discussed in Section 3.3.3, this method should be avoided.

Notice that the range of asymmetry predictions from different PDFs is substantially larger than the scale uncertainty. Providing predictions evaluated with both LO and NLO PDFs is necessary as there is ambiguity in how the asymmetry should be predicted. For example, evaluating the denominator at LO with NLO PDFs is inconsistent, as the evolution of the PDFs accounts for splittings of which the matrix element has no knowledge. Alternatively, LO PDFs with LO running of α_s do not correctly predict a value of α_s which is consistent with measurements at both high ($\mu = m_Z$) and low ($\mu = 7.5$ GeV) scales — the running does not accommodate such a behaviour. Both of these approaches therefore have disadvantages. Also, it is clear that LO PDFs with a large value of $\alpha_s(m_Z^2)$ will underestimate the asymmetry, a consequence of the corresponding denominator. An aggressive approach is therefore to quote the asymmetry prediction computed with only the NLO PDFs (numer-

ator and denominator). The prediction of differential asymmetries is presented in this way. A more conservative approach is to evaluate an uncertainty envelope based on the results obtained with both LO and NLO PDFs with $\alpha_s(m_Z^2) = 0.119$.

As the denominator is particularly sensitive to the behaviour of the gluon PDF, it is also instructive to compare the behaviour of the gluon distribution for the various PDFs which are considered in this study. In Figure 5.2, the ratio of the evolved gluon PDFs at the scale $Q^2 = m_t^2$ is shown. The left plot shows the ratio of cteq6l, cteq6ll and NNPDF NLO 0.119 gluon PDFs plotted with respect to CT10w, while on the right the NNPDF LO 0.119, NNPDF LO 0.130 , and CT10w gluon PDFs are plotted with respect to NNPDF2.3 NLO 0.119.

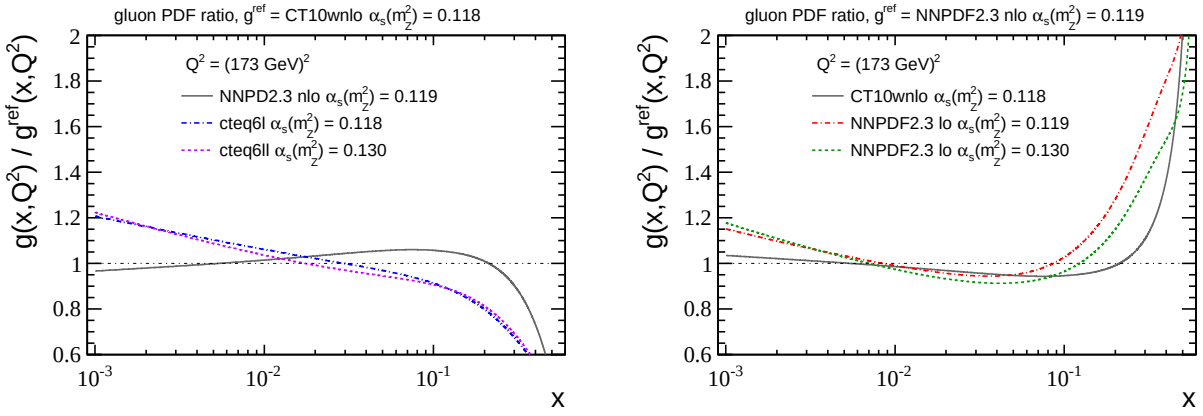


Figure 5.2: Ratio of various evolved gluon PDFs at the scale $Q^2 = m_t^2$. Left: the reference gluon PDF is CT10wnlo with $\alpha_s(m_Z^2) = 0.118$. Right: the reference PDF is NNPDF2.3 NLO 0.119.

For the prediction of the asymmetry with NNPDF NLO 0.119 PDFs, the asymmetry is largest when the denominator is also computed with NNPDF2.3 NLO 0.119 PDFs — this is a consequence of the relatively small gluon PDF beyond $x > 0.1$, and the lower value of $\alpha_s(m_Z^2) = 0.119$. If the NNPDF2.3 LO 0.119 PDFs are instead used, then the asymmetry is smaller by 13%. This difference is emphasised even further if NNPDF2.3 LO 0.130 PDFs are used. Clearly, the choice of PDFs used in the computation of the denominator has a large impact on the final asymmetry prediction. When the asymmetries are computed purely with the NLO PDFs, the CT10w and NNPDF NLO 0.119 predictions are compatible.

The differential rate asymmetry computed with CT10w PDFs is shown in Figure 5.3. The

left plot contains the contributions to the asymmetry from subprocesses at $\mathcal{O}(\alpha_s^3)$. The right plot contains the total asymmetry including terms $\mathcal{O}(\alpha_s^3)$ and $\mathcal{O}(\alpha_s^2\alpha_e)$, where the individual contributions at $\mathcal{O}(\alpha_s^2\alpha_e)$ are also highlighted. In both cases, the scale uncertainty on the total asymmetry is shown.

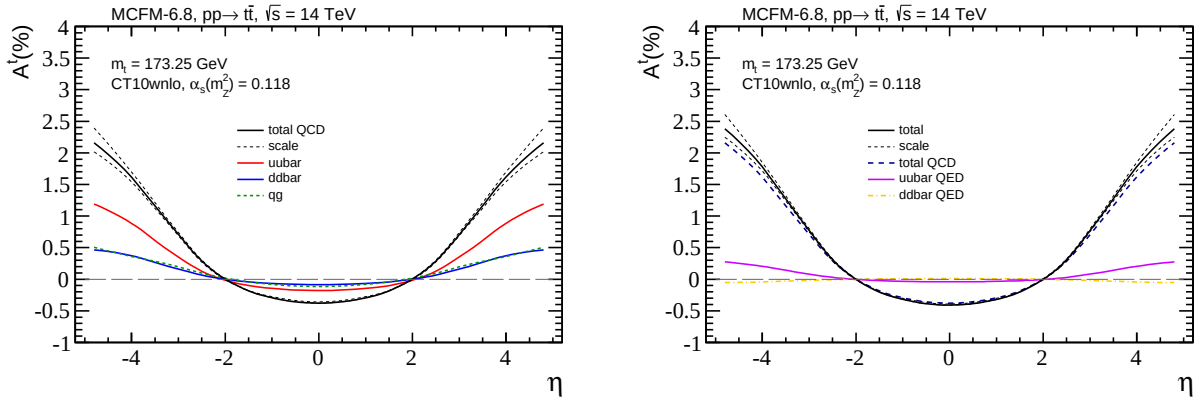


Figure 5.3: Differential top quark rate asymmetry A^t as a function of pseudorapidity at $\sqrt{s} = 14$ TeV. The asymmetry is computed with CT10w PDFs. Left: individual contributions to the QCD asymmetry. Right: total asymmetry including both QCD $\mathcal{O}(\alpha_s^3)$ and mixed QED $\mathcal{O}(\alpha_s^2\alpha_e)$ contributions. The scale uncertainty on the total asymmetry is also shown in both cases.

The asymmetry at very high pseudorapidity ($4.0 < \eta < 5.0$) is 4-5 times larger than the prediction in the central region. Note that, although the top quark is never fully reconstructed in the proposed measurements at LHCb, these predictions are still useful to investigate the size of higher-order corrections at high pseudorapidity. Such comparisons can then be used to estimate the validity of the leptonic asymmetries.

5.2.2 Leptonic rate asymmetry

The leptonic rate asymmetry prediction is provided for the lb channel, corresponding to the cross section analysis for the $\tilde{t}_{\mu b}$ channel which was proposed in Section 4.3.1. For consistency, the same cuts are also considered for the asymmetry prediction. A b-jet, clustered with the anti-k_t algorithm, and charged lepton are required to be within the LHCb acceptance ($2.0 < \eta < 4.5$), and the following kinematic cuts are applied:

- b-jet minimum $p_T > 60$ GeV;

- $l^{\pm}$ minimum $p_T > 20$ GeV.

Furthermore, the lepton and b-jet must also be isolated in rapidity-phi space according to $\Delta R(l^{\pm}, b\text{–jet}) \geq R$, where $R = 0.5$. The asymmetry is then defined with respect to the lepton pseudorapidity as

$$A^l = \int_{2.0}^{4.5} d\eta_l \left(\frac{d\sigma^{l^+b}/d\eta_l - d\sigma^{l^-b}/d\eta_l}{d\sigma^{l^+b}/d\eta_l + d\sigma^{l^-b}/d\eta_l} \right) . \tag{5.3}$$

The full sample corresponds to the combination of semileptonic and dilepton events. In the dilepton sample, events where both leptons pass the analysis cuts are vetoed. These vetoed events correspond to a subset of the full dilepton sample which is studied in Section 5.2.2. The contributions to the numerator of the leptonic rate asymmetry are provided in Table 5.4.

CT10wnlo, $\alpha_s(m_Z^2) = 0.118$, 14 TeV

N^l (fb)		$\mu = m_t/2$	$\mu = m_t$	$\mu = 2m_t$
$\mathcal{O}(\alpha_s^3)$	$u\bar{u}$	49.53	36.57	27.67
	$d\bar{d}$	20.91	15.31	11.56
	qg	3.65	2.23	1.93
$\mathcal{O}(\alpha_s^2\alpha_e)$	$u\bar{u}$	10.40	8.49	7.03
	$d\bar{d}$	-2.20	-1.78	-1.47
Total		82.30	60.82	46.73

NNPDF2.3 NLO, $\alpha_s(m_Z^2) = 0.119$, 14 TeV

N^l (fb)		$\mu = m_t/2$	$\mu = m_t$	$\mu = 2m_t$
$\mathcal{O}(\alpha_s^3)$	$u\bar{u}$	51.56	37.66	29.33
	$d\bar{d}$	21.32	15.44	11.93
	qg	3.58	3.03	1.84
$\mathcal{O}(\alpha_s^2\alpha_e)$	$u\bar{u}$	10.74	8.68	7.34
	$d\bar{d}$	-2.22	-1.78	-1.49
Total		84.98	63.03	48.94

Table 5.4: The contributions to the numerator of the leptonic rate asymmetry A^l within the LHCb acceptance at $\sqrt{s} = 14$ TeV. The results for the different scale choices $\mu_F = \mu_R = \mu$ are included. The choice of central PDFs is also highlighted.

The denominators computed with the various PDFs and resultant asymmetries are provided in Table 5.5. Notice that, including scale uncertainties, the prediction for the denominator is consistent with the results obtained with `POWHEG` matched to `Pythia8` — see Table 4.1 for the corresponding NLO+PS results.

The leptonic rate asymmetry is almost a factor of three larger than the corresponding top quark rate asymmetry. This is mainly a result of the analysis cuts placed on the lepton and b-jet. As demonstrated in Section 4.4.3, placing these analysis cuts removes events produced

		D^l (pb), 14 TeV			
PDF	$\alpha_s(m_Z^2)$	$\mu = m_t/2$	$\mu = m_t$	$\mu = 2m_t$	$A_{fb}^{t\bar{t}}$ (%)
CT10wnlo	0.118	4.877	3.713	2.886	1.65 (4)
cteq6l	0.118	4.011	3.086	2.426	1.98 (6)
cteq6ll	0.130	4.921	3.702	2.854	1.65 (2)
NNPDF2.3 NLO	0.119	4.652	3.531	2.756	1.80 (3)
NNPDF2.3 LO	0.119	6.255	4.685	3.603	1.38 (1)
NNPDF2.3 LO	0.130	6.794	4.984	3.769	1.30 (2)

Table 5.5: The contributions to the denominator (in units of pb) of the leptonic rate asymmetry A^l within the LHCb acceptance at $\sqrt{s} = 14$ TeV. The results for different (N)LO PDFs with differing values of $\alpha_s(m_Z^2)$ are indicated. The resultant asymmetry for each PDF set, with scale uncertainty, is also included.

by incoming partons at lower x_1.

$$\langle x_1 \rangle = 0.1 \underset{\text{cuts}}{\rightarrow} \langle x_1' \rangle = 0.3\,. \tag{5.4}$$

These cuts therefore reduce dilution from symmetric gg initiated events, as the gluon PDF falls off more rapidly beyond $x = 0.1$ than the valence quark PDF — see Figure 3.8. Notice that the NNPDF NLO 0.119 and CT10w asymmetries are less compatible than the corresponding top quark rate asymmetry predictions. Beyond $x = 0.3$, the NNPDF NLO 0.119 and CT10w and gluon PDF begin to deviate, resulting in this observed difference. If top quark cross section measurements within the LHCb acceptance are used to constrain PDFs, then these differences should be reduced.

The differential leptonic rate asymmetry computed with CT10w PDFs is displayed in Figure 5.4. As before, the left plot shoes the subprocesses contributing at $\mathcal{O}(\alpha_s^3)$. The right plot shows, in addition, the $\mathcal{O}(\alpha_s^2\alpha_e)$ contributions.

The lepton asymmetry is significant, particularly at high pseudorapidity where it exceeds 4%. Asymmetry measurements in this region of phase space should therefore be pursued. As shown in Figure 4.5, corresponding to the event rate in the $\tilde{t}_{\mu b}$ channel including reconstructions efficiencies, approximately 400 signal events at high pseudorapidity ($\eta_\mu > 3.5$) are

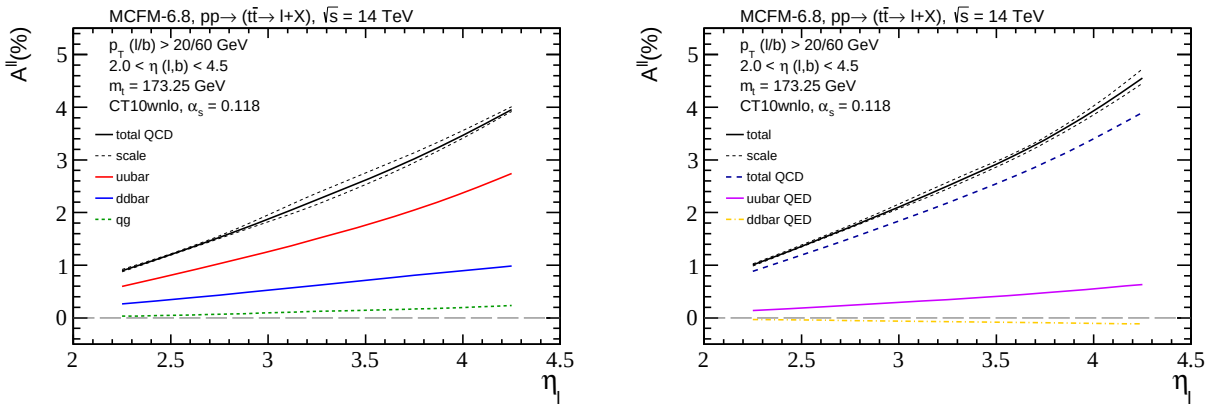


Figure 5.4: Differential leptonic rate asymmetry A^l as a function of lepton pseudorapidity at $\sqrt{s} = 14$ TeV. The asymmetry is computed with CT10w PDFs. Left: subprocesses contributing to the QCD asymmetry. Right: total asymmetry including both QCD $\mathcal{O}(\alpha_s^3)$ and mixed QED $\mathcal{O}(\alpha_s^2\alpha_e)$ contributions. The scale uncertainty on the total asymmetry is also shown in both cases.

expected within the first year of running at $\sqrt{s}$ =14 TeV. The proposed measurement is therefore statistically feasible.

5.2.3 Top quark forward-backward asymmetry

Having demonstrated the feasibility of cross section measurements in the dilepton final state $\tilde{t}_{\mu eb}$, this opens the possibility of measuring the rapidity difference between the leptons on an event-by-event basis. At the level of top quarks, the relevant charge asymmetry variable is the forward-backward asymmetry $A_{fb}^{t\bar{t}}$ defined in (3.70). It should be noted that the inclusive forward-backward asymmetry at the LHC is zero, as the initial state is symmetric around $y = 0$. However, as the LHCb detector is instrumented only in the forward region (it is asymmetric around $y = 0$), the forward-backward asymmetry is equivalent to the forward-central asymmetry. The inclusive LHCb forward-backward asymmetry is defined as

$$A_{fb}^{t\bar{t}} = \int d\Delta_y \left(\frac{d\sigma(\Delta_y > 0)/d\Delta_y - d\sigma(\Delta_y < 0)/d\Delta_y}{d\sigma/d\Delta_y} \right), \qquad \eta_t, \eta_{\bar{t}} \in [2.0, 5.0]\,. \tag{5.5}$$

The boundary choices are arbitrary, as the top quark is never fully reconstructed by the detector. This particular choice captures the necessary features, and is similar to the acceptance cuts chosen for leptons. The contributions to the numerator of the top quark

forward-backward asymmetry are provided in Table 5.6.

CT10wnlo, $\alpha_s(m_Z^2) = 0.118$, 14 TeV

$N_{fb}^{t\bar{t}}$ (fb)		$\mu = m_t/2$	$\mu = m_t$	$\mu = 2m_t$
$\mathcal{O}(\alpha_s^3)$	$u\bar{u}$	447.5	335.2	256.7
	$d\bar{d}$	188.1	139.9	107.2
	qg	-66.7	-45.6	-35.8
$\mathcal{O}(\alpha_s^2\alpha_e)$	$u\bar{u}$	94.0	77.8	65.3
	$d\bar{d}$	-19.8	-16.2	-13.6
Total		643.1	491.1	379.7

NNPDF2.3 NLO, $\alpha_s(m_Z^2) = 0.119$, 14 TeV

$N_{fb}^{t\bar{t}}$ (fb)		$\mu = m_t/2$	$\mu = m_t$	$\mu = 2m_t$
$\mathcal{O}(\alpha_s^3)$	$u\bar{u}$	464.8	349.1	272.9
	$d\bar{d}$	195.0	144.5	112.4
	qg	-67.5	-52.2	-34.7
$\mathcal{O}(\alpha_s^2\alpha_e)$	$u\bar{u}$	96.8	80.4	68.3
	$d\bar{d}$	-20.3	-16.6	-14.1
Total		668.9	505.2	404.8

Table 5.6: The contributions to the numerator of the top quark forward-backward asymmetry $A_{fb}^{t\bar{t}}$ within the LHCb acceptance at $\sqrt{s} = 14$ TeV. The results for the different scale choices $\mu_F = \mu_R = \mu$ are included. The choice of central PDFs is also highlighted.

Unlike the case of the top quark rate asymmetry, the $\mathcal{O}(\alpha_s^3)$ qg contribution to the forward-backward asymmetry is observed to be negative — though only amounting to a small fraction of the total $\mathcal{O}(\alpha_s^3)$ contribution of approximately 10%. This is not surprising, as this process receives a contribution from momentum configurations in which the forward top quark pair recoils against against a hard jet, which can occur when there is a collinear splitting in the initial state. This configuration is equivalent to the situation when the $t\bar{t}$ system is at high p_T in the central region (having recoiled against a hard jet), and is known to contribute negatively to the forward-backward asymmetry. In the forward region of phase space, the positive contribution from virtual corrections remains dominant. The denominators computed with the various PDFs and resultant asymmetries are provided in Table 5.7.

The corresponding differential asymmetry computed with CT10w PDFs is shown in Figure 5.5. The left plot shows the subprocesses contributing at $\mathcal{O}(\alpha_s^3)$. The right plot, in addition, shows the $\mathcal{O}(\alpha_s^2\alpha_e)$ contributions.

The total asymmetry exceeds 3% for large rapidity differences. In the final bin, there is an observable drop in the asymmetry due to boundary effects. This is also observed in [151] for the 'Y_{cut}' asymmetry, which introduces a minimum rapidity cut on the sum of the top and antitop quark rapidities.

		$D_{fb}^{t\bar{t}}$ (pb), 14 TeV			
PDF	$\alpha_s(m_Z^2)$	$\mu = m_t/2$	$\mu = m_t$	$\mu = 2m_t$	$A_{fb}^{t\bar{t}}$ (%)
CT10wnlo	0.118	55.09	43.17	34.39	1.14 (4)
cteq6l	0.118	43.57	34.23	27.40	1.44 (5)
cteq6ll	0.130	53.14	41.00	33.27	1.20 (2)
NNPDF2.3 NLO	0.119	55.66	43.44	34.71	1.17 (3)
NNPDF2.3 LO	0.119	59.37	46.12	36.62	1.14 (4)
NNPDF2.3 LO	0.130	65.92	50.21	39.23	1.01 (2)

Table 5.7: The contributions to the denominator (in units of pb) of the top quark forward-backward asymmetry $A_{fb}^{t\bar{t}}$ within the LHCb acceptance at $\sqrt{s} = 14$ TeV. The results for different (N)LO PDFs with differing values of $\alpha_s(m_Z^2)$ are indicated. The resultant asymmetry for each PDF set, with scale uncertainty, is also included.

5.2.4 Leptonic forward-backward asymmetry

Following the proposed analysis for the cross section measurement in the $\tilde{t}_{\mu eb}$ channel provided in Section 4.3.2, the leptonic forward-backward asymmetry is calculated after applying the same analysis cuts. Both leptons and a b-jet are required to be within the LHCb acceptance ($2.0 < \eta < 4.5$), and an isolation requirement is applied to both leptons. A minimum p_T of 20 GeV is then applied to the leptons and b-jet. The asymmetry is then defined as

$$A_{fb}^{ll} = \int d\Delta_{y_l} \left(\frac{d\sigma^{\mu eb}(\Delta_{y_l} > 0)/d\Delta_{y_l} - d\sigma^{\mu eb}(\Delta_{y_l} < 0)/d\Delta_{y_l}}{d\sigma^{\mu eb}/d\Delta_{y_l}} \right) , \qquad \Delta_{y_l} = y_{l^+} - y_{l^-} . \quad (5.6)$$

Both the symmetric and asymmetric cross sections are normalised to the μe branching fraction. The contributions to the numerator of the leptonic forward-backward asymmetry are provided in Table 5.8.

Again, the NNPDF NLO 0.119 prediction is observed to be slightly larger. It should be also noticed that the contribution from the $u\bar{u}$ subprocess is almost a factor of three larger than the $d\bar{d}$ subprocess. Requiring the decay products of both top quarks to be within the LHCb acceptance results in a larger fraction of incoming partons being at high-x_1 — in this region the u/d ratio increases, also increasing the relative size of the $\mathcal{O}(\alpha_s^2\alpha_e)$ contribution. Finally, the denominators computed with the various PDFs and resultant asymmetries are

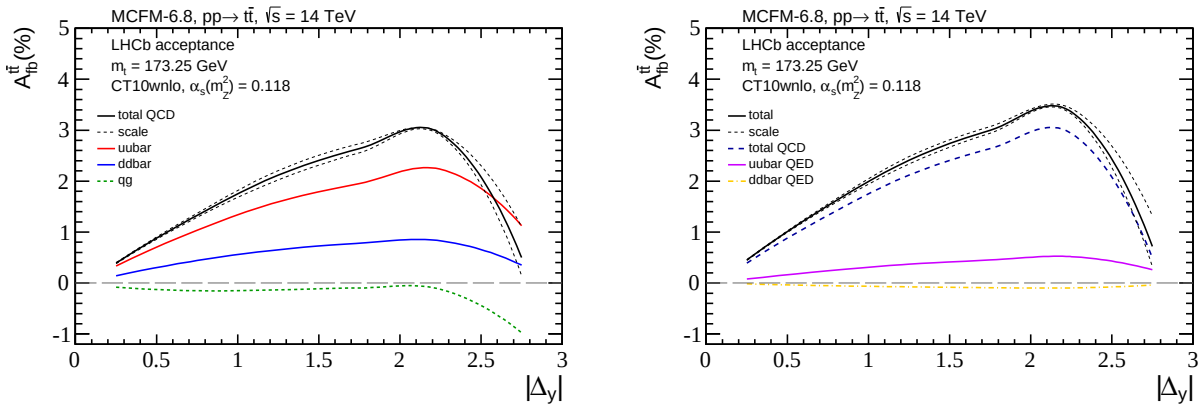


Figure 5.5: Differential top quark forward-backward asymmetry $A_{fb}^{t\bar{t}}$ as a function of absolute top quark rapidity difference at $\sqrt{s} = 14$ TeV. The asymmetry is computed with CT10w PDFs. Left: subprocesses contributing to the QCD asymmetry. Right: total asymmetry including both QCD $\mathcal{O}(\alpha_s^3)$ and QED $\mathcal{O}(\alpha_s^2\alpha_e)$ contributions. The scale uncertainty on the total asymmetry is also shown in both cases.

CT10wnlo, $\alpha_s(m_Z^2) = 0.118$, 14 TeV

N_{fb}^{ll} (fb)		$\mu = m_t/2$	$\mu = m_t$	$\mu = 2m_t$
$\mathcal{O}(\alpha_s^3)$	$u\bar{u}$	0.843	0.607	0.458
	$d\bar{d}$	0.327	0.214	0.168
	qg	0.121	0.075	0.066
$\mathcal{O}(\alpha_s^2\alpha_e)$	$u\bar{u}$	0.177	0.141	0.116
	$d\bar{d}$	-0.034	-0.025	-0.021
Total		1.433	1.013	0.788

NNPDF2.3 NLO, $\alpha_s(m_Z^2) = 0.119$, 14 TeV

N_{fb}^{ll} (fb)		$\mu = m_t/2$	$\mu = m_t$	$\mu = 2m_t$
$\mathcal{O}(\alpha_s^3)$	$u\bar{u}$	0.889	0.662	0.489
	$d\bar{d}$	0.327	0.238	0.178
	qg	0.148	0.114	0.076
$\mathcal{O}(\alpha_s^2\alpha_e)$	$u\bar{u}$	0.185	0.152	0.122
	$d\bar{d}$	-0.034	-0.027	-0.022
Total		1.516	1.139	0.842

Table 5.8: The contributions to the numerator of the leptonic forward-backward asymmetry A_{fb}^{ll} within the LHCb acceptance at $\sqrt{s} = 14$ TeV. The results for the different scale choices $\mu_F = \mu_R = \mu$ are included. The choice of central PDFs is also highlighted.

provided in Table 5.9.

The corresponding differential asymmetry computed with CT10w PDFs is shown in Figure 5.6. The left plot shows the subprocesses contributing at $\mathcal{O}(\alpha_s^3)$. The right plot, in addition, shows the $\mathcal{O}(\alpha_s^2\alpha_e)$ contributions.

The leptonic forward-backward asymmetry exceeds 4% for the extreme choice of absolute lepton rapidity difference. The inclusive asymmetry itself is also sizeable, exceeding 1%. In fact, this prediction is of comparable size to the inclusive forward-central lepton asymmetry with a cut placed on the invariant mass of the parent $t\bar{t}$ system of 1 TeV (see Table 16 of [144]).

		D^{ll}_{fb} (pb), 14 TeV			
PDF	$\alpha_s(m_Z^2)$	$\mu = m_t/2$	$\mu = m_t$	$\mu = 2m_t$	A^{ll}_{fb} (%)
CT10wnlo	0.118	0.1355	0.1041	0.0815	1.01 (5)
cteq6l	0.118	0.1103	0.0865	0.0691	1.22 (8)
cteq6ll	0.130	0.1364	0.1045	0.0818	1.00 (5)
NNPDF2.3 NLO	0.119	0.1195	0.0920	0.0732	1.21 (6)
NNPDF2.3 LO	0.119	0.1738	0.1305	0.1009	0.86 (2)
NNPDF2.3 LO	0.130	0.1914	0.1406	0.1070	0.80 (1)

Table 5.9: The contributions to the denominator (in units of pb) of the leptonic forward-backward asymmetry A^{ll}_{fb} within the LHCb acceptance at $\sqrt{s} = 14$ TeV. The results for different (N)LO PDFs with differing values of $\alpha_s(m_Z^2)$ are indicated. The resultant asymmetry for each PDF set, with scale uncertainty, is also included.

5.3 Experimental sensitivity

To gain an understanding of how accurately the leptonic asymmetries can be measured, it is necessary to consider what is experimentally achievable both statistically and systematically. The statistical precision can be estimated by applying the approximate reconstruction efficiencies introduced in Section 4.3. As a naive estimate, the statistical uncertainty is evaluated as

$$\delta A = \sqrt{\frac{(1 - A^2)}{N}}\,. \tag{5.7}$$

No attempt will be made to derive realistic systematic uncertainties. However, the main sources of potential uncertainty will be discussed.

5.3.1 Leptonic rate asymmetry

In Section 4.3.1, the main backgrounds in the $\tilde{t}_{\mu b}$ channel were identified as single top, W+(b)jets and Z+(b)jets. Precisely knowing the contribution of these backgrounds to the numerator and denominator of the total asymmetry is vital if an accurate charge asymmetry measurement is to performed in this channel.

To understand how this may be done, the expected number of events in the μb channel

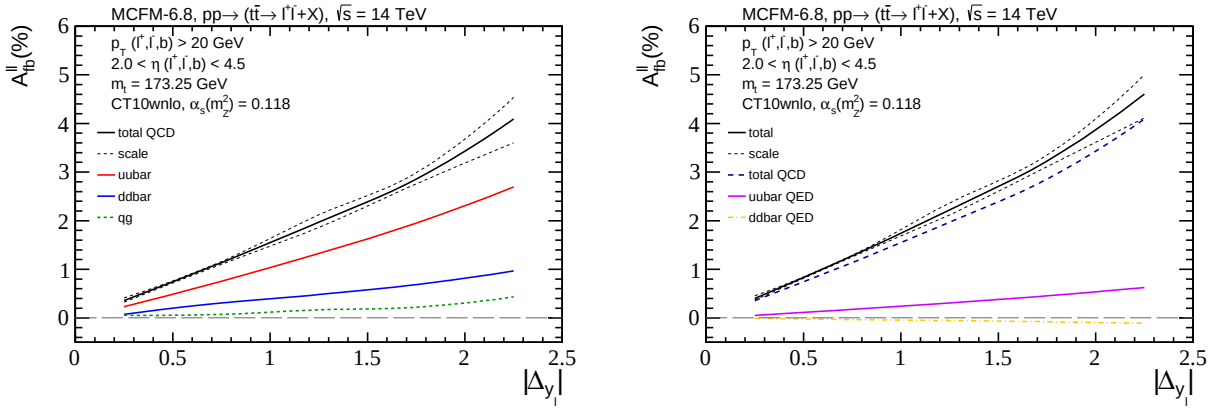


Figure 5.6: Differential leptonic forward-backward asymmetry A_{fb}^{ll} as a function of absolute lepton rapidity difference at $\sqrt{s} = 14$ TeV. The asymmetry is computed with CT10w PDFs. Left: subprocesses contributing to the QCD asymmetry. Right: total asymmetry including both QCD $\mathcal{O}(\alpha_s^3)$ and mixed QED $\mathcal{O}(\alpha_s^2\alpha_e)$ contributions. The scale uncertainty on the total asymmetry is also shown in both cases.

with 50 fb^{-1} is re-investigated. The background rates are obtained from the (N)LO+PS samples which were studied in Section 4.3.1, and the $t\bar{t}$ signal is obtained from the fixed-order results presented in Section 5.2.2. In all cases, the CT10w PDF set is used, and the central scale choice is considered. Note, the $t\bar{t}$ contribution to the numerator includes both QCD and mixed QED corrections, while the denominator is considered at LO.

In accordance with the cross section analysis for the $\tilde{t}_{\mu b}$ channel, the following reconstruction efficiencies are applied: 75% efficiency for leptons; 70% efficiency for b-jets; and 1% mis-tag rate for light jets. The usual acceptance, kinematic, and isolation cuts defined in Section 5.2.2 are also applied. The expected number of events contributing to the total denominator (left) and numerator (right) of the muonic rate asymmetry are shown in Figure 5.7. In both cases, the contribution from each process is stacked, and the displayed uncertainty is $\sqrt{N}$ in each bin.

The contribution to the numerator from the asymmetric background processes is substantially larger than the signal. This is because the asymmetry of the background processes is driven by the high-x u/d ratio, which is approximately two. Although this ratio is well constrained by DIS experiments, the total normalisation of each process is less well constrained. This means, a small uncertainty on the light jet mis-tag rate could be mistaken for a large contribution to signal.

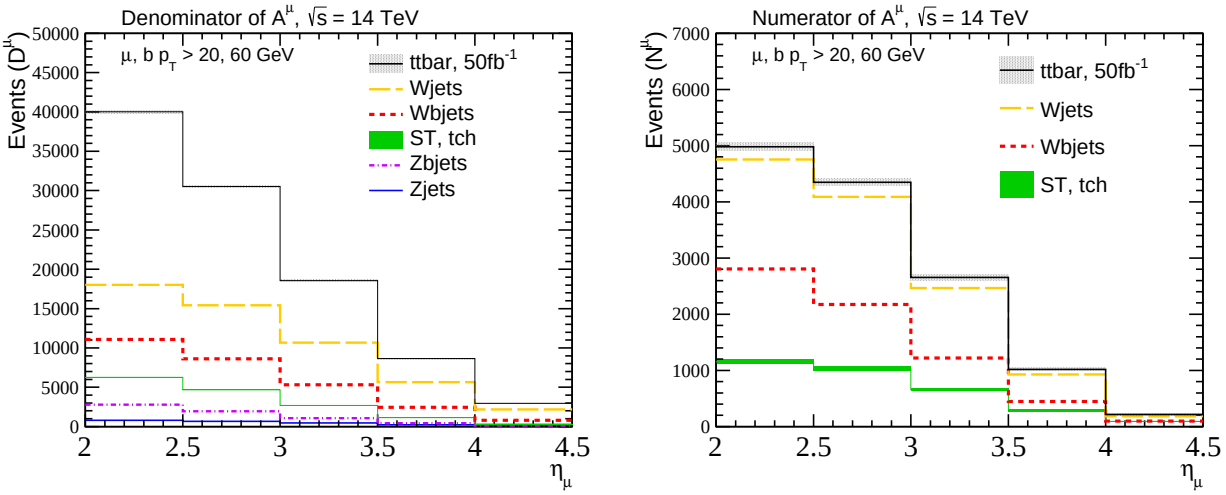


Figure 5.7: Expected contribution from signal and background to the denominator (left) and numerator (right) of the muonic rate asymmetry presented as a function of muon pseudorapidity at $\sqrt{s}$ =14 TeV with $\int \mathcal{L}dt = 50\text{fb}^{-1}$.

In principle, the normalisation of these backgrounds can be constrained by measuring the event rates of other final states. This is demonstrated in Figure 4.5, where the differential cross section for both $\tilde{t}_{\mu b}$ and $\tilde{t}_{\mu bj}$ channels are shown. As the relative contribution from the various processes is different from channel to channel, a multi-channel analysis may improve the understanding of backgrounds. An accurate cross section and asymmetry measurement of the $Wjets$ process at high pseudorapidity is extremely important to allow a meaningful top quark asymmetry measurement to be performed.

Assuming the background rates are precisely known, the precision of muonic rate asymmetry can be quantified by comparing the total asymmetry to the no-$t\bar{t}$-asymmetry hypothesis. This is shown in Figure 5.8.

To quantify the separation of these asymmetries, a χ^2 is computed between the total asymmetry and no-$t\bar{t}$-asymmetry hypothesis. For the inclusive asymmetries, the following predictions are found

$$A^{\mu}_{\text{Total}} = 13.12\%\,, \qquad A^{\mu}_{\text{no}\,t\bar{t}} = 12.33\%\,, \qquad N_{\text{Total}} \simeq 1e5\,. \tag{5.8}$$

This provides an estimate of the precision of the leptonic rate asymmetry with the full 14 TeV data. It is therefore clear that electron final states must also be considered to improve

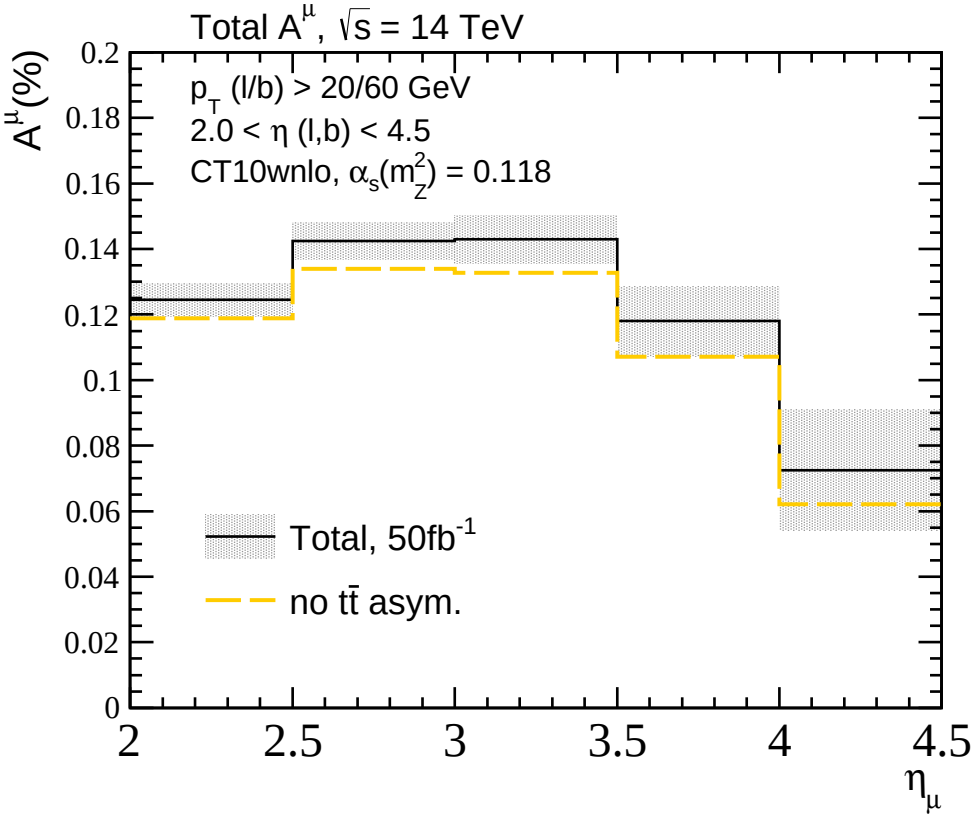


Figure 5.8: Comparison of the total muonic rate asymmetry A^{μ} as a function of pseudorapidity at $\sqrt{s} = 14$ TeV. The total asymmetry is compared to the no-$t\bar{t}$-asymmetry hypothesis, and the uncertainty corresponds to the statistical precision expected with 50 fb^{-1}.

the potential statistical precision. If this is done, a non-zero asymmetry can rejected at approximately 3.6σ CL ($\chi^2 = 12.86$). Measurements in this channel will ultimately depend on how well the backgrounds can be constrained — this must be addressed by the LHCb collaboration.

5.3.2 Leptonic forward-backward asymmetry

In Section 4.3.2, the feasibility of a cross section measurement in the $\tilde{t}_{\mu eb}$ channel was investigated. It was found that requiring a b-jet within the acceptance appears to suppress all sources of background. The feasibility of asymmetry measurements in this channel therefore predominantly depend on what is statistically possible.

To estimate the statistical uncertainty, the expected number of events is evaluated by computing the denominator of the asymmetry at NLO. In accordance with Section 5.2.4, the

usual acceptance, kinematic, and isolation cuts are applied. The following reconstruction efficiencies are also applied: 75% efficiency for leptons; 70% efficiency for b-jets. The central prediction for the inclusive asymmetry computed with CT10w PDFs, and expected number of events are

$$A_{fb}^{ll} = 1.01\% \,, \qquad N_{\text{Total}} \simeq [2500 - 5000] \,, \tag{5.9}$$

where the total number of events is estimated by considering the relevant denominator contributions in Table 5.9. The expected statistical precision is approximately (1-2)%, which is not significant. Although a statistically precise measurement is not possible in this channel, it is still important to perform this measurement as many beyond-SM theories predict a strong enhancement of the $t\bar{t}$ asymmetry at high pseudorapidity [182].

5.4 (N)LO+PS asymmetries

As it is possible for LHCb to perform a simulation of the asymmetry at NLO+PS which includes the effects of detector response, it is important to compare the prediction at NLO+PS with NLO. To do this, `POWHEG` is matched to `Pythia8`(183) and compared to the equivalent fixed-order results at $\mathcal{O}(\alpha_s^3)$. As the fixed-order predictions of lepton asymmetries also retain NLO accuracy in the decay, the comparisons are performed at the top quark level for consistency. The rate and forward-backward asymmetries discussed in this study therefore refer only to the top quark level.

Both `POWHEG` and fixed-order results are obtained with the central CT10w PDF set, with the factorisation and renormalisation scales set equal to the top mass (m_t = 173.25 GeV). In principle, the two methods should be consistent to $\mathcal{O}(\alpha_s^4)$. However, previous studies have demonstrated that the PS can introduce large effects which alter the top quark distributions [183]. For this reason, the effect of the PS on the top quark distributions must be studied in detail. To do so, the following showering options are considered.:

- `Default` (def.). The subprocess is subsequently generated with the default `Pythia8`

options. This includes initial and final state radiation, multiple parton-parton interactions, and the structure of the beam remnants.

- `Interference asymmetry` (int. off). The subprocess is subsequently generated in the usual way, with the exception of the `SpaceShower:phiIntAsym` option, which is turned off (Default = on).

- `Beam remnants` (BR). The subprocess is subsequently generated only accounting for proton beam remnants. This supplements the subprocess with the protons remnants which ensures that charge, colour and momentum are conserved in the full pp collision. The final four-momentum of the particles in the subprocess is essentially unaltered.

The numerator of the rate asymmetry A^t is plotted as a function of pseudorapidity in Figure 5.9 (left). Also shown in Figure 5.9 (right) is the numerator of the forward-backward asymmetry $A_{fb}^{t\bar{t}}$ presented as a function of the absolute top quark rapidity difference — note the requirement $\eta_t, \eta_{\bar{t}} \in [2.0, 5.0]$.

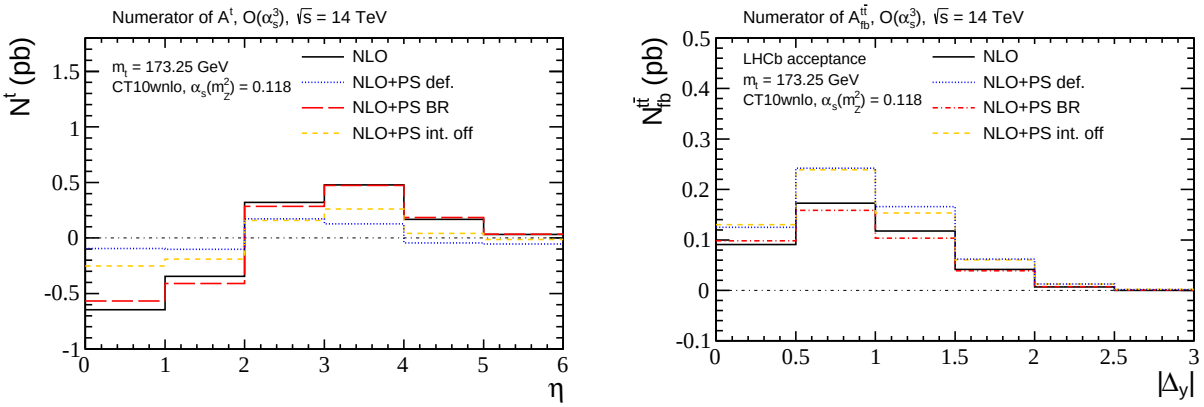


Figure 5.9: Numerator of the top quark rate asymmetry A^t (left) presented as a function of pseudorapidity, and the top quark forward-backward asymmetry $A_{fb}^{t\bar{t}}$ (right) as a function of absolute top quark rapidity difference. The NLO+PS prediction found for varying showering options is compared to the NLO result.

The NLO and NLO+PS BR predictions are consistent with one another for both variables. This demonstrates the compatibility of the `POWHEG` method with respect to the fixed-order result. However, the default showering clearly alters the distributions which ruins the NLO accuracy. For the rate asymmetry, the PS substantially reduces the magnitude of the

numerator across the entire pseudorapidity range, and even changes the sign at high pseudorapidity. These features are also observed with the interference asymmetry turned off, but are suppressed with respect to the default settings. For the forward-backward asymmetry, the PS enhances the numerator for low absolute rapidity differences. Turning off the interference asymmetry makes little difference in this case. The inclusive contribution to the numerator for both variables ,within the LHCb acceptance, is provided in Table 5.10

	NLO	NLO+PS BR	NLO+PS int. off	NLO+PS def.
N^t (pb)	1.00	0.98	0.44	0.20
$N^{t\bar{t}}_{fb}$ (pb)	0.43	0.41	0.60	0.61

Table 5.10: Contribution to the numerator (in units of pb) of the top quark rate and forward-backward asymmetry within the LHCb acceptance. The NLO+PS prediction with varying showering options is compared to the NLO result.

Within the LHCb acceptance, the default settings reduce the rate asymmetry by 80%, and enhance the forward-backward asymmetry by 50%. To understand the origin of these dramatic effects, separate samples of $q\bar{q} \to t\bar{t}$ and $gg \to t\bar{t}$ are generated at LO, and subsequently showered with the same options. These effects can then be identified by studying how different showering options impact the shapes of normalised distributions. The ratio of top and antitop quark pseudorapidity distributions are shown in Figure 5.10 for both $q\bar{q}$ (left) and gg (right) samples.

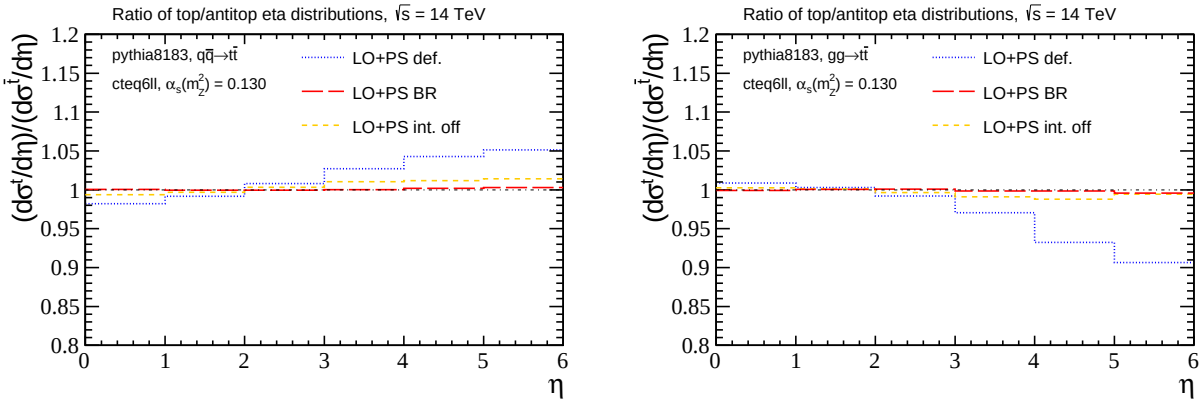


Figure 5.10: Ratio of top and antitop quark pseudorapidity distributions for different showering options. Separate samples of $q\bar{q} \to t\bar{t}$ (left) and $gg \to t\bar{t}$ (right) are generated at LO.

As expected, the LO+PS BR top and antitop quark distributions are symmetric. This

simply reflects that there is no asymmetry present in the Born cross section. With the default settings, a large asymmetry is generated by the PS — this asymmetry is also observed to have opposite behaviour for $q\bar{q}$ and gg samples. Turning off the interference asymmetry dramatically reduces this effect.

The physical origin of this asymmetry is a consequence of the implementation of a colour coherence effect in the initial state modelling. For both $q\bar{q} \to t\bar{t}$ and $gg \to t\bar{t}$ subprocesses, the colour flow is mirror symmetric. However, as the PS evolves backwards into the initial state, an asymmetry is introduced in the colour flow as there are more $q \to qg$ branchings due to the valence content of the proton. This is depicted in Figure 5.11.

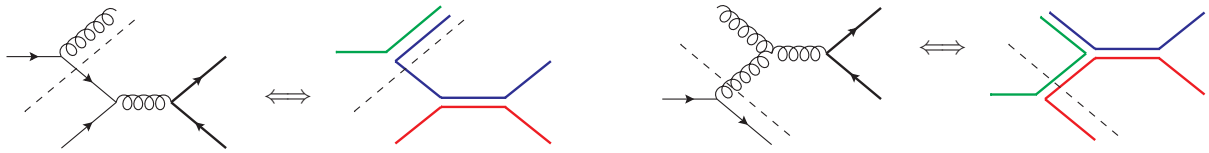


Figure 5.11: Depiction of asymmetric colour flows in $q\bar{q} \to t\bar{t}$ and $gg \to t\bar{t}$ subprocesses in association with an initial state $q \to qg$ branching.

In the case of a splitting prior to the $q\bar{q}$ subprocess, a colour dipole is created between the top quark and the gluon produced in the splitting. The interference asymmetry acts to align the azimuthal angle of the gluon to be close to that of its colour dipole partner (the antitop quark). Transforming into the transverse rest frame of the new $t\bar{t}g$ system ($p_T(t) + p_T(\bar{t}) + p_T(g) = 0$), results in the top quark being at lower p_T than the anti-top quark — or equivalently, at higher pseudorapidity. The opposite behaviour applies in the case of a splitting prior to the gg subprocess, where the colour dipole is created between the antitop quark and quark created in the splitting. For this reason, an artificial asymmetry is introduced in the top quark pseudorapidity distributions.

In the `POWHEG` generated events, this interference effect only applies to a small fraction of the full sample. This is a consequence of the colour configuration for events with a real emission, where colour dipoles are less likely to be created between the emitted parton and the outgoing (anti)top quark. As this interference is an attempt to model higher-order corrections, it should not be included at NLO+PS to avoid double counting effects which

have already been accounted for in the matrix element. Also, as the fixed-order contribution to the asymmetry from the qg subprocess has the opposite behaviour to the interference effect, as shown in Figure 5.3 (left), it should not be included at all.

When this interference effect is removed, the numerator of the rate asymmetry still receives a large modification (see the various (N)LO+PS int off. distributions), suggesting the presence of other effects. In the case of the forward-backward asymmetry, the modification of the numerator appears to be entirely due to other effects. To investigate this, the differential cross section with respect to the top quark pseudorapidity difference is studied for varying shower settings. In Figure 5.12, the ratio of Δ_y distributions is plotted with respect to the symmetric LO+PS BR distribution, which highlights the presence of asymmetric effects.

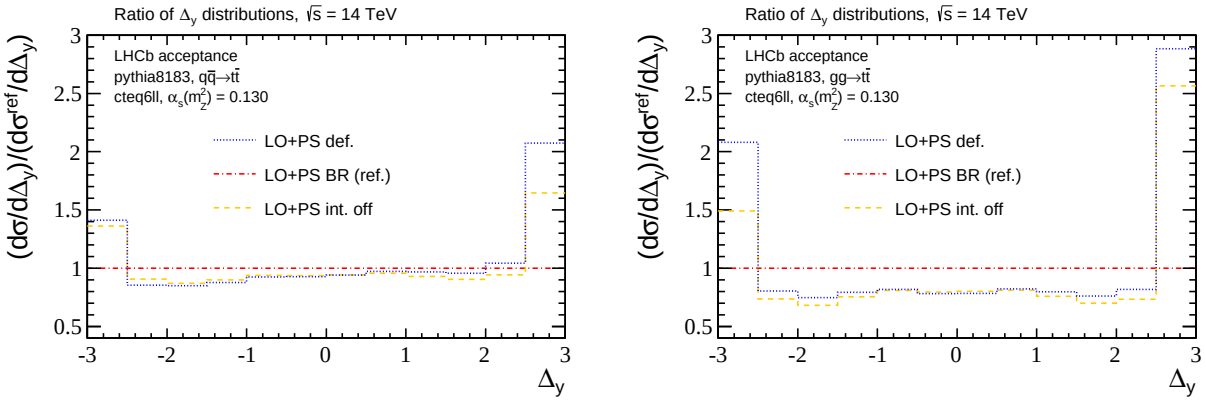


Figure 5.12: Ratio of top quark pseudorapidity difference distribution Δ_y. The reference distribution is LO+BS BR which is symmetric, and the top and antitop quark are required to be within the LHCb acceptance such that $\eta_t, \eta_{\bar{t}} \in [2.0, 5.0]$. Separate samples of $q\bar{q} \to t\bar{t}$ (left) and $gg \to t\bar{t}$ (right) are generated at LO.

This first noticeable effect is the migration of events into the large Δ_y bins. As the asymmetric cross section in this bin is extremely small, as shown in Figure 5.9 (right), this does not explain a large positive contribution to the inclusive asymmetry. For the gg subprocess, there is no apparent asymmetry generated in the Δ_y distribution. However, the $q\bar{q}$ subprocess generates a sizeable positive asymmetry. The origin of this effect is currently under investigation. In the meantime, it is clear that the effects introduced by `Pythia8` dramatically alter the NLO accuracy for these particular observables. Understanding the origin of all of these effects is necessary to provide accurate NLO+PS predictions for charge asymmetry variables at high pseudorapidity.

5.5 Summary

The potential sensitivity of charge asymmetry measurements at LHCb with the 14 TeV data has been studied. It has been proposed that lepton asymmetry measurements are possible in both the $\tilde{t}_{\mu b}$ and $\tilde{t}_{\mu eb}$ channels. In the case of the $\tilde{t}_{\mu b}$ channel, a rate asymmetry is defined which measures the rate of μ^+ to μ^- tagged events as a function of muon pseudorapidity. In the $\tilde{t}_{\mu eb}$ channel, it is possible to measure a forward-backward asymmetry by measuring the rapidity difference of the leptons on an event-by-event basis. Corresponding top quark asymmetry variables are also defined for both channels.

Fixed-order predictions, including QCD $\mathcal{O}(\alpha_s^3)$ and mixed QED $\mathcal{O}(\alpha_s^2\alpha_e)$ corrections, have been provided for all of the aforementioned asymmetries. The top quark asymmetries will be useful for estimating the size of currently unknown higher-order effects when they become available, while the lepton asymmetries have been provided with realistic analysis cuts. Both of the leptonic asymmetries are observed to be sizeable, approaching several percent in kinematically accessible regions. Potential sources of theoretical uncertainty which may affect the asymmetry predictions have also been discussed. The notable uncertainty is the choice of PDFs used to evaluate the denominator of the asymmetry. A conservative approach is to compute the denominator with NLO PDFs, while a less conservative approach is to attribute an uncertainty to the envelope of different predictions which are obtained with LO and NLO PDFs. In the latter case, LO PDFs with $\alpha_s(m_Z^2) \simeq 0.119$ should be employed.

The potential experimental sensitivity to both leptonic asymmetries has also been investigated. In the $\tilde{t}_{\mu b}$, precision asymmetry measurements are only possible if the asymmetric backgrounds are well understood. This may be possible by studying the correlations of the background shapes and normalisations for different final states. A naive statistical analysis suggests a non-zero asymmetry hypothesis may be rejected at 3.6σ CL when electron and muon final states are considered. There is essentially no background in the $\tilde{t}_{\mu eb}$ channel, meaning experimental uncertainty will be almost entirely statistical. Measurements in this channel are likely to be statistically limited. If there is a strong enhancement of the asymmetry at high pseudorapidity (a factor of 3 for example), then such an effect should be visible

with the full 14 TeV data.

Finally, it will become important to include the effects of detector response into charge asymmetry predictions. Therefore a comparison of asymmetry predictions at (N)LO+PS and NLO was performed. The NLO+PS sample is generated with `POWHEG` matched to `Pythia8`, as LHCb simulation uses `Pythia8` as the default generator. It is found that the PS introduces several effects which alter the top quark distributions, removing the NLO accuracy. Although some understanding has been gained as to the origin of these effects, there are still other effects present which are not understood.

Conclusions

The goal of this thesis was to study the feasibility of top quark physics measurements at high pseudorapidity. In order to do so, it was first necessary to develop the theoretical tools required to make reliable predictions of LHC collisions.

This is achieved by applying several theoretical techniques which are relevant at different energy scales. In particular, the factorisation theorem which separates the full hadron-hadron scattering into a chain of sequential subprocesses. This allows fixed-order perturbation theory to be applied to the calculation of a short-distance interaction, while the higher-order corrections can be accounted for in an approximate all-orders approach. It is also important to mention the recent development of theoretical tools, which now allow fixed-order calculations beyond LO to be interfaced with all-orders effects in the final state. These tools have now become an integral part of many LHC analyses.

Before performing studies of top quarks, it was necessary to discuss the top quarks properties, and their relevance within the SM. Having discussed the current experimental constraints on the top quark mass, and its relevance on both direct and indirect observables, the important features of top quark production and decay were discussed. This highlighted that forwardly produced top quarks are naturally sensitive to high-x incoming partons in their production. As the production of top quark pairs proceeds predominantly through the gg production process, this suggests that cross section measurements at high pseudorapidity may provide constraints on the large-x gluon PDF. The production of top quark pairs also receives an asymmetric contribution from quark initiated processes. As the contribution from the symmetric gg channel is relatively suppressed for forwardly produced top quark

pairs, this indicated that high pseudorapidity measurements may also be sensitive to this charge asymmetry. This is also motivated by measurements of the charge asymmetry at the TeVatron, where an enhanced asymmetry is observed for forwardly (backwardly) produced (anti)top quarks in pair production.

Top quark production has currently not been observed at high pseudorapidity. It is therefore important to investigate the feasibility of top quark measurements with LHCb data. To do this, several analysis strategies were proposed. All of the proposed analyses rely on partially reconstructing the full $t\bar{t}$ system, which is necessary to gain reasonable event rates. By requiring the presence of and isolated charge lepton, b-tagged jets, and carefully selected kinematic cuts, it becomes possible to observe the $t\bar{t}$ process in several final states with the available data. When the 14 TeV data becomes available, statistically precise measurements will become possible in both single and dilepton final states. Of particular interest is the $\tilde{t}_{\mu eb}$ channel, corresponding to the reconstruction of an opposite flavour lepton pair in association with a b-jet, where there contribution from background processes is negligible.

A detailed study of the theoretical systematics of forwardly produced top quarks in top quark pair production was also performed. This study demonstrates that forwardly produced top quarks are particularly sensitive to PDFs. To quantify this sensitivity, a reweighting procedure was applied to both Hessian and replica PDF sets based on the assumption of a parton level cross section measurement within the LHCb acceptance at 14 TeV. This was shown to provide constraints on the gluon PDF within the range $x \in [0.1, 0.3]$, where the current constraints are rather weak. It was also suggested that cross section measurements, which include analysis cuts, will be more constraining than the assumption of a parton level cross section. The constraints provided by these measurements will be important for many processes studied at the LHC as well as future hadron colliders. For example, improving the prediction for the Higgs boson cross section, which proceeds predominantly through the gg channel. These constraints should also improve the limits on searches for new strongly produced particles.

The analyses strategies developed for cross section measurements can also be extended to

charge asymmetry measurements. To do this, leptonic rate and forward-backward asymmetry variables were proposed for the single and dilepton final states respectively. By providing fixed-order predictions for both of these asymmetries, the experimental sensitivity to these asymmetries was quantified. Both of the proposed asymmetries are statistically feasible with the full 14 TeV data. Statistically, a non-zero asymmetry can be excluded beyond 3.6σ CL. The sensitivity to the leptonic rate asymmetry is ultimately dependent on how well the asymmetric background processes are known. This is a question which can only be answered by experimental investigation. The inclusive forward-backward asymmetry within the LHCb acceptance exceeds 1%, and has essentially no background. The statistical sensitivity in this channel to the SM asymmetry is poor as the expected statistical uncertainty is approximately (1-2)%. However, if new physics is responsible for the large asymmetry observed for forwardly produced top quarks at the TeVatron, this will also be observable in the leptonic forward-backward asymmetry at LHCb.

As well as the physics motivations for studying top quark physics at high pseudorapidity, these studies have also highlighted the need for an improvement in theoretical tools. In particular, how the PS treats top quark distributions. These effects, which also alter top quark predictions in the central region, were identified as they are exaggerated in extreme kinematical configurations. Gaining a better understanding of these effects will undoubtedly improve the precision of experimental measurements of both ATLAS and CMS, as well as LHCb.

Top quark measurements at high pseudorapidity are clearly well motivated, and I fully encourage the LHCb collaboration to prioritise research efforts in this direction.

Appendix A

CKM Matrix

The CKM matrix, introduced in Subsection 1.2.3, is a 3×3 unitary matrix parameterised by three mixing angles and a single complex phase. This is commonly parameterised as

$$V_{\mathrm{CKM}} = \begin{pmatrix} c_{12}c_{13} & s_{12}s_{13} & s_{13}e^{-i\delta} \\ -s_{12}c_{23} - c_{12}s_{23}s_{13}e^{i\delta} & c_{12}c_{23} - s_{12}s_{23}s_{13}e^{i\delta} & s_{23}c_{13} \\ s_{12}s_{23} - c_{12}c_{23}s_{13}e^{i\delta} & -c_{12}s_{23} - s_{12}c_{23}s_{13}e^{i\delta} & c_{23}c_{13} \end{pmatrix} \tag{A.1}$$

where $s_{ij} = sin\,\theta_{ij}$, $c_{ij} = cos\,\theta_{ij}$, and δ is the phase which introduces CP-violating effects in flavour-changing processes within the SM.

An alternative parameterisation, introduced by Wolfenstein [184], takes advantage of the observed hierarchy $s_{13} \ll s_{23} \ll s_{12} \ll 1$. This parameterisation has the following definitions

$$\begin{aligned} s_{12} = \lambda = \frac{|V_u s|}{\sqrt{|V_u d|^2 + |V_u s|^2}}\,, \qquad s_{23} = A\lambda^2 = \lambda \left|\frac{V_{cb}}{V_{us}}\right|\,, \\ s_{13}e^{i\delta} = V_{ub}^* = A\lambda^3(\rho + i\eta) = \frac{A\lambda^3(\bar{\rho} + i\bar{\eta})\sqrt{1 - A^2\lambda^4}}{\sqrt{1-\lambda^2}[1 - A^2\lambda^4(\bar{\rho} + i\bar{\eta})]}\,. \end{aligned} \tag{A.2}$$

With these definitions, the CKM matrix may then be conveniently expanded in λ as

$$V_{\text{CKM}} = \begin{pmatrix} V_{ud} & V_{us} & V_{ub} \\ V_{cd} & V_{cs} & V_{cb} \\ V_{td} & V_{ts} & V_{tb} \end{pmatrix} = \begin{pmatrix} 1-\lambda^2/2 & \lambda & A\lambda^3(\rho - i\eta) \\ -\lambda & 1-\lambda^2/2 & A\lambda^2 \\ A\lambda^3(1-\rho-i\eta) & A\lambda^2 & 1 \end{pmatrix} + \mathcal{O}(\lambda^4)\,. \quad \text{(A.3)}$$

As the CKM matrix is unitary within the SM, this imposes the relations

$$\sum_j V_{ij} V_{kj}^* = \delta_{ik}\,, \qquad \sum_i V_{ij} V_{ik}^* = \delta_{jk}\,. \quad \text{(A.4)}$$

These relations can then be used to constrain new physics which alter these relations.

A fit for the Wolfenstein parameters, provided in the PDG [15], introduced in (A.2) gives

$$\begin{aligned} \lambda &= 0.22535 \pm 0.00065\,, & A &= 0.811^{+0.022}_{-0.012}\,, \\ \bar{\rho} &= 0.131^{+0.026}_{-0.013}\,, & \bar{\eta} &= 0.345^{+0.013}_{-0.014}\,. \end{aligned} \quad \text{(A.5)}$$

Note that this fit imposes CKM unitarity. A similar fit for the magnitudes of all nine CKM elements gives

$$V_{\text{CKM}} = \begin{pmatrix} 0.97427 \pm 0.00015 & 0.22534 \pm 0.00065 & 0.00351^{+0.00015}_{-0.00014} \\ 0.22520 \pm 0.00065 & 0.97344 \pm 0.00016 & 0.0412^{+0.0011}_{-0.0005} \\ 0.00867^{+0.00029}_{-0.00031} & 0.404^{+0.0011}_{-0.0005} & 0.999146^{+0.000021}_{-0.000046} \end{pmatrix}. \quad \text{(A.6)}$$

Importantly, direct constraints on many of these elements individually is rather weak. For example, an update on the direct constraints on $|V_{tb}|$, including single top cross section measurements with available 7 and 8 TeV data, was recently provided by CMS [185] to be: $|V_{tb}| > 0.92$ at 95% confidence level.

Appendix B

Quark self-energy

As an example of how to perform dimensional regularisation, the quark self-energy is calculated. The quark mass term is neglected throughout the calculation. The calculation proceeds by evaluating the following amplitude

$$\sum_{A,B} \int \frac{d^4l}{(2\pi)^4} (ig_s)^2 t^A_{ab} \gamma^\mu \frac{-i\delta^{AB}}{l^2 + i\epsilon} g_{\mu\nu} \frac{i(\not{p} - \not{l})}{(p-l)^2 + i\epsilon} t^B_{bc} \gamma^\nu \,. \tag{B.1}$$

Continuing to d dimensions of space-time, ignoring odd powers of loop momentum gives

$$-\sum_A t^A_{ab} t^A_{bc} g_s^2 \int \frac{d^dl}{(2\pi)^d} \gamma^\mu \frac{1}{l^2 + i\epsilon} g_{\mu\nu} \frac{\not{p}}{(p-l)^2 + i\epsilon} \gamma^\nu \,. \tag{B.2}$$

In d-dimensions $\gamma_\nu \gamma^\mu \gamma^\nu = (2-d)\gamma^\mu$, and using $SU(3)$ colour relations this becomes

$$\not{p} C_F (d-2) g_s^2 \int \frac{d^dl}{(2\pi)^d} \frac{1}{l^2 + i\epsilon} \frac{1}{(p-l)^2 + i\epsilon} \,. \tag{B.3}$$

This integral now has the form

$$\mathcal{I} = \int \frac{d^dl}{(2\pi)^d} \frac{1}{l^2 + i\epsilon} \frac{1}{(p-l)^2 + i\epsilon} \,. \tag{B.4}$$

This can be evaluated using the Feynman parameterisation, which is used to isolate the divergent poles found when performing the integral in 4-dimensions. Using the parameteri-

sation

$$\frac{1}{AB} = \int_0^1 dxdy\delta(x+y-1)\frac{1}{[xA+yB]^2}\,, \tag{B.5}$$

the integral becomes

$$\mathcal{I} = \int \frac{d^dl}{(2\pi)^d}\int_0^1 dxdy\delta(x+y-1)\frac{1}{[x(l^2+i\epsilon)+y(p-l)^2+yi\epsilon]^2}\,. \tag{B.6}$$

Integrating over the Feynman parameter x, and shifting momentum to $q = l - yp$ gives

$$\mathcal{I} = \int \frac{d^dl}{(2\pi)^d}\int_0^1 dy\frac{1}{[q^2+y(1-y)p^2+i\epsilon]^2}\,. \tag{B.7}$$

Using the subsitituion $M^2 = y(1-y)p^2 i\epsilon$, finally

$$\mathcal{I} = \int \frac{d^dl}{(2\pi)^d}\int_0^1 dy\frac{1}{[q^2+M^2]^2}\,. \tag{B.8}$$

At this stage the calculation can be completed in the usual way by performing a Wick rotation and surface integral in d-dimensions. That is

$$\begin{aligned} q^0 &\to iq_E^0\,, \\ d^dq &\to d\Omega_d q^{d-1}dq\,. \end{aligned} \tag{B.9}$$

The integral then has the following form

$$\mathcal{I} = i\int \frac{d\Omega_d}{(2\pi)^d}\int_0^1 dy\int_0^\infty \frac{dq_E q_E^{d-1}}{[q_E^2+M^2]^2}\,. \tag{B.10}$$

The surface integral can be performed by using the relation for a gaussian integral

$$(\sqrt{\pi})^d = (\int dxe^{-x^2})^d = \int d^dxe^{-\sum_i^d x_i^2} = \int d\Omega_d\int_0^\infty dxx^{d-1}e^{-x^2}\,, \tag{B.11}$$

and then changing integration variables for the last term, $dx^2 = 2xdx$, gives

$$\int_0^\infty dxx^{d-1}e^{-x^2} = \frac{1}{2}\int_0^\infty dx^2(x^2)^{\frac{d}{2}-1}e^{-x^2}\,. \tag{B.12}$$

By using the definition of the Gamma function

$$\Gamma(z) = \int_0^\infty t^{z-1} e^{-t} dt \,, \tag{B.13}$$

the integral can be re-written as

$$\mathcal{I} = i \left(\frac{\sqrt{\pi}}{2\pi}\right)^d \frac{1}{\Gamma(d/2)} \int_0^1 dy \int_0^\infty \frac{dq_E^2 (q_E^2)^{\frac{d}{2}-1}}{[q_E^2 + M^2]^2} \,. \tag{B.14}$$

This is easily solved with the change of variables

$$x = \frac{M^2}{q_E^2 + M^2} \,. \tag{B.15}$$

The result is

$$\mathcal{I} = i \left(\frac{\sqrt{\pi}}{2\pi}\right)^d \frac{1}{\Gamma(d/2)} \int_0^1 dy \left(\frac{1}{M^2}\right)^{2-\frac{d}{2}} \int_0^1 dx x^{1-\frac{d}{2}} (1-x)^{\frac{d}{2}-1} \,. \tag{B.16}$$

Introducing the definition of the beta function

$$\int_0^1 dx x^{\alpha-1} (1-x)^{\beta-1} = B(\alpha, \beta) = \frac{\Gamma(\alpha)\Gamma(\alpha)}{\Gamma(\alpha+\beta)} \,, \tag{B.17}$$

the integral becomes

$$\mathcal{I} = i \left(\frac{\sqrt{\pi}}{2\pi}\right)^d \int_0^1 dy \left(\frac{1}{M^2}\right)^{2-\frac{d}{2}} \Gamma(2 - d/2) \,. \tag{B.18}$$

The final step necessary to isolate the poles and finites pieces is to perform an expansion around the pole of the gamma function at $d = 4 - 2\epsilon$, this gives

$$\mathcal{I} = i \left(\frac{1}{4\pi}\right)^2 \mu^{2\epsilon} \int_0^1 dy \left(\frac{4\pi}{M^2}\right)^\epsilon \Gamma(\epsilon) \,. \tag{B.19}$$

By expanding both the gamma function and polynomial in ϵ

$$\mathcal{I} = i\left(\frac{1}{4\pi}\right)^2 \int_0^1 dy \left(1 + \epsilon ln\left(\frac{4\pi\mu^2}{M^2}\right) + \mathcal{O}(\epsilon^2)\right)\left(\frac{1}{\epsilon} - \gamma_E + \mathcal{O}(\epsilon)\right) . \tag{B.20}$$

The divergences are now isolated in poles of $1/\epsilon$ in the expansion of the gamma function in the limit $\epsilon \to 0$. Finally

$$\mathcal{I} = i\left(\frac{1}{4\pi}\right)^2 \left(\frac{1}{\epsilon} - \gamma_E + ln(4\pi) + \int_0^1 dy ln\left(\frac{\mu^2}{M^2}\right)\right) . \tag{B.21}$$

Both finite pieces and the pole in $1/\epsilon$ are now isolated and can be re-absorbed into a re-definition of fields and parameters. Including pre-factors, the subtraction term δ_2 is given by

$$\delta_2 = -C_F \frac{\alpha_s}{4\pi}\frac{1}{\epsilon} \tag{B.22}$$

In a similar fashion, the subtraction terms for the self-energy and vertex corrections can be calculated. These are given by

$$\begin{aligned} \delta_1 &= -(C_F + C_A)\frac{\alpha_s}{4\pi}\frac{1}{\epsilon} \\ \delta_3 &= \left(\frac{5}{3}C_A - \frac{4}{3}n_f T_F\right)\frac{\alpha_s}{4\pi}\frac{1}{\epsilon} \end{aligned} \tag{B.23}$$

which together provide the first term, b_0, in the expansion of the QCD β-function.

Bibliography

[1] ATLAS Collaboration, G. Aad et al., *Observation of a new particle in the search for the Standard Model Higgs boson with the ATLAS detector at the LHC*, Phys. Lett. **B716** (2012) 1, arXiv:1207.7214.

[2] CMS Collaboration, S. Chatrchyan et al., *Observation of a new boson at a mass of 125 GeV with the CMS experiment at the LHC*, Phys. Lett. **B716** (2012) 30, arXiv:1207.7235.

[3] R. Gauld, *Feasibility of top quark measurements at LHCb and constraints on the large-x gluon PDF*, JHEP **1402** (2014) 126, arXiv:1311.1810.

[4] R. Gauld, *Leptonic top-quark asymmetry predictions at LHCb*, arXiv:1409.8631.

[5] R. Gauld, *Measuring top quark production asymmetries at LHCb*, Tech. Rep. LHCb-PUB-2013-009. CERN-LHCb-PUB-2013-009, CERN, Geneva, Jun, 2013.

[6] H. Lehmann, K. Symanzik, and W. Zimmermann, *On the formulation of quantized field theories*, Nuovo Cim. **1** (1955) 205.

[7] C. Burgess and G. Moore, *The standard model: A primer*, .

[8] R. K. Ellis, W. J. Stirling, and B. Webber, *QCD and collider physics*, Camb. Monogr. Part. Phys. Nucl. Phys. Cosmol. **8** (1996) 1.

[9] M. E. Peskin and D. V. Schroeder, *An Introduction to quantum field theory*, .

[10] M. L. Mangano, *Introduction to QCD*, .

[11] P. Skands, *Introduction to QCD*, arXiv:1207.2389.

[12] P. W. Higgs, *Broken symmetries and the masses of gauge bosons*, Phys. Rev. Lett. **13** (1964) 508.

[13] F. Englert and R. Brout, *Broken symmetry and the mass of gauge vector mesons*, Phys. Rev. Lett. **13** (1964) 321.

[14] G. Guralnik, C. Hagen, and T. Kibble, *Global Conservation Laws and Massless Particles*, Phys. Rev. Lett. **13** (1964) 585.

[15] Particle Data Group, J. Beringer et al., *Review of particle physics*, Phys. Rev. **D86** (2012) 010001.

[16] L. Faddeev and V. Popov, *Feynman Diagrams for the Yang-Mills Field*, Phys. Lett. **B25** (1967) 29.

[17] D. J. Gross and F. Wilczek, *Ultraviolet Behavior of Nonabelian Gauge Theories*, Phys. Rev. Lett. **30** (1973) 1343.

[18] S. Bethke, *The 2009 World Average of alpha(s)*, Eur. Phys. J. **C64** (2009) 689, arXiv:0908.1135.

[19] HPQCD Collaboration, C. Davies et al., *Update: Accurate Determinations of alpha(s) from Realistic Lattice QCD*, Phys. Rev. **D78** (2008) 114507, arXiv:0807.1687.

[20] S. Drell and T.-M. Yan, *Massive Lepton Pair Production in Hadron-Hadron Collisions at High-Energies*, Phys. Rev. Lett. **25** (1970) 316.

[21] R. V. Harlander and W. B. Kilgore, *Next-to-next-to-leading order Higgs production at hadron colliders*, Phys. Rev. Lett. **88** (2002) 201801, arXiv:hep-ph/0201206.

[22] C. Anastasiou et al., *Higgs boson gluon-fusion production at threshold in N3LO QCD*, arXiv:1403.4616.

[23] T. Kinoshita, *Mass singularities of Feynman amplitudes*, J. Math. Phys. **3** (1962) 650.

[24] T. Lee and M. Nauenberg, *Degenerate Systems and Mass Singularities*, Phys. Rev. **133** (1964) B1549.

[25] T. Sjostrand and P. Z. Skands, *Transverse-momentum-ordered showers and interleaved multiple interactions*, Eur. Phys. J. **C39** (2005) 129, arXiv:hep-ph/0408302.

[26] S. Schumann and F. Krauss, *A Parton shower algorithm based on Catani-Seymour dipole factorisation*, JHEP **0803** (2008) 038, arXiv:0709.1027.

[27] S. Catani and M. Grazzini, *Infrared factorization of tree level QCD amplitudes at the next-to-next-to-leading order and beyond*, Nucl. Phys. **B570** (2000) 287, arXiv:hep-ph/9908523.

[28] G. Altarelli and G. Parisi, *Asymptotic Freedom in Parton Language*, Nucl. Phys. **B126** (1977) 298.

[29] V. Gribov and L. Lipatov, *Deep inelastic e p scattering in perturbation theory*, Sov. J. Nucl. Phys. **15** (1972) 438.

[30] Y. L. Dokshitzer, *Calculation of the Structure Functions for Deep Inelastic Scattering and e+ e- Annihilation by Perturbation Theory in Quantum Chromodynamics.*, Sov. Phys. JETP **46** (1977) 641.

[31] W. Furmanski and R. Petronzio, *Singlet Parton Densities Beyond Leading Order*, Phys. Lett. **B97** (1980) 437.

[32] G. Curci, W. Furmanski, and R. Petronzio, *Evolution of Parton Densities Beyond Leading Order: The Nonsinglet Case*, Nucl. Phys. **B175** (1980) 27.

[33] S. Moch, J. Vermaseren, and A. Vogt, *The Three loop splitting functions in QCD: The Nonsinglet case*, Nucl. Phys. **B688** (2004) 101, arXiv:hep-ph/0403192.

[34] A. Vogt, S. Moch, and J. Vermaseren, *The Three-loop splitting functions in QCD: The Singlet case*, Nucl. Phys. **B691** (2004) 129, arXiv:hep-ph/0404111.

[35] S. Catani, F. Krauss, R. Kuhn, and B. Webber, *QCD matrix elements + parton showers*, JHEP **0111** (2001) 063, arXiv:hep-ph/0109231.

[36] S. Frixione and B. R. Webber, *Matching NLO QCD computations and parton shower simulations*, JHEP **0206** (2002) 029, arXiv:hep-ph/0204244.

[37] P. Nason, *A New method for combining NLO QCD with shower Monte Carlo algorithms*, JHEP **0411** (2004) 040, arXiv:hep-ph/0409146.

[38] K. Hamilton, P. Nason, C. Oleari, and G. Zanderighi, *Merging H/W/Z + 0 and 1 jet at NLO with no merging scale: a path to parton shower + NNLO matching*, JHEP **1305** (2013) 082, arXiv:1212.4504.

[39] K. Hamilton, P. Nason, E. Re, and G. Zanderighi, *NNLOPS simulation of Higgs boson production*, JHEP **1310** (2013) 222, arXiv:1309.0017.

[40] P. Nason and B. Webber, *Next-to-Leading-Order Event Generators*, Ann. Rev. Nucl. Part. Sci. **62** (2012) 187, arXiv:1202.1251.

[41] S. Frixione, P. Nason, and C. Oleari, *Matching NLO QCD computations with Parton Shower simulations: the POWHEG method*, JHEP **0711** (2007) 070, arXiv:0709.2092.

[42] S. Alioli, P. Nason, C. Oleari, and E. Re, *A general framework for implementing NLO calculations in shower Monte Carlo programs: the POWHEG BOX*, JHEP **1006** (2010) 043, arXiv:1002.2581.

[43] T. Sjostrand, S. Mrenna, and P. Z. Skands, *A Brief Introduction to PYTHIA 8.1*, Comput. Phys. Commun. **178** (2008) 852, arXiv:0710.3820.

[44] J. M. Campbell and R. Ellis, *MCFM for the Tevatron and the LHC*, Nucl. Phys. Proc. Suppl. **205-206** (2010) 10, arXiv:1007.3492.

[45] S. Alioli, P. Nason, C. Oleari, and E. Re, *NLO vector-boson production matched with shower in POWHEG*, JHEP **0807** (2008) 060, arXiv:0805.4802.

[46] Y. I. Azimov, Y. L. Dokshitzer, V. A. Khoze, and S. Troyan, *Similarity of Parton and Hadron Spectra in QCD Jets*, Z. Phys. **C27** (1985) 65.

[47] B. Andersson, G. Gustafson, G. Ingelman, and T. Sjostrand, *Parton Fragmentation and String Dynamics*, Phys. Rept. **97** (1983) 31.

[48] B. Webber, *A QCD Model for Jet Fragmentation Including Soft Gluon Interference*, Nucl. Phys. **B238** (1984) 492.

[49] J.-C. Winter, F. Krauss, and G. Soff, *A Modified cluster hadronization model*, Eur. Phys. J. **C36** (2004) 381, arXiv:hep-ph/0311085.

[50] X. Artru and G. Mennessier, *String model and multiproduction*, Nucl. Phys. **B70** (1974) 93.

[51] D. Amati and G. Veneziano, *Preconfinement as a Property of Perturbative QCD*, Phys. Lett. **B83** (1979) 87.

[52] R. D. Field and S. Wolfram, *A QCD Model for e+ e- Annihilation*, Nucl. Phys. **B213** (1983) 65.

[53] M. Creutz, *Monte Carlo Study of Quantized SU(2) Gauge Theory*, Phys. Rev. **D21** (1980) 2308.

[54] M. Cacciari, G. P. Salam, and G. Soyez, *The Anti-k(t) jet clustering algorithm*, JHEP **0804** (2008) 063, arXiv:0802.1189.

[55] LHCb Collaboration, *Measurement of jet production in $Z^0/\gamma^* \to \mu^+\mu^-$ events at LHCb in $\sqrt{s} = 7$ TeV pp collisions*, .

[56] LHCb collaboration, R. Aaij et al., *First measurement of the charge asymmetry in beauty-quark pair production*, arXiv:1406.4789.

[57] CMS Collaboration, S. Chatrchyan et al., *Identification of b-quark jets with the CMS experiment*, JINST **8** (2013) P04013, arXiv:1211.4462.

[58] S. Alekhin, J. Blumlein, and S. Moch, *Parton Distribution Functions and Benchmark Cross Sections at NNLO*, Phys. Rev. **D86** (2012) 054009, arXiv:1202.2281.

[59] H.-L. Lai et al., *New parton distributions for collider physics*, Phys. Rev. **D82** (2010) 074024, arXiv:1007.2241.

[60] ZEUS Collaboration, H1 Collaboration, A. Cooper-Sarkar, *PDF Fits at HERA*, PoS **EPS-HEP2011** (2011) 320, arXiv:1112.2107.

[61] A. Martin, W. Stirling, R. Thorne, and G. Watt, *Parton distributions for the LHC*, Eur. Phys. J. **C63** (2009) 189, arXiv:0901.0002.

[62] R. D. Ball et al., *Impact of Heavy Quark Masses on Parton Distributions and LHC Phenomenology*, Nucl. Phys. **B849** (2011) 296, arXiv:1101.1300.

[63] R. Thorne, *The effect on PDFs and $\alpha_S(M_Z^2)$ due to changes in flavour scheme and higher twist contributions*, Eur. Phys. J. **C74** (2014) 2958, arXiv:1402.3536.

[64] F. James and M. Roos, *Minuit: A System for Function Minimization and Analysis of the Parameter Errors and Correlations*, Comput. Phys. Commun. **10** (1975) 343.

[65] D. Stump et al., *Uncertainties of predictions from parton distribution functions. 1. The Lagrange multiplier method*, Phys. Rev. **D65** (2001) 014012, arXiv:hep-ph/0101051.

[66] J. Pumplin et al., *Uncertainties of predictions from parton distribution functions. 2. The Hessian method*, Phys. Rev. **D65** (2001) 014013, arXiv:hep-ph/0101032.

[67] R. Thorne et al., *Questions on uncertainties in parton distributions*, J. Phys. **G28** (2002) 2717, arXiv:hep-ph/0205233.

[68] J. Pumplin et al., *New generation of parton distributions with uncertainties from global QCD analysis*, JHEP **0207** (2002) 012, arXiv:hep-ph/0201195.

[69] S. Forte, L. Garrido, J. I. Latorre, and A. Piccione, *Neural network parametrization of deep inelastic structure functions*, JHEP **0205** (2002) 062, arXiv:hep-ph/0204232.

[70] NNPDF Collaboration, L. Del Debbio et al., *Unbiased determination of the proton structure function F(2)**p with faithful uncertainty estimation*, JHEP **0503** (2005) 080, arXiv:hep-ph/0501067.

[71] NNPDF Collaboration, L. Del Debbio et al., *Neural network determination of parton distributions: The Nonsinglet case*, JHEP **0703** (2007) 039, arXiv:hep-ph/0701127.

[72] R. D. Ball et al., *Parton distributions with LHC data*, Nucl. Phys. **B867** (2013) 244, arXiv:1207.1303.

[73] M. Whalley, D. Bourilkov, and R. Group, *The Les Houches accord PDFs (LHAPDF) and LHAGLUE*, arXiv:hep-ph/0508110.

[74] NNPDF Collaboration, R. D. Ball et al., *Reweighting NNPDFs: the W lepton asymmetry*, Nucl. Phys. **B849** (2011) 112, arXiv:1012.0836.

[75] R. D. Ball et al., *Reweighting and Unweighting of Parton Distributions and the LHC W lepton asymmetry data*, Nucl. Phys. **B855** (2012) 608, arXiv:1108.1758.

[76] G. Watt and R. Thorne, *Study of Monte Carlo approach to experimental uncertainty propagation with MSTW 2008 PDFs*, JHEP **1208** (2012) 052, arXiv:1205.4024.

[77] H. Paukkunen and P. Zurita, *PDF reweighting in the Hessian matrix approach*, arXiv:1402.6623.

[78] B. Watt, P. Motylinski, and R. Thorne, *The Effect of LHC Jet Data on MSTW PDFs*, arXiv:1311.5703.

[79] CDF Collaboration, F. Abe et al., *Observation of top quark production in $\bar{p}p$ collisions*, Phys. Rev. Lett. **74** (1995) 2626, arXiv:hep-ex/9503002.

[80] D0 Collaboration, S. Abachi et al., *Observation of the top quark*, Phys. Rev. Lett. **74** (1995) 2632, arXiv:hep-ex/9503003.

[81] D0 Collaboration, *Publicly available top quark results*, http://www-d0.fnal.gov/Run2Physics/top/top_public_web_pages/top_results_runII.html.

[82] CDF Collaboration, *Publicly available top quark results*, http://www-cdf.fnal.gov/physics/new/top/top.html.

[83] ATLAS Collaboration, *Publicly available top quark results*, https://twiki.cern.ch/twiki/bin/view/AtlasPublic/TopPublicResults.

[84] CMS Collaboration, *Publicly available top quark results*, https://twiki.cern.ch/twiki/bin/view/CMSPublic/PhysicsResultsTOP.

[85] CDF Collaboration, T. Aaltonen et al., *Measurement of the top quark forward-backward production asymmetry and its dependence on event kinematic properties*, Phys. Rev. **D87** (2013) 092002, arXiv:1211.1003.

[86] CDF Collaboration, T. A. Aaltonen et al., *Measurement of the leptonic asymmetry in ttbar events produced in ppbar collisions at sqrt(s)=1.96 TeV*, Phys. Rev. D 88, **072003** (2013) , arXiv:1308.1120.

[87] D0 Collaboration, V. M. Abazov et al., *Measurement of the forward-backward asymmetry in top quark-antiquark production in ppbar collisions using the lepton+jets channel*, arXiv:1405.0421.

[88] D0 Collaboration, V. M. Abazov et al., *Measurement of the forward-backward asymmetry in the distribution of leptons in $t\bar{t}$ events in the lepton+jets channel*, arXiv:1403.1294.

[89] D0 Collaboration, V. M. Abazov et al., *Measurement of the asymmetry in angular distributions of leptons produced in dilepton ttbar final states in $p\bar{p}$ collisions at $\sqrt{s} =$ 1.96 TeV*, arXiv:1308.6690.

[90] R. Tarrach, *The Pole Mass in Perturbative QCD*, Nucl. Phys. **B183** (1981) 384.

[91] K. Melnikov and T. v. Ritbergen, *The Three loop relation between the MS-bar and the pole quark masses*, Phys. Lett. **B482** (2000) 99, arXiv:hep-ph/9912391.

[92] W. J. Marciano, *Fermi constants and 'New Physics'*, Phys. Rev. **D60** (1999) 093006, arXiv:hep-ph/9903451.

[93] D. Ross and M. Veltman, *Neutral Currents in Neutrino Experiments*, Nucl. Phys. **B95** (1975) 135.

[94] G. Buchalla and A. J. Buras, *The rare decays $K \to$ pi neutrino anti-neutrino, $B \to$ X neutrino anti-neutrino and $B \to$ lepton+ lepton: An Update*, Nucl. Phys. **B548** (1999) 309, arXiv:hep-ph/9901288.

[95] I. I. Bigi, *UPPER BOUNDS ON THE TOP QUARK MASS FROM B(s) anti-B(s) MIXING*, Phys. Lett. **B162** (1985) 383.

[96] A. Akhundov, D. Y. Bardin, and T. Riemann, *Electroweak One Loop Corrections to the Decay of the Neutral Vector Boson*, Nucl. Phys. **B276** (1986) 1.

[97] G. Degrassi et al., *Higgs mass and vacuum stability in the Standard Model at NNLO*, JHEP **1208** (2012) 098, arXiv:1205.6497.

[98] ATLAS Collaboration, CDF Collaboration, CMS Collaboration, D0 Collaboration, *First combination of Tevatron and LHC measurements of the top-quark mass*, arXiv:1403.4427.

[99] CDF Collaboration, A. Abulencia et al., *Top quark mass measurement using the template method in the lepton + jets channel at CDF II*, Phys. Rev. **D73** (2006) 032003, arXiv:hep-ex/0510048.

[100] CDF Collaboration, A. Abulencia et al., *Precise measurement of the top quark mass in the lepton+jets topology at CDF II*, Phys. Rev. Lett. **99** (2007) 182002, arXiv:hep-ex/0703045.

[101] P. Z. Skands and D. Wicke, *Non-perturbative QCD effects and the top mass at the Tevatron*, Eur. Phys. J. **C52** (2007) 133, arXiv:hep-ph/0703081.

[102] S. Alekhin, A. Djouadi, and S. Moch, *The top quark and Higgs boson masses and the stability of the electroweak vacuum*, Phys. Lett. **B716** (2012) 214, arXiv:1207.0980.

[103] ATLAS Collaboration, G. Aad et al., *Measurement of the $t\bar{t}$ production cross-section using $e\mu$ events with b-tagged jets in pp collisions at $\sqrt{s} = 7$ and 8 TeV with the ATLAS detector*, arXiv:1406.5375.

[104] U. Baur, A. Juste, L. Orr, and D. Rainwater, *Probing electroweak top quark couplings at hadron colliders*, Phys. Rev. **D71** (2005) 054013, arXiv:hep-ph/0412021.

[105] C. Englert and E. Re, *Bounding the top Yukawa with Higgs-associated single-top production*, Phys. Rev. **D89** (2014) 073020, arXiv:1402.0445.

[106] D0 Collaboration, V. M. Abazov et al., *An Improved determination of the width of the top quark*, Phys. Rev. **D85** (2012) 091104, arXiv:1201.4156.

[107] ATLAS Collaboration, G. Aad et al., *Measurement of the W boson polarization in top quark decays with the ATLAS detector*, JHEP **1206** (2012) 088, arXiv:1205.2484.

[108] M. Gillioz, R. Grber, A. Kapuvari, and M. Mhlleitner, *Vector-like Bottom Quarks in Composite Higgs Models*, JHEP **1403** (2014) 037, arXiv:1311.4453.

[109] C. Grojean, O. Matsedonskyi, and G. Panico, *Light top partners and precision physics*, JHEP **1310** (2013) 160, arXiv:1306.4655.

[110] CMS Collaboration, S. Chatrchyan et al., *Measurement of the $t\bar{t}$ production cross section in the dilepton channel in pp collisions at $\sqrt{s} = 8$ TeV*, JHEP **1402** (2014) 024, arXiv:1312.7582.

[111] CMS Collaboration, S. Chatrchyan et al., *Measurement of the $t\bar{t}$ production cross section in the dilepton channel in pp collisions at $\sqrt{s} = 7$ TeV*, JHEP **1211** (2012) 067, arXiv:1208.2671.

[112] P. Nason, S. Dawson, and R. K. Ellis, *The Total Cross-Section for the Production of Heavy Quarks in Hadronic Collisions*, Nucl. Phys. **B303** (1988) 607.

[113] W. Beenakker, H. Kuijf, W. van Neerven, and J. Smith, *QCD Corrections to Heavy Quark Production in p anti-p Collisions*, Phys. Rev. **D40** (1989) 54.

[114] P. Nason, S. Dawson, and R. K. Ellis, *The One Particle Inclusive Differential Cross-Section for Heavy Quark Production in Hadronic Collisions*, Nucl. Phys. **B327** (1989) 49.

[115] W. Beenakker et al., *QCD corrections to heavy quark production in hadron hadron collisions*, Nucl. Phys. **B351** (1991) 507.

[116] M. Czakon, P. Fiedler, and A. Mitov, *The total top quark pair production cross-section at hadron colliders through O(alpha_S$\hat{4}$)*, Phys. Rev. Lett. **110** (2013) 252004, arXiv:1303.6254.

[117] P. Baernreuther, M. Czakon, and A. Mitov, *Percent Level Precision Physics at the Tevatron: First Genuine NNLO QCD Corrections to $q\bar{q} \to t\bar{t} + X$*, Phys. Rev. Lett. **109** (2012) 132001, arXiv:1204.5201.

[118] M. Czakon and A. Mitov, *NNLO corrections to top-pair production at hadron colliders: the all-fermionic scattering channels*, JHEP **1212** (2012) 054, arXiv:1207.0236.

[119] M. Czakon and A. Mitov, *NNLO corrections to top pair production at hadron colliders: the quark-gluon reaction*, JHEP **1301** (2013) 080, arXiv:1210.6832.

[120] E. Laenen, J. Smith, and W. van Neerven, *All order resummation of soft gluon contributions to heavy quark production in hadron hadron collisions*, Nucl. Phys. **B369** (1992) 543.

[121] N. Kidonakis and G. F. Sterman, *Subleading logarithms in QCD hard scattering*, Phys. Lett. **B387** (1996) 867.

[122] N. Kidonakis and G. F. Sterman, *Resummation for QCD hard scattering*, Nucl. Phys. **B505** (1997) 321, arXiv:hep-ph/9705234.

[123] N. Kidonakis and R. Vogt, *The Theoretical top quark cross section at the Tevatron and the LHC*, Phys. Rev. **D78** (2008) 074005, arXiv:0805.3844.

[124] U. Langenfeld, S. Moch, and P. Uwer, *Measuring the running top-quark mass*, Phys. Rev. **D80** (2009) 054009, arXiv:0906.5273.

[125] M. Czakon, A. Mitov, and G. F. Sterman, *Threshold Resummation for Top-Pair Hadroproduction to Next-to-Next-to-Leading Log*, Phys. Rev. **D80** (2009) 074017, arXiv:0907.1790.

[126] M. Beneke, P. Falgari, and C. Schwinn, *Soft radiation in heavy-particle pair production: All-order colour structure and two-loop anomalous dimension*, Nucl. Phys. **B828** (2010) 69, arXiv:0907.1443.

[127] N. Kidonakis, *Next-to-next-to-leading soft-gluon corrections for the top quark cross section and transverse momentum distribution*, Phys. Rev. **D82** (2010) 114030, arXiv:1009.4935.

[128] V. Ahrens et al., *RG-improved single-particle inclusive cross sections and forward-backward asymmetry in $t\bar{t}$ production at hadron colliders*, JHEP **1109** (2011) 070, arXiv:1103.0550.

[129] N. Kidonakis and B. D. Pecjak, *Top-quark production and QCD*, Eur. Phys. J. **C72** (2012) 2084, arXiv:1108.6063.

[130] M. Cacciari et al., *Top-pair production at hadron colliders with next-to-next-to-leading logarithmic soft-gluon resummation*, Phys. Lett. **B710** (2012) 612, arXiv:1111.5869.

[131] M. Beneke et al., *Inclusive Top-Pair Production Phenomenology with TOPIXS*, JHEP **1207** (2012) 194, arXiv:1206.2454.

[132] M. Guzzi, K. Lipka, and S.-O. Moch, *Top-quark production at the LHC: differential cross section and phenomenological applications*, arXiv:1308.1635.

[133] A. Ferroglia, B. D. Pecjak, and L. L. Yang, *Top-quark pair production at high invariant mass: an NNLO soft plus virtual approximation*, JHEP **1309** (2013) 032, arXiv:1306.1537.

[134] A. Ferroglia, S. Marzani, B. D. Pecjak, and L. L. Yang, *Boosted top production: factorization and resummation for single-particle inclusive distributions*, JHEP **1401** (2014) 028, arXiv:1310.3836.

[135] M. Czakon and A. Mitov, *Inclusive Heavy Flavor Hadroproduction in NLO QCD: The Exact Analytic Result*, Nucl. Phys. **B824** (2010) 111, arXiv:0811.4119.

[136] S. Frixione, P. Nason, and G. Ridolfi, *A Positive-weight next-to-leading-order Monte Carlo for heavy flavour hadroproduction*, JHEP **0709** (2007) 126, arXiv:0707.3088.

[137] S. Frixione, P. Nason, and B. R. Webber, *Matching NLO QCD and parton showers in heavy flavor production*, JHEP **0308** (2003) 007, arXiv:hep-ph/0305252.

[138] R. Frederix, S. Frixione, F. Maltoni, and T. Stelzer, *Automation of next-to-leading order computations in QCD: The FKS subtraction*, JHEP **0910** (2009) 003, arXiv:0908.4272.

[139] F. Halzen, P. Hoyer, and C. Kim, *Forward - Backward Asymmetry of Hadroproduced Heavy Quarks in QCD*, Phys. Lett. **B195** (1987) 74.

[140] J. H. Kuhn and G. Rodrigo, *Charge asymmetry in hadroproduction of heavy quarks*, Phys. Rev. Lett. **81** (1998) 49, arXiv:hep-ph/9802268.

[141] J. H. Kuhn and G. Rodrigo, *Charge asymmetry of heavy quarks at hadron colliders*, Phys. Rev. **D59** (1999) 054017, arXiv:hep-ph/9807420.

[142] F. A. Berends, K. Gaemer, and R. Gastmans, *Hard photon corrections for the process* $e^+e^- \to \mu^\pm\mu^\mp$, Nucl. Phys. **B57** (1973) 381.

[143] F. A. Berends, R. Kleiss, S. Jadach, and Z. Was, *QED RADIATIVE CORRECTIONS TO ELECTRON - POSITRON ANNIHILATION INTO HEAVY FERMIONS*, Acta Phys. Polon. **B14** (1983) 413.

[144] W. Bernreuther and Z.-G. Si, *Top quark and leptonic charge asymmetries for the Tevatron and LHC*, Phys. Rev. **D86** (2012) 034026, arXiv:1205.6580.

[145] S. Berge and S. Westhoff, *Top-Quark Charge Asymmetry Goes Forward: Two New Observables for Hadron Colliders*, JHEP **1307** (2013) 179, arXiv:1305.3272.

[146] ATLAS Collaboration, *Measurement of the charge asymmetry in dileptonic decay of top quark pairs in pp collisions at ?s = 7 TeV using the ATLAS detector*, Tech. Rep. ATLAS-CONF-2012-057, CERN, Geneva, Jun, 2012.

[147] CMS Collaboration, S. Chatrchyan et al., *Measurements of the $t\bar{t}$ charge asymmetry using the dilepton decay channel in pp collisions at $\sqrt{s} = 7$ TeV*, arXiv:1402.3803.

[148] CMS Collaboration, *Combination of ATLAS and CMS ttbar charge asymmetry measurements using LHC proton-proton collisions at 7 TeV*, Tech. Rep. CMS-PAS-TOP-14-006, CERN, Geneva, 2014.

[149] CMS Collaboration, *Measurement of the ttbar charge asymmetry with lepton+jets events at 8 TeV*, Tech. Rep. CMS-PAS-TOP-12-033, CERN, Geneva, 2013.

[150] S. Westhoff, *Top Charge Asymmetry – Theory Status Fall 2013*, arXiv:1311.1127.

[151] J. H. Kuhn and G. Rodrigo, *Charge asymmetries of top quarks at hadron colliders revisited*, JHEP **1201** (2012) 063, arXiv:1109.6830.

[152] LHCb Collaboration, J. Alves, A. Augusto et al., *The LHCb Detector at the LHC*, JINST **3** (2008) S08005.

[153] LHCb : Technical Proposal, Tech. Proposal, CERN, Geneva, 1998.

[154] LHCb Collaboration, R. Aaij et al., *Inclusive W and Z production in the forward region at $\sqrt{s} = 7$ TeV*, JHEP **1206** (2012) 058, arXiv:1204.1620.

[155] LHCb collaboration, I. Bediaga et al., *Framework TDR for the LHCb Upgrade: Technical Design Report*, Tech. Rep. CERN-LHCC-2012-007. LHCb-TDR-12, CERN, Geneva, Apr, 2012.

[156] A. L. Kagan, J. F. Kamenik, G. Perez, and S. Stone, *Top LHCb Physics*, Phys. Rev. Lett. **107** (2011) 082003, arXiv:1103.3747.

[157] M. Cacciari, G. P. Salam, and G. Soyez, *FastJet User Manual*, Eur. Phys. J. **C72** (2012) 1896, arXiv:1111.6097.

[158] LHCb collaboration, R. Aaij et al., *Study of forward Z + jet production in pp collisions at $\sqrt{s} = 7$ TeV*, JHEP **1401** (2014) 033, arXiv:1310.8197.

[159] LHCb Collaboration, W. Barter, *Current and future jet measurements with LHCb, https://cds.cern.ch/record/1610595/files/LHCb-TALK-2013-338.pdf*, Tech. Rep. LHCb-TALK-2013-338, CERN, Geneva, Oct, 2013.

[160] LHCb collaboration, R. Aaij et al., *Measurement of the cross-section for $Z \to e^+e^-$ production in pp collisions at $\sqrt{s} = 7$ TeV*, JHEP **1302** (2013) 106, arXiv:1212.4620.

[161] S. Alioli, P. Nason, C. Oleari, and E. Re, *Vector boson plus one jet production in POWHEG*, JHEP **1101** (2011) 095, arXiv:1009.5594.

[162] S. Alioli, P. Nason, C. Oleari, and E. Re, *NLO single-top production matched with shower in POWHEG: s- and t-channel contributions*, JHEP **0909** (2009) 111, arXiv:0907.4076.

[163] R. Frederix, E. Re, and P. Torrielli, *Single-top t-channel hadroproduction in the four-flavour scheme with POWHEG and aMC@NLO*, JHEP **1209** (2012) 130, arXiv:1207.5391.

[164] C. Oleari and L. Reina, *W +- b $\bar{b}$ production in POWHEG*, JHEP **1108** (2011) 061, arXiv:1105.4488.

[165] J. Alwall et al., *MadGraph 5 : Going Beyond*, JHEP **1106** (2011) 128, arXiv:1106.0522.

[166] T. Melia, P. Nason, R. Rontsch, and G. Zanderighi, *W+W-, WZ and ZZ production in the POWHEG BOX*, JHEP **1111** (2011) 078, arXiv:1107.5051.

[167] E. Re, *Single-top Wt-channel production matched with parton showers using the POWHEG method*, Eur. Phys. J. **C71** (2011) 1547, arXiv:1009.2450.

[168] H. Brown, T. Bowcock, and D. Hutchcroft, Monitoring Radiation Damage in the Vertex Locato PhD thesis, Liverpool U., Sep, 2013, Presented 07 Nov 2013.

[169] ATLAS Collaboration, G. Aad et al., *Measurement of the WW cross section in $\sqrt{s} = 7$ TeV pp collisions with ATLAS*, Phys. Rev. Lett. **107** (2011) 041802, arXiv:1104.5225.

[170] CMS Collaboration, S. Chatrchyan et al., *Measurement of W^+W^- Production and Search for the Higgs Boson in pp Collisions at $\sqrt{s} = 7$ TeV*, Phys. Lett. **B699** (2011) 25, arXiv:1102.5429.

[171] ATLAS Collaboration, G. Aad et al., *Evidence for the associated production of a W boson and a top quark in ATLAS at $\sqrt{s} = 7$ TeV*, Phys. Lett. **B716** (2012) 142, arXiv:1205.5764.

[172] CMS Collaboration, S. Chatrchyan et al., *Evidence for associated production of a single top quark and W boson in pp collisions at $\sqrt{s} = 7$ TeV*, Phys. Rev. Lett. **110** (2013) 022003, arXiv:1209.3489.

[173] T. M. Tait, *The tW^- mode of single top production*, Phys. Rev. **D61** (2000) 034001, arXiv:hep-ph/9909352.

[174] M. Czakon, M. L. Mangano, A. Mitov, and J. Rojo, *Constraints on the gluon PDF from top quark pair production at hadron colliders*, JHEP **1307** (2013) 167, arXiv:1303.7215.

[175] Particle Data Group, J. Beringer et al., *Review of Particle Physics (RPP)*, Phys. Rev. **D86** (2012) 010001.

[176] LHC Higgs Cross Section Working Group, S. Dittmaier et al., *Handbook of LHC Higgs Cross Sections: 1. Inclusive Observables*, arXiv:1101.0593.

[177] R. D. Ball et al., *Parton Distribution Benchmarking with LHC Data*, JHEP **1304** (2013) 125, arXiv:1211.5142.

[178] M. Guzzi, K. Lipka, and S.-O. Moch, *Top-quark pair production at hadron colliders: differential cross section and phenomenological applications with DiffTop*, arXiv:1406.0386.

[179] *Measurement of the $t\bar{t}$ production cross-section in pp collisions at $\sqrt{s} = 8$ TeV using $e\mu$ events with b-tagged jets*, Tech. Rep. ATLAS-CONF-2013-097, CERN, Geneva, Sep, 2013.

[180] J. M. Campbell and R. K. Ellis, *Top-quark processes at NLO in production and decay*, arXiv:1204.1513.

[181] W. Hollik and D. Pagani, *The electroweak contribution to the top quark forward-backward asymmetry at the Tevatron*, Phys. Rev. **D84** (2011) 093003, arXiv:1107.2606.

[182] J. Brod et al., *Stealth QCD-like Strong Interactions and the t-tbar Asymmetry*, arXiv:1407.8188.

[183] P. Skands, B. Webber, and J. Winter, *QCD Coherence and the Top Quark Asymmetry*, JHEP **1207** (2012) 151, arXiv:1205.1466.

[184] L. Wolfenstein, *Parametrization of the Kobayashi-Maskawa Matrix*, Phys. Rev. Lett. **51** (1983) 1945.

[185] CMS Collaboration, V. Khachatryan et al., *Measurement of the t-channel single-top-quark production cross section and of the $| V_{tb} |$ CKM matrix element in pp collisions at $\sqrt{s}$= 8 TeV*, JHEP **1406** (2014) 090, arXiv:1403.7366.